

VALIDATION OF A NOVEL DOWNDRAFT OUTFLOW SIMULATOR:
A SLOT JET WIND TUNNEL

(Spine title: Validation of a novel downdraft outflow simulator)

(Thesis format: Integrated-Article)

by

William E. Lin

Graduate Program in Engineering Science

A thesis submitted in partial fulfilment
of the requirements for the degree of
Doctor of Philosophy

The School of Graduate and Postdoctoral Studies
The University of Western Ontario
London, Ontario, Canada

© William E. Lin 2010

THE UNIVERSITY OF WESTERN ONTARIO
SCHOOL OF GRADUATE AND POSTDOCTORAL STUDIES

CERTIFICATE OF EXAMINATION

Supervisor

Dr. Eric Savory

Supervisory Committee

Dr. Gregory A. Kopp

Dr. Robert J. Martinuzzi

Examiners

Dr. Horia Hangan

Dr. Wayne K. Hocking

Dr. Kamran Siddiqui

Dr. Theodore Stathopoulos

The thesis by

William Elroy Lin

entitled:

Validation of a Novel Downdraft Outflow Simulator:

A Slot Jet Wind Tunnel

is accepted in partial fulfilment of the
requirements for the degree of
Doctor of Philosophy

Date April 2010

Dr. Martin Zinke-Allmang

ABSTRACT

Downdraft outflows are known to inflict catastrophic damage to built structures. An experimental test facility is needed, in which models of built structures are subjected to this type of wind load to ensure adequate structural design. This thesis investigates the physical simulation of a downdraft outflow using a novel approach. It is hypothesized that a downdraft outflow could be adequately represented, for wind engineering purposes, by a plane wall jet arising from a rectangular slot nozzle. A physical test facility was developed and validated against available downdraft outflow observations, and results from numerical and experimental simulation of wall jets.

Wall jets are typically generated in a plane or radial configuration. The feasibility of approximating one configuration with the other was investigated. The discrepancy between the normalised mean velocity profiles for the developed plane wall jet and the developing radial wall jet was generally less than the range attributable to total measurement uncertainty. Where maximum turbulence intensities and turbulent kinetic energy production occurred, turbulence quantity profiles for the developing radial wall jet provided the best match with those of the developed plane wall jet.

The wall jet findings aided the design of a downdraft outflow simulator based on generating a plane wall jet with a rectangular slot nozzle. The outflow gust was modelled with an actuated gate that generated a dominant roll vortex. Wind speed measurements were compared to predictions by a sub-cloud numerical model. Simulator performance was compared with field observations of a 2002 Texas event. Wind speed records were decomposed according to classical time series analysis. Length scales, characterising the coarse and fine flow structure, were determined from the time-varying mean and residual components, respectively. The simulated downdraft outflow was approximately 1200 times smaller in spatial extent than the 2002 Texas event. Keeping in mind the variability of downdraft size, microburst outflows would be modelled at 1:100 to 1:500 length scaling in the Wind Tunnel 1 Downdraft Outflow Simulator at The University of Western Ontario, i.e. a range comparable to that of conventional boundary layer wind tunnels.

Keywords: downdraft outflow, downburst, microburst, thunderstorm gust, turbulent wall jet, slot jet, plane wall jet, hot-wire anemometry, wind tunnel, time series analysis.

CO-AUTHORSHIP

This thesis has been prepared in accordance with the regulations for an Integrated-Article format thesis, as stipulated by the School of Graduate and Postdoctoral Studies at The University of Western Ontario. This thesis includes co-authored articles and the following passages explicitly state the contributors, and the nature and extent of their contribution. At the Thesis Examination, the Supervisor attested to the accuracy of the following co-authorship statements.

Chapter 2: A comparison of plane and radial turbulent wall jets

The experiments were designed by W.E. Lin with guidance from E. Savory. The experiments were conducted by W.E. Lin with physical assistance from C. Novacco. W.E. Lin processed and analysed the data, completed comparisons with the literature, and authored the document. E. Savory supervised the work, provided advice, read the draft versions, and suggested revisions. An expanded version of this chapter is being prepared for submission to the *ASME Journal of Fluids Engineering*, 2010.

Chapter 3: Quasi-steady modelling of a downdraft outflow

The experiments were designed by W.E. Lin with guidance from E. Savory. The experiments were conducted by W.E. Lin. Some data collection was done by C. Novacco with guidance from W.E. Lin. W.E. Lin processed and analysed the data, completed comparisons with the literature, and authored the document. E. Savory supervised the work, provided advice, read the draft versions, and suggested revisions. Excerpts from this chapter were published as *Wind and Structures* **9**(6), 2006.

Chapter 4: Transient modelling of a downdraft outflow

The experiments were designed by W.E. Lin with guidance from E. Savory. Experiments were conducted by W.E. Lin and C. Novacco. C. Novacco performed some data processing with guidance from W.E. Lin, with some data processing also done by the latter. L.G. Orf and W.E. Lin determined the numerical simulations to be performed. L.G.

Orf conducted the numerical simulations. W.E. Lin analysed the experimental and numerical data, completed comparisons with the literature, and authored the document.

E. Savory supervised the work, provided advice, read the draft versions, and suggested revisions. Excerpts from this chapter were published as *Wind and Structures* **10**(4), 2007.

Chapter 5: UWO Wind Tunnel 1 downdraft outflow simulator

W.E. Lin designed and conducted the experiments, processed and analysed the data, and authored the document. E. Savory supervised the work, provided advice, read the draft versions, and suggested revisions. A condensed version of this chapter is in press for publication in *Wind and Structures*.

To those who are to follow...

*I hope I have left something of use
and something of joy.*

ACKNOWLEDGMENTS

This work could not have been completed without the financial support of the following sponsors: Natural Sciences and Engineering Research Council of Canada (NSERC), Manitoba Hydro, the Centre for Energy Advancement through Technological Innovation, and the Institute for Catastrophic Loss Reduction. The author gratefully acknowledges the Association of Universities and Colleges of Canada for awarding a Public Safety Canada Research Fellowship, and NSERC for awarding a Postgraduate Scholarship.

The author thanks the staff at the Alan G. Davenport Wind Engineering Group who supported this work. Mr. C. Vandelaar and Dr. J.P.C. King led the design and implementation of the structural additions to Wind Tunnel 1. Mr. C. Vandelaar and the UWO University Machine Shop provided design expertise and implemented the experimental facilities. Some experimental equipment was kindly made available by Dr. G.A. Kopp and Dr. R.J. Martinuzzi. Dr. L.G. Orf and Ms. C. Novacco were exceedingly pleasant and bright collaborators on parts of this research. Dr. J.L Schroeder at Texas Tech University kindly made the raw measurements from the 2002 Lubbock downdraft available. Dr. J.D. Holmes provided helpful feedback and insight.

Colleagues at the Advanced Fluid Mechanics research group deserve credit for providing a warm place to conduct research. The author expresses his deepest appreciation to Dr. E. Savory for providing the opportunity to do this research. His patience, hardy support, and helpful disposition aided the completion of this thesis.

TABLE OF CONTENTS

CERTIFICATE OF EXAMINATION	ii
ABSTRACT	iii
CO-AUTHORSHIP	iv
DEDICATION	vi
ACKNOWLEDGMENTS	vii
TABLE OF CONTENTS	viii
LIST OF TABLES	xi
LIST OF FIGURES	xii
LIST OF ABBREVIATIONS	xv
LIST OF SYMBOLS	xvi
CHAPTER 1: INTRODUCTION	1
1.1 Surface-level winds from downdrafts	1
1.2 Physical simulation of atmospheric wind loads	6
1.3 Computational fluid dynamics of downbursts	7
1.4 Scope	8
1.5 Objective	8
1.6 References	10
CHAPTER 2: COMPARISON OF PLANE & RADIAL TURBULENT WALL JETS	13
2.1 Introduction	13
2.2 Previous literature	14
2.2.1 Radial wall jet	14
2.2.2 Plane wall jet	17
2.3 Present experiment	20
2.3.1 Prototype slot jet wind tunnel	20
2.3.2 Velocity measurement system	20
2.3.3 Uncertainty analysis	22
2.4 Comparison of the plane and the radial wall jet	23
2.4.1 Time-averaged velocity profiles	23
2.4.2 Turbulence quantity profiles	26
2.4.3 Jet spread and velocity decay	31
2.5 Conclusions	33
2.6 References	34
CHAPTER 3: QUASI-STEADY MODELLING OF A DOWNDRAFT OUTFLOW	36
3.1 Introduction	36
3.2 Experimental methodology	38
3.2.1 Previous approaches	38
3.2.2 Present approach	41
3.2.3 Prototype test facility	43
3.2.4 Velocity profile measurements	43
3.3 Comparison of plane and radial wall jet data	44
3.4 Estimated model scale	53
3.5 Validity of the 2-D assumption for an idealised outflow	55
3.6 Conclusions	59
3.7 References	61

CHAPTER 4: TRANSIENT MODELLING OF A DOWNDRAFT OUTFLOW	64
4.1 Introduction	64
4.2 Background	64
4.2.1 Previous experimental modelling studies	64
4.2.2 Previous numerical modelling studies	67
4.3 Key considerations	69
4.4 Experimental simulation	74
4.4.1 Test facility	74
4.4.1.1 Translating gate	77
4.4.1.2 Rotating gate	78
4.4.2 Velocity measurements	79
4.5 Discussion of results	80
4.5.1 Slot jet results	80
4.5.1.1 Flow visualisation	80
4.5.1.2 Lateral correlation of vertical profiles	81
4.5.1.3 $\langle U \rangle$ profile evolution	82
4.5.1.4 Turbulence intensity	83
4.5.1.5 Comparison of flow with translating and rotating gate designs	84
4.5.2 Bryan Cloud Model results	85
4.5.3 Comparison of velocity profiles	96
4.5.4 Comparison of velocity histories	98
4.6 Scale of simulations	101
4.7 Conclusions	104
4.8 References	105
CHAPTER 5: UWO WIND TUNNEL 1 DOWNDRAFT OUTFLOW SIMULATOR	108
5.1 Introduction	108
5.2 Description of the simulator	109
5.2.1 Facility development	109
5.2.2 Facility characteristics	110
5.2.3 Anemometry and measurement procedures	113
5.2.4 Initial flow conditions	113
5.2.5 Downstream flow conditions	115
5.2.5.1 Ensemble-averaging	116
5.2.5.2 Sample function averaging	118
5.3 Time-varying mean wind speed from simulator and field observations	122
5.3.1 Comparison metrics	123
5.3.2 Length scaling of the coarse flow features	129
5.4 Residual wind speed from simulator and field observations	130
5.4.1 Stationarity	130
5.4.2 Residual wind speed distribution	138
5.4.3 Residual wind speed relative to mean wind speed	141
5.4.4 Correlation and spectral analysis	146
5.4.5 Length scaling of the fine flow features	150
5.5 Conclusions and future work	150
5.6 References	153

CHAPTER 6: CLOSURE	155
6.1 Summary	155
6.2 Conclusions	155
6.3 Recommendations	158
CURRICULUM VITÆ	159

LIST OF TABLES

Table 2.1: Uncertainty of time-averaged streamwise velocity measurements	23
Table 2.2: Turbulence profile similarity	27
Table 2.3: Summary of plane wall jet spread parameters	32
Table 2.4: Summary of radial wall jet spread parameters	33
Table 3.1: Comparison of full-scale and impinging jet studies	40
Table 3.2: Estimated length scale of various downdraft outflow simulators	54
Table 3.3: Lag distance	56
Table 3.4: Diffluence of an outflow from a translating downburst	59
Table 3.5: Diffluence of an outflow from a downburst line	59
Table 4.1: Released fluid parcel simulations	66
Table 4.2: Transient impinging jet simulations	67
Table 4.3: Reported and estimated scales for time-dependent experiments	102
Table 5.1: Characteristics of the boundary layers at the slot nozzle	115
Table 5.2: Crossed hot-wire probe locations	118
Table 5.3: Characteristics of ensemble-averaged wind speed histories	124
Table 5.4: Characteristics of running mean wind speed histories (WT1 DOS)	125
Table 5.5: Characteristics of running mean wind speed histories (2002 RFD)	126
Table 5.6: Comparison of normalised wind speed history characteristics	127
Table 5.7: Integral time scale of residual wind speed (2002 RFD)	147
Table 5.8: Integral time scale of residual wind speed (WT1 DOS)	147

LIST OF FIGURES

Figure 1.1: Lattice tower failure	2
Figure 1.2: Horizontal wind speed record from the Andrews AFB downburst	3
Figure 1.3: Expected frequency of downbursts of various intensities	5
Figure 1.4: Depiction of a thunderstorm downdraft outflow	9
Figure 1.5: Depiction of a plane wall jet arising from a rectangular slot nozzle	9
Figure 2.1: Two common wall jet configurations	16
Figure 2.2: Radial jet apparatus used by Bakke (1957)	16
Figure 2.3: Normal-to-wall profile of time-averaged streamwise velocity	25
Figure 2.4: Difference between streamwise velocity of plane and radial wall jets	26
Figure 2.5: Normal-to-wall profile of streamwise turbulence intensity	28
Figure 2.6: Normal-to-wall profile of normal-to-wall turbulence intensity	29
Figure 2.7: Normal-to-wall profile of the dominant Reynolds stress component	30
Figure 3.1: Velocity profiles for different types of wind	38
Figure 3.2: Radial wall jet from a round nozzle	39
Figure 3.3: Plane wall jet from a rectangular nozzle	42
Figure 3.4: Prototype slot jet wind tunnel for downburst outflow simulation	43
Figure 3.5: Mean streamwise velocity for plane wall jets and full-scale events	47
Figure 3.6: Mean streamwise velocity for plane and radial wall jets	48
Figure 3.7: Streamwise turbulence intensity profiles for plane and radial wall jets	50
Figure 3.8: Vertical turbulence intensity profiles for plane and radial wall jets	51
Figure 3.9: Turbulent shear stress profiles for plane and radial wall jets	52
Figure 3.10: Plan view of a radially-expanding gust front	56
Figure 3.11: Plan view of a curved gust front	57
Figure 3.12: Damage footprint of a translating downburst	58
Figure 4.1: Velocity history at 4.9 m above ground level for a severe outflow	70
Figure 4.2: Histogram of full-scale peak wind longevity	71
Figure 4.3: A sequence of photographs for an outflow vortex from JAWS	72
Figure 4.4: Coordinate system in the slot jet facility	75
Figure 4.5: Linear motion gate assembly	76

Figure 4.6: Rotating gate at start position and extreme positions during actuation	78
Figure 4.7: Data flow for transient jet results	79
Figure 4.8: Transient simulation vortex from prototype slot jet facility	81
Figure 4.9: Composite wind speed profiles	82
Figure 4.10: Moving-averaged wind speed history	84
Figure 4.11: Peak composite wind speed profiles for two gate designs	85
Figure 4.12: Contours of velocity when $U_{p, \max}$ occurs in CM1-Case 1	87
Figure 4.13: Contours of velocity when $U_{p, \max}$ occurs in CM1-Case 2	88
Figure 4.14: Evolution of velocity and potential temperature for CM1-Case 3	90, 1
Figure 4.15: Movement of Structures A and B through the CM1-Case 3 flow field	92
Figure 4.16: Contours of velocity as encountered by Structure A	94
Figure 4.17: Contours of velocity as encountered by Structure B	95
Figure 4.18: Vertical profiles of horizontal wind velocity	96
Figure 4.19: Comparison of vertical profiles of horizontal wind velocity	97
Figure 4.20: Vertical profiles of vertical wind velocity	99
Figure 4.21: Comparison of horizontal wind velocity history	100
Figure 4.22: Characteristic velocity and time for an observed downburst outflow	103
Figure 5.1: Modifications to UWO WT1 for downburst outflow simulation	111
Figure 5.2: WT1 DOS assembly and nomenclature	112
Figure 5.3: Initial conditions of the slot jet	114
Figure 5.4: Flow visualisation from the WT1 DOS	117
Figure 5.5: Wind speed history from single hot-wire probe	118
Figure 5.6: Ensemble-averaged wind speed history from single hot-wire probe	119
Figure 5.7: Running mean and residual wind speed history	119
Figure 5.8: Effect of moving-average filter duration on time-averaged residual	120
Figure 5.9: Effect of moving-average filter duration on gust factor	121
Figure 5.10: Velocity history from 2002 RFD	122
Figure 5.11: Streamwise advection of the dominant vortex centre	124
Figure 5.12: Wind speed histories in WT1 DOS and 2002 RFD	128
Figure 5.13: Variation of wind speed history with span-wise location	128
Figure 5.14: Probe locations	129

Figure 5.15: Dependency of MS residual on window duration (2002 RFD)	132
Figure 5.16: Dependency of MS residual on window location (2002 RFD)	133-5
Figure 5.17: Dependency of MS residual on window duration (WT1 DOS)	136
Figure 5.18: Dependency of MS residual on window location (WT1 DOS)	137
Figure 5.19: Residual wind speed distribution (2002 RFD)	139
Figure 5.20: Residual wind speed distribution (WT1 DOS)	140
Figure 5.21: Vertical profiles of peak wind speed	142
Figure 5.22: Vertical profiles of gust factor	144
Figure 5.23: Turbulence quantities and moving-averaged wind speed (2002 RFD)	145
Figure 5.24: Turbulence quantities and moving-averaged wind speed (WT1 DOS)	145
Figure 5.25: Integral time scale of residual wind speed fluctuations (2002 RFD)	146
Figure 5.26: Integral time scale of residual wind speed fluctuations (WT1 DOS)	147
Figure 5.27: Auto-spectral density of residual wind speed fluctuations	149

LIST OF ABBREVIATIONS

ABL	atmospheric boundary layer
AFB	air force base
AGL	above ground level
A/D	analog to digital
CAPE	convective available potential energy
CFD	computational fluid dynamics
CHW	crossed hot-wire
CM1	Bryan Cloud Model
HWA	hot-wire anemometry
H2008	Holmes <i>et al.</i> (2008)
JAWS	Joint Airport Weather Studies
LES	large-eddy simulation
MS	mean square
NIMROD	Northern Illinois Meteorological Research On Downburst
PIV	particle-image velocimetry
RFD	rear-flank downdraft
RMS	root mean square
SHW	single hot-wire
TKE	turbulent kinetic energy
URANS	unsteady Reynolds-averaged Navier-Stokes
UWO	University of Western Ontario
WT1 DOS	Wind Tunnel 1 downdraft outflow simulator

LIST OF SYMBOLS

Chapter 2

A_p, A_r	wall jet spread constant (plane, radial)
b	slot height
B_p, B_r	wall jet decay constant (plane, radial)
C_0, C_1, C_2, \dots	voltage-to-velocity transfer function constants
D	nozzle diameter
E	calibration voltage
I_u, I_w	turbulence intensity (streamwise, wall-normal)
k_1, k_2	crossed hot-wire yaw coefficients
K	constant
m_p, m_r	wall jet spread exponent (plane, radial)
n_p, n_r	wall jet decay exponent (plane, radial)
r	radial coordinate
r_0 (or x_0)	virtual origin of the radial wall jet (or plane wall jet)
$Re_b \equiv U_j \cdot b / \nu$	slot Reynolds number (plane)
$Re_x \equiv U_m \cdot x / \nu$	distance Reynolds number
$Re_D \equiv W_j \cdot D / \nu$	nozzle Reynolds number (radial)
t	slot top thickness in z-direction
$\overline{u'w'}$	dominant component of Reynolds stress
U	time-averaged streamwise velocity
U_{cal}	calibration velocity
U_j, W_j	velocity at slot or nozzle exit
U_m	maximum U at a given x-location
U_1, U_2	velocity in wire coordinate system
x	streamwise coordinate
X_1	distance from test facility inlet to slot exit
X_2	distance from slot exit to test facility exit
y	spanwise coordinate
Y	test section dimension in y-direction

z	wall-normal coordinate
z_m	z where U_m occurs
z_D	nozzle exit z -location
$z_{0.5}$	outer half-width $\equiv z$ where $0.5 \cdot U_m$ occurs ($z_{0.5} > z_m$)
Z	test section dimension in z -direction
δ	jet extent in the z -direction
ν	kinematic viscosity

Chapter 3

b	slot height
D	downdraft diameter
D_n	nozzle diameter
I_u, I_w	turbulence intensity
m	transverse width
n	transverse coordinate (normal to s -direction)
r	radial coordinate
r^*	lag distance
$Re_b \equiv U_j \cdot b / \nu$	slot Reynolds number (plane)
$Re_D \equiv W_j \cdot D / \nu$	nozzle Reynolds number (radial)
s	longitudinal coordinate (normal to n -direction)
$\overline{u'w'}$	dominant component of Reynolds stress
U	time-averaged streamwise velocity
U_e	external streamwise velocity
U_j, W_j	velocity at slot or nozzle exit
U_m	maximum U
U_r	wind velocity in the longitudinal direction
x	streamwise coordinate
z	wall-normal coordinate
z_m	z where U_m occurs
$z_{0.5}$	outer half-width $\equiv z$ where $0.5 \cdot U_m$ occurs ($z_{0.5} > z_m$)
θ	angular deviation from the s -direction

Chapter 4

A (subscript)	Structure A (CM1)
b	slot height
B (subscript)	Structure B (CM1)
C_{DN}	drag coefficient for statically neutral environmental conditions
D	downdraft diameter
D_n	nozzle or cylinder exit diameter
g	gravitational acceleration
\hat{I}_u	estimated effective turbulence intensity
m (subscript)	largest value in space
n	number of realisations
nt	time step index (CM1)
N	number of measurement locations in a profile
p (subscript)	largest value in time
r	radial coordinate (axisymmetric flow)
R_0	length scale (released fluid)
Re_D	nozzle Reynolds number (impinging jet)
Re_ρ	flow Reynolds number (released fluid)
s	ordered sample number
t	time
t_p	time to peak velocity with respect to the simulation start time (CM1)
$t_{p, max}$	time to peak maximum velocity with respect to the simulation start time (CM1)
t_s	time corresponding to ordered sample number s
t^*	total duration to open and close gate
T_0	time scale (released fluid)
$T_{0.5-U_p'}$	velocity history time scale
U	horizontal velocity
U_j	slot exit velocity

$U_{j, steady}$	steady slot exit velocity
U_m	maximum velocity \equiv largest value in space (typically pertaining to a vertical profile at fixed r or x)
U_t	downburst translational velocity
U_p	peak velocity \equiv largest value in time
$U_{p, max}$	peak maximum velocity \equiv largest overall value in an unsteady flow field
U_p'	peak velocity excess above baseline velocity
U_{MA}	moving average of U history
$\langle U \rangle$	ensemble-averaged velocity
V_0	velocity scale (released fluid)
w_1, w_2, w_3	moving average weights
W	vertical velocity
W_{min}	minimum vertical velocity
W_n	nozzle exit velocity (impinging jet)
x	streamwise coordinate (slot jet)
x'	horizontal distance from geometric centre of cooling source volume (CM1)
y	spanwise coordinate (slot jet)
Y	working section span (slot jet)
z	vertical coordinate
z_{axis}	height of vortex axis above solid boundary
z_n	nozzle or cylinder exit height above impingement plane
z_0	aerodynamic roughness height
$z_{0.5}$	outer half-width \equiv z where $0.5 \cdot U_m$ occurs ($z_{0.5} > z_m$)
$\Delta\theta$	change in angular position (rotating gate)
ν	kinematic viscosity
ρ	fluid density
$\Delta\rho$	fluid density difference

Chapter 5

b	slot nozzle height
c	hot-wire probe configuration index
$E[\bullet]$	expected value operator
f	frequency
f_s	sampling frequency
G	gust factor
H	shape factor $\equiv \delta^* / \Theta$
$I_u(t), I_w(t)$	time-varying turbulence intensity (streamwise, vertical)
k	ensemble index
K	ensemble size = total no. of simulator trials for a fixed set of conditions
ℓ	characteristic length
m	slope of a piecewise linear segment of a wind speed history; see Eq. (5.4)
<i>maximum</i>	largest value over space
M	filter size (no. of samples)
<i>peak</i>	largest value over time (at a fixed point)
\bullet_p	peak value operator
R^2	coefficient of determination (regression)
S_{ss}	auto-spectral density estimate for an input signal s
St	Strouhal number; see Eq. (5.14)
t	time
T_I	Eulerian integral time scale (i.e. de-correlation time of turbulence)
T_W	averaging window duration
$T_{n, \alpha}$	duration between a pre- and a post-peak occurrence of $U/U_p = \alpha$
$T_{0.5}$	half-duration = duration between a pre- and a post-peak occurrence of $U_{0.5}$
u	wind speed (as acquired from anemometer)

U	moving-averaged wind speed (i.e. running mean)
U_c	advective wind speed
$U_{0.5}$	half-speed for a U record; see Eq. (5.3)
x	distance downstream of the slot exit
X	wind tunnel length
y	distance from the wind tunnel centreline
Y	wind tunnel span
z	distance above the working section floor
z_0	aerodynamic roughness height
Z	wind tunnel height
α	threshold U/U_p value for determining a characteristic duration
δ	normal-to-wall distance over which \bar{u} increases monotonically to the constant external velocity of the boundary layer
$\delta^* \equiv \int_0^\delta \left(1 - \frac{u}{\bar{u}}\right) dz$	displacement thickness
$\Delta\bullet$	finite change of a variable
λ_L	ratio of characteristic lengths
λ_T	ratio of characteristic times
λ_V	ratio of characteristic velocities
$\Theta \equiv \int_0^\delta \frac{u}{\bar{u}} \left(1 - \frac{u}{\bar{u}}\right) dz$	momentum thickness
ρ_{ss}	auto-correlation coefficient for an input signal s
τ	auto-correlation lag duration
$\{\bullet\}$	random process
$\langle\bullet\rangle$	ensemble-average operator
$\overline{\bullet}$	time-average operator

CHAPTER 1 INTRODUCTION

1.1 Surface-level winds from downdrafts

Meteorological field studies have identified downdrafts that persist to ground level as potential severe wind hazards in the lowest portion of the troposphere. In particular, the term “downburst” refers to a convective downdraft that impacts the surface, and results in a divergent wind flow. A star-shaped damage imprint is remnant on some types of terrain (Fujita 1985). Convective storm conditions are distinguished from the neutral conditions of the conventional boundary layer by the presence of updrafts and downdrafts. Thus, downbursts have traditionally been discussed with reference to thunderstorms.

It has been put forth that depictions of downdrafts can be traced back to Leonardo da Vinci’s notebook. Gedzelman (1990) espoused that the Renaissance man’s *Deluge* sketches were careful and deliberate studies of eddy motion related to thunderstorm downbursts. Lugt (1983) presented a comprehensive historical and technical review that explained how eddying fluid motion, even in ancient times, has been relevant to humans. Kessler (1983) compiled social and technical commentary on the impact of thunderstorms in human affairs. Thunderstorm winds tend to be disruptive to human concerns such as agriculture, aviation and the built environment (e.g. the high-voltage power transmission infrastructure of Fig. 1.1). Exposure of power transmission systems to damaging winds is of particular concern because line targets are at greater risk of exposure than point targets. Risk models found that the return period for intersection of a transmission line by a storm was inversely proportional to the length of the line (Holmes 1999). Qualitative assessments of tower damage and aerial surveys of debris scatter patterns suggested downbursts have caused catastrophic failure of transmission lines throughout the world.

Developments in downdraft research have been well-documented by the meteorological community (Wakimoto 2001, Wilson and Wakimoto 2001, Hjelmfelt 2003). Early studies in the 1970s were motivated by serious concerns of the downburst as an aviation hazard. Numerous incidents of downed aircraft and other calamities involving intense downdraft outflows were documented by Fujita (1985).

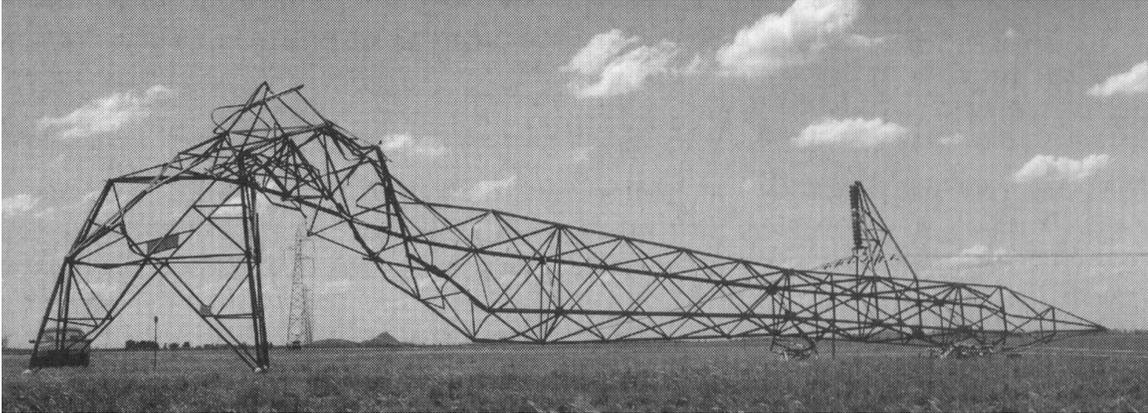


Figure 1.1: Lattice tower failure north of Bendigo, Australia in 1993 (Holmes 2001)

Fujita and Wakimoto (1981) initially classified downdrafts based on the order of magnitude of their damaging wind region size. Surface damage patterns from burst swaths, microbursts, and downbursts had horizontal scales of 1×10^2 , 1×10^3 , and 1×10^4 m, respectively. Additionally, downbursts, with a damage radius greater than 4 km, were referred to as macrobursts; smaller ones were microbursts. This length scale was a typical runway length at a large airport. Microbursts were generally regarded as having more destructive potential than macrobursts.

Several types of convectively-driven downdrafts and their interactions have since been identified, as reviewed by Wakimoto (2001). Strong local downdrafts can be embedded within mesoscale convection systems, such as bow echoes and derechos. Furthermore, the rear-flank, forward-flank, and occlusion downdrafts are associated with supercell thunderstorms. These larger types of downdrafts often occur in concert with more localised phenomena, i.e. tornados and/or downbursts.

Downburst clusters are known constituents of complex supercell flows. However, isolated downbursts of damaging intensity have also been observed to occur with little warning (Fujita 1985, Hjelmfelt 1988, McNulty 1991); although, detailed records of extreme events are rare. As shown by Fig. 1.2, the Andrews Air Force Base (AFB) downburst yielded a peak gust in excess of 67 m/s at a propeller anemometer located 4.9 m above ground level (Fujita 1985, 1990). This event appeared to be an isolated wet downburst.

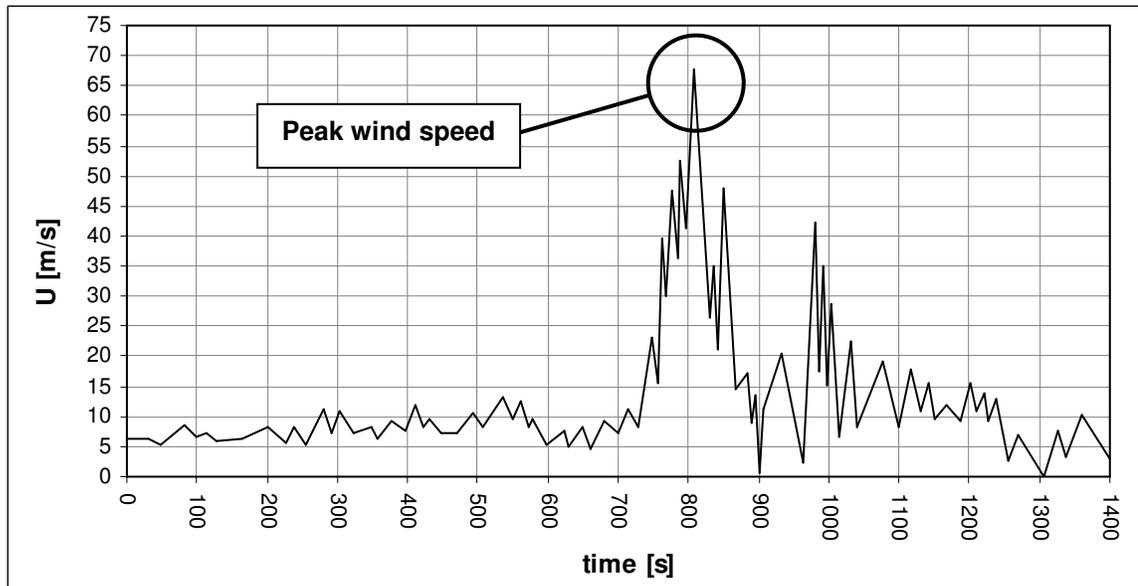


Figure 1.2 Horizontal wind speed record from the Andrews AFB downburst on 1 August 1983 (data from Fujita 1985)

For clarity, a few definitions are given here. Chapters 2 and 3 primarily deal with the largest wind speed in space, which will be referred to as “maximum” wind speed. Chapters 4 and 5 address the largest value in time at a fixed spatial location, which will be referred to as “peak” wind speed. The peak maximum velocity of an outflow is of primary interest for structural loading.

Fieldwork limitations are a significant obstacle to the study and forecasting of damaging events. Satellite imaging can track general storm motion but cannot discern internal structure with the accuracy required for engineering applications. Lidar may be useful if clouds do not interfere with optical radiation (Doviak and Zrníc 1988). Doppler radar has been the meteorologist’s instrument of choice, as it permitted the detection of clear air downbursts that were associated with virga and the study of the internal structure of thunderstorm cumulonimbi.

Although it was originally questioned whether downdrafts could reach close enough to the planetary surface to have any noticeable effect, field photography¹ provided evidence that this was in fact the case. Measurements with Doppler radar networks documented the structure and morphology of downbursts. Key studies included the

¹ See National Oceanic and Atmospheric Administration photo library (World Wide Web).

Northern Illinois Meteorological Research On Downburst (NIMROD) and the Joint Airport Weather Studies (JAWS) project in Colorado (Wakimoto 1982, Wilson *et al.* 1984, Fujita 1985, Hjelmfelt 1988). In the NIMROD study, three Doppler radars were located at 60 km spacing, in order to increase the likelihood of downburst detection. This preliminary investigation detected approximately 50 events during the spring and summer of 1978. With a radar spacing of 15 to 28 km, the subsequent JAWS study produced well-defined vector plots of the horizontal mean velocity field, showed the variability of the reconstructed 3-D wind field from event to event, and corroborated that downburst occurrence was more common than previously thought.

Dedicated radar stations at sufficiently close spacing can resolve the low-level kinematic structure of downbursts. However, technological challenges for detection include contamination of radar echoes by ground clutter and a possible lack of tracer particles in dry downbursts. Some of the strongest downbursts analyzed by Hjelmfelt (1988) occurred with very low reflectivity at the velocity maximum. This characteristic would make it difficult to forecast and study damaging outflows. Observation of extreme events is complicated by several other factors. Compared to typical meteorological scales, the duration and spatial extent of a strong downburst outflow are brief and small, respectively. An event with strong winds near peak gust that last for more than 5 minutes is considered long-lived. A strong outflow generally affects an area of less than 4 km diameter. In conjunction with the fact that active storm regions (e.g. Canadian Prairie provinces and American Midwestern states) have relatively low population density, it is probable that the historical meteorological record underestimated the number of downburst occurrences due to an absence of observers or mistaken identification as a tornado (Fujita 1990). The historical record should become more accurate as modern weather tracking and current meteorological knowledge become more pervasive.

Fortunately, the majority of observed downbursts in these field studies were likely not of sufficient intensity to damage built structures. The peak wind speeds recorded in NIMROD and JAWS downbursts were mostly less than F1 on the damage specification F-scale (Fujita 1981). Likely structural damage is expected at F1 and greater. The largest speeds reported for 50 NIMROD and 186 JAWS downbursts were only 31.3 and 32.6 m/s, respectively. Fujita projected that annual frequency decreases exponentially as

intensity increases, as indicated in Fig. 1.3. Nonetheless, the annual occurrence of four events as intense as the Andrews Air Force Base (AFB) downburst in the contiguous United States is not trivial since they can cause considerable damage and loss of life if they occur in a populous area. Furthermore, the projected annual frequency of events at F1, and greater, is not trivial.

More recently, Gast and Schroeder (2003) mounted instrumentation on mobile towers. By timely deployment of the towers in the path of an approaching supercell, they obtained high-resolution measurements of the kinematic and thermodynamic structure of a rear-flank downdraft (RFD) with a peak wind speed of 43 m/s. Clearly, simultaneous field measurements at multiple points of a transient phenomenon are difficult to obtain. For engineering applications where a large population of observed events is needed to meet required confidence levels, researchers have turned to laboratory and computer simulations to supplement full-scale observations. A modelling approach helped the wind engineering pioneers study the wind loading of structures by the atmospheric boundary layer, and it is even more imperative for the study of wind loading of structures by downdraft outflows.

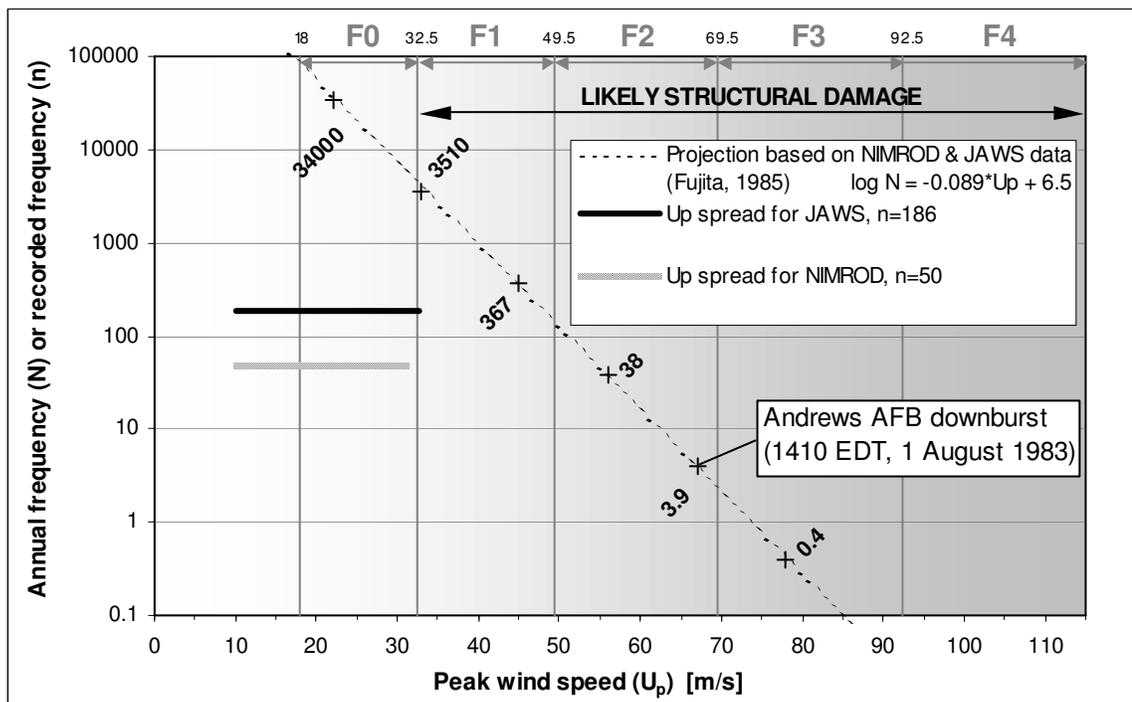


Figure 1.3: Expected frequency of downbursts of various intensities

1.2 Physical simulation of atmospheric wind loads

The atmospheric boundary layer wind tunnel has had a remarkable progression from the early developments in the 1950s to its current role as a refined design tool that assists structural designers, civil engineers and architects (Cermak 2003). It is used to simulate near-surface winds that have long-duration gusts and statistically stationary wind speed over a defined averaging duration. The ability to repeatedly test structural models under realistic wind conditions and in numerous configurations has enabled advances in building design.

From the field studies discussed in Section 1.1, it is well-known that downdraft outflows have different characteristics than boundary layer winds. The recognition that downdraft outflows represent the design loads, in many locales, motivates the further development of physical test facilities. Advances in the meteorological understanding of storms (Wakimoto 2001) further encourage the development of the next generation of wind tunnels. The engineering challenge has been to achieve a simulation of sufficiently large physical size, such that properly-scaled structural models can be readily fabricated and tested.

Letchford *et al.* (2002) review the early work on physical simulation of downdraft outflows. The conventional approach to downdraft simulation utilises a jet impinging on a flat surface, as discussed by Walker (1992). The most sophisticated simulations of this approach use a moving jet nozzle (Letchford and Chay 2002; Sengupta and Sarkar 2008) or an actuated aperture at the nozzle (Mason *et al.* 2005; McConville *et al.* 2009). Recent development of impinging jet facilities is towards larger jet nozzles to promote fully-turbulent flow (e.g. nozzle of 1 m diameter used by McConville *et al.* 2009).

However, a tremendous amount of laboratory space would be required to simulate the entire outflow region on a physical scale that is amenable to wind loading and aeroelastic testing of models. With the impinging jet approach, the height to the maximum outflow velocity is less than 3% of the initial jet diameter. The largest impinging jet facility found in the literature created a 1.60 m diameter downdraft (Sarkar and Haan, Jr 2002). As well, simulating additional full-scale features such as downburst translation has proven problematic. Translation of a large nozzle was described as unwieldy or “clumsy” (Mason *et al.* 2003).

1.3 Computational fluid dynamics of downbursts

Numerical models hold the promise of complete and highly-resolved results. However, it is necessary to validate numerical models with physical measurements. Provided that validation is done, numerical simulation may yield insight into aspects of downbursts that are difficult to study by direct observation or by physical modelling.

Proctor (1988, 1989) simulated the thermodynamics and microphysics that lead to intense downburst outflows. An axisymmetric model with a constant grid spacing of 40 m was used. Below the normalised profile maximum, the computed instantaneous vertical profile of radial outflow velocity matched the full-scale measurements from NIMROD (Fujita 1981), within less than $\pm 2\%$. Above the normalised profile maximum, the numerical simulation under-predicted the NIMROD result by approximately 10 %

The dynamic equations for the full thermodynamics and microphysics are computationally expensive to solve. Selvam and Holmes (1992) simplified the problem to the two-dimensional, steady, incompressible Navier-Stokes equation and applied the k- ϵ turbulence model for closure. Predicted outflow velocities were larger than those from Proctor (1988).

Caracena (1982) hypothesized that the vertical downdraft column can be circumscribed by a ring vortex. Lundgren *et al.* (1992) investigated vortex ring development with an inviscid model. Surface friction produced counter-vorticity that retarded and elevated the dominant roll vortex, in agreement with Proctor (1988). The outflow region was modelled at low spatial resolution, though.

Orf *et al.* (1996) and Orf and Anderson (1999) introduced a dry, sub-cloud numerical model to investigate downburst flow dynamics at high resolution. Microphysical cooling was modelled using a cooling function, whose parameters were prescribed to generate outflows that resembled field observations. The outflow was well-resolved. Interactions between multiple downbursts and the effect of ambient wind shear were investigated.

Kim and Hangan (2007) investigated an impinging jet model by solving the unsteady Reynolds-averaged Navier-Stokes (URANS) equations. Mason *et al.* (2009, 2010) combined an improved URANS method with initial forcing of the flow by a cloud-level cooling source (Orf *et al.* 1996). Vermeire *et al.* (2009, 2010) present large-eddy simulations with a cloud-level cooling source.

1.4 Scope

The present work heeds the call for wind engineering beyond the boundary layer wind tunnel (Walker 1992). The impinging jet approach is a logical way to achieve flow similarity of a downdraft. However, the present work seeks a better solution to the practical problem of generating a flow that is (1) adequately similar to the high-intensity, near-surface winds in a convective downdraft event, such that realistic wind loads can be applied to structural models and (2) sufficiently large in physical size, such that it is feasible to construct appropriately-scaled structural models.

For wind engineering concerns, the most critical part of a downdraft is the region which contains the highest-intensity winds that damage near-surface built structures. This region is shown in the inset of Fig. 1.4. The present approach is to approximate the region within the red dashed lines of Fig. 1.4 with the plane wall jet that arises from a rectangular slot nozzle, which is the region enclosed by red dashed lines in Fig. 1.5. By limiting the simulation domain of the downdraft to the critical outflow region, an increased simulation length scale is achievable, whilst retaining the main features of a convective downdraft outflow. The underlying basis of this approach is similar to that of part-depth wind tunnel simulations of the atmospheric boundary layer (Cook 1973, De Bortoli *et al.* 2002).

Section 1.1 discussed the difficulties of acquiring field data of adequate completeness and resolution for validation purposes. Thus, comparisons with numerical simulation results were pursued as part of the present work to validate the slot jet wind tunnel. The flow in the numerical model was driven by negative buoyancy.

1.5 Objective

It was hypothesized that a downdraft outflow could be adequately represented by a plane wall jet arising from a rectangular slot nozzle, for wind engineering purposes. The objective of this thesis was to implement and validate a physical test facility that can subject a structural model to a downdraft outflow. Thorough validation involved extensive comparisons with numerical and experimental results from the literature for plane wall jets, radial wall jets, and downdraft outflows.

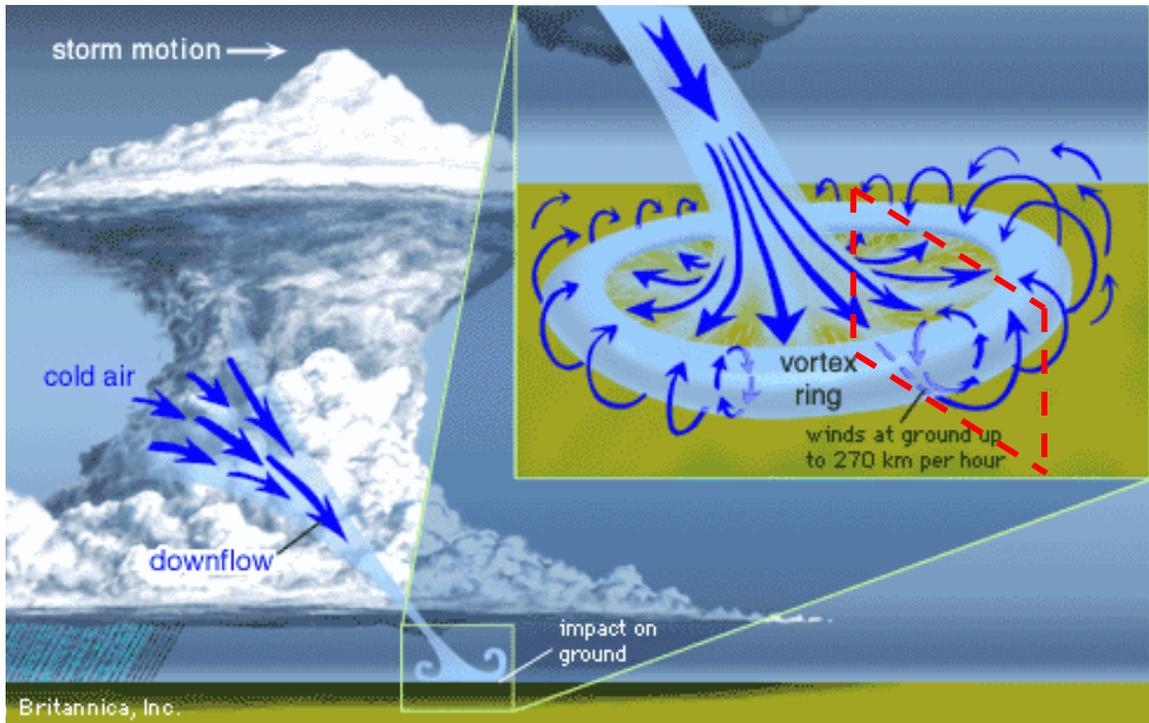


Figure 1.4: Depiction of a thunderstorm downdraft outflow
(adapted from image from the Encyclopædia Britannica)

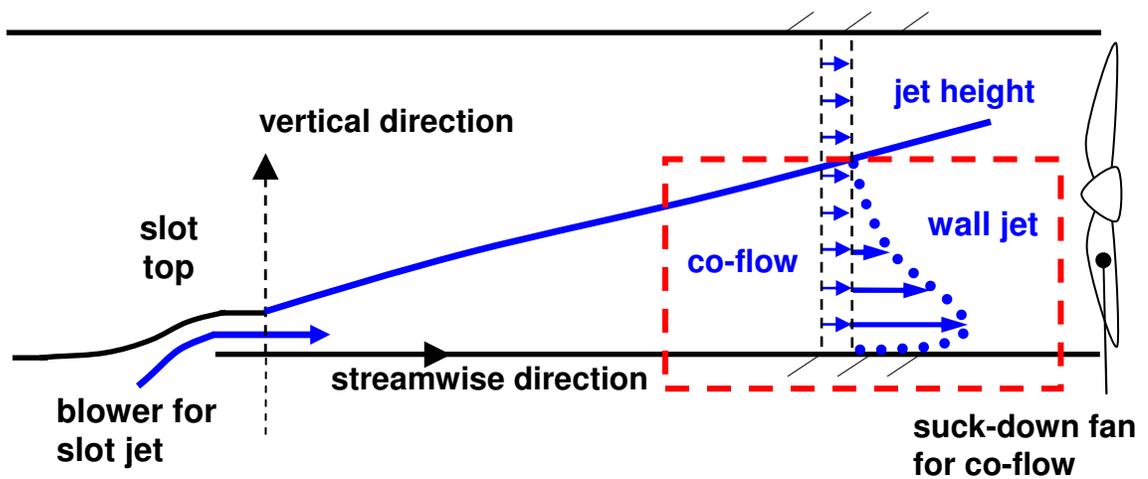


Figure 1.5: Depiction of a plane wall jet arising from a rectangular slot nozzle

1.6 References

- Caracena, F. (1982), “Is the microburst a large vortex ring imbedded in a thunderstorm downdraft?”, *EOS Transactions of the American Geophysical Union*, **63**, 899.
- Cermak, J.E. (2003), “Wind-tunnel development and trends in applications to civil engineering”, *J. Wind Eng. Ind. Aerodyn.*, **91**(3), 355-370.
- Cook, N. J. (1973), “On simulating the lower third of the urban adiabatic boundary layer in a wind tunnel”, *Atmos. Env.*, **7**, 691-705.
- De Bortoli, M.E., Natalini, B., Paluch, M.J., and Natalini, M.B. (2002), “Part-depth wind tunnel simulations of the atmospheric boundary layer”, *J. Wind Eng. Ind. Aerodyn.*, **90**, 281-291.
- Doviak, R.J. and Zrnić, D.S. (1988), “The Doppler weather radar”, in *Aspects of modern radar*, edited by E. Brookner, Artech House, Norwood, MA, USA, 487-561.
- Fujita, T.T. (1981), “Tornadoes and downbursts in the context of generalized planetary scales”, *J. Atmos. Sci.*, **38**(8), 1511-1534.
- Fujita, T.T. (1985), “The downburst: Microburst and macroburst”, University of Chicago, Department of Geophysical Sciences, *Satellite and Mesometeorology Research Project*, Research Paper #210, 122 pp.
- Fujita, T.T. (1990), “Downbursts: Meteorological features and wind field characteristics”, *J. Wind Eng. Ind. Aerodyn.*, **36**, 75-86.
- Fujita, T.T. and Wakimoto, R.M. (1981), “Five scales of airflow associated with a series of downbursts on 16 July 1980”, *Mon. Wea. Rev.*, **109**, 1438-1456.
- Gast, K.D. and Schroeder, J.L. (2003), “Supercell rear-flank downdraft as sampled in the 2002 thunderstorm outflow experiment”, *Proceedings of the 11th International Conference on Wind Engineering*, Lubbock, TX, USA, 2-5 June, 2233-2240.
- Gedzelman, S.D. (1990), “Leonardo da Vinci and the downburst”, *Bull. Am. Meteorol. Soc.*, **71**(5), 649-655.
- Hjelmfelt, M.R. (1988), “Structure and life cycle of microburst outflows observed in Colorado”, *J. Appl. Meteor.*, **27**, 900-927.
- Hjelmfelt, M.R. (2003), “Microbursts and their numerical simulation”, *Preprints of the Harold D. Orville Symposium*, 26 April, Rapid City, SD, USA, 51-67.
- Holmes, J.D. (1999), “Modelling of extreme thunderstorm winds for wind loading of structures and risk assessment”, in *Wind engineering into the 21st century*, edited by Larsen, Larose and Livesey, Balkema, Rotterdam, the Netherlands, 1409-1415.
- Holmes, J.D. (2001), *Wind loading of structures*, Spon Press, London, UK, viii, 356 pp.
- Kessler, E. (1983), *The thunderstorm in human affairs*, Volume 1 of Thunderstorms: A social, scientific, and technological documentary, 2nd edition, University of Oklahoma Press, Norman, OK, USA, xiii, 186 pp.
- Kim, J. and Hangan, H. (2007), “Numerical simulations of impinging jets with application to downbursts”, *J. Wind Eng. Ind. Aerodyn.*, **95**, 279-298.
- Letchford, C.W. and Chay, M.T. (2002), “Pressure distributions on a cube in a simulated thunderstorm downburst – Part B: moving downburst observations”, *J. Wind Eng. Ind. Aerodyn.*, **90**, 733-753.
- Letchford, C.W., Mans, C., and Chay, M.T. (2002), “Thunderstorms – their importance in wind engineering”, *J. Wind Eng. Ind. Aerodyn.*, **90**, 1415-1433.
- Lugt, H.J. (1983), *Vortex flow in nature and technology*, Wiley, New York, NY, USA, xv, 297 pp.

- Lundgren, T.S., Yao, J., and Mansour, N.N. (1992), "Microburst modelling and scaling", *J. Fluid Mech.*, **239**, 461-488.
- Mason, M., Letchford, C.W., and James, D. (2003), "Pulsed jet simulation of a thunderstorm downburst", *Proceedings of the 11th International Conference on Wind Engineering*, Lubbock, TX, USA, 2-5 June, 2249-2256.
- Mason, M.S., Letchford, C.W., and James, D.L. (2005), "Pulsed wall jet simulation of a stationary thunderstorm downburst, Part A: Physical structure and flow field characterization", *J. Wind Eng. Ind. Aerodyn.*, **93**, 557-580.
- Mason, M.S., Wood, G.S., Fletcher, D.F. (2009), "Numerical simulation of downburst winds", *J. Wind Eng. Ind. Aerodyn.*, **97**, 523-539.
- Mason, M.S., Wood, G.S., Fletcher, D.F. (2010), "Numerical investigation of the influence of topography on simulated downburst wind fields", *J. Wind Eng. Ind. Aerodyn.*, **98**, 21-33.
- McConville, A.C., Sterling, M. and Baker, C.J. (2009), "The physical simulation of thunderstorm downbursts using an impinging jet", *Wind Struct.*, **12**(2), 133-149.
- McNulty, R.P. (1991), "Downbursts from innocuous clouds: an example", *Wea. Forecasting*, **6**(1), 148-154.
- Orf, L.G. and Anderson, J.R. (1999), "A numerical study of traveling microbursts", *Mon. Wea. Rev.*, **127**(6), 1244-1258.
- Orf, L.G., Anderson, J.R., and Straka, J.M. (1996), "A three-dimensional numerical analysis of colliding microburst outflow dynamics", *J. Atmos. Sci.*, **53**(17), 2490-2511.
- Proctor, F.H. (1988), "Numerical simulations of an isolated microburst. Part I: dynamics and structure", *J. Atmos. Sci.*, **45**(21), 3137-3160.
- Proctor, F.H. (1989), "Numerical simulations of an isolated microburst. Part II: sensitivity experiments", *J. Atmos. Sci.*, **46**(14), 2143-2165.
- Sarkar, P.P. and Haan, Jr, F.L. (2002), "Next generation wind tunnels for simulation of straight-line, thunderstorm- and tornado-like winds", *Proceedings of the 34th Joint Meeting of the U.S.-Japan Panel on Wind and Seismic Effects*, Gaithersburg, MD, USA, 13-15 May.
- Selvam, R.P. and Holmes J.D. (1992), "Numerical simulation of thunderstorm downdrafts", *J. Wind Eng. Ind. Aerodyn.*, **41-44**, 2817-2825.
- Sengupta, A. and Sarkar, P.P. (2008), "Experimental measurement and numerical simulation of an impinging jet with application to thunderstorm microburst winds", *J. Wind Eng. Ind. Aerodyn.*, **96**, 345-365.
- Vermeire B.C., Orf L.G., and Savory E. (2009), "A comparison of impinging jet and cooling source downburst models", *5th European Conference on Severe Storms*, Landshut, Germany, 12-16 October, 173-174.
- Vermeire, B.C., Orf, L.G., and Savory, E. (2010), "A parametric study of near surface downburst line outflows", *5th International Symposium on Computational Wind Engineering*, Chapel Hill, NC, USA, 23-27 May, 8 pp.
- Wakimoto, R.M. (1982), "The life cycle of thunderstorm gust fronts as viewed with Doppler radar and rawinsonde data", *Mon. Wea. Rev.*, **110**, 1060-1082.
- Wakimoto, R.M. (2001), "Convectively driven high wind events", *Meteor. Monogr.*, **28**(50), 255-298.

- Walker, G.R. (1992), "Wind engineering beyond the boundary layer wind tunnel", *J. Wind Eng. Ind. Aerodyn.*, **41-44**, 93-104.
- Wilson, J.W. and Wakimoto, R.M. (2001), "The discovery of the downburst: T.T. Fujita's contribution", *Bull. Am. Meteorol. Soc.*, **82**(1), 49-62.
- Wilson, J.W., Roberts, R.D., Kessinger, C., and McCarthy, J. (1984), "Microburst wind structure and evaluation of Doppler radar for airport wind shear detection", *J. Clim. Appl. Meteorol.*, **28**(50), 255-298.

CHAPTER 2

COMPARISON OF PLANE AND RADIAL TURBULENT WALL JETS*

2.1 Introduction

Turbulent wall jets have been discussed extensively in the fluid mechanics literature. This interest stems from (1) academic curiosity in a flow that is regarded as a boundary layer interacting with a free shear layer and (2) the widespread usage of wall jets in engineering applications for heating/cooling, drying/wetting, or removal/deposition of particles/films on a solid surface. The identifying feature of a wall jet is its normal-to-wall profile of time-averaged streamwise velocity. This characteristic velocity profile attains a maximum value at an intermediate location between the ground plane and the external stream, and it can be generated in a plane or radial flow configuration. The former uses a slot nozzle that expels fluid parallel to a wall. The latter arises from an axisymmetric jet that impinges normal to a wall.

Plane wall jet flow characteristics have been the subject of dedicated reviews (Launder and Rodi 1981, Launder and Rodi 1983) and extensive discussions that survey the literature (Narasimha *et al.* 1973, Abrahamsson *et al.* 1994, Schneider and Goldstein 1994, Eriksson *et al.* 1998). The radial wall jet has been investigated to a lesser extent as a result of the tendency to focus on the flow near the impinging jet stagnation point for heat transfer applications.

Although a slot jet parallel to a wall and an impinging axisymmetric jet represent vastly different initial conditions, both configurations give rise to wall jets. One cannot help but wonder how the resulting flows compare to each other. Furthermore, the possible interchangeability of plane and radial wall jets can be useful in specific engineering applications. The compact physical arrangement of a slot jet can make it preferable to an impinging jet. The main objective of the present work is to establish the degree of difference between the flow characteristics of plane and radial turbulent wall jets.

* Excerpts from this chapter were presented as a paper at the *Canadian Society for Mechanical Engineering Forum*, 2008. An expanded version of this chapter is being prepared for submission to the *ASME Journal of Fluids Engineering*, 2010.

Section 2.2 discusses previous findings in the wall jet literature. Section 2.3 presents experimental details of hot-wire anemometry (HWA) measurements of a plane wall jet by the present authors, where detailed turbulence results are obtained. Section 2.4 compares available plane and radial wall jet data.

2.2 Previous literature

2.2.1 Radial wall jet

The radial wall jet has received considerable attention from fluid mechanics researchers (Glauert 1956, Bakke 1957, Bradshaw and Love 1959, Poreh *et al.* 1967, Cooper *et al.* 1993, Knowles and Myszko 1998). More recently, it has received attention from the wind engineering community for meteorological downburst outflow modelling (Wood *et al.* 2001, Chay and Letchford 2002, Xu and Hangan 2008).

Fluid is expelled at a velocity of U_j from an axisymmetric nozzle, of diameter D located at a distance z_D from a plane solid wall, with the dominant flow direction being orthogonal towards the wall as shown in Fig. 2.1a. A wall jet develops downstream of the impingement region. Due to the high convective heat transfer from the wall near the stagnation point, the impingement regime has been of primary interest for industrial applications. The wall jet regime has been investigated to a lesser extent.

For large nozzle-to-wall separation ($z_D/D = 18$), Bradshaw and Love (1959, $Re_D = 1.8 \times 10^5$) conducted dynamic and static pressure measurements. Pressure field changes associated with the progression from free jet to wall jet occurred within a hemisphere of radius $3D$ centred on $r = 0$. However, the wall jet spread rate still showed evidence of this progression out to approximately $r/D = 8$. At $r/D > 8$, the radial wall jet exhibited the expected linear growth rate of an ideal point source wall jet.

For $z_D/D > 12$, measurements by Poreh and Cermak (following Poreh *et al.* (1967)) indicated that the initial jet diameter and velocity need not appear as independent variables in the wall jet flow field relations. Instead, they are combined as a kinematic momentum flux. Furthermore, from dimensional analysis, they concluded that the dependency of the wall jet velocity decay and spread rate on z_D cannot vanish, even at

large radial distance from the nozzle axis. It was found that the maximum velocity (U_m) and the half-width ($z_{0.5}$) varied with $z_D^{0.1}$ and $z_D^{1.1}$, respectively.

For $2 \leq z_D/D \leq 10$, Cooper *et al.* (1993, $Re_D = 2.3 \times 10^4$ and 7.1×10^4) conducted hot-wire anemometry measurements and found a linear wall jet spread rate for $r/D > 3$, with the spread rate increasing slightly with increasing z_D . Over the z_D/D range studied, spread rate increased by approximately 10%. The radial variation of $(U_m/U_j)(r/D)$ was used to investigate the extent of the impingement regime. Assuming $(U_m/U_j) \propto K(r/D)^a$, with K as a constant and $a = -1$ for the radial wall jet, $(U_m/U_j)(r/D) \rightarrow K$ with increasing distance from the stagnation point. At $r/D > 2$, the parameter tended towards a constant value, but this was not achieved, likely because the exponent was not precisely unity. Bakke (1957) and Poreh *et al.* (1967) reported $a = -1.12 \pm 0.03$ and -1.1 , respectively. Also, the latter value resulted in an adequate fit to data from Bradshaw and Love (1959). Dependence on z_D/D was also manifest in the spatial extent of the impingement regime. Data from Cooper *et al.* (1993) suggested that as z_D/D decreased, the transition to the wall jet regime was essentially complete at slightly smaller r/D .

Further HWA results for $2 \leq z_D/D \leq 10$ (Knowles and Myszko 1998, $Re_D = 9.0 \times 10^4$) showed that the wall-normal profiles of time-averaged velocity became approximately self-similar. The $z/z_{0.5}$ profiles of U/U_m approximately collapsed to a single curve for $r/D \geq 2.5$. The corresponding profiles of I_u , I_w , and dominant Reynolds stress tended towards similarity at $r/D \geq 5$. As expected, a smaller nozzle-to-surface separation resulted in higher turbulent kinetic energy (TKE) production, with an order of magnitude difference from $z_D/D = 2$ to 10. Maximum turbulence values occurred at $r/D = 2$.

Particle image velocimetry with $z_D/D = 2$ (Fairweather and Hargrave 2002) has been compared to the previous HWA measurements. Mean velocity profiles from the far-field wall jet ($5 \leq r/D \leq 30$) agreed with those from Poreh *et al.* (1967, $12 \leq r/D \leq 33$). Considering the reported experimental uncertainty, the profiles of mean velocity, turbulence intensity, and Reynolds stress could be interpreted as being self-similar.

Along with $z_D/D = 0.53$, Bakke (1957) used a nozzle that included a prominent flange as depicted in Fig. 2.2. Essentially, this was an axisymmetric slot jet (i.e. a configuration that had characteristics of both arrangements shown in Fig. 2.1. At $r/D \geq 8.5$, profiles of mean radial velocity matched those for $z_D/D = 0.53$ (Bradshaw and Love 1959).

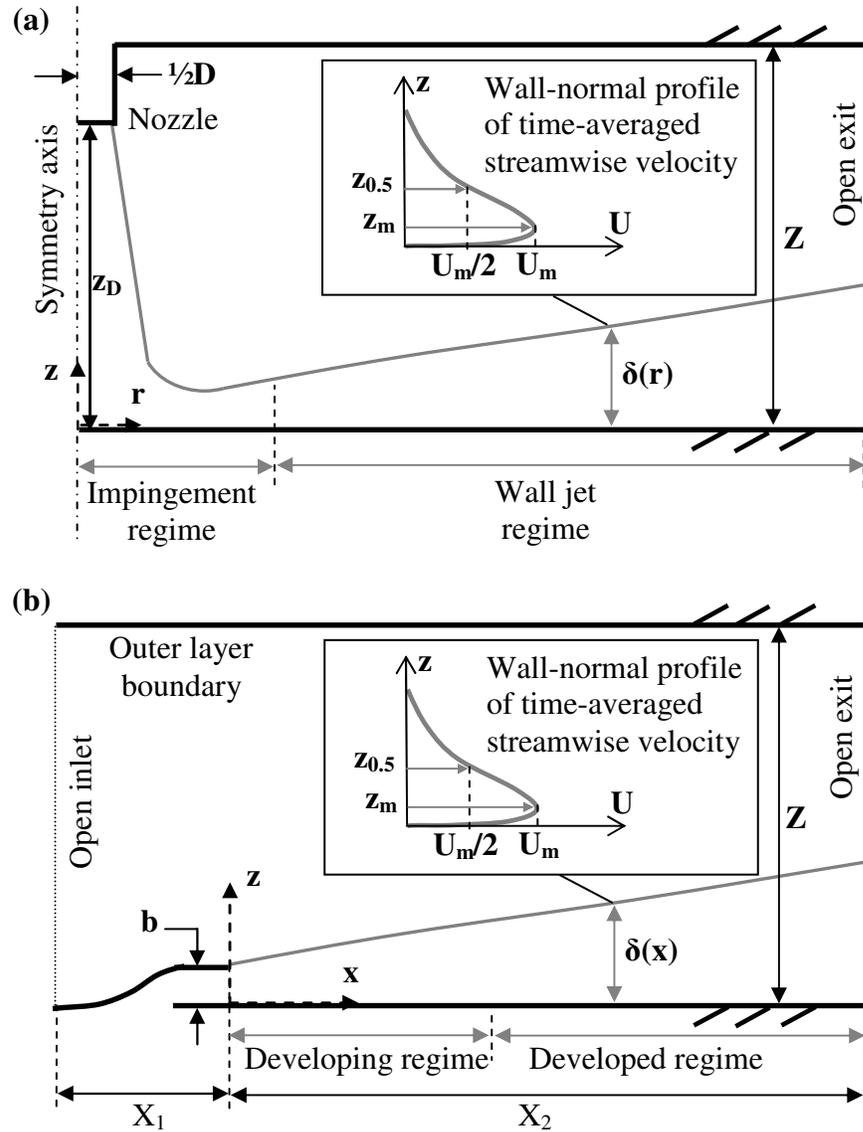


Figure 2.1: Two common wall jet configurations (a) radial (b) plane

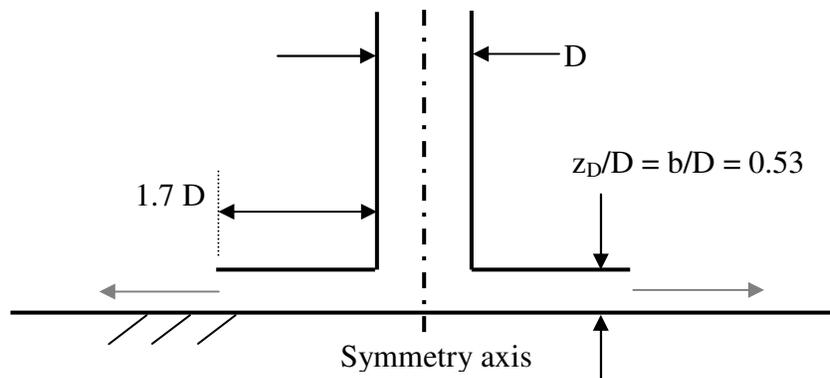


Figure 2.2: Radial jet apparatus used by Bakke (1957)

2.2.2 Plane wall jet

The seminal theoretical work by Glauert (1956) and accompanying experiments by Bakke (1957) raised interest in the behaviour and characteristics of the plane wall jet. Subsequent experiments presented more extensive results and discussed the similarity argument (Bradshaw and Gee 1960, Schwarz and Cosart 1961, Gartshore and Hawaleshka 1964, Verhoff 1970, Narasimha *et al.* 1973, Wygnanski *et al.* 1992, Abrahamsson *et al.* 1994, Schneider and Goldstein 1994, Eriksson *et al.* 1998). Extensive reviews of the early literature are available (Launder and Rodi 1981, 1983). Recent work investigated the possibility of using the plane wall jet as a convenient *ersatz* for the radial wall jet in large-scale modelling of the meteorological downburst outflow (Lin and Savory 2006).

Fluid expelled from a two-dimensional slot, parallel to a solid boundary, gives rise to a plane wall jet as shown by Fig. 2.1b. The flow is confined in the spanwise direction by solid boundaries. A spanwise extent of $Y/b > 20$ is required to maintain nominal two-dimensionality of the wall jet (Förthmann 1934). Approaching ideal two-dimensionality (e.g. Bradshaw and Gee 1960, $Y/b = 2000$), it becomes increasingly difficult to maintain a perfectly rectangular nozzle. Larger slot top thickness and intrusive supports across the slot span are generally required. The slot top and support wakes disappear relatively close to the slot exit and are not detectable in the downstream regions of interest.

Launder and Rodi (1981) assessed flow two-dimensionality by examining momentum conservation since skin friction losses were deemed small compared to the initial ideal momentum flux (e.g. at $x/b = 100$, skin friction losses $\approx 8\%$ of initial flux). If the momentum flux calculated from normalised U profiles varied substantially between the various profile measurement stations at different x/b and on the jet centreline, lack of flow two-dimensionality was inferred. Variations of 5% and 10% of the initial momentum flux for profiles from Bradshaw and Gee (1960) and Verhoff (1970), respectively, were identified as having the best momentum conservation. Direct checks of flow two-dimensionality by spanwise velocity measurements may also be performed (Gartshore and Hawaleshka 1964).

Early plane wall jet measurements were performed over a very limited x/b range (Förthmann 1934; Schwarz and Cosart 1961). The developing regime has been reported

as extending from $x/b = 0$ to as close as $x/b = 20$ (Förthmann 1934) and as far as $x/b = 104$ (Verhoff 1970). This wide range of values is likely in part due to the subjective assessment of collapse of normalised profiles and varying flow quality in the literature, as well as slight variations in experimental configuration.

Previous investigations have used various slot geometries. The slot top can range from a thin lip thickness as depicted in Fig. 2.1b (minimum $t/b \sim 1/10$ to maintain slot two-dimensionality) to a vertical wall that extends to the top boundary of the flow domain (Abrahamsson *et al.* 1994; Eriksson *et al.* 1998). The former design is useful when a plane wall jet with co-flow is desired. The present experiments pertain to a ($t < b$) slot geometry with a partially-open slot top boundary. The latter design with well-defined solid boundaries is favoured by workers who use a numerical or analytical approach. However, one has to be wary of a return flow downstream of the slot exit, which can affect the character of the wall jet.

An outer layer solid boundary (see Fig. 2.1b) has generally been used in previous studies. Exceptions were experiments with an open condition (Förthmann 1934) or a free surface condition (Eriksson *et al.* 1998, water as working fluid).

For $z < z_m$, U profiles conformed to the well-known $1/7^{\text{th}}$ power relation for a turbulent boundary layer (Schlichting 1979, p. 599). The main premise of the early similarity argument (Glauert 1956) was to approximate the wall jet profile by combining Blasius's empirical formula for turbulent pipe flow in the inner region ($z < z_m$) with Prandtl's hypothesis for free turbulent flow in the outer region ($z > z_m$). Turbulence was treated by assuming an effective eddy viscosity, which was not well-supported by subsequent experimental results. This formulation also implied that, with increasing x , the inner region gradually comprised a larger proportion of δ . In other words, self-similarity was only approximate. Asymptotic theory indicated exact similarity is possible only in the limit of infinite Reynolds number (George *et al.* 2000).

At x/b locations that are well downstream of those in other studies, the traditional methods of describing the boundary layer near-wall region did not carry over satisfactorily for the wall jet inner region (Bradshaw and Gee 1960). The boundary layer semi-logarithmic region, where Prandtl's law of the wall overlaps von Kármán's velocity-defect law, was not apparent in the wall jet without an external stream. With the

addition of a co-flow though, the wall jet exhibited a distinct semi-logarithmic inner region.

Reynolds stress, for both radial (Poreh *et al.* 1967) and plane (Bradshaw and Gee 1960) wall jet, was observed as non-vanishing at z_m . This finding differed from what was observed for turbulent boundary layer Reynolds stress. The wall jet Reynolds stress at z_m was of opposite sign and approximately equal magnitude as the wall shear stress. Together with the absence of an overlap region, these results have been regarded as being indicative of strong interaction between the inner and outer regions.

The early investigations, using U_j and b as scaling parameters, showed that wall jet spread and streamwise velocity decay were dependent on Reynolds number. An extensive discussion of the no co-flow plane wall jet (Narasimha *et al.* 1973) promoted the use of an alternative scaling where the sole parameter determining the wall jet evolution was the slot exit kinematic momentum flux. Subsequent studies have supported a momentum flux scaling (Wyganski *et al.* 1992, Zhou and Wyganski 1993). Combining the two slot exit parameters as momentum flux appears to be a more concise approach. However, the idea was less effective in practice since an additional parameter (a coefficient of value less than unity) was needed to account for a realistic slot exit velocity profile.

Later studies using laser-based measurement techniques provided comprehensive turbulence results. However, they used a vertical wall above the slot exit (Abrahamsson *et al.* 1994; Eriksson *et al.* 1998) or an irregular nozzle geometry (Schneider and Goldstein 1994) instead of a thin plate as the slot top. Previous studies (Verhoff 1970, Bradshaw and Gee 1960, Wyganski *et al.* 1992) that used a thin-plate slot top generally focused on mean quantities and did not provide complete turbulence data. In order to obtain a complete set of time-averaged and turbulence data for this slot configuration, the following plane wall jet measurements were undertaken by the present author. These measurements were necessary for the main objective of this chapter, a comprehensive comparison of the fundamental fluid mechanics aspects of plane and radial wall jets, to be completed.

2.3 Present experiment

2.3.1 Prototype slot jet wind tunnel

A plane wall jet prototype facility was implemented, as shown in Fig. 2.1b, with a test section of rectangular cross-section (0.36 m span by 0.28 m height). The physical dimensions of the prototype are listed below, where Y is the test section spanwise width and t is the lip thickness of the slot top. These proportions were based on the ultimate goal of implementing the slot jet design in an existing and large-scale atmospheric boundary layer wind tunnel.

- $X_1/b = 20$
- $X_2/b = 225$
- $Y/b = 24$
- $Z/b = 19$
- $t/b = 1/9$

In this chapter, the fundamental fluid mechanics aspects of the flow in this prototype facility are discussed. Chapters 3 and 4 apply the prototype results to the wind engineering problem of downburst outflow simulation. The full-size implementation of the slot jet apparatus is covered in Chapter 5.

The slot top was supported by two ribs located at the one-third points of the test facility span. The supporting ribs had a width of $b/9$, and their influence on the downstream wall jet was investigated by velocity profiles across the span at a constant fixed height (z_m for various x/b). At $x/b = 50$, across the central 60% of Y , time-averaged streamwise velocity (U) varied within $\pm 7\%$ of the spanwise-averaged U . At $x/b = 100$ and 150, across the central 60% of Y , U varied within $\pm 5\%$ of the spanwise-averaged U . Spanwise variations of turbulence intensity (I_u and I_w) were $\pm 3\%$ of their respective spanwise-averaged values.

2.3.2 Velocity measurement system

The time-averaged and fluctuating velocity quantities were of primary interest. Hot-wire anemometry (HWA) measurements were conducted with a Dantec Dynamics MiniCTA 54T30 system. A 55P61 crossed-wire probe (wire diameter and length of 5 μm and 1.25 mm, respectively) allowed two velocity components to be measured simultaneously. The crossed-wire probe was mounted at the end of the horizontal leg of an L-shaped holder, and the vertical leg of the holder was 75 mm downstream of the

probe. The holder was mounted to a two-axis traverse, which allowed probe positioning with an accuracy of ± 0.2 mm.

The crossed-wire voltage was output to a National Instruments SCB-100 chassis, which connected to a National Instruments PCI-6071E data acquisition card. The HWA system was capable of sampling at 10 kHz, but 1 kHz was selected to expedite the data processing. One-dimensional spectra of the streamwise velocity fluctuations at $z = z_m$ and streamwise locations of $x/b = 50, 100$ and 150 were evaluated. The majority of the turbulent kinetic energy (TKE) was captured. The $-5/3$ power relation, indicative of the inertial sub-range (Hinze 1975), was applicable near 100 Hz.

The recorded voltage values were converted to velocity with a 6th-order polynomial transfer function that was determined from a calibration procedure conducted before and after each set of measurements. The HWA system was calibrated in-situ, with an independent measure of velocity provided by a pitot-static tube probe and U-tube manometer. By curve-fitting the calibration measurements, the constants (C_0 to C_6) in Eq. 2.1 were determined, where U_{cal} is the set of calibration velocities and E is the corresponding set of calibration voltages.

After measured voltages from an experiment were correlated to calibration velocities using Eq. 2.1, velocities in the wire coordinate system (U_1 and U_2) were calculated from the calibration velocities, using Eqs. 2.2 and 2.3 where the k values were crossed hot-wire yaw coefficients. The final step was to transform the wire coordinate system velocities into the test facility coordinate system velocity (U) with Eq. 2.4. This is the standard two-wire decomposition for two-dimensional flow (Jørgensen 2005).

$$U_{cal} = C_6 E^6 + C_5 E^5 + C_4 E^4 + C_3 E^3 + C_2 E^2 + C_1 E + C_0 \quad (2.1)$$

$$U_1 = \left(\frac{(1 + k_2^2) U_{cal2}^2 - k_2^2 U_{cal1}^2}{2} \right)^{1/2} \quad (2.2)$$

$$U_2 = \left(\frac{(1 + k_1^2) U_{cal1}^2 - k_1^2 U_{cal2}^2}{2} \right)^{1/2} \quad (2.3)$$

$$U = \frac{(U_1 + U_2)}{2^{1/2}} \quad (2.4)$$

2.3.3 Uncertainty analysis

The following sources of systematic measurement uncertainty were considered:

- possible pitot-static tube misalignment ($\leq 2^\circ$) in the HWA calibration procedure,
- gain, offset, and differential non-linearity error related to the analog-to-digital conversion of the HWA voltage signal, and
- uncertainty of yaw coefficient values (k_1 and k_2).

The following sources of random measurement uncertainty were considered:

- scale readability limitation of the manometer used with the reference pitot-static probe for HWA calibration,
- error introduced in the curve-fitting of the calibration data to obtain the 6th-order polynomial transfer function,
- noise and quantization errors related to the analog-to-digital conversion,
- potential crossed-wire probe misalignment ($\leq 2^\circ$),
- ambient temperature variations, and
- random variation of the measurand, U .

Uncertainties from these sources were propagated through Eqs. 2.1 to 2.4 to determine an overall uncertainty (Wheeler and Ganji 1996). The contributions from the yaw coefficient uncertainties and crossed-wire probe misalignment were negligible. Table 2.1 indicates that the % uncertainty on U was inversely related to the U magnitude being measured. When measuring at the high end of the velocity range, the main sources of uncertainty were from the HWA calibration and the A/D conversion of the HWA output signal. When measuring at the low end of the velocity range, the dominant source of uncertainty was the curve-fitting of the calibration data. The U measurements for the plane wall jet, presented in the following section, had an uncertainty of less than $\pm 9\%$.

Table 2.1: Uncertainty of time-averaged streamwise velocity measurements

U (m/s)	uncertainty range (%)
41	± 3.2
37	± 3.3
31	± 3.4
28	± 3.5
24	± 3.7
20	± 4.1
15	± 4.3
12	± 4.8
7.9	± 6.1
5.0	± 8.4

2.4 Comparison of the plane and the radial wall jet

The present HWA measurements of a plane wall jet were compared to the results from a comprehensive radial wall jet study (Knowles and Myszkowski 1998). The crossed-wire probe and HWA system used in the impinging jet study were identical to the present set-up. A 16-bit A/D converter was used in the impinging jet study, whereas the PCI-6071E card in the plane wall jet study had 12-bit resolution. The estimated uncertainty of time-averaged horizontal velocity in the wall jet region of the impinging jet was stated as 4.8%.

2.4.1 Time-averaged velocity profiles

Fig. 2.3 compares the spatial variation of time-averaged streamwise velocity in the direction normal to the wall. Previous studies of plane wall jets indicated that transition occurs at distance and slot Reynolds numbers of $Re_x \sim 2 \times 10^5$ and $Re_b \sim 6 \times 10^2$, respectively (Bajura and Catalano 1975; Bajura and Szewczyk 1970). The present plane wall jet measurements at $x/b = 50$ corresponded to $Re_x \sim 1 \times 10^6$ and $Re_b \sim 4 \times 10^4$. All plane wall jet data shown were from the turbulent regime. With $z_D/D = 18$, the impinging jet was observed to slow down by a factor of 2.6 from the nozzle to the near-wall region (Bradshaw and Love 1959). For the radial wall jet data (Knowles and Myszkowski 1998), $Re_D/2.6 = 3.5 \times 10^4$. Noting that $z_D/D = 10$, the radial wall jet data shown are expected to be from the turbulent regime as well.

The velocity profile of a developed plane wall jet was described by Eq. 2.5 (Verhoff 1970). It was determined by combining the Blasius boundary layer formula and Görtler's free jet solution. Constants were found from experiments. The profile agreed well with measurements for the largest Reynolds number found in the plane wall jet literature (Förthmann 1934, $Re_b = 5.4 \times 10^4$).

The present plane wall jet measurements were scattered about Eq. 2.5. Notable discrepancies occurred at $z/z_{0.5} > 1$, where the velocity magnitudes decreased to the 6 to 12 m/s range, and the uncertainty from the HWA system increased. Rather than simply taking the largest sampled value as U_m without consideration for experimental variability, U_m for the present plane wall jet measurements was determined from a curve-fit to the entire z -range of data. This approach resulted in some U/U_m values exceeding unity.

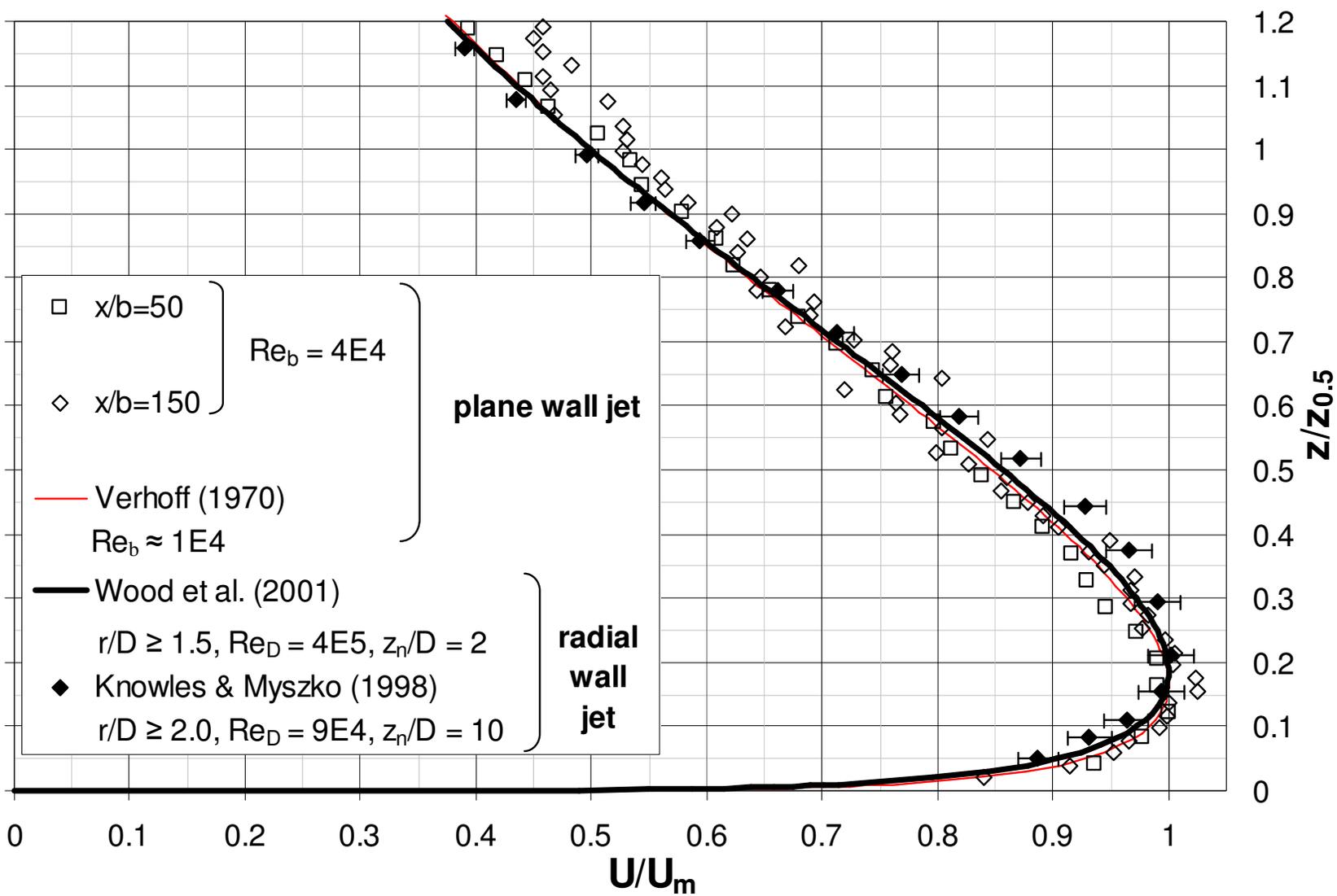
Eq. 2.6 has been found to fit radial wall jet profiles between $r/D = 1.5$ to 3 (Wood *et al.* 2001). This equation had the same mathematical form as the relation for the plane wall jet. Both equations involved an exponent component that dominated in the inner region ($z < z_m$) and an error function component that dominated in the outer region ($z > z_m$). By virtue of its smaller exponent of $1/7$, the plane wall jet relation represented larger velocities in the inner region than the radial wall jet relation. The discrepancy between Eqs. 2.5 and 2.6, as plotted in Fig. 2.4, is minor near $U/U_m = 1$ ($z/z_{0.5} = 0.18$).

Radial wall jet measurements by Knowles and Myszko (1998) were also plotted on Fig. 2.3 with their stated uncertainty indicated by error bars. The uncertainty on the normalised velocity was $> 2\%$. When considered together with Table 2.1, the difference between plane and radial wall jet mean profiles can be seen as comparable in magnitude to the experimental uncertainties.

$$\left(\frac{U}{U_m}\right)_{\text{plane}} = 1.48 \left(\frac{z}{z_{0.5}}\right)^{1/7} \left(1 - \text{erf}\left(0.68 \left(\frac{z}{z_{0.5}}\right)\right)\right) \quad (2.5)$$

$$\left(\frac{U}{U_m}\right)_{\text{radial}} = 1.55 \left(\frac{z}{z_{0.5}}\right)^{1/6} \left(1 - \text{erf}\left(0.70 \left(\frac{z}{z_{0.5}}\right)\right)\right) \quad (2.6)$$

Figure 2.3: Normal-to-wall profile of time-averaged streamwise velocity



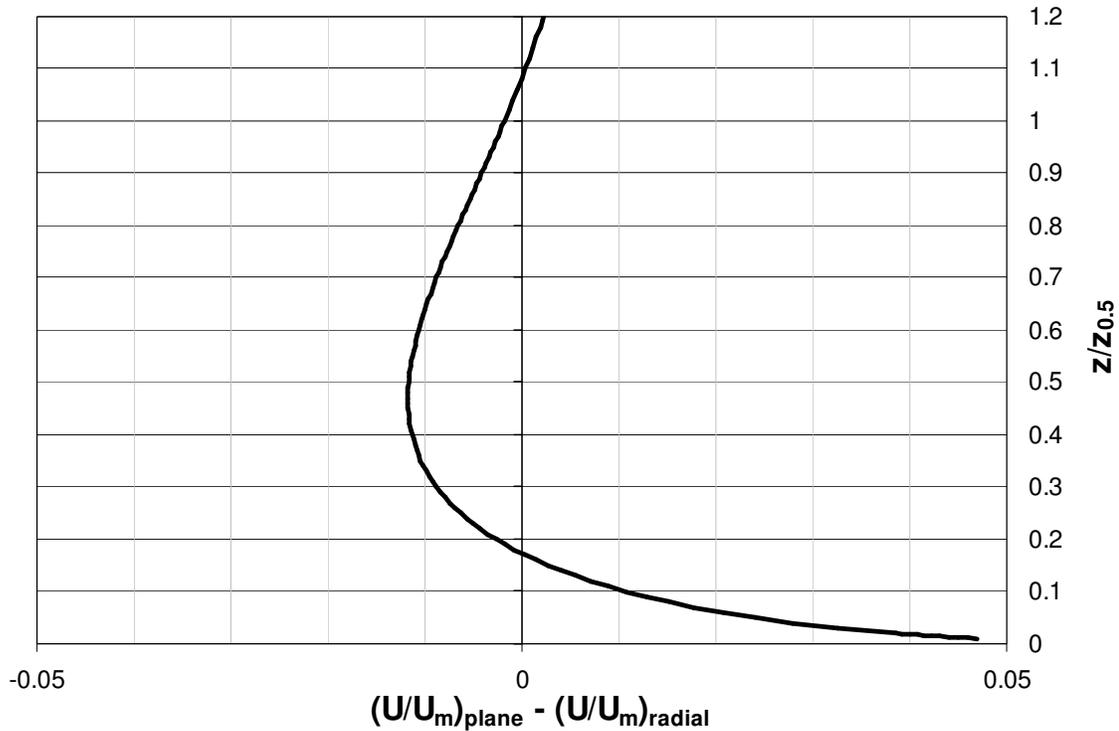


Figure 2.4: Difference between the normal-to-wall profiles of time-averaged streamwise velocity of plane and radial wall jets

2.4.2 Turbulence quantity profiles

The similarity of turbulence quantity profiles appeared to have a strong dependency on the boundary condition above the slot exit. Workers who found evidence for collapse of turbulence quantity profiles with outer half-width, $z_{0.5}$, scaling (Abrahamsson *et al.* 1994; Eriksson *et al.* 1998) used test facilities with a vertical wall above the slot (essentially $t \rightarrow \infty$). Plane wall jet measurements by Abrahamsson *et al.* (1994) at $x/b = 70$ to 150 for $Re_b = 1 \times 10^4$ to 2×10^4 collapsed reasonably well onto the single curve shown for their data in Fig. 2.5.

As reported by other workers who used a thin slot lip condition (Wynanski *et al.* 1992), the present plane wall jet turbulence profiles did not collapse onto a single curve when outer half-width scaling was used. Fig. 2.5 shows that the data from Wynanski *et al.* (1992) for $60 \leq x/b \leq 120$ remained within the range of the present profiles for $50 \leq x/b \leq 150$. The profile shapes showed agreement with each other, as well as with the

self-similar profile of the large t/b experiment (Abrahamsson *et al.* 1994). Agreement occurred between the upper limit profile of Wygnanski *et al.* (1992) and the self-similar profile (Abrahamsson *et al.* 1994) near the wall. These two profiles started to differ for $z/z_{0.5} > 0.4$, which suggested that the slot top boundary condition only affects the outer layer of the wall jet, at a significant distance from the wall jet maximum. As shown in Figs. 2.6 and 2.7, respectively, there is agreement between Abrahamsson *et al.* (1994) and the present measurements for the normal-to-wall turbulence intensity and the dominant component of Reynolds stress. Table 2.2 summarises these findings and suggests that turbulence profile similarity depends on t/b . The effects of t/b and Z/b on the downstream wall jet have yet to be thoroughly explored.

A review of experiments that used optically-based flow measurement techniques (Schneider and Goldstein 1994) showed turbulence intensity and Reynolds stress profiles in the range of magnitudes of the present HWA data. The near-wall inflection in the profiles in Fig. 2.5 occurs in all HWA measurements, as well as in the LDV measurements by Eriksson *et al.* (1998).

The radial wall jet turbulence quantity profiles tended towards self-similarity at $r/D \geq 5$ (Knowles and Myszko 1998). Data was available only above z_m ($z/z_{0.5} > 0.2$). The radial wall jet profile magnitudes in Figs. 2.5 to 2.7 are slightly less than those for the plane wall jet, indicating that agreement of magnitude is best at r/D slightly greater than 2. In Figs. 2.6 and 2.7, the radial wall jet profile shape deviates somewhat from those of the plane wall jet. Nonetheless, it is interesting that there are regions of the radial wall jet that show a surprising likeness to the plane wall jet.

Table 2.2: Turbulence profile similarity

Study	Re_b	x/b	t/b	Z/b	turbulence profile similarity?
Present	4.0×10^4	50, 150	0.1	21	no
Wygnanski <i>et al.</i> (1992)	1.9×10^4	60 to 120	< 1	61	no
Eriksson <i>et al.</i> (1998)	9.6×10^3	40 to 150	107	108	yes
	1.0×10^4	70 to 150	239	240	yes
Abrahamsson <i>et al.</i> (1994)	2.0×10^4	125 to 150			

Figure 2.5: Normal-to-wall profile of streamwise turbulence intensity

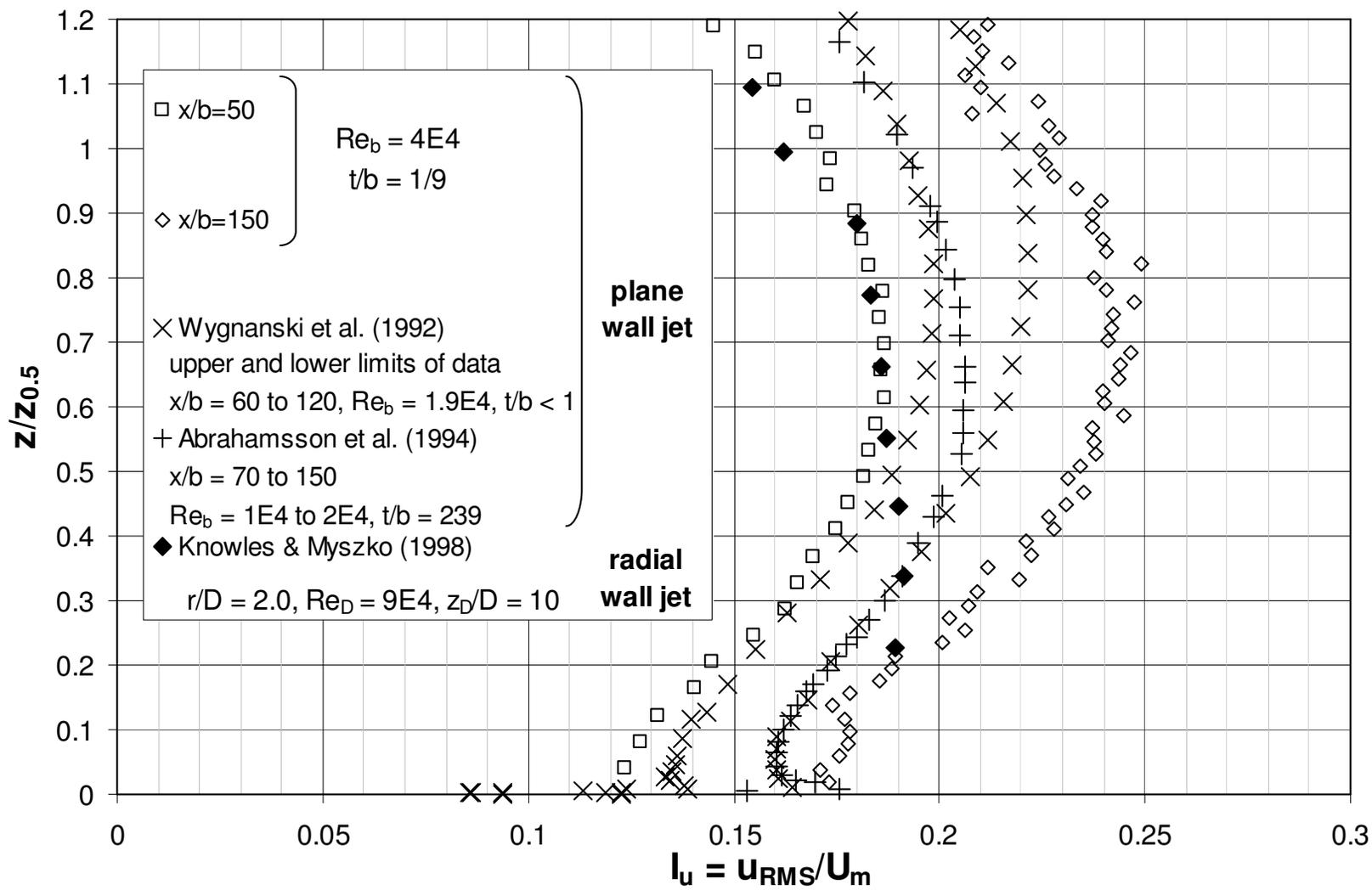


Figure 2.6: Normal-to-wall profile of normal-to-wall turbulence intensity

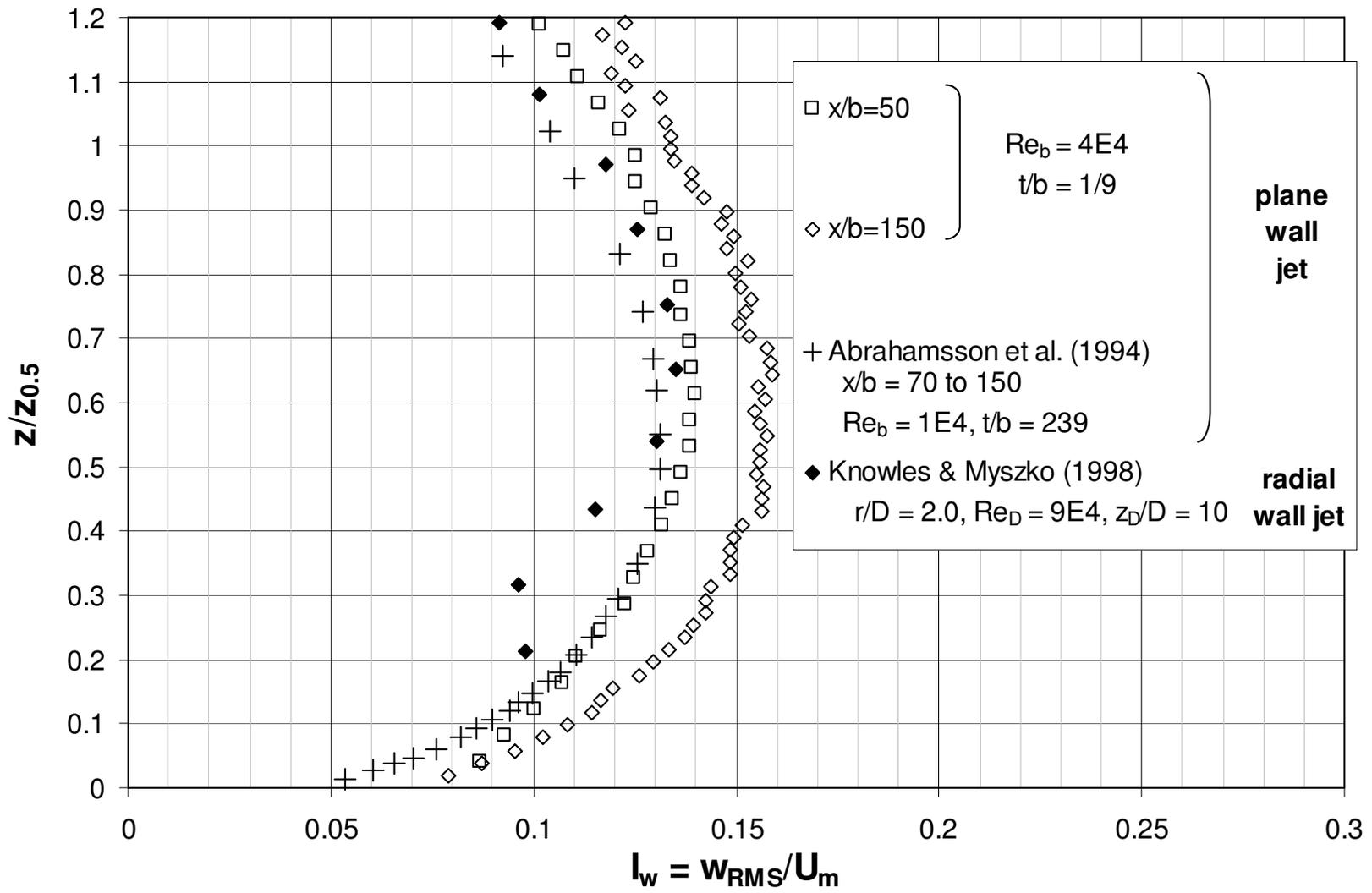
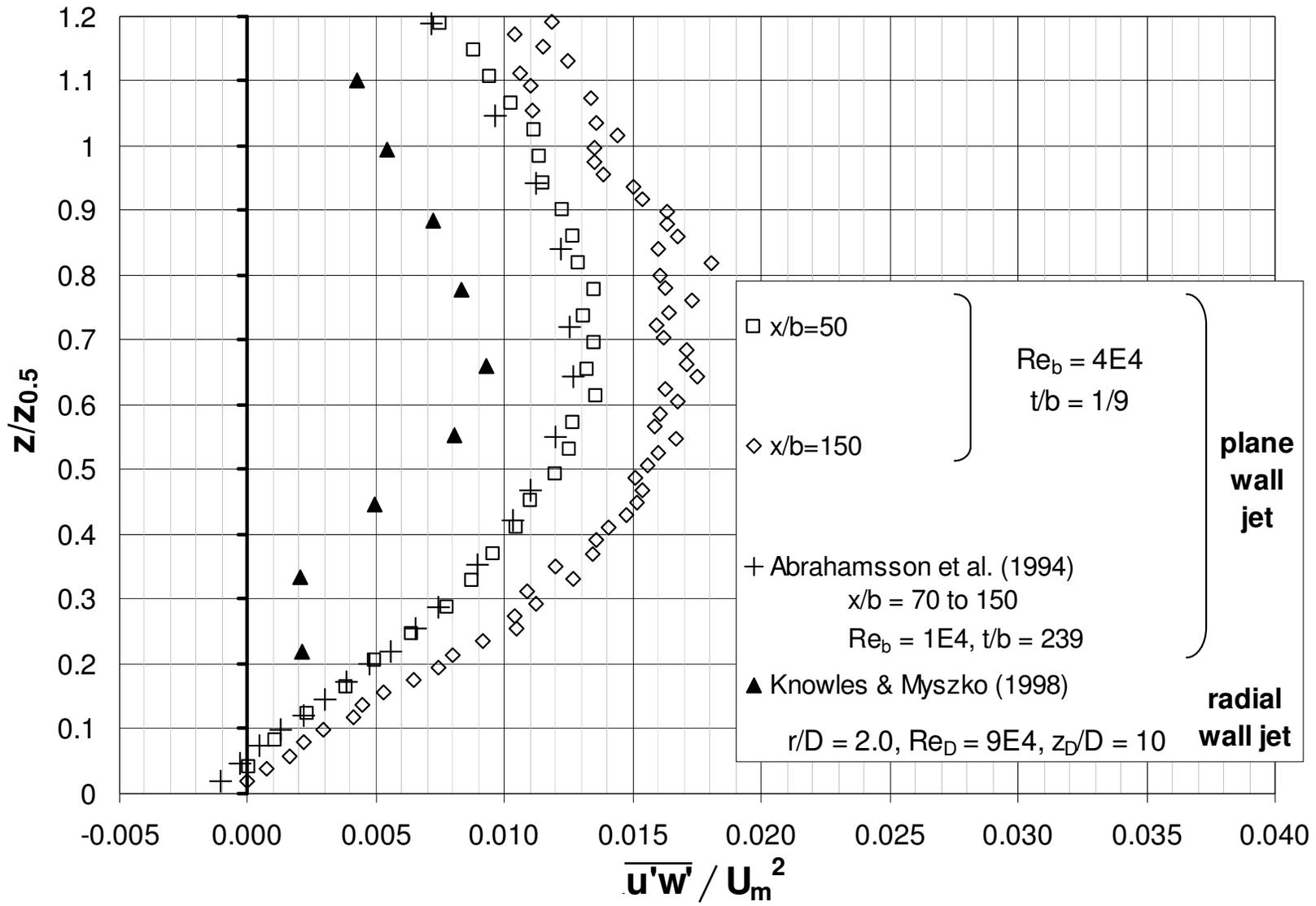


Figure 2.7: Normal-to-wall profile of the dominant Reynolds stress component



2.4.3 Jet spread and velocity decay

The spread rates of the plane and radial wall jets are given by Eqs. 2.7 and 2.8, respectively. The velocity decay rates of the plane and radial wall jets are given by Eqs. 2.9 and 2.10, respectively. The virtual origin (x_0 and r_0) is typically found from the spread rate equation, but as Schneider and Goldstein (1994) reported, a range of x_0 values can be valid for a given experimental data set. This parameter is not documented rigorously in all studies. For the region of interest ($x \gg b$ for the plane wall jet), the effect of the virtual origin is reduced.

$$\frac{z_{0.5}}{b} = A_p \left(\frac{x + x_0}{b} \right)^{m_p} \quad (2.7)$$

$$\frac{z_{0.5}}{D} = A_r \left(\frac{r + r_0}{D} \right)^{m_r} \quad (2.8)$$

$$\frac{U_m}{U_j} = B_p \left(\frac{x + x_0}{b} \right)^{n_p} \quad (2.9)$$

$$\frac{U_m}{U_j} = B_r \left(\frac{r + r_0}{D} \right)^{n_r} \quad (2.10)$$

Table 2.3 summarises published values of the plane wall jet spread (m_p , A_p) and decay (n_p , B_p) parameters. The various studies were sorted in terms of slot Reynolds number (Re_b). Aside from Wygnanski *et al.* (1992), who found that an exponent of $m_p = 0.88$ resulted in a better fit than a linear relationship, there is consensus that the plane wall jet half-width increased linearly with streamwise distance.

Table 2.4 summarises published values of the radial wall jet spread (m_r , A_r) and decay (n_r , B_r) parameters. There appeared to be evidence of a linear jet spread for radial wall jets as well. The arithmetic mean of the listed A_p values was 83% of that of the listed A_r values, which supported the intuition that a three-dimensional flow would entrain more

ambient fluid than a two-dimensional flow and thus have a greater spread rate. Although, since the radial wall jet expands azimuthally (with increasing r), whilst the plane wall jet maintains a constant spanwise dimension (with increasing x), the conservation of mass flux suggests the opposite effect with respect to spread rate.

Velocity decay is well-documented for the plane wall jet. For the studies listed in Table 2.3, the arithmetic means for the decay exponent (n_p) and constant (B_p) were -0.52 and 4.19, respectively. Bakke (1957) found that the velocity decay of the radial wall jet was described by a power relation with an exponent of -1.12; however, no other decay data was found for the radial wall jet.

The Pearson product-moment correlation coefficient was calculated to investigate the relationship between the test facility parameters (e.g. Re_b , t/b , Y/b , Z/b for the plane wall jet) and the resulting flow conditions. With respect to the jet spread and velocity decay parameters, the strongest correlations were with Reynolds number. Correlation coefficients between -0.43 and +0.69 were found.

Table 2.3: Summary of plane wall jet spread parameters

Authors	Data range x/b	Re_b	Jet spread		Velocity decay	
			m_p	A_p	n_p	B_p
Bradshaw & Gee (1960)	339 to 1459	6.0E+03	1	0.071	-0.53	3.47
Eriksson <i>et al.</i> (1998)	5.2 to 208	9.6E+03	1	0.078	-0.56	4.25
Wyganski <i>et al.</i> (1992)	30 to 100	1.0E+04	0.88	?	-0.47	2.76
Abrahamsson <i>et al.</i> (1994)	30 to 175	1.0E+04	1	0.081	-0.50	3.37
Verhoff (1970)	104 to 417	1.0E+04	1	0.082	-0.48	3.20
	57 to 229	1.2E+04	1	0.077	-0.55	4.47
Schwarz & Cosart (1961)	24 to 42	1.4E+04	1	0.085	-0.50	4.67
Schneider & Goldstein (1994)	43 to 110	1.4E+04	1	0.077	-0.51	3.68
Abrahamsson <i>et al.</i> (1994)	30 to 175	1.5E+04	1	0.077	-0.50	3.58
Wyganski <i>et al.</i> (1992)	30 to 140	1.9E+04	0.88	?	-0.47	3.06
Abrahamsson <i>et al.</i> (1994)	70 to 175	2.0E+04	1	0.075	-0.50	3.85
Schwarz & Cosart (1961)	24 to 42	2.0E+04	1	0.069	-0.50	4.05
		3.0E+04	1	0.056	-0.62	6.90
Gartshore & Hawaleshka (1964)	18 to 124	3.1E+04	1	0.066	-0.53	4.47
Schwarz & Cosart (1961)	24 to 42	4.2E+04	1	0.061	-0.60	6.06
Förthmann (1934)	3 to 33	5.4E+04	1	0.082	-0.56	5.26
			arithmetic mean	0.074	-0.52	4.19
			sample standard deviation	0.008	0.04	1.11

Table 2.4: Summary of radial wall jet spread parameters

Authors	Data range r/D	Re_D	z_D/D	Jet spread		Velocity decay	
				m_r	A_r	n_r	B_r
Bakke (1957)	5 to 10.7	6.4E4	0.53	0.94	?	-1.12	?
Cooper <i>et al.</i> (1993)	3 to 7	2.3E4	2	1	0.073	?	?
	3 to 6		10	1	0.083	?	?
Knowles & Myszko (1998)	2 to 9	9.0E4	2	1	0.091	?	?
	3 to 10		10	1	0.109	?	?
Bradshaw & Love (1959)	3.2 to 20	1.8E5	18	1	0.088	?	?
				arithmetic mean	0.089		
				sample standard deviation	0.013		

2.5 Conclusions

For plane wall jets, the self-similarity of turbulence quantity profiles appeared to depend upon the slot top boundary condition. Studies with a wall condition above the slot exit found turbulence quantity profiles that tended towards a self-similar state. In contrast, studies using a thin lip above the slot exit indicated turbulence quantities continued to increase in magnitude in the streamwise direction. At distances downstream of the slot that are of practical interest, the magnitudes of the self-similar profiles (wall condition) are within the range of the developing profiles (thin slot top condition). The profile shapes agreed well, especially in the inner layer (between the wall and z_m). The slot top boundary condition did not appear to significantly affect the inner layer of the wall jet.

Minimal discrepancies were found between the profiles of time-averaged streamwise velocity for the developed plane wall jet ($x/b \geq 50$) and for the developing radial wall jet ($r/D = 2.0$). Near the wall, the difference between profiles of time-averaged velocity from plane and radial wall jets was essentially less than the experimental uncertainty. The uncertainty of the present plane wall jet velocity measurements was typically less than $\pm 8.4\%$ of the measured value.

The turbulence quantity profiles for the radial wall jet approached self-similarity at $r/D \geq 5.0$, but agreement with the magnitude of the plane wall jet profiles was best in the developing regime at slightly greater than $r/D = 2.0$, where the maximum turbulence

intensities and turbulent kinetic energy production occurred. Plane and radial wall jet turbulence profiles showed general likeness with regards to shape, but turbulence measurements closer to the wall are required for the radial wall jet to verify this. Between $x/b = 50$ and 150, at the height of U_m , the streamwise turbulence intensity for the plane wall jet increased from 0.14 to 0.19. At all other heights, a similar streamwise increase in streamwise turbulence intensity was observed. The developing profile of radial wall jet turbulence intensity remained within this band.

The majority of studies in the literature indicated that the radial and plane wall jets grow linearly with streamwise distance, in their respective developed flow regimes. The plane wall jet spread rate appeared to be about 83% of the radial wall jet spread rate. It is recommended that further fundamental investigations focus on the sensitivity of the jet spread/decay to the facility characteristics. This chapter advanced the discussion of previous wall jet reviews, and compared the plane and radial configurations.

2.6 References

- Abrahamsson, H., Johansson, B., and Löfdahl, L. (1994), "A turbulent plane two-dimensional wall-jet in a quiescent surrounding", *Eur. J. Mech. B-Fluids*, **13**(5), 533-556.
- Bajura, R.A. and Catalano, M.A. (1975), "Transition in a two-dimensional plane wall jet", *J. Fluid Mech.*, **70**(4), 773-799.
- Bajura, R.A. and Szewczyk, A.A. (1970), "Experimental investigation of a laminar two-dimensional plane wall jet", *Phys. Fluids*, **13**, 1653-1664.
- Bakke, P. (1957), "An experimental investigation of a wall jet", *J. Fluid Mech.*, **2**, 467-472.
- Bradshaw, P. and Gee, M.T. (1960), "Turbulent wall jets with and without an external stream", *Aeronaut. Res. Counc. R & M*, 3252.
- Bradshaw, P. and Love, E.M. (1959), "The normal impingement of a circular air jet on a flat surface", *Aeronaut. Res. Counc. R & M*, 3205.
- Chay, M.T. and Letchford, C.W. (2002), "Pressure distributions on a cube in a simulated thunderstorm downburst – Part A: stationary downburst observations", *J. Wind Eng. Ind. Aerodyn.*, **90**, 711-732.
- Cooper, D., Jackson, D.C., Launder, B.E., and Xiao, G.X. (1993), "Impinging jet studies for turbulence model assessment-I. Flow-field experiments", *Int. J. Heat Mass Transfer*, **36**(10), 2675-2684.
- Eriksson, J.G., Karlsson, R.I., and Persson, J. (1998), "An experimental study of a two-dimensional plane turbulent wall jet", *Exp. Fluids*, **25**, 50-60.
- Fairweather, M. and Hargrave, G.K. (2002), "Experimental investigation of an axisymmetric, impinging turbulent jet. 1. Velocity field", *Exp. Fluids*, **33**, 464-471.

- Förthmann, E. (1934), “Über turbulente Strahlausbreitung” (in German), *Ing. Arch. (Arch. Appl. Mech.)*, **5**(1), 42-54. “Turbulent jet expansion” (English translation, March 1936), *NACA Tech Memo* No. 789.
- Gartshore, I. and Hawaleshka, O. (1964), “The design of a two-dimensional blowing slot and its application to a turbulent wall jet in still air”, *McGill Engineering Research Laboratory Technical Note*, 64-5, McGill University, Canada.
- George, W.K., Abrahamsson, H., Eriksson, J., Karlsson, R.I., Löfdahl, L., and Wosnik, M. (2000), “A similarity theory for the turbulent plane wall jet without external stream”, *J. Fluid Mech.*, **425**, 367-411.
- Glauert, M.B. (1956), “The wall jet”, *J. Fluid Mech.*, **1**, 625-643.
- Hinze, J.O. (1975), *Turbulence*, 2nd edition, McGraw-Hill, New York, NY, USA, x, 790 pp.
- Jørgensen, F.E. (2005), *How to measure turbulence with hot-wire anemometers - a practical guide*, Publication No. 9040U6151, Dantec Dynamics A/S, Skovlunde, Denmark.
- Knowles, K. and Myszko, M. (1998), “Turbulence measurements in radial wall-jets”, *Exp. Therm. Fluid Sci.*, **17**, 71-78.
- Lauder, B.E. and Rodi, W. (1981), “The turbulent wall jet”, *Prog. Aerosp. Sci.*, **19**, 81-128.
- Lauder, B.E. and Rodi, W. (1983), “The turbulent wall jet – measurements and modeling”, *Ann. Rev. Fluid Mech.*, **15**, 429-459.
- Lin, W.E. and Savory, E. (2006), “Large-scale quasi-steady modelling of a downburst outflow using a slot jet”, *Wind Struct.*, **9**(6), 419-440.
- Narasimha, R., Narayan, K.Y., and Parthasarathy, S.P. (1973), “Parametric analysis of turbulent wall jets in still air”, *Aeronaut. J. Roy. Aeronaut. Soc.*, **77**, 355-359.
- Poreh, M., Tsuei, Y.G., and Cermak, J.E. (1967), “Investigation of a turbulent radial wall jet”, *J. Appl. Mech.*, **34**, 457-463.
- Schlichting, H. (1979), *Boundary-layer theory*, 7th edition, McGraw-Hill, New York, NY, USA, xxii, 817 pp.
- Schneider, M.E. and Goldstein, R.J. (1994), “Laser Doppler measurement of turbulence parameters in a two-dimensional plane wall jet”, *Phys. Fluids*, **6**(9), 3116-3129.
- Schwarz, W.H. and Cosart, W.P. (1961), “The two-dimensional turbulent wall-jet”, *J. Fluid Mech.*, **10**, 481-495.
- Verhoff, A. (1970), “Steady and pulsating two-dimensional turbulent wall jets in a uniform stream”, PhD thesis, Princeton University, USA, 383 pp.
- Wheeler, A.J. and Ganji, A.R. (1996), *Introduction to engineering experimentation*, Prentice Hall, Englewood Cliffs, NJ, USA, xiii, 417 pp.
- Wood, G.S., Kwok, K.C.S., Motteram, N.A., and Fletcher, D.F. (2001), “Physical and numerical modelling of thunderstorm downbursts”, *J. Wind Eng. Ind. Aerodyn.*, **89**, 535-552.
- Wyganski, I., Katz, Y., and Horev, E. (1992), “On the applicability of various scaling laws to the turbulent wall jet”, *J. Fluid Mech.*, **234**, 669-690.
- Xu, Z. and Hangan, H. (2008), “Scale, boundary and inlet condition effects on impinging jets”, *J. Wind Eng. Ind. Aerodyn.*, **96**, 2383-2402.
- Zhou, M.D. and Wygnanski, I. (1993), “Parameters governing the turbulent wall jet in an external stream”, *AIAA J.*, **31**(5), 848-853.

CHAPTER 3

QUASI-STEADY MODELLING OF A DOWNDRAFT OUTFLOW*

3.1 Introduction

Downdrafts are known to persist to planetary surface level. Impingement at the surface results in a divergent flow that spreads outwards from the downdraft column. Fujita (1990) addressed his findings to wind engineers, who are primarily concerned with damage to the built environment by the outflow region (Selvam and Holmes 1992, Nicholls *et al.* 1993, Letchford *et al.* 2002). Fujita and Wakimoto (1981) described downburst clusters on 16 July 1980 that caused \$650 million of damage in Wisconsin, Illinois and Michigan. Simplifying assumptions of axisymmetric and steady flow have been applied, when considering the approximate wind loading in the outflow region (Selvam and Holmes 1992).

The following considerations need to be addressed in downdraft outflow simulations:

- a) Fig. 3.1 depicts how the vertical profile of the quasi-steady horizontal wind speed has a different shape than that of the conventional atmospheric boundary layer (ABL). The characteristic mean velocity profile associated with the downdraft outflow has a maximum velocity that occurs near ground level and decreases with further increase in height. The ABL profile increases monotonically with height and is commonly modelled with either a power or logarithmic law equation (American Society of Civil Engineers 1999). For lattice tower designs in which specific members are designed for a specific load case, this difference in the vertical variation of the wind load may be critical.
- b) A quasi-steady model neglects the evolution in time of the outflow and simply assumes a steady velocity profile. The early experiments, related to wind engineering applications, were developed on this basis (Holmes 1992, Letchford and Illidge 1999, Wood *et al.* 2001). The quasi-steady approach is the focus of this chapter.
- c) More realistic models consider the transient nature of the outflow. From the perspective of a stationary object, a downdraft outflow passes by as a sudden and short-lived event. Anemometer records of the outflow show a sharp rise in velocity with near-peak winds generally lasting less than 5 minutes, as indicated by full-scale time histories

* Excerpts from this chapter were published as *Wind and Structures* 9(6), 2006.

(Fujita 1985, Gast and Schroeder 2003). Wind tunnel simulation beyond a simple quasi-steady approach is discussed in the following chapter, where the present slot jet approach is developed further to incorporate transient wind effects.

d) A primary vortex ring that expands radially outward from the central axis of the downburst is a dominant feature in the outflow region (Fujita 1985, Hjelmfelt 1988). Near the ground plane, the circulating fluid of the vortex ring moves in the same outward direction as the divergent impinging flow, so maximum outflow velocities are expected there (Proctor 1988). This vortex ring may cause a significant vertical velocity component in the outflow. Comparison of the instantaneous vertical profile of radial velocity of a transient impinging jet (Mason *et al.* 2005) to the time-averaged vertical profile of radial velocity of a steady impinging jet (Chay and Letchford 2002) show significant differences in profile shape and suggest that the vortex ring leads to higher peak maximum velocities.

e) Since the downdraft outflow event is a non-stationary process, it is problematic to quantify the downdraft outflow gustiness using the traditional definition of turbulence intensity. As proposed by Choi and Hidayat (2002), assessment of the variations about a moving average seems to be more appropriate. Their approach allows an effective turbulence intensity to be determined.

f) Local surface flows with reported speeds of up to 11 m/s (Hjelmfelt 1988) may distort the idealised, axisymmetric flow and cause a pronounced directionality of the outflow, which is associated with tilting of the downdraft from the vertical. As well, the overall motion of the parent storm is thought to translate embedded downbursts. Assuming superposition of the storm translation velocity onto the axisymmetric model flow field, the maximum velocities are expected to be in the direction of the storm motion and just behind the leading edge of the translating downburst (Fujita 1981). A simulation facility should have the capability to model both stationary and translating events.

The present chapter focuses on the first two items above. By extension of the present approach, the other considerations are discussed in the next chapter. As described in Section 4.4.1, an actuated control gate that was added to the test facility is of particular relevance to the later items.

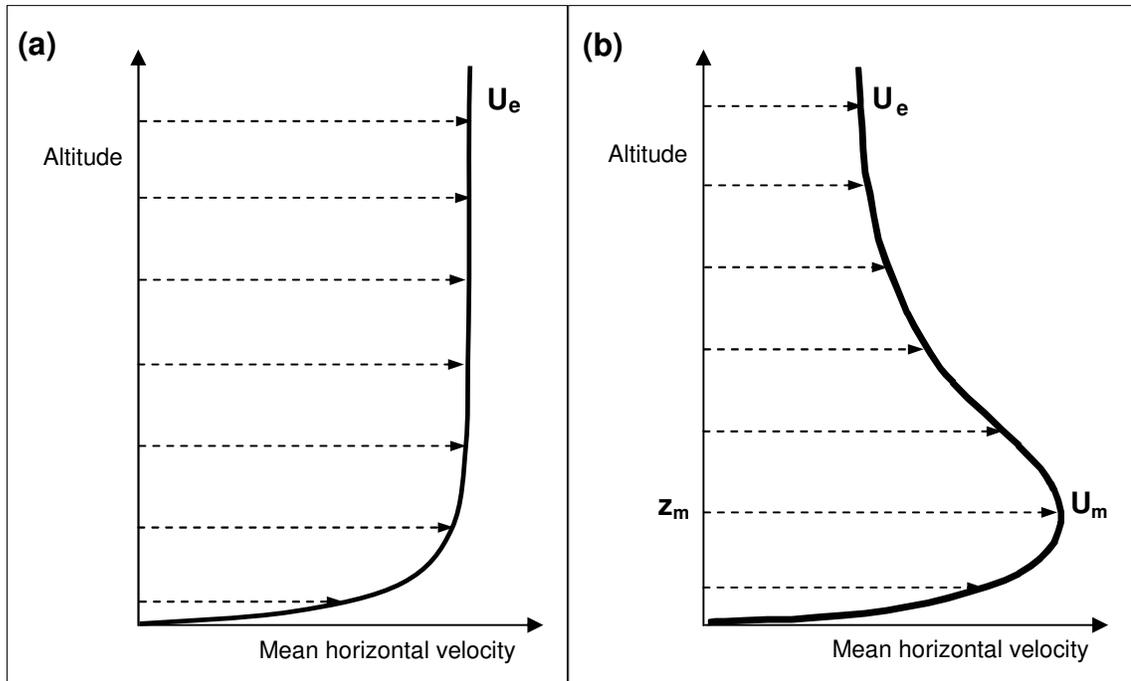


Figure 3.1: Velocity profiles for (a) conventional atmospheric boundary layer and (b) downdraft outflow

3.2 Experimental methodology

As noted by Hjelmfelt (1988), the downdraft outflow profile bears a strong resemblance to the classical wall jet. In contrast to field observation, wall jet simulations in a controlled environment are reproducible. Furthermore, more detailed measurements are feasible in laboratory experiments than in field studies.

3.2.1 Previous approaches

Previous downburst experiments used one of the two following methods. Investigations of downburst morphology and structure have been conducted at very small geometric and velocity scales by the release of a liquid mass into a larger body of less dense liquid (Lundgren *et al.* 1992, Alahyari and Longmire 1995, Yao and Lundgren 1996). This approach is not suitable for wind loading studies on models. Larger scale simulations used an impinging jet as shown in Fig. 3.2 (Letchford and Illidge 1999, Wood *et al.* 2001, Chay and Letchford 2002, Xu and Hangan 2008).

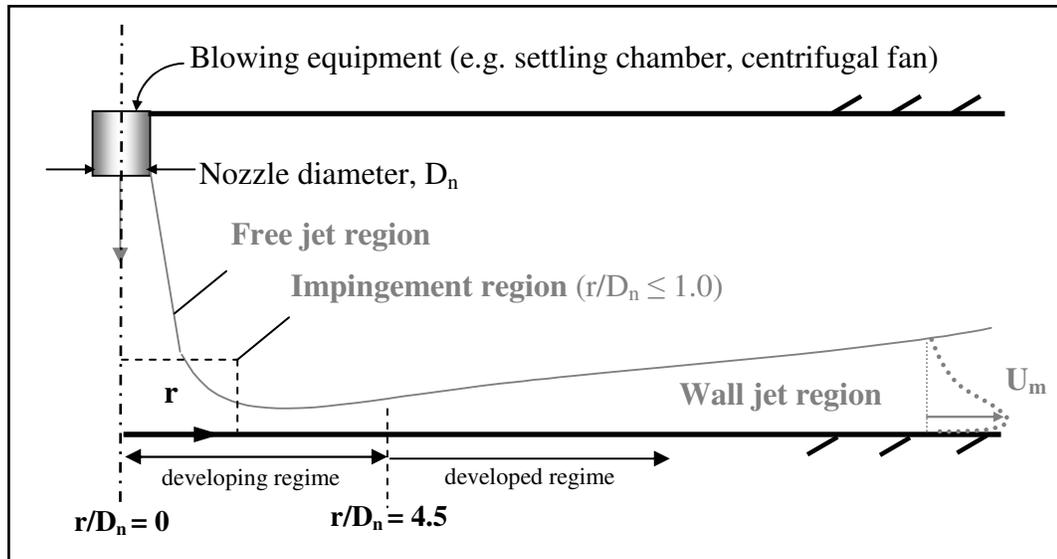


Figure 3.2: Radial wall jet from a round nozzle

A centrifugal fan was typically used to drive air through a circular nozzle, with flow conditioning devices located between the fan and nozzle. The flow travelled from the nozzle towards the impingement plane as an axisymmetric free jet. Measurements by Chay and Letchford (2002) indicated that the impingement region extended from the free jet axis to somewhere between $r/D_n = 1.0$ and 1.25 . Xu and Hangan (2008) suggested a value of $r/D_n < 1.4$. The normal-to-impingement-plane profiles of mean radial velocity and turbulence quantities reached a developed state after 3.0 and 4.5 nozzle diameters downstream of the nozzle axis, respectively (Knowles and Myszko 1998). These impinging jet studies defined a jet Reynolds number (Re_D) based on nozzle diameter (D_n) and exit velocity (W_j).

Table 3.1 compares the key parameters from various impinging jet studies to those found in the full-scale outflow. Note that full-scale downdraft diameter (D) was a best estimate, whereas D_n was accurately known in laboratory experiments. The reported maximum radial velocities compiled in Table 3.1 should be treated with caution. The full-scale values were the largest reported wind speeds over time and space. However, the impinging jet studies used a continuous jet with a quasi-steady assumption, so they reported a spatial maximum that has been time-averaged.

Table 3.1: Comparison of full-scale and impinging jet studies

Study	Downdraft		Outflow		Comments
	diameter [m]	reported max U [m/s]	z_m [m]	radial position of reported max U	
Full-scale	D			r/D	
Fujita (1981, 1985, 1990)	2000 at $z/D \sim 0.45$	32 27	50 30	1.1 no data	Yorkville downburst. ^a (NIMROD) 29 May 1978.
Fujita (1985)	likely < 2000	likely > 67	likely > 4.9	no data	Andrews AFB downburst. 1 August 1983. Single point measurement.
Hjelmfelt (1988)	1500 - 3000 at $z = 1500$ m AGL	≈ 18	no data	0.75 - 1.0	Downdraft data from 11 events. Outflow data from 14 July D. (JAWS) June - August 1982.
Impinging jet	D_n			r/D_n	
Letchford & Illidge (1999)	1.01 at $z/D_n = 0.90$	10	≈ 0.01	1.5	Flow from wind tunnel exit with octagonal cross-section.
Wood <i>et al</i> (2001)	0.31 at $z/D_n = 2$	19	0.004	1	Flow from circular nozzle attached to rectangular settling chamber.
Chay & Letchford (2002)	0.51 at $z/D_n = 1.7$	10	≈ 0.006	≈ 1	Flow from circular nozzle (with lip) attached to settling chamber.
Xu (2004)	0.22 at $z/D_n = 1, 2, 3, 4$	≤ 13	< 0.006 in all cases	1	Flow from ≈ 15 m long circular pipe attached to settling chamber.

^a Two records of the event made 6 minutes apart (Fujita, 1985)

Since z_m from an impinging jet was dependent on D_n , generating a large-scale wall jet required a tremendous nozzle diameter. The separation distance between nozzle and ground plane also increased as D_n increased, if z/D_n was to be kept similar to observed cloud base height to downdraft diameter ratios. D_n in previous studies was fairly large in terms of what is feasible in a laboratory, yet the largest z_m (at the radial position of reported max U as compiled in Table 3.1) was only a few centimetres.

In addition to practical space requirements, it was also difficult to refine a large-scale impinging jet to include further complexities beyond the basic stationary downburst configuration. The present approach addressed this practical engineering problem of

maximizing the flow size, whilst retaining the key features of an intense downburst outflow. It was also readily extended to model the outflow from a translating event.

This section discussed experimental simulation and field observations. Computational fluid dynamics (CFD) has also been used extensively to simulate downbursts. Kim and Hangan (2007) investigated an impinging jet model by solving the unsteady Reynolds-averaged Navier-Stokes (URANS) equations. Mason *et al.* (2009, 2010) combined an improved URANS method with initial forcing of the flow by a cloud-level cooling source (Orf *et al.* 1996). Vermeire *et al.* (2009, 2010) investigated large-eddy simulation (LES), where the flow was forced by a cloud-level cooling source. Chapter 4 presents a more detailed discussion of the CFD modelling of downbursts.

3.2.2 Present approach

By treating the outflow separately from the downdraft column, the outflow region was simulated at a larger scale than in previous experiments. An analogous approach is well-established for ABL wind loading studies. Wind tunnel boundary layer spectra showed good agreement with full-scale data when only the lower third of the total ABL thickness was simulated at 1:100 to 1:250 scale (Cook 1973). Thus, a suitably large boundary layer for model testing was achieved in a wind tunnel of economical size (typically ≈ 2 m height and ≈ 10 m fetch).

The present work modelled the downburst outflow by introducing a strong secondary flow at the beginning of the working section of a conventional ABL wind tunnel. A schematic of the slot jet flow with conventional nomenclature is shown as Fig. 3.3. A centrifugal fan beneath the tunnel ground plane directed the air flow through a rectangular slot located near the tunnel inlet. With distance downstream of the slot exit (x), velocity decayed and wall jet height (δ) increased.

The development x -distance was typically normalised by the slot height, b . A slot Reynolds number (Re_b) was defined based on slot height (b) and mean velocity at the slot exit (U_j). The x -distance required for the U profile to become “developed” appeared to be inversely related to Re_b . For the studies in Table 2.3, values as low as $x/b = 20$ (Förthmann 1934 with $Re_b = 5.4 \times 10^4$) and as high as $x/b = 104$ (Verhoff 1970 with $Re_b = 1.0 \times 10^4$) were reported. As side wall boundary layer growth became significant,

the wall jet lost its nominal two-dimensionality. For the present application, it was desirable to maximise Re_b and to work in the region of the plane wall jet that maintained satisfactory two-dimensionality.

The wind tunnel flow may also be run simultaneously as a co-flow with the slot jet. Superposition of the co-flow and wall jet yielded downstream velocity profiles that can be used to model the outflow from a translating downburst. Hjelmfelt (1988) noted local surface cross-flows of up to 11 m/s in various Colorado downbursts that can contribute to the downburst outflow velocity.

The following results in Section 3.3 are for a slot jet without a co-flow, which corresponds to a stationary downdraft. A further complexity was that the wind loading may have a significant vertical component depending on the location of the downdraft relative to the structure. Mara *et al.* (2010) designed and tested a section model mount with three rotational degrees of freedom. Implemented with a slot jet facility, vertical loads from a downburst can be simulated. For a quasi-steady approach, the horizontal component was regarded as the dominant load in the outflow since the vertical velocity in the impingement region decreased to zero at the impingement plane.

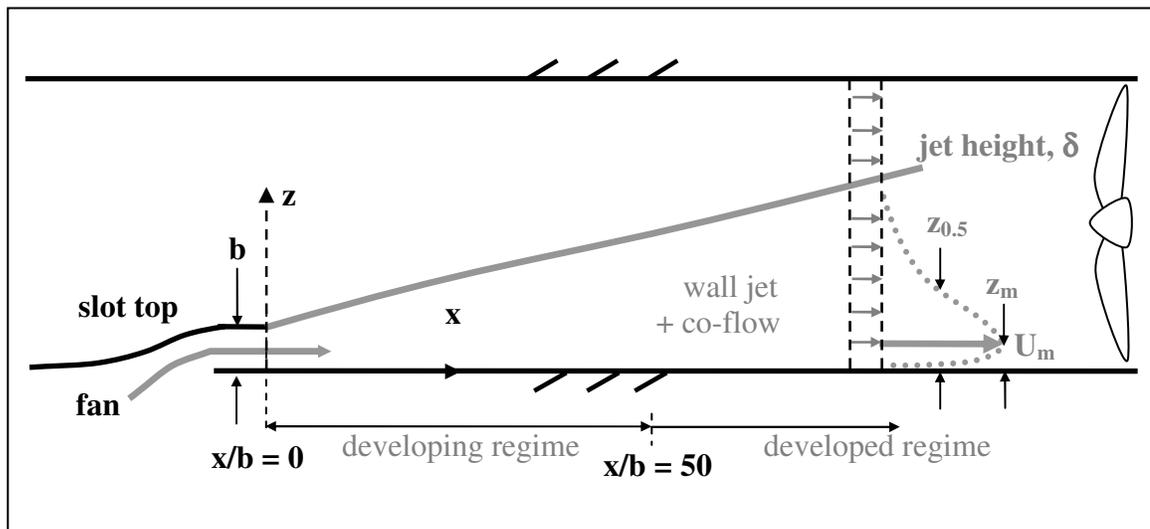


Figure 3.3: Plane wall jet from a rectangular nozzle

3.2.3 Prototype test facility

Fig. 3.4 depicts the proof-of-concept prototype that was implemented. Chapters 2 to 4 pertain to results from this test facility. Chapter 5 discusses the full-size implementation of this prototype in the large Wind Tunnel 1 at The University of Western Ontario. A rectangular slot nozzle was flush with the ground plane, allowing the expelled slot jet to develop into a plane wall jet.

Sizing of the fan and system components (e.g. screens) involved an iterative procedure similar to that used for pipe/duct flows. The design guidelines by Mehta (1977) for blower tunnels were incorporated. The detailed design and specifications of the prototype and full-size facilities were given by Lin (2005).

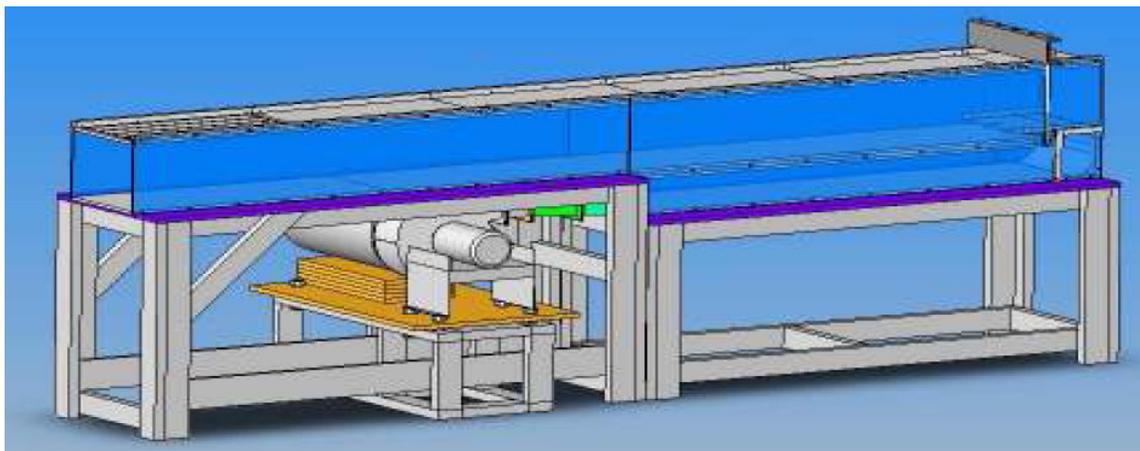


Figure 3.4: Prototype slot jet wind tunnel for downburst outflow simulation

3.2.4 Velocity profile measurements

Mean and turbulent velocity quantities were of primary interest, and crossed hot-wire anemometry (HWA) was utilised in this study. The Dantec MiniCTA 54T30 outputs were sampled with a National Instruments PCI-6071E data acquisition card (12-bit resolution). This measurement system had a frequency response of up to 10 kHz. The following prototype facility results were from 30 s samples at 1 kHz sampling rate.

A computer-controlled, two-axis traverse system allowed fine positioning of the crossed-wire probe. The traverse slides were controlled using stepper motors and the

overall positioning accuracy of the probe in the following data was ± 0.2 mm. The measurement of a velocity profile was completely automated using LabVIEW software programs that were developed by the author.

Measurements of larger velocities were more certain with this system. Since slot jet velocity decayed with distance from the slot exit, vertical profile maximum velocity (U_m) at smaller x/b had more certainty. The uncertainty on U_m was estimated as $\pm 7\%$ (± 1.7 m/s) at $x/b = 50$ and $\pm 11\%$ (± 1.1 m/s) at $x/b = 208$, for a 95% confidence level. Accuracy of the HWA and scale readability of the calibration manometry were considered. The sources of systematic and random uncertainty were listed in Section 2.3.3.

3.3 Comparison of plane and radial wall jet data

Flow conditioning prior to the slot exit consisted of three wire mesh screens (total pressure loss coefficient of 4.6) located at the diffuser, fairings for the 180° bend from the anterior duct to the slot, and a cross-sectional area contraction ratio of 9-to-1 from the duct to the slot. As found in the high-precision facility of Gartshore and Hawaleshka (1964), the exit profile of the slot jet exhibited a larger boundary layer thickness on the bottom surface than the top surface of the slot. At the slot exit, the jet was nominally two-dimensional. Across the central 75% of the span, U variation was within $\pm 1.5\%$ of the spanwise mean. Slot exit streamwise turbulence intensity was less than 6%.

In the outflow simulator prototype, mean streamwise velocity profiles (variation of U across the z -direction) were measured at four distances downstream of the slot exit ($x/b = 50, 100, 150,$ and 208). Based on the studies reviewed by Lin (2005), the plane slot jet should be well-developed at $x/b = 50, 100,$ and 150 , and was possibly losing its two-dimensionality at $x/b = 208$. The exit velocity was 46 m/s and the slot jet Reynolds number was $Re_b = 4.0 \times 10^4$. The working section ground plane was an aerodynamically-smooth melamine surface.

Following the fluid mechanics convention, U was normalised by the vertical profile maximum (U_m). The normal-to-wall distance was non-dimensionalised by the normal distance at which $U = 0.5 \cdot U_m$ occurred in the outer part of the wall jet. This distance,

referred to as the half-width ($z_{0.5}$), is shown in Fig. 3.3. However, in Fig. 3.5, the prototype facility measurements are normalised by z_m in order to compare with full-scale data that were presented in this manner (Hjelmfelt 1988). It may also be argued that z_m is appropriate as a length scale for the region close to the ground, whereas $z_{0.5}$ is a better representation of the typical size of eddies that are further away from the wall. The larger scatter for data at $x/b = 150$ and 208 is likely due to higher uncertainty of the HWA for lower velocity measurements. U_m values are 25, 19, 14 and 10 m/s at the four streamwise locations.

Rather than simply taking U_m as the largest measured value without any consideration for experimental variability, U_m was determined from the maximum value of a curve fit to the experimental data. The form of the equation suggested by Verhoff (1970) for developed plane wall jets was used in the fitting procedure. Experimental scatter of data points about the best-fit curve maximum results in some points exceeding $U/U_m = 1$ in Fig. 3.5. Nevertheless, the measured data show general agreement with the empirical function suggested by Verhoff (1970). Verhoff found the constants in his empirical function from experiments where Re_b was less than a third of the present value, suggesting that the shape of the downstream mean profiles are not strongly dependent on the slot jet Reynolds number. Verhoff's function also matched the plane wall jet experimental results of other investigators, as discussed in Chapter 2.

Hjelmfelt (1988) presented full-scale profiles of eight downbursts from the JAWS field study. The upper and lower bounds on these profiles, and the mean, are shown in Fig. 3.5. As well, full-scale measurements from the NIMROD study were essentially identical to Hjelmfelt's mean curve for points near the velocity maximum (Wood *et al.* 2001). The plane wall jet profiles from the present study fell within the range of the full-scale profiles, and tended towards the upper bound.

Fig. 3.6 compares mean profiles from plane and radial wall jet experiments. Here, z was normalised by the half-width. Due to the jet growth, the half-width at $x/b = 208$ in the prototype facility was influenced by the upper boundary of the test section. The half-width at $x/b = 208$ was influenced by the solid roof boundary, thus this profile is omitted from Fig. 3.6. Although normalising by half-width is problematic at the largest x/b , it is done at the smaller x/b locations here in order to compare with previous results.

The prototype facility data were represented fairly well by the developed plane wall jet empirical function (Verhoff 1970). Wood *et al.* (2001) suggested a function of identical form for the mean radial velocity profile of the radial wall jet, based on their impinging jet results for $r/D_n \geq 1.5$. Both functions involved raising $(z/z_{0.5})$ to an exponent to account for the region beneath the profile maximum that resembles a boundary layer. Due to the exponent term (1/7 for plane and 1/6 for radial wall jets), the plane wall jet function had larger near-wall velocities than the radial wall jet function. Agreement was within a few percent otherwise. Note that previous investigators reported maximum horizontal mean velocity at a radial distance of $r/D_n \approx 1$, as Table 3.1 indicated.

Besides the agreement with Wood *et al.* (2001), the representative 2-D wall jet profile (Verhoff 1970) also agreed well with the developing region from high- Re_D impinging jet experiments by Chay and Letchford (2002) and Xu (2004). Letchford and Illidge (1999) generated the downdraft using a wind tunnel with a non-circular cross-section, which may explain why their data were the poorest match to the plane wall jet data. In addition, radial confinement effects may be a concern since their flow was bounded on two sides by solid surfaces at $1.06 D_n$ and $1.29 D_n$. Xu (2004) found that a minimum radius of $8 D_n$ from the jet centreline was required to completely avoid perturbation of the surface pressure field by physical boundaries. The results from Letchford and Illidge (1999) were of interest though, because the outflow was one of the larger wall jets generated with an impinging jet.

The general agreement between the 2-D profiles and the full-scale results extracted from Hjelmfelt (1988) is encouraging, given that ground roughness effects have not been addressed. All of the aforementioned results were from experiments that used a flat and aerodynamically-smooth surface, which is the simplest terrain that a downburst outflow may encounter. CFD and experiments indicated that profile shape is dependent on surface roughness in a predictable manner (Wood *et al.* 2001, Xu 2004, Choi 2004, Lin 2005, Mason *et al.* 2010). For flow over a flat surface, surface roughness height is inversely related to the wall jet mean horizontal velocity and directly related to the height at which the maximum horizontal velocity occurs.

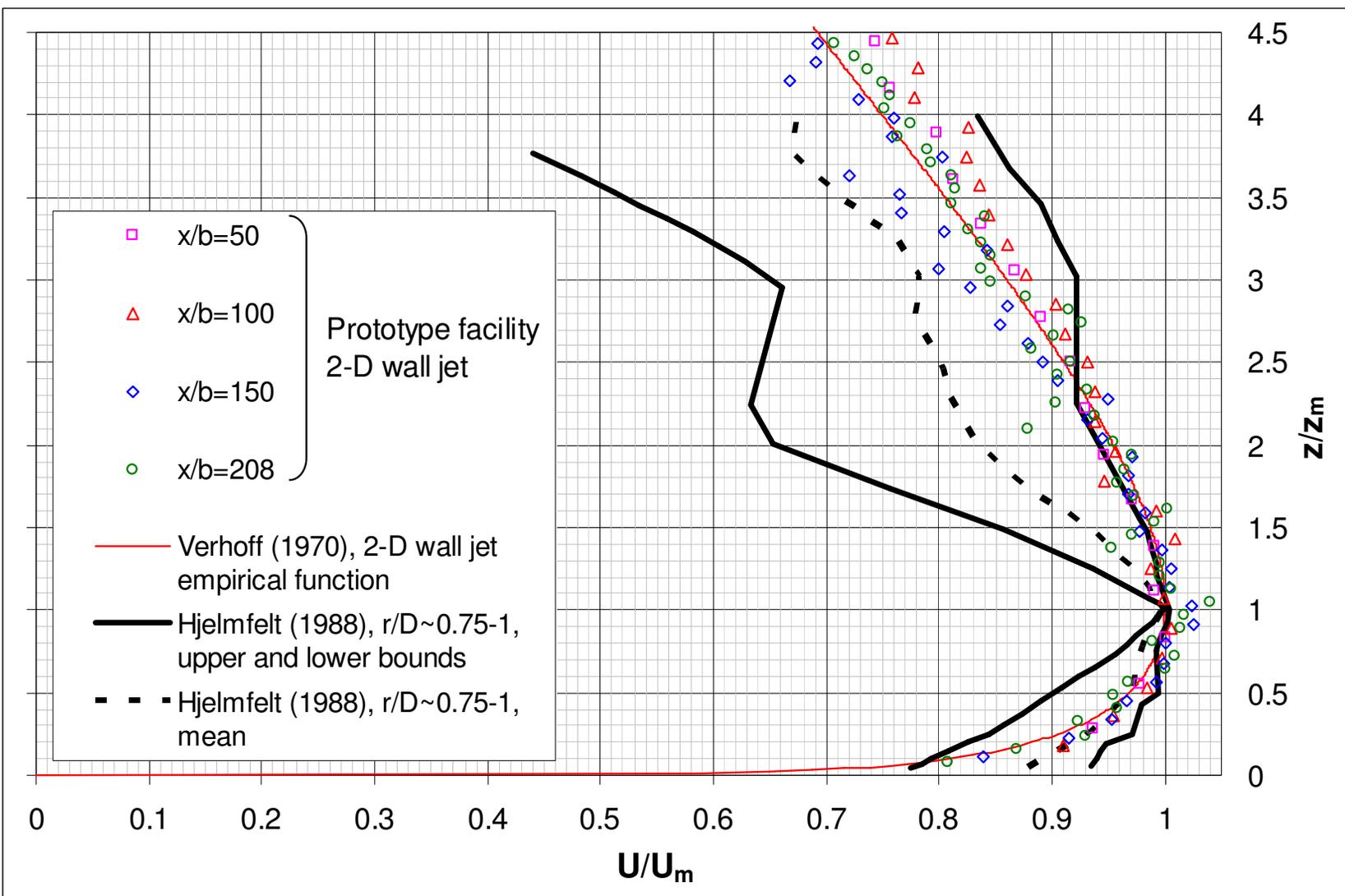
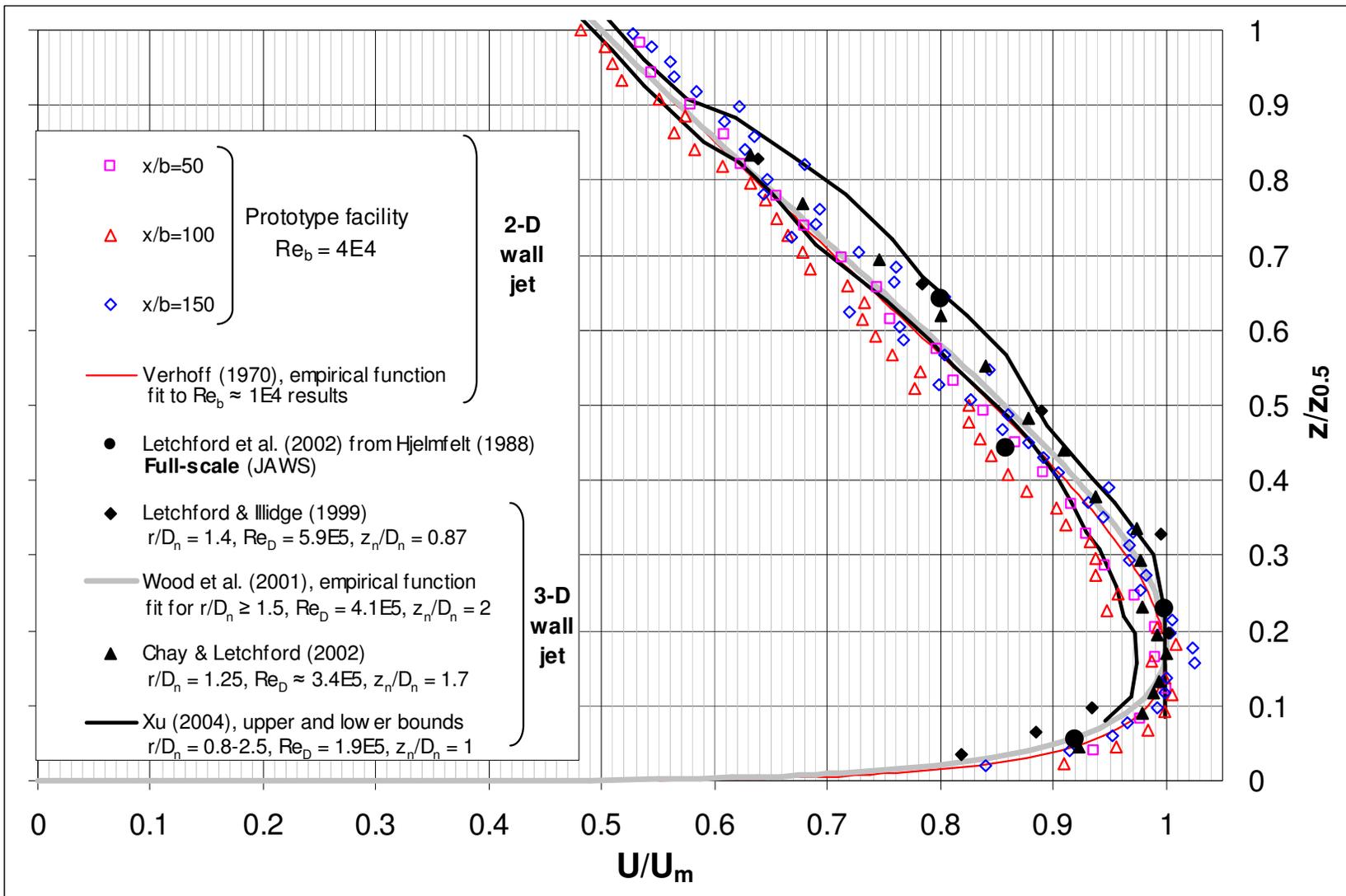


Figure 3.5: Mean streamwise velocity profile for plane wall jets and full-scale events

Figure 3.6: Mean streamwise velocity profiles for plane and radial wall jets



Given complete full-scale velocity time histories, it is still problematic to quantify the gustiness of a downburst outflow due to its strong transient nature. With a simple quasi-steady approach, it is recognised that the conventional definition of turbulence intensity does not properly account for the gustiness, and the next chapter will examine these issues. However, in order to further compare the wall jet region of steady impinging jets and slot jets, the conventional statistical measures are used.

Respectively, Figs. 3.7, 3.8 and 3.9 compare vertical profiles of the streamwise turbulence intensity, the vertical turbulence intensity, and the dominant component of turbulent shear stress. The literature presents turbulence profiles using $z_{0.5}$ scaling (Irwin 1973, Knowles and Myszko 1998, Letchford and Illidge 1999, Xu 2004), so this convention is followed. Note that known values of $z_m/z_{0.5}$ (Launder and Rodi 1981) permit conversion to z_m scaling, but such re-scaling does not add any new information.

Although the mean velocity profiles of the plane wall jet reach a fully-developed state at $x/b = 100$ and 150 , the corresponding turbulence profiles do not. A clear consensus, amongst previous workers, is not evident regarding similarity of the turbulence profiles. Wagnanski *et al.* (1992) did not find similarity for $x/b = 60$ to 120 and $Re_b = 5.0 \times 10^3$ to 1.9×10^4 . Abrahamsson *et al.* (1994) found similarity for $x/b = 70$ to 150 and $Re_b = 1.0 \times 10^4$ to 2.0×10^4 , but their facility had a vertical wall above the slot nozzle (i.e. an infinite slot lip thickness). The mean velocity profiles in these two studies match well.

Fig. 3.7 indicates that streamwise turbulence intensity (I_u) profiles in the fully-developed region of the plane wall jet are comparable to the radial wall jet profiles at $r/D_n = 1.4$ and 1.6 (Xu 2004), and at $r/D_n = 2.0$ (Knowles and Myszko 1998). Although the most intense winds in full-scale occur at slightly smaller radial distance, I_u in the self-similar region of the plane wall jet shows good agreement with I_u in the developing region of the radial wall jet. Notably, the radial wall jet profiles show an increase in I_u close to $z = 0$, which is not seen in the present plane wall jet data. However, the plane wall jet with co-flow examined by Irwin (1973) shows this increase close to the wall. In Figs. 3.7 to 3.9, the location of the maximum in the corresponding vertical profile of mean streamwise velocity, for the developed plane wall jet, is indicated by a horizontal dashed line.

Figure 3.7: Streamwise turbulence intensity profiles for plane and radial wall jets

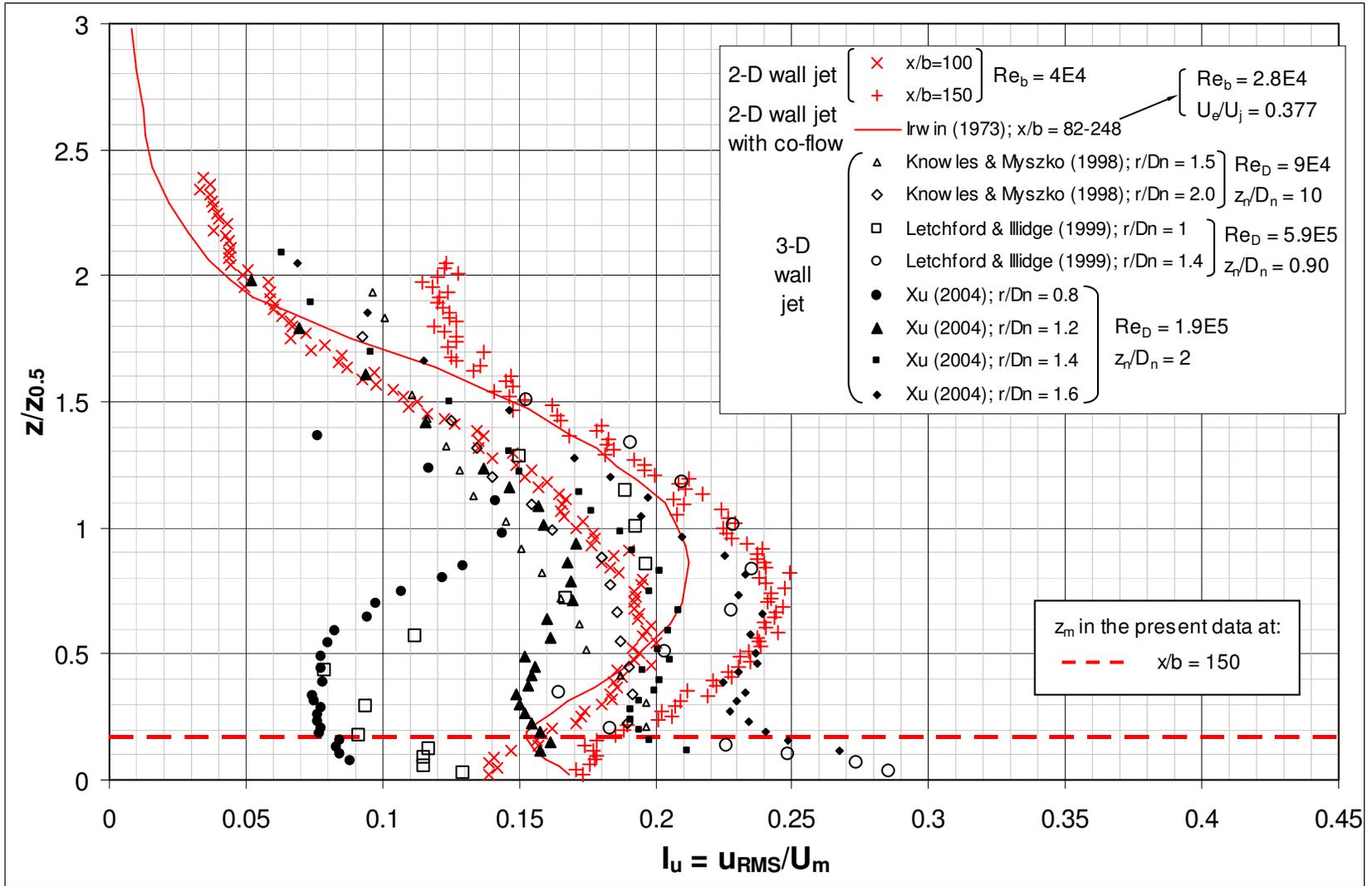


Figure 3.8: Vertical turbulence intensity profiles for plane and radial wall jets

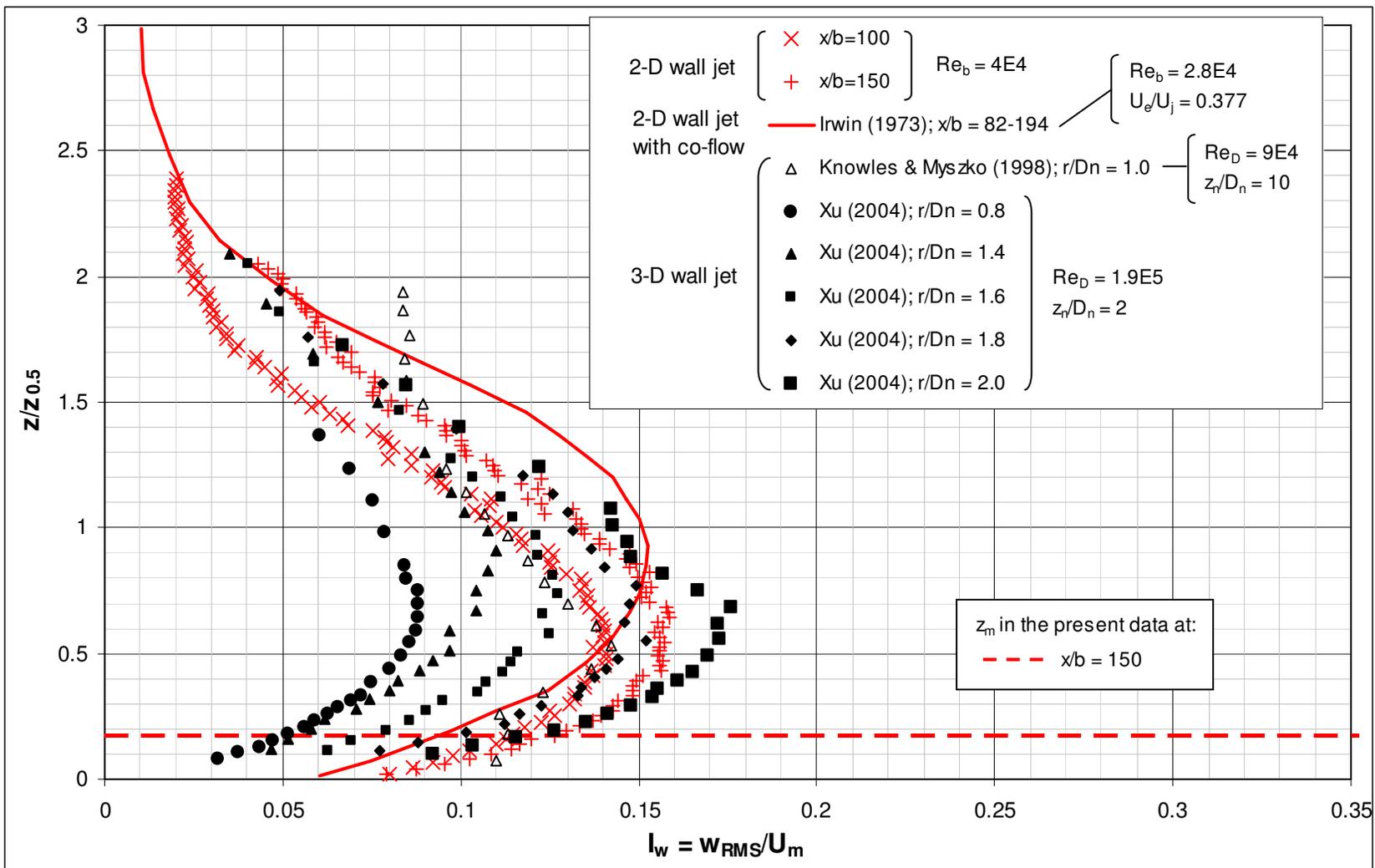
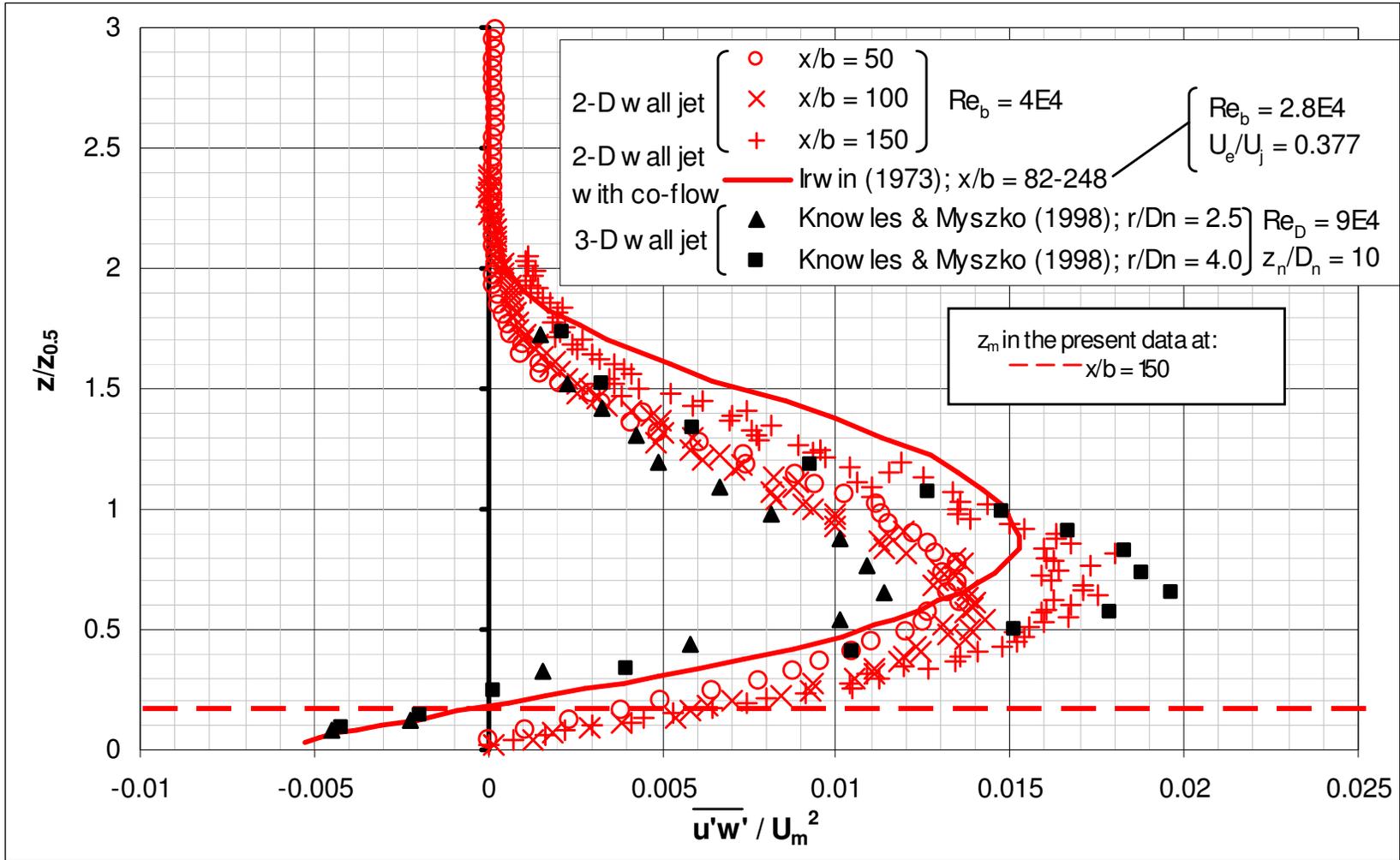


Figure 3.9: Turbulent shear stress profiles for plane and radial wall jets



Below $z/z_{0.5} = 1$, the profiles by Letchford and Illidge (1999) vary over a larger range of I_u than the other results. The impinging jet data from Poreh *et al.* (1967) has been used in the literature for comparison to downbursts. However, they measured turbulence quantities in the developed region only ($r/D_n > 9$) and used a nozzle height ($z/D_n = 12$) that is several times larger than what is realistic for downbursts.

Figs. 3.8 and 3.9 show good agreement in profile shape between the plane and radial wall jet for vertical turbulence intensity (I_w) and turbulent shear stress ($\overline{u'w'}$), respectively. Where the maximum in the mean profile occurs, the I_w profiles for the developed plane wall jet match the I_w profiles for the developing radial wall jet ($r/D_n = 1.0$, Knowles and Myszko 1998 and $r/D_n = 2.0$, Xu 2004). Turbulent shear stress profiles in the fully-developed region of the plane wall jet match the radial wall jet profiles at larger radial distance than for the I_u and I_w profiles - but the matching profiles are still in the region where the turbulence quantities of the radial wall jet are still developing ($r/D_n < 4.5$, Knowles and Myszko 1998).

The radial positions of the maximum turbulence intensities and maximum mean velocity do not coincide. As the mean velocity decays with distance from the jet origin, fluctuations are expected to be more significant relative to the local mean velocity. In terms of simulating a translating event with the present approach, it is encouraging that the profiles for the plane wall jet with co-flow have comparable magnitude and shape as the wall jet arising from impinging flow, for streamwise and vertical turbulence intensity in addition to turbulent shear stress.

3.4 Estimated model scale

Table 3.2 shows the estimated model scale of the flow in the prototype and full-size slot jet facilities for downburst outflow simulation. The model scale of impinging jet simulations was estimated by relating the nozzle diameter to full-scale downdraft diameter. Although a nominal value has occasionally been stated by previous investigators, a range of scales is more appropriate since diameter can vary by up to an order of magnitude for the same class of downdraft event.

The field data in Table 3.1 suggests that strong downbursts have a downdraft diameter of less than 2000 m. As well, Fujita (1981) estimated the smallest downbursts

have a diameter of at least 400 m. These two values and the nozzle diameter yielded the geometric scale ranges in Table 3.2 for impinging jet simulations.

The model scale of the slot jet facility was estimated based on local flow conditions, rather than the initial conditions of the test apparatus. Based on $z_m/D \approx 2.5\%$ at the radial location in the Yorkville downburst (Fujita 1985), where the maximum outflow velocity is expected (see Table 3.1), z_m at a desired test location in the facility was related to a corresponding downdraft diameter. For example, z_m equals 0.035 m at $x/b = 208$ in the prototype facility. This height-of-maximum-velocity corresponds to a 1.4 m downdraft diameter. Relating this value to downdraft diameters of 400 m and 2000 m, the prototype facility outflow was estimated as being 280 to 1400 times smaller than actual downburst outflows.

The velocity scale range in Table 3.2 was based upon 32.5 and 75 m/s – the former being the lowest wind speed where moderate structural damage is expected (Fujita 1981) and the latter being an estimate of the largest attainable velocity by a downburst¹ (Fujita 1985). Positioning the test model closer to the slot jet will result in larger wind loads. However, this comes at the cost of a smaller height-of-maximum-velocity, z_m .

Table 3.2: Estimated length scale of various downdraft outflow simulators

Experiment	Geometric scale	Velocity scale	Comments
3-D impinging jet			
Letchford & Illidge (1999)	1:400 - 1:2000	1:3.3 - 1:7.5	Steady jet from wind tunnel exit (octagonal cross-section).
Wood <i>et al</i> (2001)	1:1300 - 1:6500	1:1.6 - 1:3.8	Steady jet from circular nozzle.
Chay & Letchford (2002)	1:800 - 1:3900	1:3.3 - 1:7.5	Steady jet from circular nozzle with 5 cm lip.
Xu (2004)	1:1800 - 1:9300	1:2.5 - 1:5.8	Steady jet from large circular pipe.
2-D slot jet			
Prototype facility	1:280 - 1:1400	1:3.3 - 1:7.7	Based on current HWA results.
Full-size facility (BLWT1)	1:60 - 1:300	1:3.3 - 1:7.5	Based on predicted values for z_m and U_m at $x/b=208$.

¹ Fujita projected JAWS and NIMROD data to estimate annual downburst frequency for the contiguous USA. The estimated annual frequency was less than one at 75 m/s, as shown by Fig. 2.

3.5 Validity of the 2-D assumption for an idealised outflow

The geometry shown in Fig. 3.10 was examined to evaluate the accuracy of approximating a 3-D downburst outflow with a 2-D wall jet. The idealised outflow from a stationary downburst spreads radially outwards from a central stagnation point. To investigate the importance of downburst front curvature on the resultant wind loading of a structure, half of the transverse width of the structure is denoted as m and the shortest distance from the structure to the downburst stagnation point is denoted as r .

From the perspective of the exposed face of the structure, the lag distance (r^*) at the transverse ends of the exposed face is the largest distance that a radially expanding gust front lags behind a corresponding two-dimensional gust front. In other words, r^* , for a specified transverse width, is a direct indicator of the correlation of the wind load across the exposed face of the structure. The lag distance is a function of structure width and structure location relative to the downburst, as shown by Eq. (3.1).

$$r^* = \sqrt{m^2 + r^2} - r \quad (3.1)$$

The lag distances, for various combinations of structure location and exposed width, are shown in Table 3.3 as a percentage of r . The lag distance is insignificant for exposed widths of typical structures. For instance, Savory *et al.* (2001) considered a free-standing lattice tower of 50.5 m height and 9.1 m width. The range of exposed widths ($2 \cdot m$) in Table 3.3 covers multiple conductor spans of a transmission line system. Assuming a lag distance of less than 2 % of the shortest distance from the exposed face to the stagnation point as an acceptable downburst front curvature, the lower left (unshaded) values in Table 3.3 indicate that the two-dimensional assumption is valid for wide structures located far from the stagnation point. For an event with $D = 1000$ m, the high-intensity region is near $r = 1250$ m. For a 500 m transmission line section in this outflow, curvature effects are not expected to be significant and a two-dimensional approach appears to be a reasonable simplification.

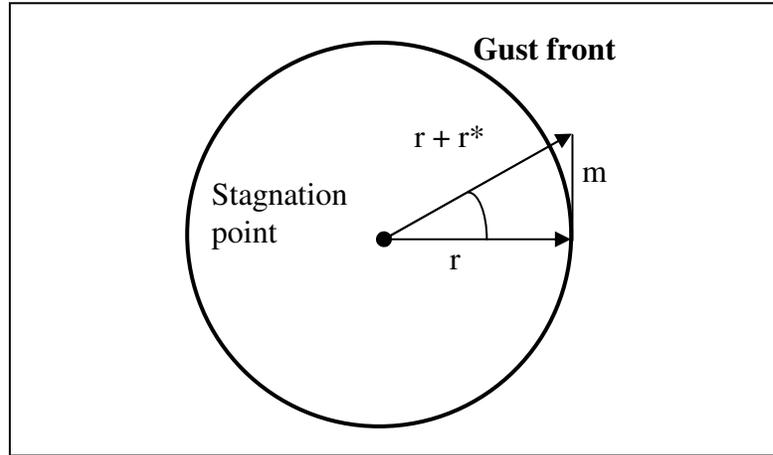


Figure 3.10: Plan view of a radially-expanding gust front

Table 3.3: Lag distance as a percentage of distance of structure from the stagnation point

r [m]	2·m [m]							
	10	100	200	300	400	500	1000	2000
250	0.020	2.0	7.7	17	28	41	124	312
500	0.005	0.5	2.0	4.4	7.7	12	41	124
750	0.002	0.2	0.9	2.0	3.5	5.4	20	67
1000	0.001	0.1	0.5	1.1	2.0	3.1	12	41
1250	0.001	0.08	0.3	0.7	1.3	2.0	7.7	28
1500	0.0006	0.06	0.2	0.5	0.9	1.4	5.4	20
1750	0.0004	0.04	0.2	0.4	0.7	1.0	4.0	15
2000	0.0003	0.03	0.1	0.3	0.5	0.8	3.1	12

The frontal curvature of the outflow of a translating downburst is expected to be less important than that of a stationary one, due to the stronger directionality of the former. Next, the outflow is approximated as emitting from a line source rather than a point source, and the validity of the two-dimensional gust front simplification is examined by considering the divergence of velocity. Expressing the horizontal divergence of velocity in the coordinate system and variables shown in Fig. 3.11, Eq. (3.2) is re-stated as the sum of longitudinal and transverse components, as shown by Eq. (3.3):

$$\nabla_h \cdot \vec{U} = \frac{\partial u}{\partial x} + \frac{\partial v}{\partial y} = (\text{longitudinal divergence}) + (\text{transverse divergence}) \quad (3.2)$$

$$\nabla_h \cdot \vec{U} = \frac{\partial U_r}{\partial s} + U_r \frac{\partial \theta}{\partial n} \quad (3.3)$$

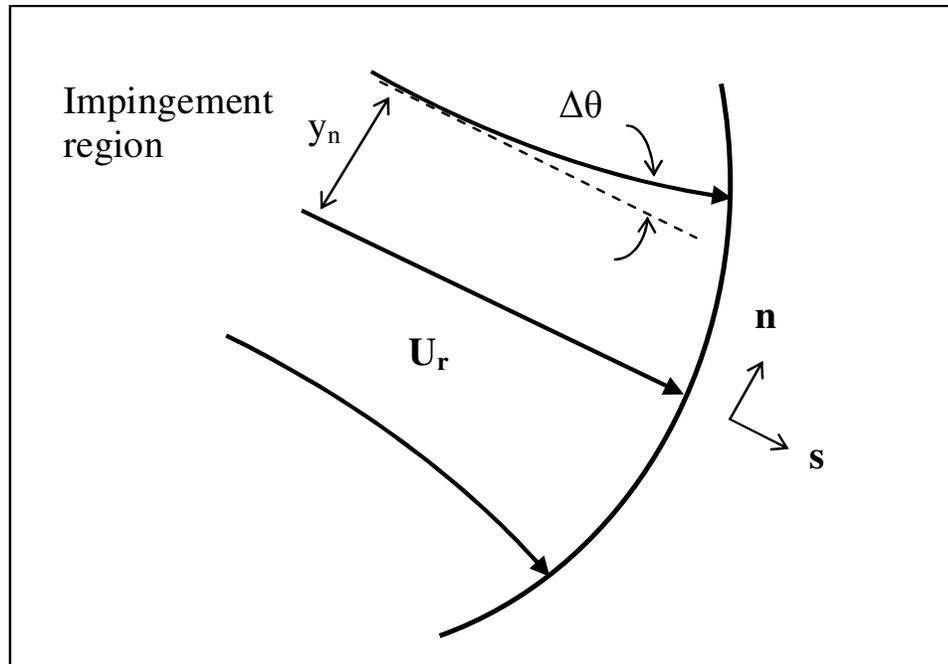


Figure 3.11: Plan view of a curved gust front
(coordinate system aligned with the flow direction at the middle of the front)

Following Wakimoto's treatment of the thunderstorm gust front (1982), the values listed below are used to estimate $\Delta\theta$ at which the transverse divergence (also known as diffluence) becomes significant with respect to the longitudinal divergence. The following values are estimated from the region within the dashed circle in Fig. 3.12.

- $\Delta U_r = 11.2 \text{ m/s}$ (25 mph)
- $\Delta s = 900 \text{ m}$ (approximate longitudinal extent of circled region)
- $y_n = 400 \text{ m}$ (approximate transverse extent of the hatched region)
- $U_r = 39.1 \text{ m/s}$ (average of 75 and 100 mph)

The resulting longitudinal divergence is on the order of 0.01 s^{-1} .

For small angular deviations of the flow from the s -direction, Table 3.4 indicates that the diffluence is one order of magnitude smaller than the longitudinal divergence. Wakimoto (1982) showed that a two-dimensional simplification was a good approximation for gust fronts, which are generally at least an order of magnitude larger than downburst outflows (Charba 1974). Diffluence was more than an order of magnitude smaller than the longitudinal divergence, for $\Delta\theta = 15^\circ$ in a gust front with $y_n = 20 \text{ km}$.

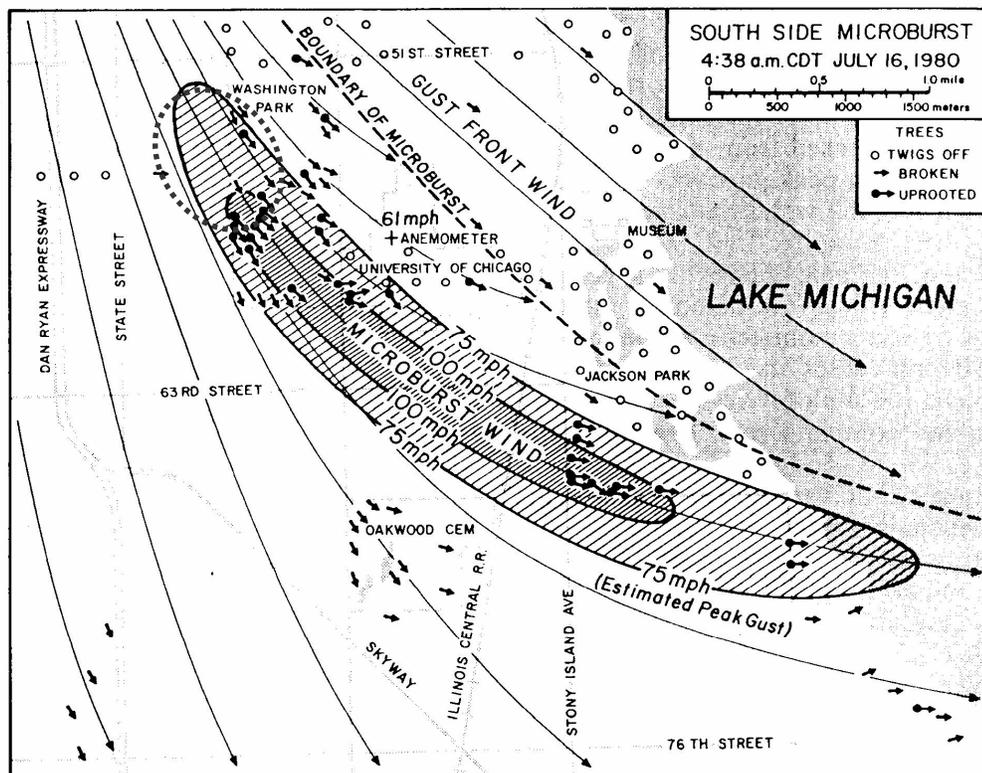


Figure 3.12: Damage footprint of a translating downburst
(adapted from Fujita and Wakimoto 1981)

The JAWS field campaign identified the simultaneous occurrence of multiple downbursts in line formation, which Hjelmfelt (1988) referred to as “microburst lines”². Continuous occurrence of the individual downbursts at their respective locations allowed downburst lines to persist for over two hours. Hjelmfelt (1988) reported an average line length of 17 km based on twenty cases. Depending on the proximity of the individual downbursts to each other, the outflow was described as homogeneous or discrete. Half of the lines studied were homogeneous and half were discrete. The exact outflow velocity profile depended on the spacing and relative strength of the individual downbursts.

Clearly, the 2-D simplification is more valid for a downburst line than an isolated event. Diffuence is compared to longitudinal divergence using reported downburst line parameters (Hjelmfelt 1988). Table 3.5 suggests that the effect of diffuence in a downburst line is weak even for large angular deviations of the flow from the s-direction.

² Downburst clusters produced by extratropical mesoscale convective weather systems have also been referred to as “derechos” (Wakimoto 2001).

Table 3.4: Diffluence of an outflow from a translating downburst (0.8 km frontal width)

$\Delta\theta$ [$^{\circ}$]	diffluence [s^{-1}]	ratio of diffluence to longitudinal divergence
1	0.002	0.1
2	0.003	0.3
3	0.005	0.4
4	0.007	0.5
5	0.009	0.7

Table 3.5: Diffluence of an outflow from a downburst line (17 km length)

$\Delta\theta$ [$^{\circ}$]	diffluence [s^{-1}]	ratio of diffluence to longitudinal divergence
10	0.0003	0.03
20	0.0006	0.07
30	0.0008	0.10
40	0.0011	0.14
50	0.0014	0.17

3.6 Conclusions

As seen from Wakimoto's review of convective downdrafts (2001), meteorologists are making efforts towards describing thunderstorms in greater detail and explaining how downdraft outflows fit into large and complex convective systems. The difficulty of investigating intense downburst outflows in the field has led to laboratory simulations as an additional means to gain insight. Previous downburst simulations helped clarify the structure and morphology of the phenomenon. The impinging jet and released fluid models served well in this regard. However, scaling considerations dictate that it is not very practical to generate a large-scale outflow using these approaches. This chapter introduced a slot jet approach as a means to address the problem of generating a flow, which closely represents a downburst outflow and is of sufficient size to allow aeroelastic testing of structural models. This approach has the advantage of being readily extended to transient simulations and also has the potential to readily simulate more complex scenarios beyond the outflow from a non-translating downburst.

It was shown that time-averaged outflow wind speed profiles can be reproduced reasonably well with a rectangular slot nozzle that generates a plane wall jet. Direct

comparison of the developed plane wall jet profiles with profiles in the intense flow region of radial wall jets indicated good agreement. The turbulence quantity profiles of the developed plane wall jet matched the corresponding profiles from the developing radial wall jet slightly downstream of where the maximum radial mean velocity was located in field observations. In other words, the turbulence quantities of the plane wall jet were slightly higher than desired. In the full-size facility implementation of Chapter 5, these profiles are several times larger in size than previous approaches have generated.

In terms of frontal curvature effects, the present analysis found that it is valid to simplify a radially-expanding outflow with a two-dimensional assumption. This simplification is applicable to multiple spans of a transmission line. The present findings agreed with those of Mason *et al.* (2005), who examined the plan curvature of simulated outflow fronts. The exposed transverse width of a structure and its location relative to the downburst impingement point are the key wind loading parameters relevant to an axisymmetric, isolated downburst.

The rear-flank downdraft (RFD) appears to be “the strongest downdraft associated with the supercell” (Wakimoto 2001). The axisymmetric column of descending air, described by Fujita (1981), seems to match descriptions of forward-flank downdrafts more so than RFDs. Data from the 4 June 2002 RFD near Lubbock, Texas (Gast and Schroeder 2003) indicated that frontal curvature was negligible over a span of 1578 m, at 3 m to 15 m height AGL. Wind speed time histories were well-correlated across the span. The irrelevance of frontal curvature for the strongest impinging convective downdrafts supports the validity of a modelling approach based on the plane wall jet.

A quasi-steady model does not account for all features of a downburst outflow. It inherently neglects fluctuations in time, as it is intended to be a simplified model to aid practitioners and designers. The relevant question is whether or not all of these details need to be considered in the design of structures. Is dynamic response significant in downburst wind loading of particular structures? Is it sufficient to simulate the mean profile in a quasi-steady manner to capture the essential differences between wind loading from a downburst outflow and the conventional ABL? The extension of the slot jet approach to transient flow simulation, in the next chapter, may eventually lead to additional insight into these questions.

3.7 References

- Abrahamsson, H., Johansson, B., and Löfdahl, L. (1994), "A turbulent plane two-dimensional wall-jet in a quiescent surrounding", *Euro. J. Mech., B/Fluids*, **13**(5), 533-556.
- Alahyari, A. and Longmire, E.K. (1995), "Dynamics of experimentally simulated microbursts", *AIAA J.*, **33**(11), 2128-2136.
- American Society of Civil Engineers (1999), *Wind tunnel studies of buildings and structures*, Manuals and Reports on Engineering Practice No. 67, 2nd edition, edited by N. Isyumov, published by ASCE, Reston, VA, USA, xiii, 214 pp.
- Charba, J. (1974), "Application of gravity current model to analysis of squall-line gust front", *Mon. Wea. Rev.*, **102**(February), 140-156.
- Chay, M.T. and Letchford, C.W. (2002), "Pressure distributions on a cube in a simulated thunderstorm downburst – Part A: Stationary downburst observations", *J. Wind Eng. Ind. Aerodyn.*, **90**, 711-732.
- Choi, E.C.C. (2004), "Field measurement and experimental study of wind speed profile during thunderstorms", *J. Wind Eng. Ind. Aerodyn.*, **92**, 275-290.
- Choi, E.C.C. and Hidayat F.A. (2002), "Dynamic response of structures to thunderstorm winds", *Prog. Struct. Engng Mater.*, **4**, 408-416.
- Cook, N.J. (1973), "On simulating the lower third of the urban adiabatic boundary layer in a wind tunnel", *Atmos. Environ.*, **7**, 691-705.
- Förthmann, E. (1934), "Über turbulente Strahlausbreitung", *Ing. Arch. (Arch Appl. Mech.)*, **5**(1), 42-54. Translated as NACA Technical Memorandum #789, 1936.
- Fujita, T.T. (1981), "Tornadoes and downbursts in the context of generalized planetary scales", *J. Atmos. Sci.*, **38**(8), 1511-1534.
- Fujita, T.T. (1985), "The downburst: Microburst and macroburst", University of Chicago, Department of Geophysical Sciences, Satellite and Mesometeorology Research Project, Research Paper #210.
- Fujita, T.T. (1990), "Downbursts: Meteorological features and wind field characteristics", *J. Wind Eng. Ind. Aerodyn.*, **36**, 75-86.
- Fujita, T.T. and Wakimoto, R.M. (1981), "Five scales of airflow associated with a series of downbursts on 16 July 1980", *Mon. Wea. Rev.*, **109**, 1439-1456.
- Gartshore, I. and Hawaleshka, O. (1964), "The design of a two-dimensional blowing slot and its application to a turbulent wall jet in still air", McGill University, McGill Engineering Research Laboratory, Technical Note 64-5.
- Gast, K.D. and Schroeder, J.L. (2003), "Supercell rear-flank downdraft as sampled in the 2002 thunderstorm outflow experiment", *Proceedings of the 11th International Conference on Wind Engineering*, Lubbock, TX, USA, 2-5 June, 2233-2240.
- Hjelmfelt, M.R. (1988), "Structure and life cycle of microburst outflows observed in Colorado", *J. Appl. Meteor.*, **27**, 900-927.
- Holmes, J.D. (1992), "Physical modelling of thunderstorm downdrafts by wind-tunnel jet", *Australian Wind Engineering Society Second Workshop on Wind Engineering*, Melbourne, Australia, 20-21 February.
- Irwin, H.P.A.H. (1973), "Measurements in a self-preserving plane wall jet in a positive pressure gradient", *J. Fluid Mech.*, **61**(1), 33-63.
- Kim, J. and Hangan, H. (2007), "Numerical simulations of impinging jets with application to downbursts", *J. Wind Eng. Ind. Aerodyn.*, **95**, 279-298.

- Knowles, K. and Myszko, M. (1998), "Turbulence measurements in radial wall-jets", *Exp. Therm. Fluid Sci.*, **17**, 71-78.
- Lauder, B.E. and Rodi, W. (1981), "The turbulent wall jet", *Prog. Aerospace Sci.*, **19**, 81-128.
- Letchford, C.W. and Illidge, G. (1999), "Turbulence and topographic effects in simulated thunderstorm downdrafts by wind tunnel jet", in *Wind engineering into the 21st century, Proceedings of the 10th International Conference on Wind Engineering*, (Copenhagen, Denmark, 21-25 June), edited by Larsen, Larose and Livesey, published by Balkema, Rotterdam, the Netherlands, 1907-1912.
- Letchford, C.W., Mans, C., and Chay, M.T. (2002), "Thunderstorms – their importance in wind engineering (a case for the next generation wind tunnel)", *J. Wind Eng. Ind. Aerodyn.*, **90**(12-15), 1415-1433.
- Lin, W.E. (2005), "Large-scale physical simulation of a microburst outflow using a slot jet", MEng thesis, The University of Western Ontario, Canada, 207 pp.
- Lundgren, T.S., Yao, J., and Mansour, N.N. (1992), "Microburst modelling and scaling", *J. Fluid Mech.*, **239**, 461-488.
- Mara, T.G., Galsworthy, J.K., and Savory, E. (2010), "Assessment of vertical wind loads on lattice framework with application to thunderstorm and convective winds", *Wind Struct.*, in press.
- Mason, M.S., Letchford, C.W., and James, D.L. (2005), "Pulsed wall jet simulation of a stationary thunderstorm downburst, Part A: Physical structure and flow field characterization", *J. Wind Eng. Ind. Aerodyn.*, **93**, 557-580.
- Mason, M.S., Wood, G.S., and Fletcher, D.F. (2009), "Numerical simulation of downburst winds", *J. Wind Eng. Ind. Aerodyn.*, **97**, 523-539.
- Mason, M.S., Wood, G.S., and Fletcher, D.F. (2010), "Numerical investigation of the influence of topography on simulated downburst wind fields", *J. Wind Eng. Ind. Aerodyn.*, **98**, 21-33.
- Mehta, R.D. (1977), "The aerodynamic design of blower tunnels with wide-angle diffusers", *Prog. Aero. Sci.*, **18**, 59-120.
- Nicholls, M., Pielke, R., and Meroney, R. (1993), "Large eddy simulation of microburst winds flowing around a building", *J. Wind Eng. Ind. Aerodyn.*, **46 & 47**, 229-237.
- Orf, L.G., Anderson, J.R., and Straka, J.M. (1996), "A three-dimensional numerical analysis of colliding microburst outflow dynamics", *J. Atmos. Sci.*, **53**(17), 2490-2511.
- Poreh, M., Tsuei, Y.G., and Cermak, J.E. (1967), "Investigation of a turbulent radial wall jet", *J. Appl. Mech.*, **34**, 457-463.
- Proctor, F.H. (1988), "Numerical simulations of an isolated microburst. Part I: Dynamics and structure. *J. Atmos. Sci.*, **45**(21), 3137-3160.
- Savory, E., Parke, G.A.R., Zeinoddini, M., Toy, N., and Disney, P. (2001), "Modelling of tornado and microburst-induced wind loading and failure of a lattice transmission tower", *Engng. Struct.*, **23**, 365-375.
- Selvam, R.P. and Holmes J.D. (1992), "Numerical simulation of thunderstorm downdrafts", *J. Wind Eng. Ind. Aerodyn.*, **41-44**, 2817-2825.
- Verhoff, A. (1970), "Steady and pulsating two-dimensional turbulent wall jets in a uniform stream", PhD thesis, Princeton University, USA, 383 pp.

- Vermeire B.C., Orf L.G., and Savory E. (2009), "A comparison of impinging jet and cooling source downburst models", *5th European Conference on Severe Storms*, Landshut, Germany, 12-16 October, 173-174.
- Vermeire, B.C., Orf, L.G., and Savory, E. (2010), "A parametric study of near surface downburst line outflows", *5th International Symposium on Computational Wind Engineering*, Chapel Hill, NC, USA, 23-27 May, 8 pp.
- Wakimoto, R.M. (1982), "The life cycle of thunderstorm gust fronts as viewed with Doppler radar and rawinsonde data", *Mon. Wea. Rev.*, **110**, 1060-1082.
- Wakimoto, R.M. (2001), "Convectively driven high wind events", *Meteor. Monogr.*, **28**(50), 255-298.
- Wood, G.S., Kwok, K.C.S., Motteram, N.A., and Fletcher, D.F. (2001), "Physical and numerical modelling of thunderstorm downbursts", *J. Wind Eng. Ind. Aerodyn.*, **89**, 535-552.
- Wynnanski, I., Katz, Y., and Horev, E. (1992), "On the applicability of various scaling laws to the turbulent wall jet", *J. Fluid Mech.*, **234**, 669-690.
- Xu, Z. (2004), "Experimental and analytical modeling of high intensity winds", PhD thesis, The University of Western Ontario, Canada, 169 pp.
- Xu, Z. and Hangan, H. (2008), "Scale, boundary and inlet condition effects on impinging jets", *J. Wind Eng. Ind. Aerodyn.*, **96**, 2383-2402.
- Yao, J. and Lundgren, T.S. (1996), "Experimental investigation of microbursts", *Exp. Fluids*, **21**, 17-25.

CHAPTER 4

TRANSIENT MODELLING OF A DOWNDRAFT OUTFLOW*

4.1 Introduction

Section 4.2 reviews the previous approaches to simulation of the transient features of a downburst. Section 4.3 discusses the primary considerations relevant to wind loading on structures. Subsequent sections pertain to the present numerical and experimental approaches, whereby the outflow region was studied at high resolution.

4.2 Background

4.2.1 Previous experimental modelling studies

Physical simulation of the transient features of a downburst, without translating environmental winds, has mainly been performed by the following two methods:

(1) Impulsive release of a fluid parcel into a larger volume of fluid of lower density

Lundgren *et al.* (1992) described their experimental conditions with parameters similar to those used in earlier gravity current studies. The length scale (R_0) was the equivalent spherical radius of the cylindrical fluid release. The time scale, velocity scale, and flow Reynolds number were defined by Eqs. (4.1) to (4.3), respectively.

$$T_0 = \left(\frac{R_0 \rho}{g \Delta \rho} \right)^{0.5} \quad (4.1)$$

$$V_0 = \frac{R_0}{T_0} \quad (4.2)$$

$$Re_\rho = \frac{R_0 V_0}{\nu} \quad (4.3)$$

* Excerpts from this chapter were published as *Wind and Structures* **10**(4), 2007.

The large-scale features of the outflow were independent of flow Reynolds number when the density differential and released parcel volume were sufficiently large ($Re_p > 3000$). In order to compare with results from the other simulation method, Table 4.1 provides downdraft and outflow information based on the container exit diameter (D_n). For an impulsive release that is driven by density-differential, the velocity and length scales achieved are extremely small.

Later experiments (Alahyari and Longmire 1995, Alahyari 1995, Yao and Lundgren 1996) refined the apparatus and technique of Lundgren *et al.* (1992). Particle image velocimetry (PIV) results affirmed that the extreme outflow velocities were attributable to a dominant, horizontal roll vortex. This roll vortex trails closely behind the outflow front. A stationary observer would experience the roll vortex as a transient load due to the large horizontal gradient of horizontal velocity.

(2) Impulsively-started jet

Mason *et al.* (2003, 2005) modified the impinging jet of round cross-section, which Letchford and Chay (2002) used for quasi-steady downburst simulations, to generate a manually-actuated jet pulse. A stationary nozzle approach was employed with a 16-blade gate device near the nozzle exit. The gate was similar to a camera iris. The gate actuation was non-linear in time since equal durations were taken to open the initial 15 % and the final 85 % of the nozzle area. The quoted radial position of U_p in Table 4.2 may be underestimated, since the nozzle diameter was used as the normalising value and the dominant vortex formed before the aperture was fully open. The radial position of peak outflow velocity in the quasi-steady simulations discussed in Lin and Savory (2006) was $r/D_n \approx 1$.

The opening time of the aperture in the experiments of Mason *et al.* (2005) was similar to that achieved by Xu (2004) for jet actuation by valve. A sharp rise and decay was not apparent in the velocity history from the latter. This was likely due to the valve being located at greater than $60 D_n$ upstream of the nozzle exit.

Although the density differential that drives a downburst is modelled by the released fluid parcel approach, such experiments are extremely small-scale and generate low wind speeds. It is more practical to generate intense flows using jets. However, the driving mechanism is the initial momentum supplied by blowing equipment rather than negative buoyancy.

Table 4.1: Released fluid parcel simulations

Study	Buoyancy		Downdraft		Outflow		Comments
	$\Delta\rho/\rho$	Re_ρ	D_n (m)	z_n/D_n	U_p (m/s) at (r/D_n)	data range (r/D_n)	
Lundgren, Yao & Mansour (1992)	0.01						Agreement with a JAWS downburst for peak U/W and radial position of peak U.
	0.03	1377 -	0.045	1.7	no data	no data	
	0.05	6279		2.3			
	0.10						
Alahyari & Longmire (1995), Alahyari (1995)	0.03	3600	0.064	2.3	0.264* (0.74)	< 1.23	Coarse PIV vector fields of outflow.
				2.7			
Yao & Lundgren (1996)	0.05	3077	0.045	2.3	0.248 (0.71)	0.282 - 2.82	Outflow velocities measured at $z/D_n=0.028$ only.

* Peak value from azimuthal averages at fixed radial distances.

Table 4.2: Transient impinging jet simulations

Study	Nozzle parameters			Aperture opening time (s)	Radial position of U_p (r/D_n)
	D_n (m)	z_n/D_n	Re_D^*		
Mason, Letchford & James (2003)	0.51	1.7	3.4E+05	not reported	0.75**
Xu (2004)	0.22	1	1.8E+05	≈ 0.2	≈ 1
Mason, Letchford & James (2005)	0.51	1.7	3.1E+05	0.2	0.75**

* Based on D_n and steady W_n .

** May be under-estimated.

4.2.2 Previous numerical modelling studies

Numerical simulations can provide insight into aspects of downbursts that are difficult to study by direct observation or by physical modelling. Proctor (1988, 1989) used an axisymmetric numerical model (TASS) with a constant grid spacing of 40 m to simulate the thermodynamics and microphysics that lead to intense downburst outflows. Proctor (1988) found that the computed instantaneous vertical profile of radial outflow velocity agreed with results from a laboratory experiment of a steady impinging jet (Bakke 1957) and full-scale measurements from NIMROD (Fujita 1981).

Violent motion of the atmosphere is typically associated with high convective available potential energy (CAPE), which is essentially the temperature difference between fluid parcels and the environment integrated over height (Stull 1995). However, in very low CAPE environments in the Western Plains of the United States, dry downbursts can produce F1 winds ($32.5 \text{ m/s} < U < 49.5 \text{ m/s}$). An environment conducive to dry downburst³ occurrence exhibits:

1. a high cloud base ($> 5 \text{ km AGL}$) and a thick sub-cloud layer with an approximately dry-adiabatic lapse rate (Wakimoto 1985), and
2. dry air near the melting level and moist air near the surface (Proctor 1989).

³ Observable precipitation at ground level $< 0.254 \text{ mm}$ (Fujita 1985).

The combination of a statically neutral environment and enhanced negative buoyancy associated with phase change of hydrometeors (i.e. melting in wet downbursts, and evaporation and sublimation in dry downbursts) can lead to downdraft speeds of approximately 20 m/s. However, no clear relationship was apparent between peak horizontal outflow speed and peak downdraft speed. Proctor (1989) found this ratio to be very sensitive to environmental conditions (temperature and humidity profiles), downdraft radius, and precipitation type.

The dynamic equations for the full thermodynamics and microphysics are computationally expensive to solve. As a preliminary wind engineering study, Selvam and Holmes (1992) simplified the problem to the two-dimensional, steady, incompressible Navier-Stokes equation and applied the k - ϵ turbulence model closure. The non-dimensional vertical profile of outflow velocity ($z/z_{0.5}$ vs. U/U_m) predicted larger velocities near ground level than the corresponding peak profile from Proctor (1988).

Lundgren *et al.* (1992) investigated the development of the vortex ring with an inviscid model. Although the outflow region was modelled at low spatial resolution, the following results were comparable to those from a full-scale downburst in neutrally stable conditions: (1) U_m/W_{\min} , (2) radial location of U_m , and (3) characteristic time scale of the event. Surface friction produced counter-vorticity that retarded and elevated the dominant roll vortex, in agreement with Proctor (1988).

Orf *et al.* (1996) and Orf and Anderson (1999) introduced a dry, sub-cloud numerical model that was designed to simulate downburst flow dynamics at high resolution. Microphysical cooling was modelled using a cooling function, whose parameters were prescribed to generate outflows that resembled field observations. Small flow structures were resolved, and complexities such as colliding outflows and environmental wind shear were investigated.

Kim and Hangan (2007) investigated an impinging jet model by solving the unsteady Reynolds-averaged Navier-Stokes (URANS) equations. Mason *et al.* (2009, 2010) combined an improved URANS method with initial forcing of the flow by a cloud-level cooling source (Orf *et al.* 1996). Vermeire *et al.* (2009, 2010) present large-eddy simulations with a cloud-level cooling source.

This chapter presents results from numerical simulations that use a cooling source approach with the Bryan Cloud Model (CM1, Bryan and Fritsch 2002) at high resolution. Section 4.5.2 presents the numerical results from three simulated events. Section 4.5.3 compares the current findings with field observations from the literature.

4.3 Key considerations

The following issues arise for time-dependent simulation of outflows:

- a) Vertical profiles of horizontal velocity resembled a wall jet profile (Fujita 1981, Hjelmfelt 1988). However, these downburst outflow profiles were extracted from Doppler radar scans between zenith and horizon. Strictly speaking, these earlier studies did not capture instantaneous profiles if the scanning duration of the beam was significant relative to the downburst duration (2-15 min). It is of interest to examine simultaneous records from, say, a tower with instrumentation at multiple heights. Instead of synchronicity in time, the problem then is to attain sufficient spatial resolution to resolve the profile maximum.
- b) From the perspective of a stationary object, a burst front passes as a sudden and short-lived event. Outflow wind speed records exhibited a brief peak gust with an abrupt rise and fall. Prior to $t = 700$ s in Fig. 4.1, the velocity history of the Andrews AFB downburst outflow showed little warning of the impending intense gust. The rise to the leading peak gust and the corresponding average duration⁴ each lasted for approximately one minute.

Some nomenclature should be clarified at this point. “Maximum” wind speed will be used to refer to the largest value over space at a specific time. “Peak” wind speed will refer to the largest value over time at available spatial locations. If complete velocity field data is available, such that the largest overall value for an event can be identified over time and space, this value will be referred to as the “peak maximum”.

Fig. 4.1 relates the velocity history features to various regions of the flow as the downburst translates past the anemometer. Inset 1 indicates that the extreme wind region on the leading side was responsible for the initial velocity peak. The subsequent lull in wind speed corresponded to the eye of the downburst shown in Inset 2. The back-side

⁴ Defined as the duration for which $U > 0.5 \cdot U_p$.

outflow in Inset 3 was detected as the second peak in the velocity history. The wind direction at $t = 0$ is shown as 0° . Wind direction was fairly constant until after the first velocity peak. As the eye of the downburst translated over the anemometer, the wind direction changed by approximately 180° as expected from Insets 1 to 3.

The NIMROD and JAWS meteorological datasets had average durations of 3.1 and 2.9 min, respectively (Fujita 1985). More than 90 % of the downbursts recorded had an average duration of < 5 min. Fig. 4.2 suggests that the duration of the peak outflow gust was slightly longer in Illinois downbursts than in Colorado ones, but the average duration distributions are comparable for these two studies in different climates.

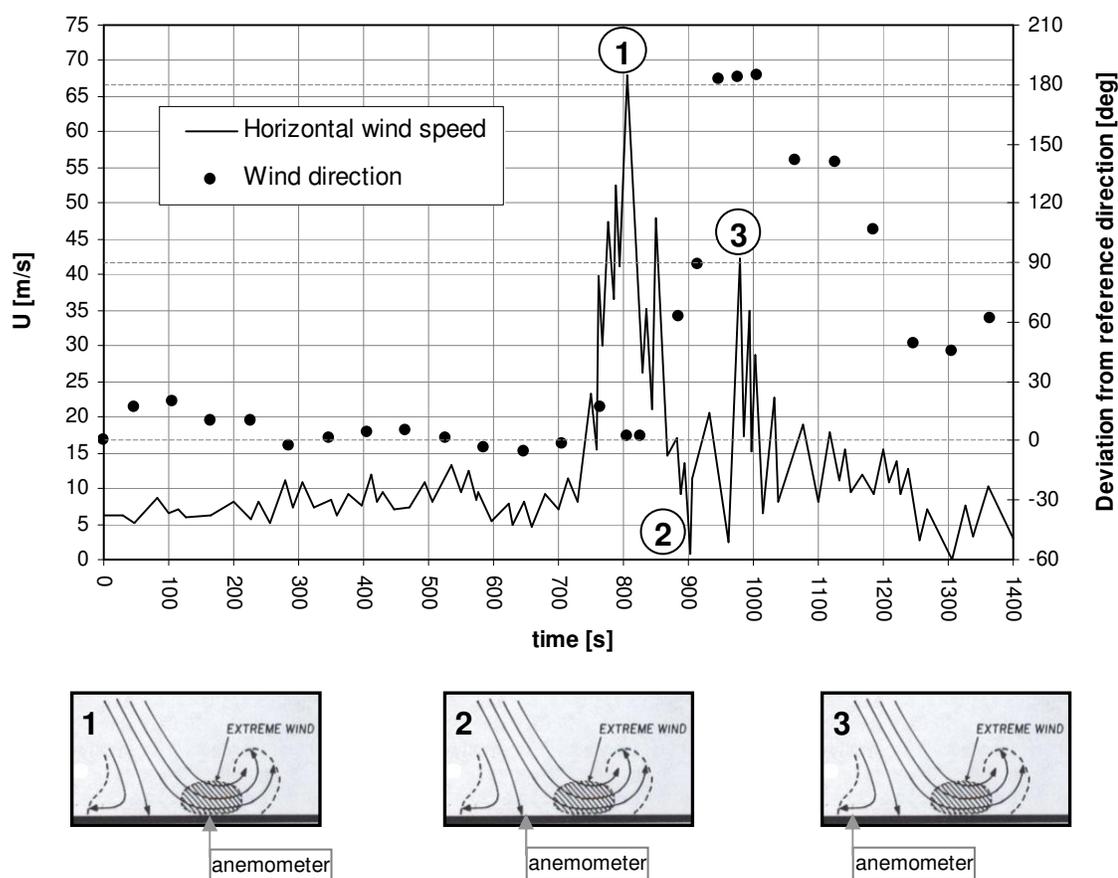


Figure 4.1: Velocity history at 4.9 m above ground level for a severe outflow (1 Aug 1983, Andrews AFB downburst data from Fujita 1985 and diagrams adapted from Wakimoto 2001)

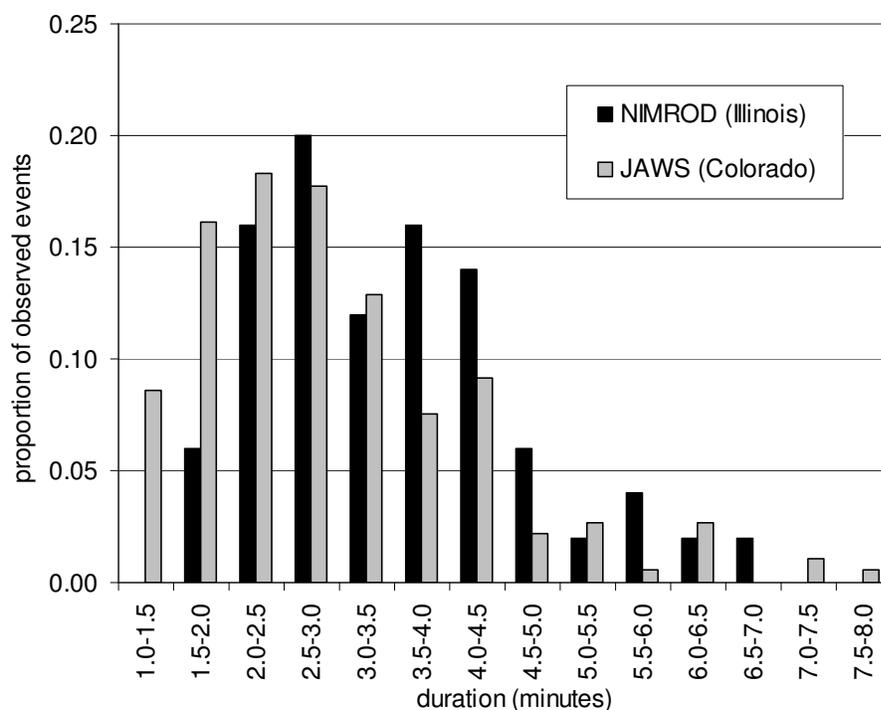


Figure 4.2: Histogram of full-scale peak wind longevity (data from Fujita 1985)

c) Caracena (1982) proposed that a vortex ring develops about a non-translating (spatially stationary) downdraft. Subsequent observations corroborated that a vortex ring is advected to the surface, at which point it spreads radially as part of the outflow. The opportune photographs in Fig. 4.3 showed the vortical motion of entrained particles in the outflow as it advanced leftward in the image. With respect to a plan view, Fujita (1985) described a central high-pressure region associated with the downdraft stagnation point, which was encircled by a low-pressure ring. Time-dependent simulations indicated that a dominant, horizontal roll vortex was a primary feature of the outflow region (Proctor 1988, Lundgren *et al* 1992, Mason *et al.* 2005).

d) The downburst outflow is a statistically non-stationary process, and so it is problematic to quantify the gustiness with conventional definitions of turbulence quantities. Choi and Hidayat (2002) found that it was more appropriate to use fluctuations about a moving average to characterise the turbulent velocity component. An averaging time of approximately 60 seconds was suitable for thunderstorm data from Singapore. Holmes *et al.* (2008) applied this approach to outflow velocity measurements from a rear-flank downdraft (RFD) and derecho captured by Gast and Schroeder (2003).

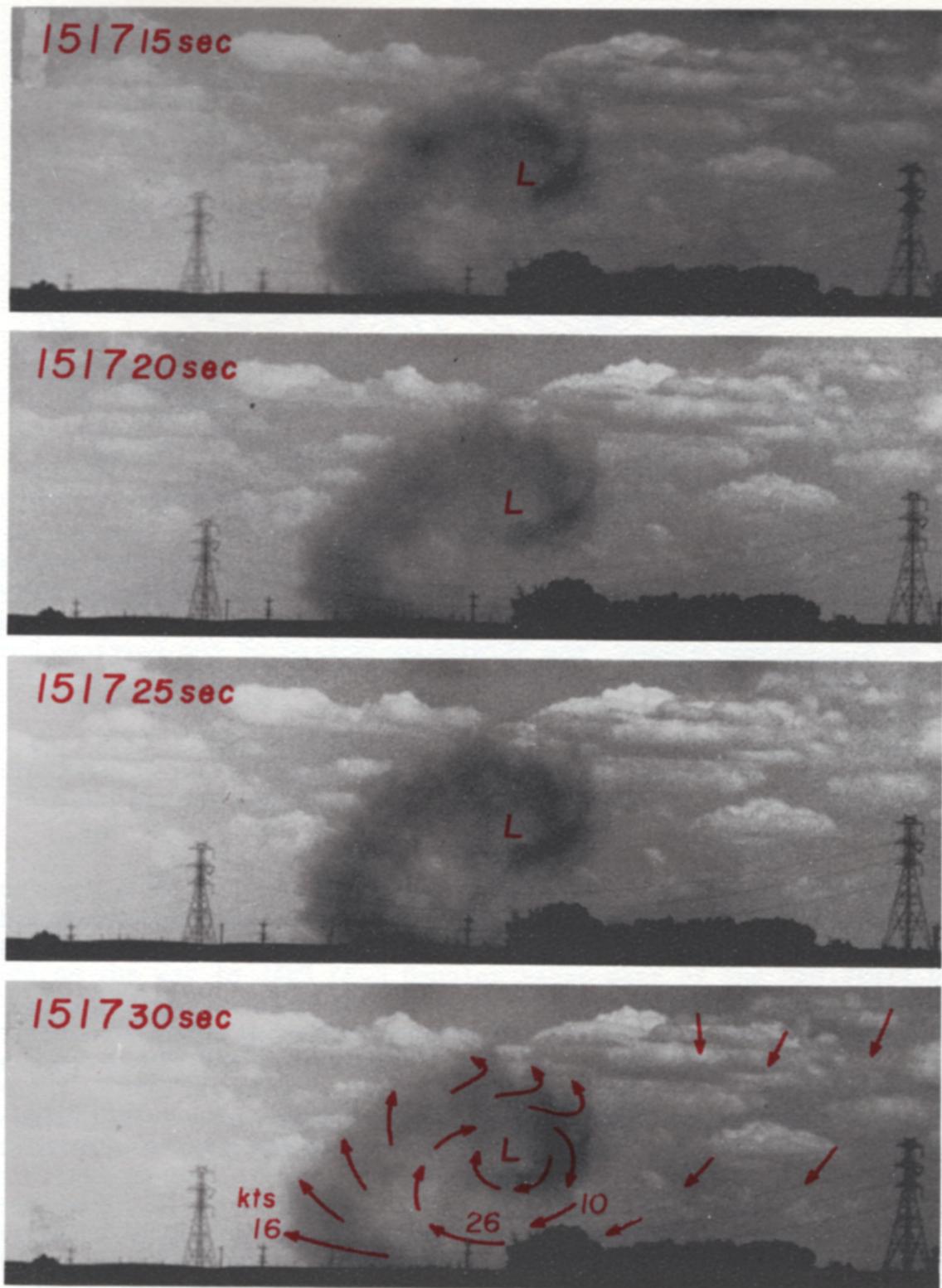


Figure 4.3: A sequence of photographs for an outflow vortex from JAWS
(Reproduced from Fujita 1983 where photography was by B. Waranauskas)

Wavelets are particularly suitable for analysing signals with abrupt changes, such as the peak gusts in Fig. 4.1. With the data from Gast and Schroeder (2003), Chen and Letchford (2005) used wavelet shrinkage and a two-stage moving average method to infer the time-varying mean and standard deviation wind speeds, respectively. Proper orthogonal decomposition indicated that essentially all of the energy was located in the first mode for mean speeds, standard deviations, and normalised fluctuations.

e) Intense convectively-driven downdrafts were identified as distinct features of thunderstorm supercells (Wakimoto 2001). In the 2002 Thunderstorm Outflow Experiment near Lubbock, Texas, seven mobile towers with instrumentation up to 15 m in height were deployed in a line arrangement (Gast and Schroeder 2003, 2004). A RFD of a non-tornadic supercell and a derecho were observed.

Analyses of the RFD suggest that the outflow was well-correlated over a lateral extent of at least 789 m (Chen and Letchford 2006, Holmes *et al.* 2008). Although it appears possible to model an RFD outflow as being two-dimensional for wind engineering purposes, this chapter focuses on simulation of isolated downdrafts. Aside from observations suggesting that the RFD is generally an order of magnitude larger than an isolated downburst, the former is more complex in origin and morphology than the latter (see Figure 7.7 of Wakimoto 2001). The RFD is specific to a supercell and occurs in a high-shear environment, which is usually not accounted for in basic downburst modelling. Generalising wall jet models from individual downbursts to more complex convective downdraft outflows is a possible direction for future work.

f) Incidentally, in the meteorological literature, the general term “thunderstorm outflow” was occasionally used to refer to gust fronts (Goff 1976, Droegemeier and Wilhelmson 1987). These outflows were generally weaker and an order of magnitude larger in lateral extent than intense downburst outflows. They were described by the gravity current model (Charba 1974). Linden and Simpson (1985) briefly presented their gravity current experiments in the context of downbursts.

However, there were some fundamental differences between gravity currents and downbursts. In the former, there was frontogenesis, i.e. the “sharpening up of horizontal gradients to form a front” (Linden and Simpson 1986). The vorticity in a gravity current was related to the shielding of dense fluid from ambient fluid by a stable density

interface. Dense fluid from the rear was restricted by the propagating front, and thus circulated up and to the rear of the horizontal flow to form the characteristic head of the gravity current (see Figure 1 from Droegeleier and Wilhelmson 1987).

On the other hand, the vortex formation in the downburst was initiated prior to the outflow stage. In physical experiments, Lundgren *et al.* (1992) found vortex ring development due to baroclinic vorticity generation after the released parcel had fallen less than $1 D_n$. The released parcel deformed, and then entrained ambient fluid into the core of the downdraft column. Their axisymmetric, sub-cloud, numerical model also indicated that the vortex ring was initiated aloft about the downdraft column. Although the mixing effect of diffusion was neglected, the winding of the density discontinuity interface persisted and intensified in the outflow region.

Laser-induced fluorescence visualisation by Alahyari (1995) also indicated that ambient and released parcel fluid significantly interacted at the location of peak outflow velocity. In contrast, mixing in the gravity current occurred in the turbulent wake, after the dense fluid circulated away from the head region. The gravity current model may apply to the later, dissipating stage of a downburst outflow, but not at its peak intensity.

4.4 Experimental simulation

Field observations (Fujita 1985, Hjelmfelt 1988) and buoyancy-driven numerical simulations (Proctor 1988, Orf *et al.* 1996) described the transient nature of the downburst outflow and the dominant horizontal vortex. The speed-up associated with the dominant roll vortex, relative to an equivalent quasi-steady outflow (Chay and Letchford 2002, Mason *et al.* 2005), is of interest for structural design. The quasi-steady outflow simulation of the preceding chapter was readily extended to model the transient features outlined in Section 4.3.

4.4.1 Test facility

The prototype slot jet wind tunnel was introduced in Sections 2.3.1 and 3.2.3. This test facility was developed further to allow transient flow capability, i.e. actuation of the slot jet. Essentially, this involved the installation of a gate device at the slot nozzle such that pulses of air could be released into the working section, as depicted by Fig. 4.4.

Fan speed was held constant, so that the transient effect was produced solely by the gate actuation. Since the main purpose was to investigate the feasibility of a slot jet model of the downburst outflow, further complexities such as a co-flow above the slot top were not implemented in the prototype. A co-flow configuration can be used to model a downburst with “surface environmental wind” (see Hjelmfelt 1988, p. 906) or a downburst embedded in a translating storm (Holmes and Oliver 2000). This aspect of the slot jet wind tunnel is discussed in the next chapter for the full-size implementation.

A coarse screen was installed at the prototype test section inlet, indicated in Fig. 4.5, in order to minimise potential disturbances from external air and to approximate the conditions in the full-size facility. Aside from the screen, external air was free to be entrained into the working section. Sections 4.4.1.1 and 4.4.1.2 discuss the two gate designs that were implemented in the prototype facility.

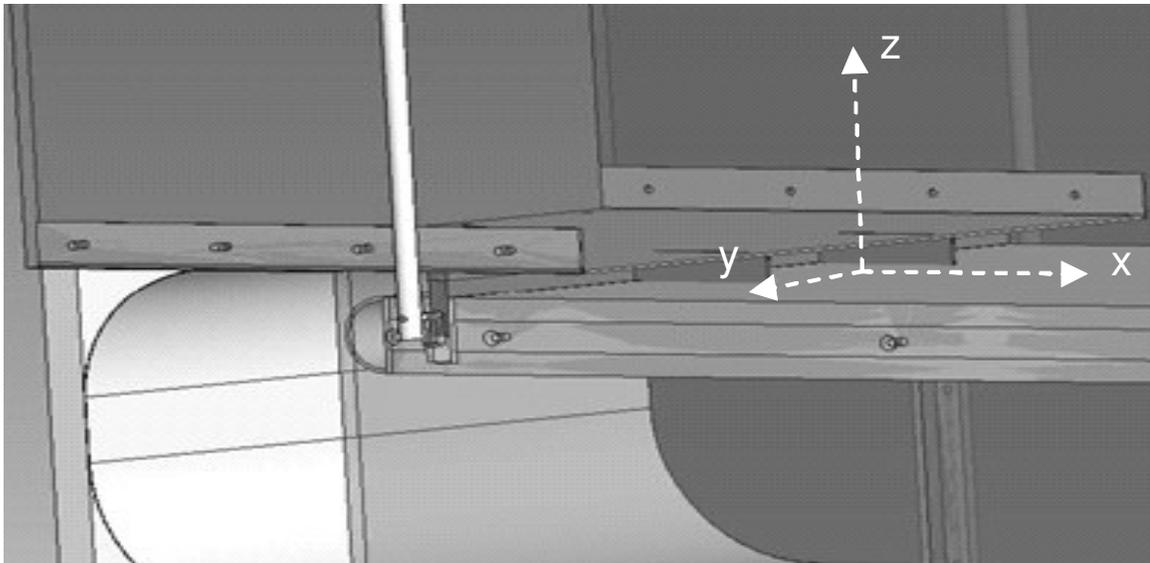


Figure 4.4: Coordinate system in the slot jet facility

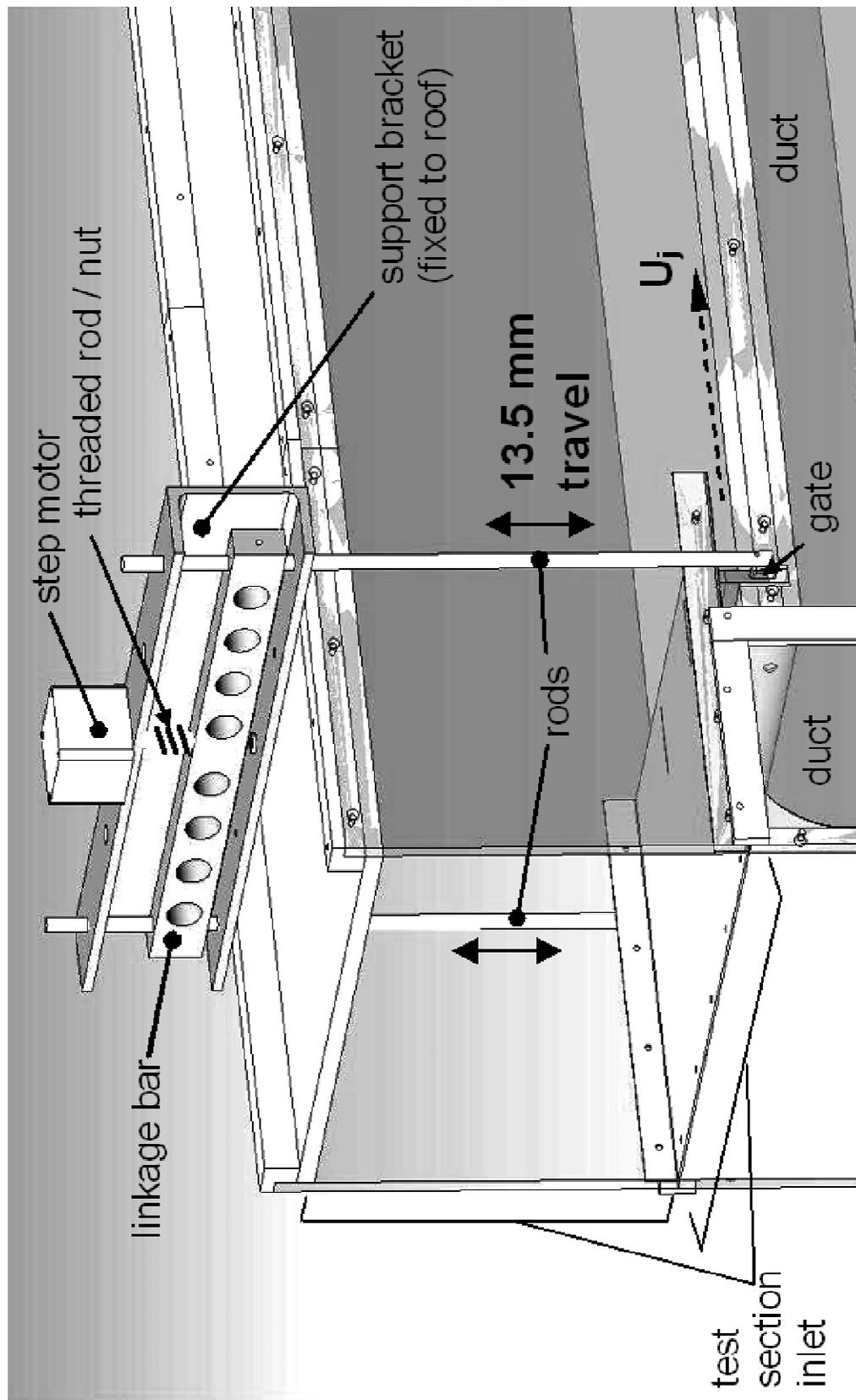


Figure 4.5: Linear motion gate assembly

4.4.1.1 Translating gate

The assembly in Fig. 4.5 allowed the flow to be actuated with a linear motion gate. Each realisation of the transient flow began with the gate shut (at its highest vertical position). The fan operated under steady conditions and pressurised the duct and slot. A static pressure port on the side wall behind the gate allowed the pressurization to be monitored to ensure consistency between slot jet actuations. When the gate was quickly translated downwards until its top surface was flush with the $z = 0$ plane, the static pressure behind the gate converted to the dynamic pressure of the slot exit velocity (U_j). After achieving the fully-open slot condition, the gate quickly returned to the fully-shut slot condition.

A thin layer of rubber foam was attached to the top surface of the gate to improve the seal of the fully-shut slot and to lessen the effects of gate impact on the slot top. The achieved opening and closing durations were 0.10 and 0.19 s, respectively. The objective was to reproduce the wind speed history from field observations.

The stainless steel gate was driven by a step motor mounted above the tunnel. Fig. 4.5 shows the rigid assembly that consisted of the gate, rods, and linkage bar. The step motor was fixed to the C-section support bracket. A precision, multi-threaded rod was coupled concentrically to the step motor shaft and the matching nut was fixed to the linkage bar. Thus, the rotary motion of the step motor shaft was converted into smooth linear gate motion (25.4 mm/rev or 200 steps/rev). A digital pulse train input allowed repeatable gate positioning. In the powered stand-still condition, the large holding torque of the step motor allowed the gate to be held firmly shut.

As seen in Fig. 4.4, the gate was pinned to the rods through small slits in the tunnel side walls. These slits did not affect the flow when the gate was open because the gate itself was designed to block off the entire slit. When the gate was fully closed, the slits were partially open but the close fit between the gate and adjacent components allowed negligible leakage from the working section. The gate was restrained such that its only degree of freedom was vertical translation across the 13.5 mm slot height (b).

4.4.1.2 Rotating gate

The alternative gate design introduced a rod at the centre of the 13.5 mm slot height. The gate consisted of two 1.6-mm-thick steel flaps that were welded onto the rod. The gate was free to rotate in brass bushings that were press-fit into the tunnel sides. Fig. 4.6a shows the start position and initial direction of rotation for all of the trials. Fig. 4.6b shows the sign convention for $\Delta\theta$ and the sequence of gate positions during an actuation. There was no pause in the gate motion at the fully-open slot condition.

The following gate sequences were studied: (1) a half-revolution in one direction ($\Delta\theta = +180^\circ$) and (2) two quarter-revolutions with an intermediate change in direction ($\Delta\theta = +90^\circ - 90^\circ$). The step motor described in Section 4.4.1.1 was relocated to drive the rotating gate. Total actuation times of 0.10 and 0.20 s were investigated, where the opening and closing phases were of approximately equal duration.

At Position 2 shown in Fig. 4.6b, blockage of 26 % of $(Y \cdot b)$ was incurred due to the rod at the slot mid-height. However, the following results in Section 4.5 showed that a significant wake was not evident in the downstream velocity profiles and that the velocity histories were more repeatable than those obtained with the translating gate. However, sealing the slot in the fully-closed position was challenging. The observed leakage had an associated wind speed of approximately 25 % of the peak horizontal wind speed.

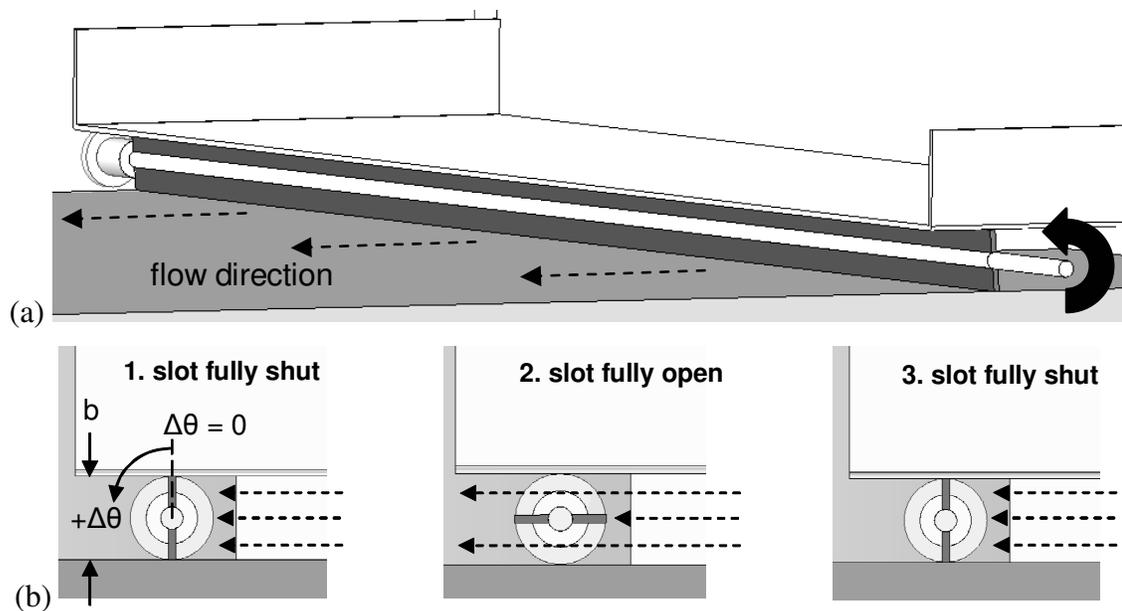


Figure 4.6: Rotating gate at (a) start position and (b) extreme positions during actuation

4.4.2 Velocity measurements

The crossed-wire (x-wire) anemometry set-up, described in the previous chapter, permitted a velocity sampling rate of 10 kHz. The x-wire and gate systems were synchronised so that data acquisition and gate actuation started simultaneously. Ten realisations ($n = 10$) were performed at each x-wire location for the translating gate tests. For the rotating gate, $n = 5$ since improved repeatability was observed.

Velocity histories at each x-wire location were graphed together and inspected for anomalous realisations that were due to occasional inconsistent gate actuation (likely resulting from slight variations of friction in the mechanical system). These realisations were excluded from subsequent analysis. The accepted histories were ensemble-averaged to give a composite velocity history ($\langle U \rangle$) at $N = 50$ probe locations. Vertical profiles were constructed as shown in Fig. 4.7 and the temporal development of the composite profile was determined.

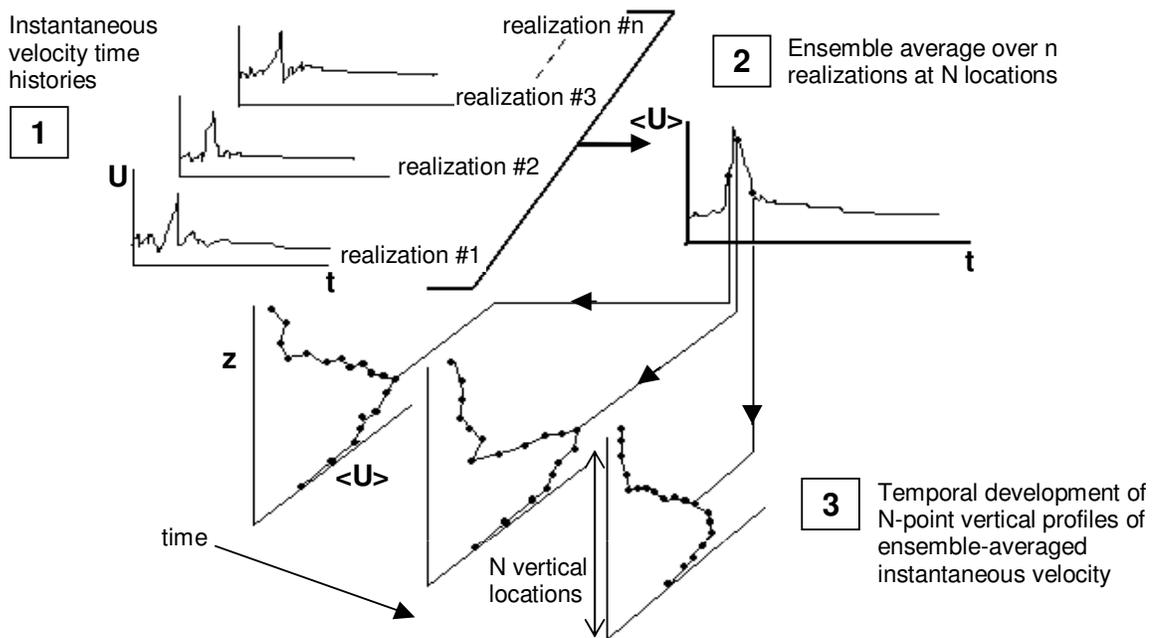


Figure 4.7: Data flow for transient jet results

Hot-wire anemometry is an intrusive technique that can affect the flow if the inserted apparatus is too large. Verhoff (1970) extensively investigated the effect of a 6.35 mm diameter rod on a transient 2-D slot jet. Photographs at 800 fps, as well as hot-wire outputs, did not show any noticeable influence of the rod on dominant roll vortices. The probe holder diameter in the present apparatus was 6 mm and the L-shaped holder placed the probe upstream of the vertical support tube.

The x-wire probes gave accurate results only when the flow approach angle remained within the cone of acceptance of $\pm 45^\circ$ with respect to the probe axis (Jørgensen 2005). The instantaneous approach angle generally remained $< 20^\circ$ in the region of interest (maximum value of 27°). Measurements in the outer region of the wall jet were less reliable because of the high local turbulence intensity there. The flow reversal of the dominant vortex was not discerned due to signal rectification. Since the region of present interest was near the maximum of the vertical profile of mean streamwise velocity, signal rectification did not limit the applicability of the measurements.

4.5 Discussion of results

Following the slot jet experimental results in Section 4.5.1, the Bryan Cloud Model (CM1) numerical simulation results are presented in Section 4.5.2. Both horizontal and vertical velocities were examined in the numerical work. The numerical and experimental results were then compared with available field data. The velocity profile shapes and the evolution of the intense flow regions were of particular interest.

4.5.1 Slot jet results

4.5.1.1 Flow visualisation

The dominant roll vortex in the transient 2-D slot jet flow was visualised by filling the slot and anterior duct with a fog fluid. This substance was composed of low-molecular-weight glycol and de-ionised water vapour. The gate actuation generated a dominant vortex near the leading edge of the streamwise propagating gust front. In Fig. 4.8, the tower model was located at $x/b = 20$ and the roll vortex axis was at $z/b \approx 4.5$.

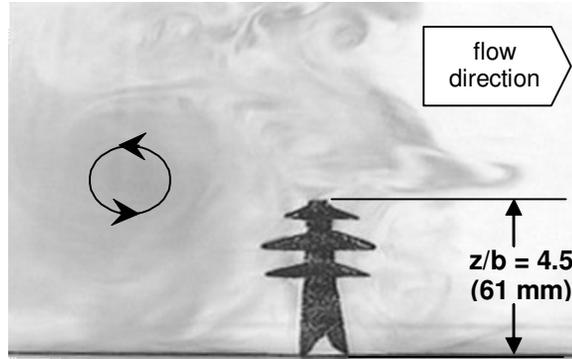


Figure 4.8: Transient simulation vortex from prototype slot jet facility

Verhoff (1970) investigated pulsing a 2-D slot jet at ≥ 1 Hz. The continuous stream of turbulent vortices reached a developed state at $\approx 100 x/b$, independent of the pulse rate, pulse shape and uniform co-flow velocity. An increase in co-flow velocity decreased $\partial z_{\text{axis}}/\partial x$, likely because of the following reasons: (1) an increased restraining influence of the co-flow on the slot jet and (2) a decrease in time for vertical growth since the vortex was advected downstream more rapidly.

4.5.1.2 Lateral correlation of vertical profiles

Verhoff (1970) observed two-dimensionality of a pulsed slot jet at the slot exit ($x/b = 0$) based on smoke visualisation. Furthermore, measurements with a total head probe indicated total pressure varied by less than ± 1 % of the maximum value away from the flow boundaries. The transient wall jet in the present prototype facility retained two-dimensionality as shown in Fig. 4.9. $\langle U \rangle$ was normalised by the corresponding steady velocity at $x = 0 = y$ and $z/b = 0.5$ (i.e. the fan was in steady operation, as in the transient tests, but the gate was fixed in the fully-open slot position). For all of the present results, $U_{j, \text{steady}} = 45$ m/s. Profiles are shown for $t = 0.07, 0.10,$ and 0.12 s after the gate began opening. The largest variation between profiles was at $t = 0.12$ s and $z/b = 0.56$, where the $y/Y = +0.22$ profile decayed to 83 % of the centreline profile. Furthermore, transient round impinging jet experiments suggested that the dominant vortex ring was correlated over $0.25 D_n$, which was estimated to be 400 m in full-scale (Mason *et al.* 2005).

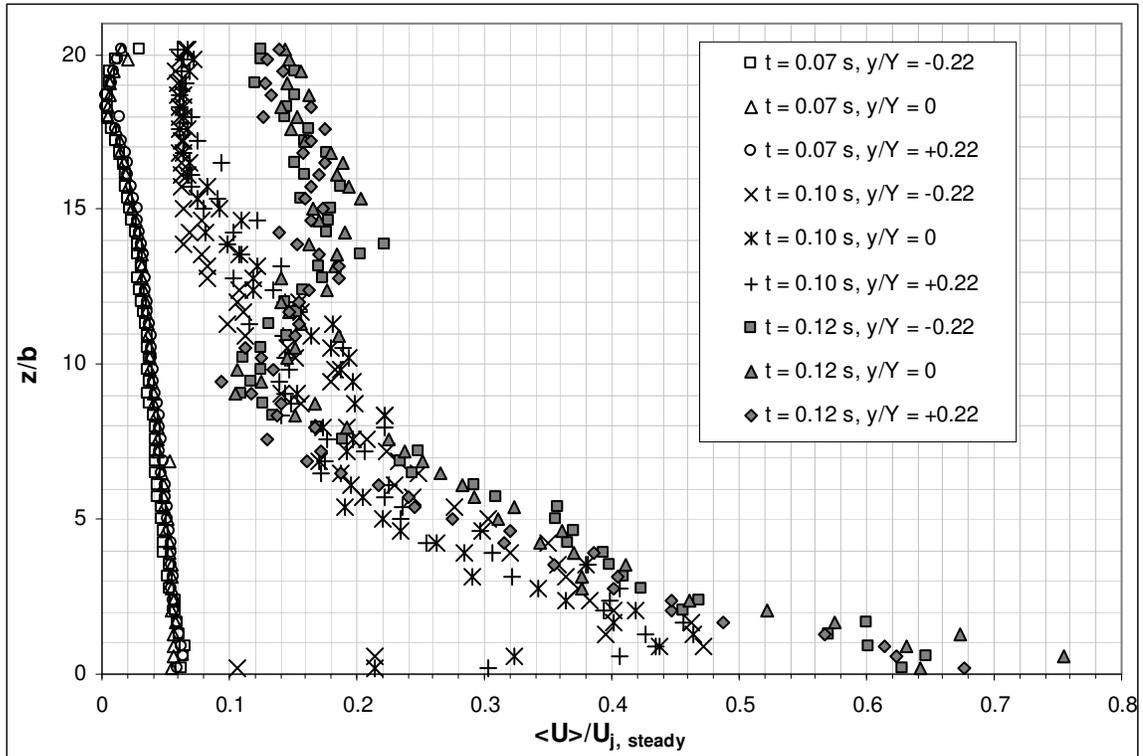


Figure 4.9: Composite wind speed profiles (prototype facility, $x/b = 30$, translating gate)

4.5.1.3 $\langle U \rangle$ profile evolution

The temporal development of the composite profiles at $x/b = 30$ is also depicted by Fig. 4.9. The maximum in the composite profile approached the ground plane near the occurrence of peak $\langle U \rangle$. This finding was consistent with previous simulations that suggested the rotation of the dominant vortex resulted in dynamic speed-up of the outflow (Proctor 1988, Lundgren *et al.* 1992). Mason *et al.* (2003) found that the ensemble-averaged peak velocity, over five realisations of the transient impinging jet, exceeded the corresponding peak mean velocity in the steady impinging jet (Chay and Letchford 2002) by greater than a factor of two.

4.5.1.4 Turbulence intensity

For time-dependent wind events, the velocity history should be separated into time-varying mean and residual fluctuation components (Choi and Hidayat 2002). Fig. 4.10 presents a weighted 3-point moving average for the field observation in Fig. 4.1. The moving average value at a given time, $U_{MA}(t_s)$, was calculated as shown by Eq. (4.4). Without weighting, the U_{MA} peak tends to precede the U peak.

$$U_{MA}(t_s) = \frac{w_1 \cdot U(t_{s-1}) + w_2 \cdot U(t_s) + w_3 \cdot U(t_{s+1})}{w_1 + w_2 + w_3} \quad (4.4)$$

where s is the ordered sample number, $w_1 = w_3 = 0.2$, and $w_2 = 0.6$.

The low temporal resolution of the Andrews AFB anemometer data required that an effective turbulence intensity (\hat{I}_u) be estimated from the ratio of the instantaneous deviation ($U - U_{MA}$) to U_{MA} at the same instant. At the time of peak velocity in Fig. 4.10, $\hat{I}_u \approx 25\%$ at 4.9 m AGL. A similar analysis was applied to velocity histories from the slot jet experiments. A 70-point moving average smoothed the slot jet wind speed that was sampled at 10 kHz, whilst retaining the velocity peak associated with the roll vortex. At the height and time of peak velocity at $x/b = 30$ and $y = 0$, the actuated slot jet yielded \hat{I}_u between 20 and 30%. This \hat{I}_u range was based on the analysis of nine realisations of the translating gate outflow.

With improved time resolution data from the 2002 Thunderstorm Outflow Experiment, other investigators used more involved approaches to calculate effective turbulence intensity. Chen and Letchford (2005) employed a two-stage, weighted moving-average method (window width of 32 s) to estimate the time-varying standard deviation. At 4 and 6 m AGL, the effective turbulence intensity near the peak time-varying mean wind speed was approximately 8 and 15% for the RFD and derecho events, respectively. For the RFD event, Holmes *et al.* (2008) used the ratio of the time-varying root-mean-square (RMS) of residual fluctuations to the time-varying mean velocity. The time-varying RMS and mean were both calculated based on a 40 s window width. At 10 m AGL, the effective turbulence intensity was $\approx 10\%$ at the peak time-varying mean velocity and reached approximately 25% during the rise to this peak.

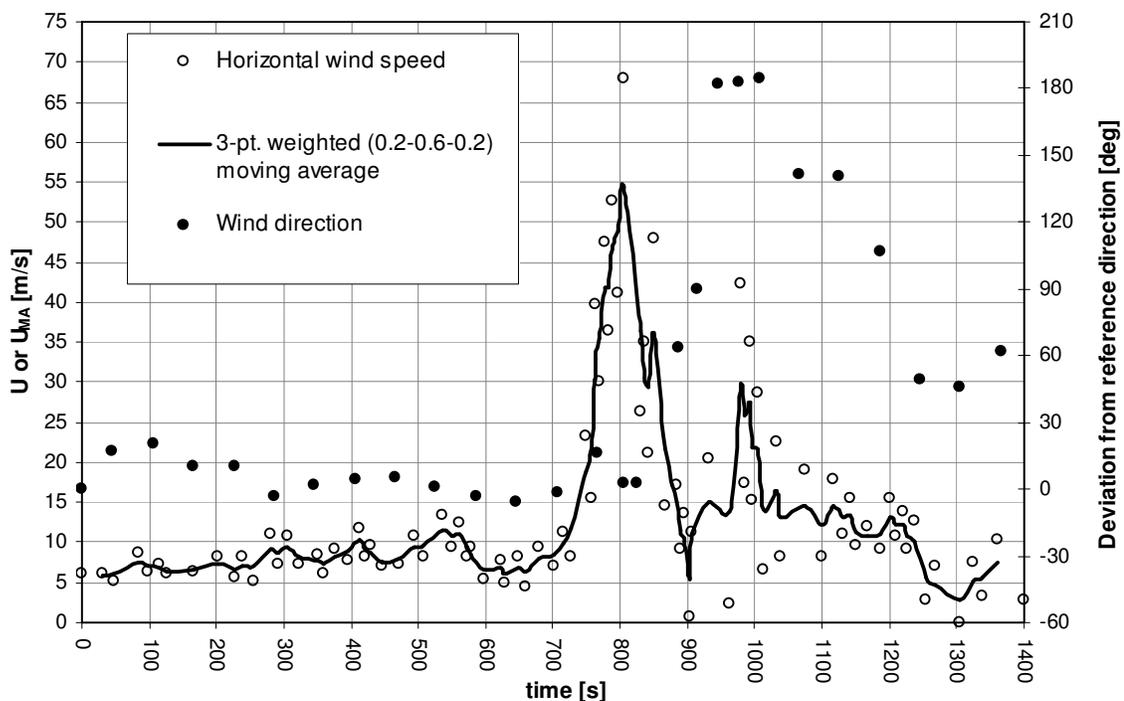


Figure 4.10: Moving-averaged wind speed history (Andrews AFB downburst)

4.5.1.5 Comparison of flow with translating and rotating gate designs

Fig. 4.11 compares peak $\langle U \rangle$ profiles from the translating and the rotating gate designs. Fan operating conditions were consistent between all of these experiments. A total actuation time (t^*) of 0.29 s was the quickest translating gate actuation achieved. Two rotating gate sequences (see Section 4.4.1.2) with two different t^* values (0.10 and 0.20 s) were investigated.

Compared with the translating gate peak profile, the maximum in the rotating gate peak profiles occurred at larger z . There is a distinct maximum in the rotating gate profiles, and as may be expected from the direction of rotation indicated in Fig. 4.6, the flow near the wall was slowed. The $\Delta\theta = +180^\circ$ gate sequence slowed the near-wall flow more than the $\Delta\theta = +90^\circ$ - 90° sequence. In the former, the lower half of the gate was always moving against the slot jet. In the latter, the lower half of the gate moved against the slot jet for the first half of its motion and with the slot jet for the second half. Changing the rotating gate t^* by a factor of two did not significantly affect the resulting downstream $\langle U \rangle$ profiles.

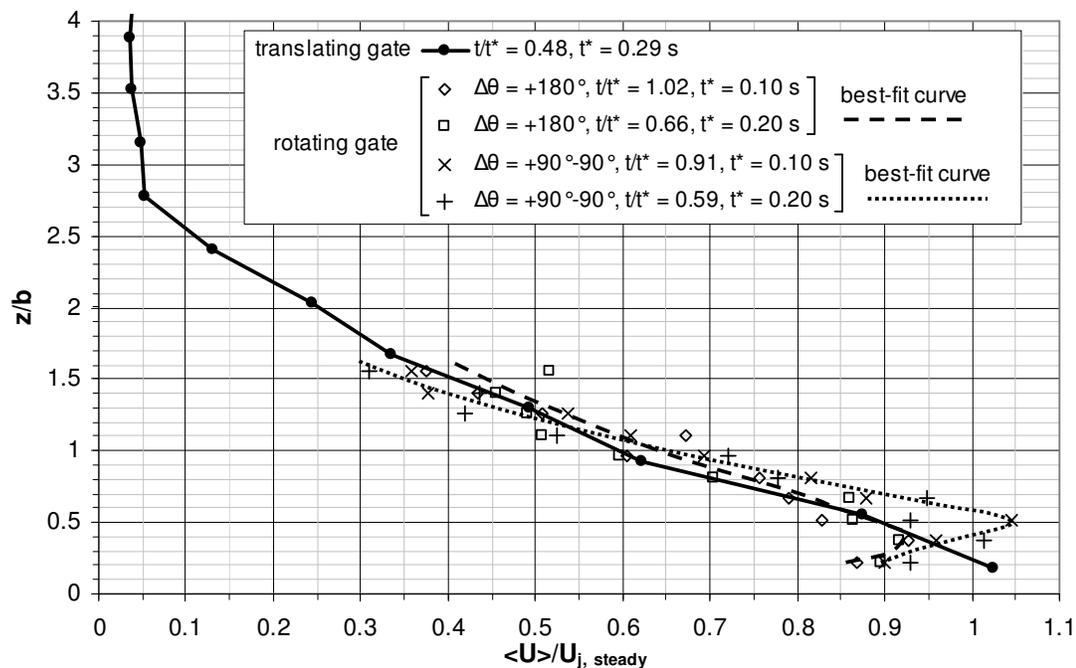


Figure 4.11: Peak composite wind speed profiles for two gate designs ($x/b = 10, y = 0$)

4.5.2 Bryan Cloud Model (CM1) results

The slot jet measurements are compared to the numerical simulations using a cooling source approach. In the same spirit as the simulations presented in Orf and Anderson (1999) and Orf *et al.* (1996), a realistic downburst was generated by parameterising the thermodynamic cooling found in a downburst-producing thunderstorm, without modelling the microphysical processes found in such a storm. The numerical simulations used a cooling forcing shape identical to that described in Orf and Anderson (1999), but the intensity of the cooling was increased by a factor of four. This adjustment provided sufficient negative buoyancy to force an intense downdraft with resulting horizontal winds that reached damaging intensity.

The 40 grid points closest to the surface were spaced 5 m apart in the vertical direction; above this, the grid was stretched to 25 m spacing at the top of the model domain (3.8 km AGL). The grid point closest to the surface was at 2.5 m AGL. Vertical resolution was enhanced near the ground in order to sufficiently resolve the vertical flow structure in this region of interest. The horizontal grid spacing was a constant 10 m

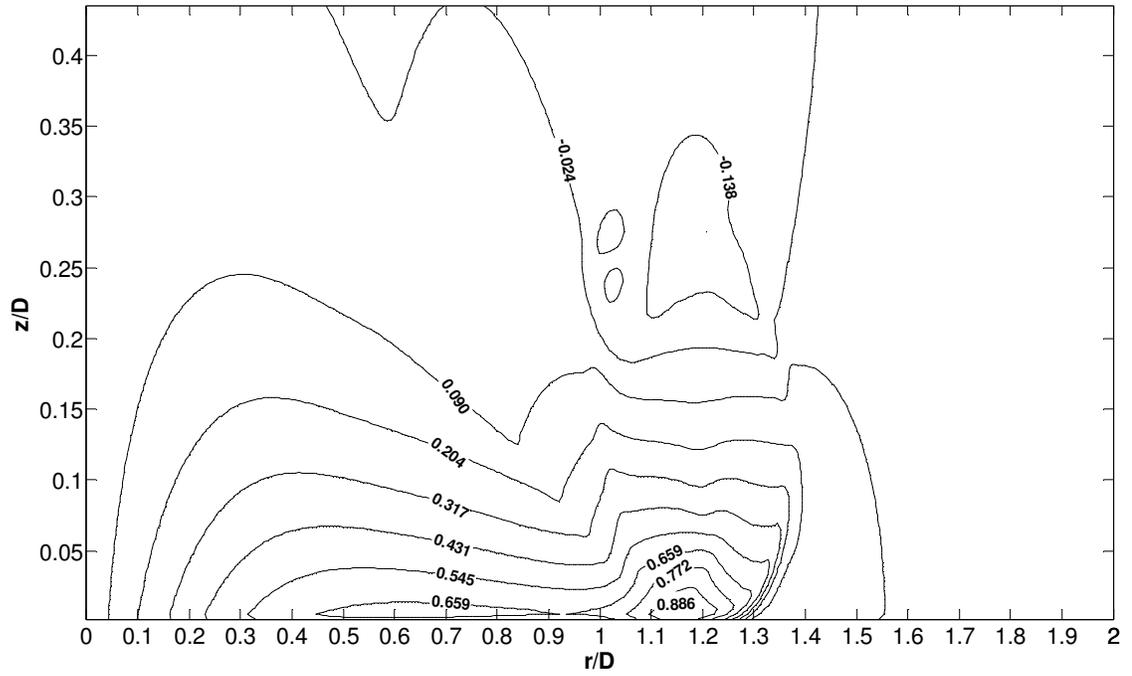
throughout the simulation domain. The model used open lateral boundary conditions and a semi-slip bottom boundary condition with a constant drag coefficient (C_{DN}) that produced an outflow head structure that was consistent with observations (e.g., Fig. 4.3). For reference, this C_{DN} value corresponded to $z_0 = 0.0001$ m (calm, open sea terrain) for a steady logarithmic wind profile (Stull 1988, pp. 262-267).

Results from three numerical simulation cases were compared to the slot jet measurements. All cases used a cooling function with a horizontal half-width of 1200 m, but it was more physically meaningful to normalise the computed results by a length scale that was representative of the downdraft diameter (D) which developed during the transient simulation. At the height of peak vertical velocity (W) magnitude and after the dominant roll vortex passed, D ranged between 1400 and 1650 m in all cases, based on the horizontal extent where $W < -3$ m/s. Thus, $D = 1500$ m was used in normalising the following Bryan Cloud Model (CM1) results.

Cases 1 and 2 simulated a non-translating, axisymmetric, isolated downburst. The cooling source was fixed at a single location with a cooling forcing of shorter duration in Case 2 than in Case 1. The peak maximum velocity ($U_{p, \max}$) occurred at 320 and 326 s into the simulation for Cases 1 and 2, respectively. $U_{p, \max}$ in Case 2 (37 m/s at $z/D = 0.005$ and $r/D = 1.11$) was significantly reduced from that in Case 1 (47 m/s at $z/D = 0.005$ and $r/D = 1.17$) as expected.

The potential flow solution for a stagnation point flow assumed that U increased linearly from the stagnation point out to r/D where peak U occurred (Holmes and Oliver 2000 after Schlichting 1979, p. 101). Comparing Figs. 4.12a and 4.13a, the potential flow solution appeared to be less valid at small z/D in Case 1 (stronger forcing) than Case 2. In Fig. 4.12a, there was a local velocity increase ($U/U_{p, \max} = 0.659$ contour) that occurred between the stagnation point and $U_{p, \max}$. Instead of an increase, there was a local velocity plateau in Fig. 4.13a between the stagnation point and $U_{p, \max}$. Figs. 4.12a and 4.13a show agreement with field observations of the horizontal velocity variation in the radial direction (Hjelmfelt 1988, Figure 12). The effect of cooling forcing duration on the outflow velocity history is examined in Section 4.5.4.

(a)



(b)

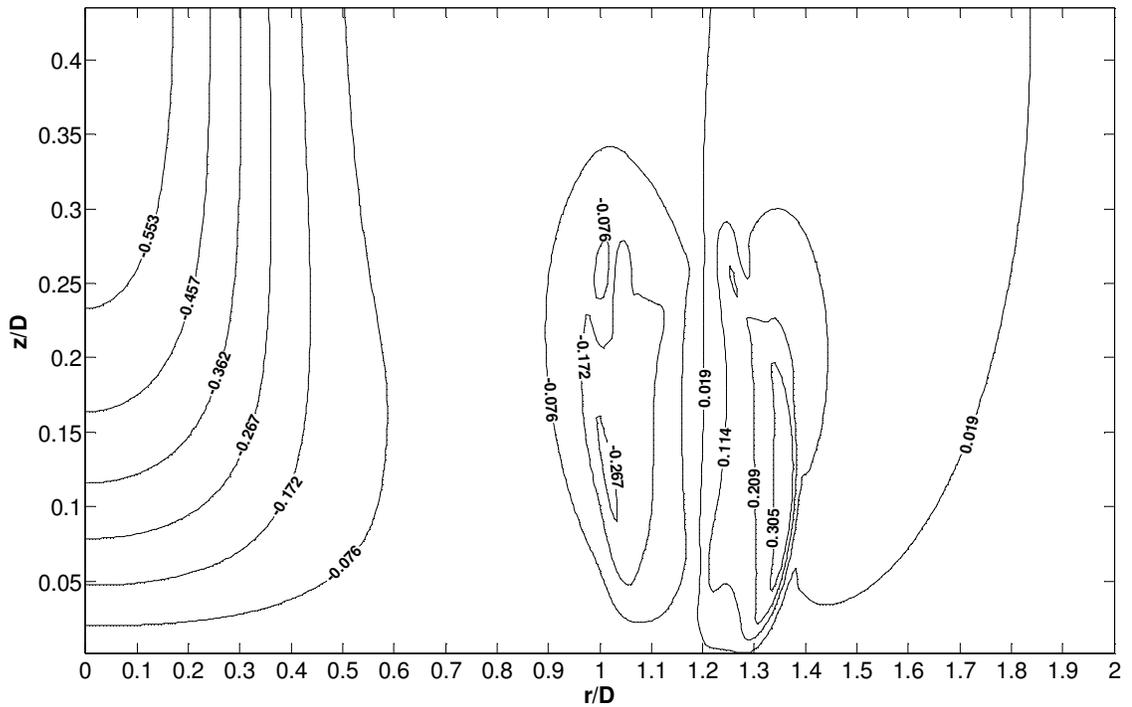
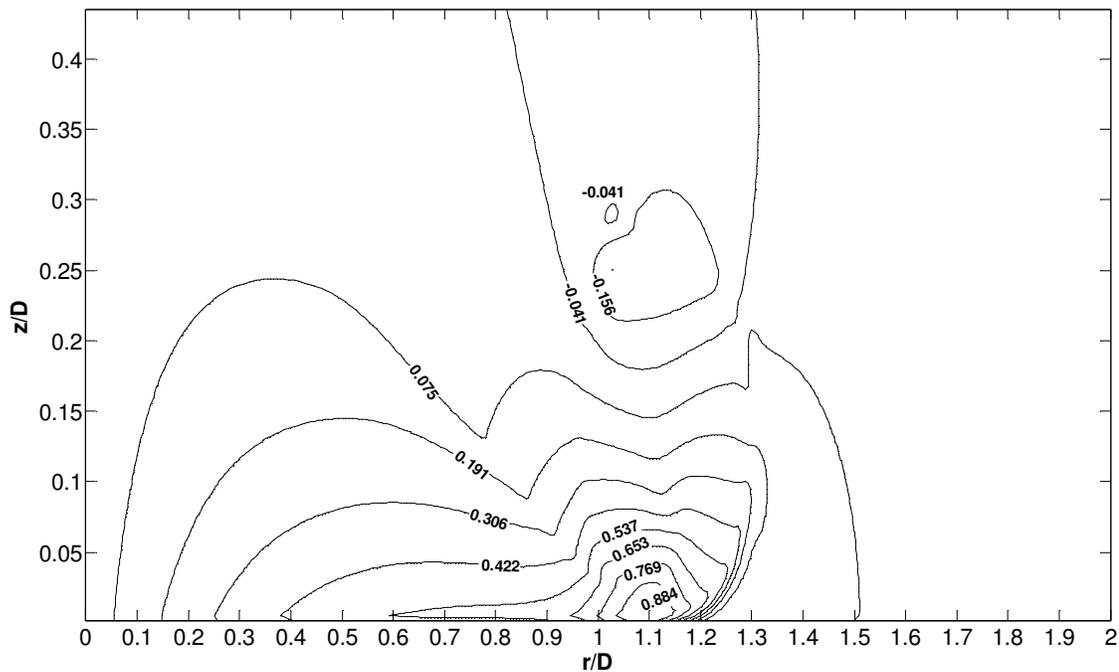


Figure 4.12: Contours of (a) $U/U_{p, \max}$ and (b) $W/U_{p, \max}$

when $U_{p, \max}$ occurs in CM1-Case 1

(a)



(b)

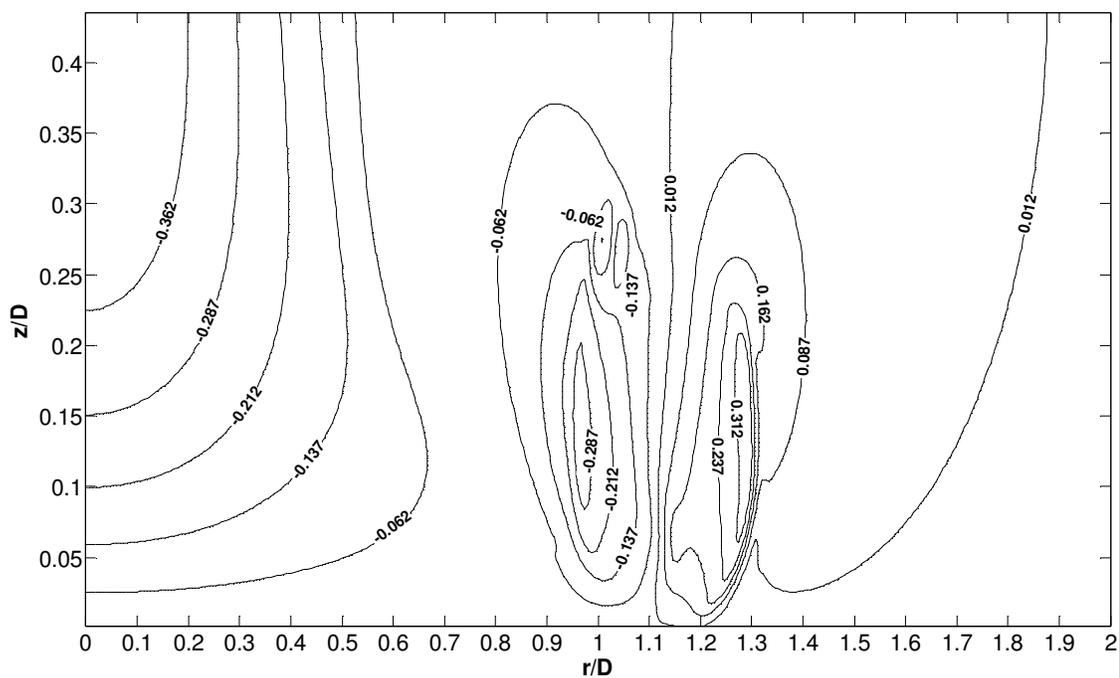


Figure 4.13: Contours of (a) $U/U_{p,max}$ and (b) $W/U_{p,max}$ when $U_{p,max}$ occurs in CM1-Case 2

Figs. 4.12 and 4.13 indicate that the occurrence of $U_{p, \max}$ coincided with essentially zero vertical velocity. In fact, $W/U_{p, \max}$ was -0.002 and 0.0004 at the location of $U_{p, \max}$ in Cases 1 and 2, respectively. The peak positive W , associated with the leading edge of the dominant vortex, was $W/U_{p, \max} = 0.4$ in both Cases 1 and 2. These values occurred at $z/D = 0.125$ and 0.167 , respectively. The peak negative W , associated with the trailing edge of the dominant vortex, was $W/U_{p, \max} = -0.3$ in both Cases 1 and 2. These values occurred at $z/D = 0.125$ and 0.135 , respectively. In the lowest 50 m AGL, the extreme vertical velocities occurred at radial locations between the peak maximum U and extreme W locations. These were $W/U_{p, \max} = 0.25$ and -0.11 for Case 1, and $W/U_{p, \max} = 0.23$ and -0.13 for Case 2.

Case 3 simulated a moving, isolated downburst by horizontally translating the cooling source. A quasi-Lagrangian perspective was taken, in the sense that the model domain followed the cooling source as it moved eastward relative to the ground (cardinal directions are indicated below Fig. 4.14a). The peak maximum horizontal gust (69 m/s) and constant translational speed of the cooling source ($U_t = 8$ m/s) were in close agreement with the observed peak speed and the baseline wind speed prior to the peak gust, respectively, in the Andrews AFB event (see Fig. 4.1).

The cooled air in the simulation can be treated as air parcels that are distinct from the ambient environment. In the dry adiabatic environment, vertical motions of a cold air parcel do not affect its potential temperature. By regarding potential temperature as a passive tracer that is advected with the flow field, potential temperature contours give a fair indication of the corresponding velocity field, as shown by Fig. 4.14.

The first 500 seconds of the computed wind field was used to determine wind speed histories as experienced by two stationary structures, each with a height of 653 metres⁵, that encountered the simulated downburst outflow. The time resolution was 1 s. In Fig. 4.14, the geometric centre of the cooling source was fixed to the centre of the Lagrangian model domain ($x' = 0$) that translated eastward at a constant rate of 8 m/s. The initial location of Structure A was chosen to be the eastern edge of the model domain as depicted in Fig. 4.15 ($x'/D = +1.397$ and $nt_A = 1$).

⁵ The 653 m height corresponded to a computational grid point. Since the grid was graded above $z \approx 200$ m, the upper boundary of the presented data did not coincide with a “round” number.

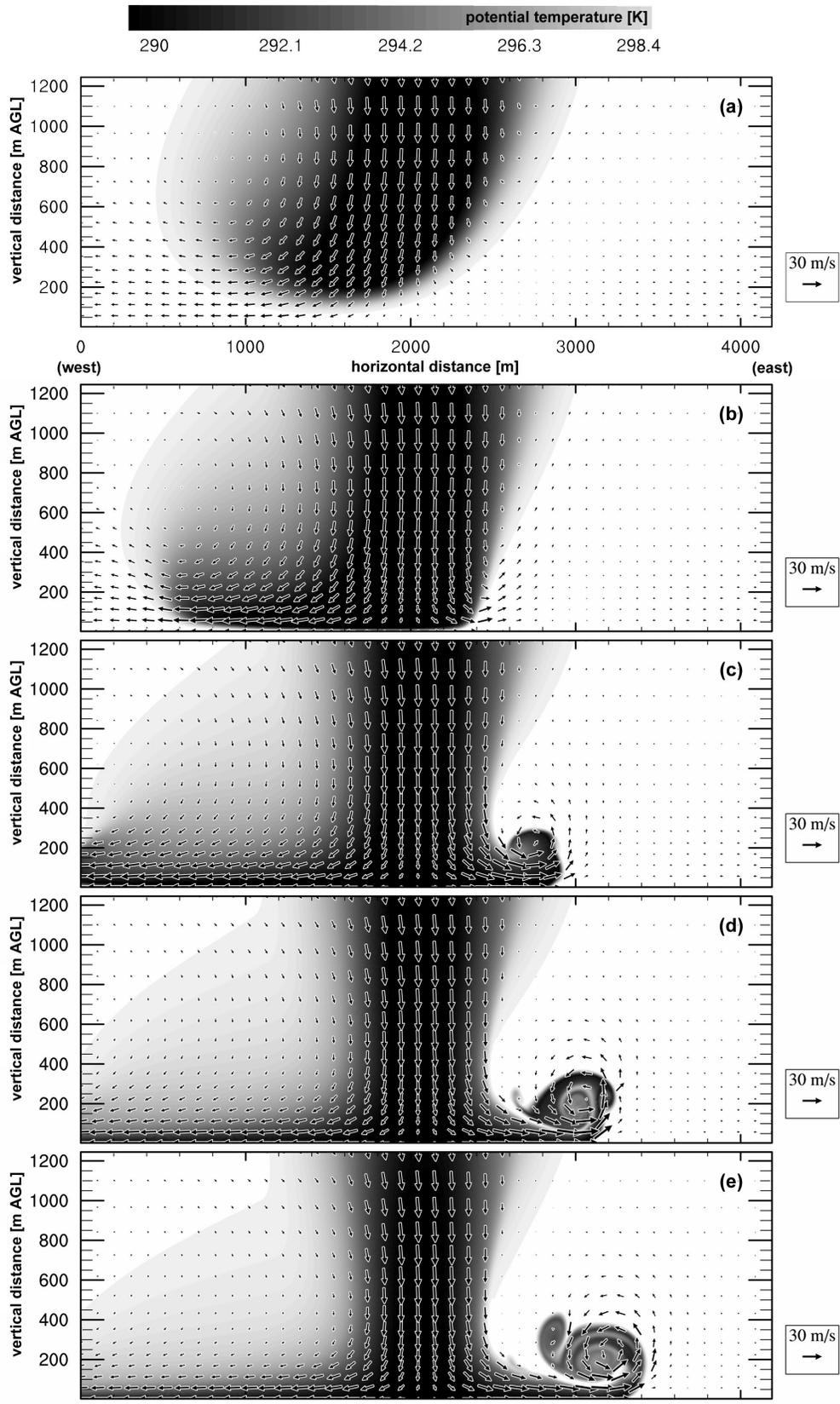


Figure 4.14 continues on following page

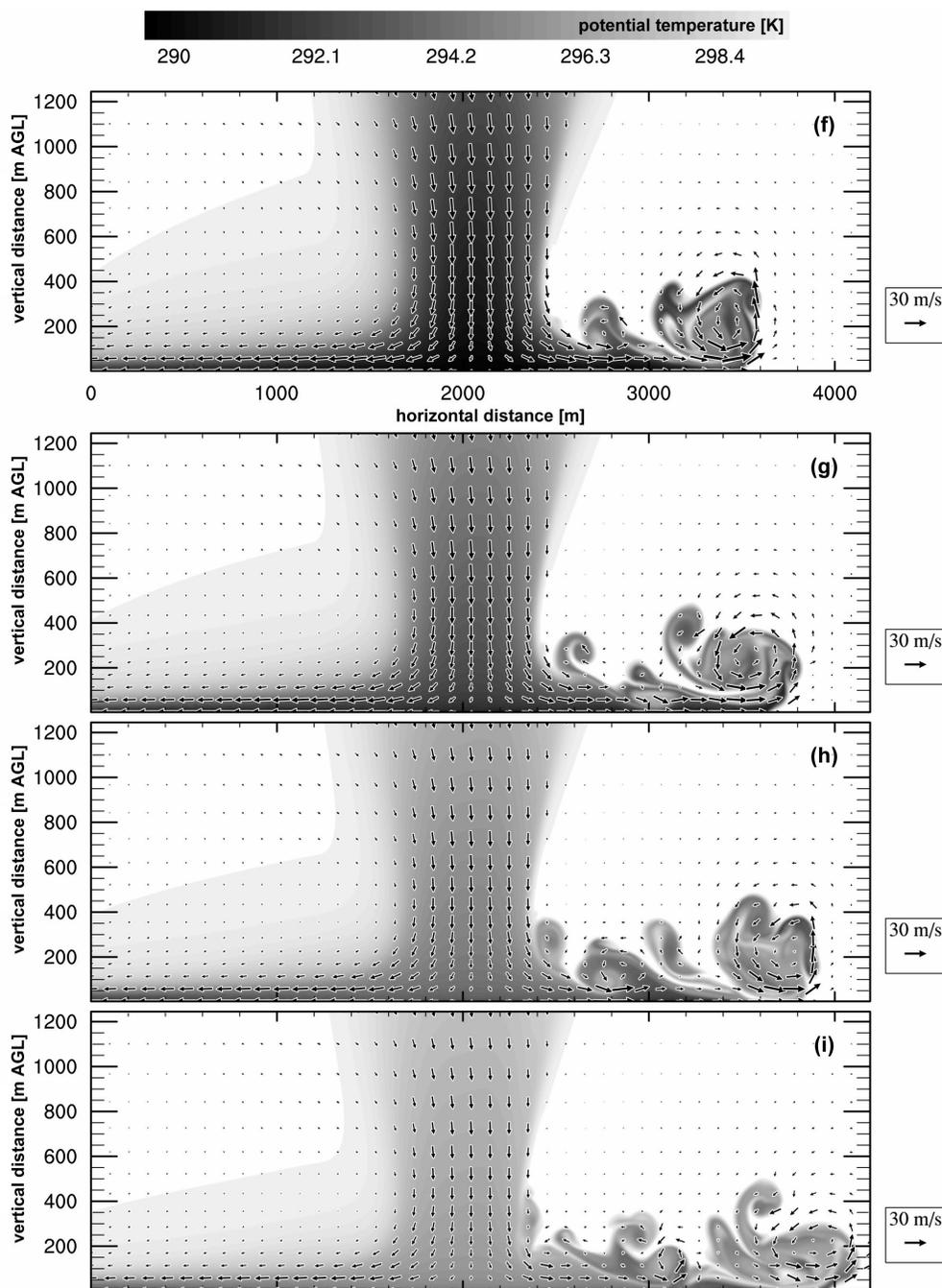


Figure 4.14: Evolution of the velocity vectors and potential temperature contours for CM1-Case 3 at the following times after the start of the simulation: (a) 210 s, (b) 240 s, (c) 270 s, (d) 300 s, (e) 330 s, (f) 360 s, (g) 390 s, (h) 420 s, (i) 450 s.

N.B. Vectors are shown at only every tenth grid point in both spatial directions, for clarity of presentation.

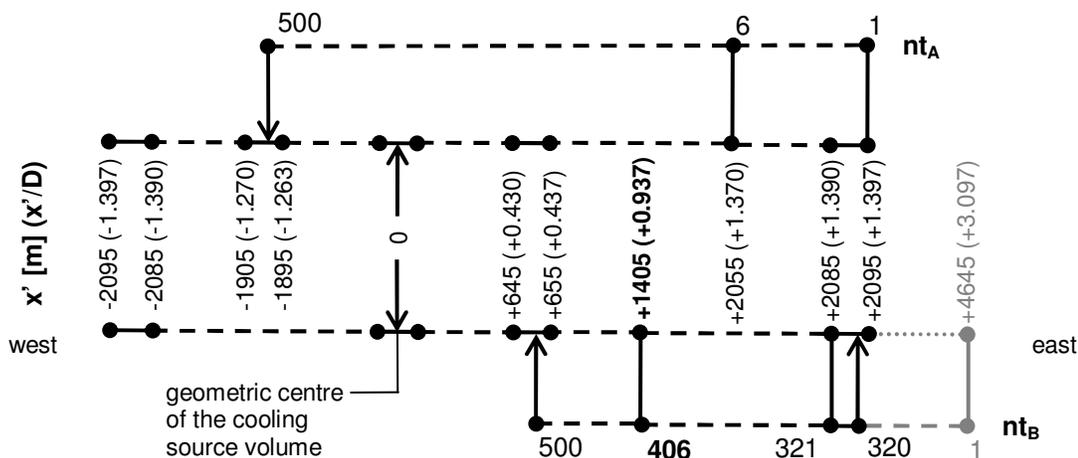


Figure 4.15: Movement of Structures A and B through the CM1-Case 3 flow field

The model domain was spatially resolved into 420 horizontal grid points. Velocity was linearly interpolated when the structure location fell between simulation grid points, i.e. when $nt \pmod{5} \neq 1$. For instance, at the last time step ($nt_A = 500$), Structure A was between two grid points on the western side of the model domain.

Structure A encountered peak U of 38 m/s at $z/D = 0.005$ and $t_p = 240$ s. Fig. 4.16a shows that, at $z/D < 0.05$, this positive peak U was followed shortly in time by a zero value and a negative peak U . As depicted in the Fig. 4.1 insets, these features of the U history corresponded to the leading side outflow, the downdraft stagnation region, and the trailing side outflow, respectively. The peak westward U was 24 m/s at $z/D = 0.005$ and 123 s after Structure A encountered the peak eastward U .

Vertical velocities near the peak U/U_p contours were small compared to the corresponding horizontal velocities. W magnitude in Fig. 4.16b was less than 20% of U_p where and when $U/U_p > 0.851$ in Fig. 4.16a. As the downdraft core passed over the structure, for $z/D < 0.067$ (< 100 m AGL), W linearly tended to zero.

In order for Structure B to encounter the peak maximum U gust in the Case 3 flow field, its initial location was chosen beyond the eastern edge of the model domain (3.097 D east of the geometric centre of the cooling source volume). As depicted in Fig. 4.15, Structure B did not enter the simulated domain until $nt_B = 320$, when it was located between the first and second gridpoints at the eastern edge. Structure B

experienced the peak maximum gust (69 m/s) in the Case 3 flow field at $z/D = 0.005$, $x'/D = 0.937$, and $t_{p, \max} = 405$ s ($nt_B = 406$).

Fig. 4.17 reveals some interesting aspects of the trailing wake behind the dominant roll vortex (Figs. 4.14f to i). Two distinct, trailing regions of rotational flow were identifiable. In addition to decreased U and W magnitudes, there were noticeable decreases in spatial extent and height AGL, associated with each subsequent region of rotational flow. These rotational flow regions were encountered by Structure B with a period of 0.5 to 0.6 $t_{p, \max}$ (between 0.005 and 0.004 Hz). As a point of interest, the currently-tallest guyed structure in the world (KVLY-TV mast near Blanchard, North Dakota, USA) extends to $z/D = 0.4192$.

Fig. 4.17b gives an indication that W was negligible (< 1 m/s) at the instant and location of the peak U gust ($U/U_{p, \max} = 0.912$ contour in Fig. 4.17a). However, at the timestep prior to $t_{p, \max}$, there was a fine scale flow feature near ground level. It was associated with the $W/U_{p, \max} = 0.125$ contour.

As discussed previously, precise instantaneous vertical profiles have been difficult to obtain by field observation. Analysis of the CM1 numerical simulations provided some insight into the instantaneous profile shapes. At the instant $U_{p, \max}$ (47 m/s) occurred in CM1-Case 1, vertical profiles were plotted at the four radial locations depicted in the inset of Fig. 4.18. The results for CM1-Case 2 were similar to those shown in Fig. 4.18.

The profile shapes were strongly related to the passage of the dominant outflow vortex. Radial locations of interest corresponded to the following flow features: (1) the peak maximum horizontal wind speed at the middle of the dominant vortex, (2) the local vertical wind speed minimum in the trailing region of the dominant vortex, and (3) the local vertical wind speed maximum in the leading region. The only profile with a notably different shape was for the third location, which resulted from flow complexities⁶ below the elevated leading part of the dominant vortex (shaded region in Fig. 4.18 inset). Nevertheless, the U values did not exceed 10 m/s for $z/D < 0.04$ at $r/D = 1.37$. A fourth profile was plotted at an intermediate location. Fig. 4.19 in Section 4.5.3 shows that the height of the profile maximum at $r/D = 1.30$ agreed well with available field data.

⁶ An adverse pressure gradient causes boundary layer separation and subsequent roll-up into secondary vortices (Alahyari and Longmire 1995).

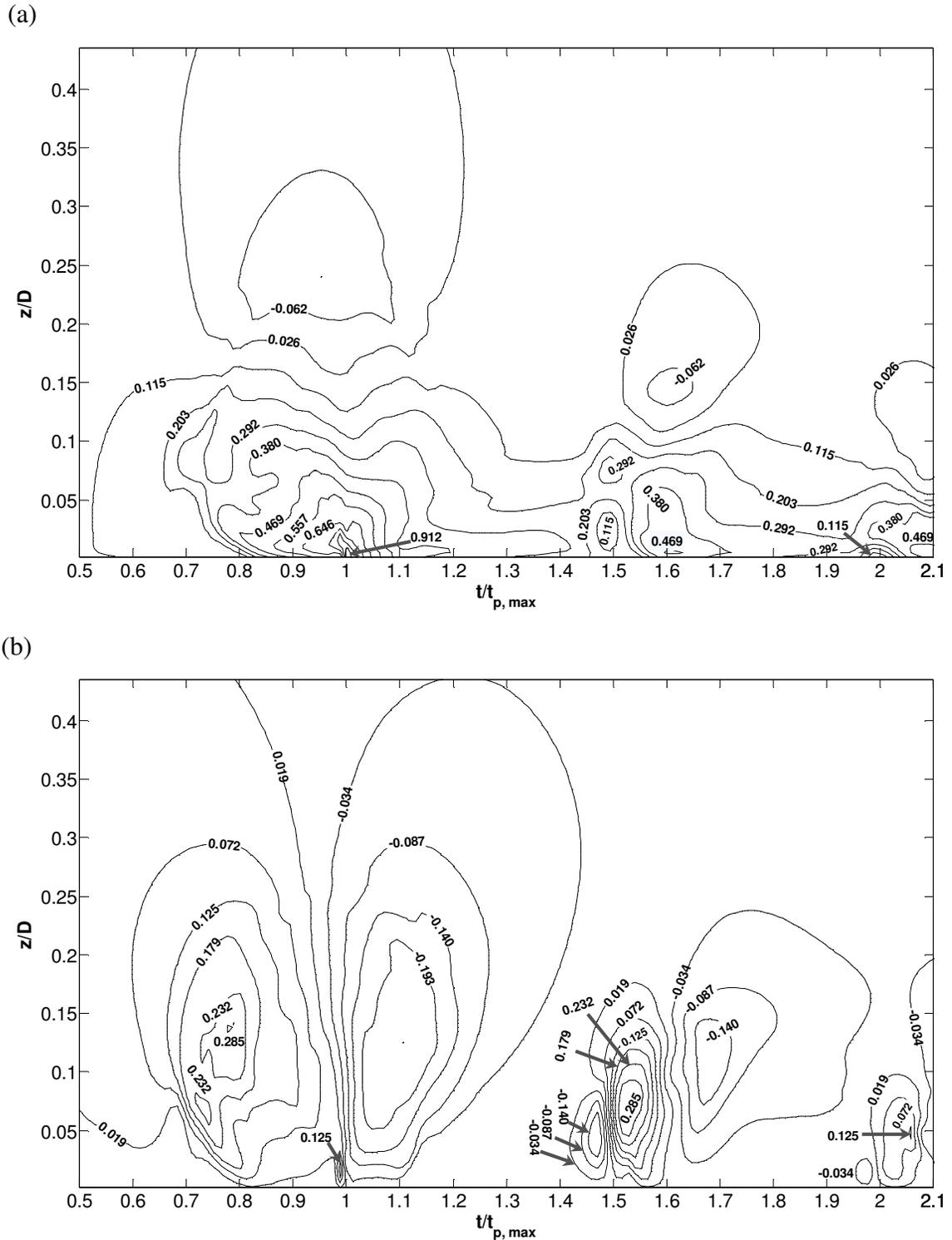


Figure 4.17: Contours of (a) $U/U_{p, \max}$ and (b) $W/U_{p, \max}$ as encountered by Structure B as it moved through the CM1-Case 3 domain and experienced the peak maximum gust

N.B. $t_{p, \max}$ is time to peak maximum velocity

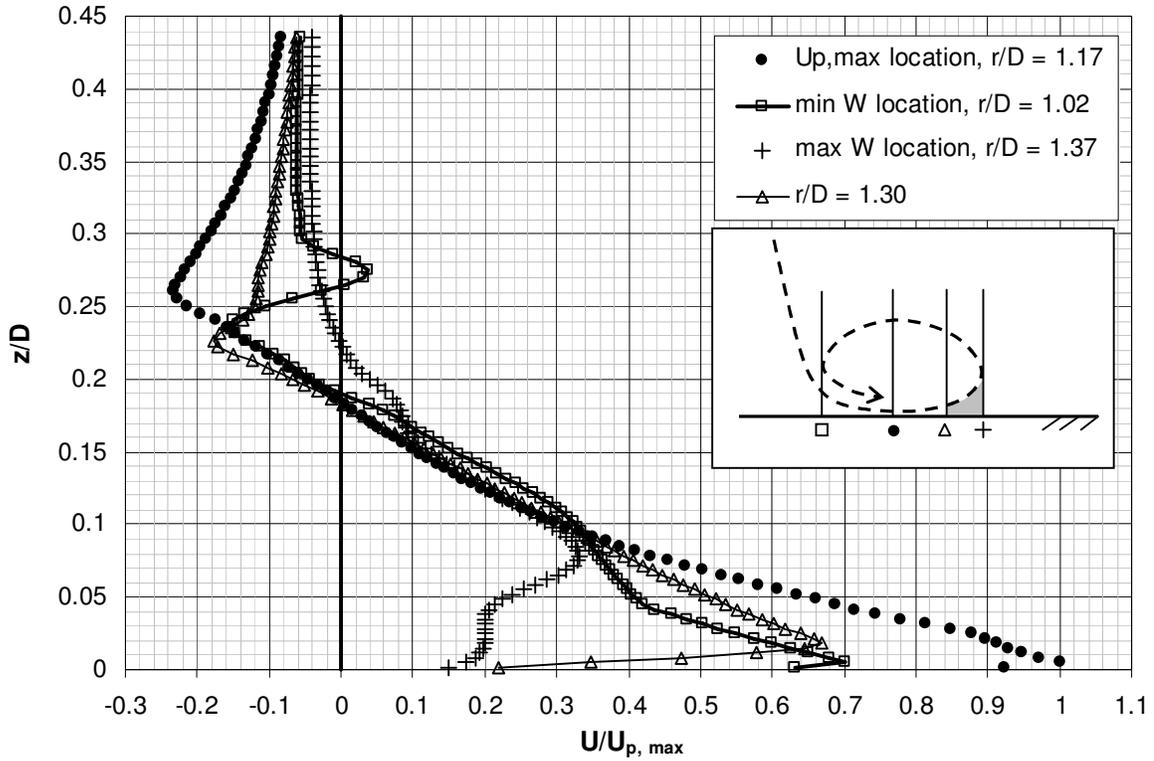


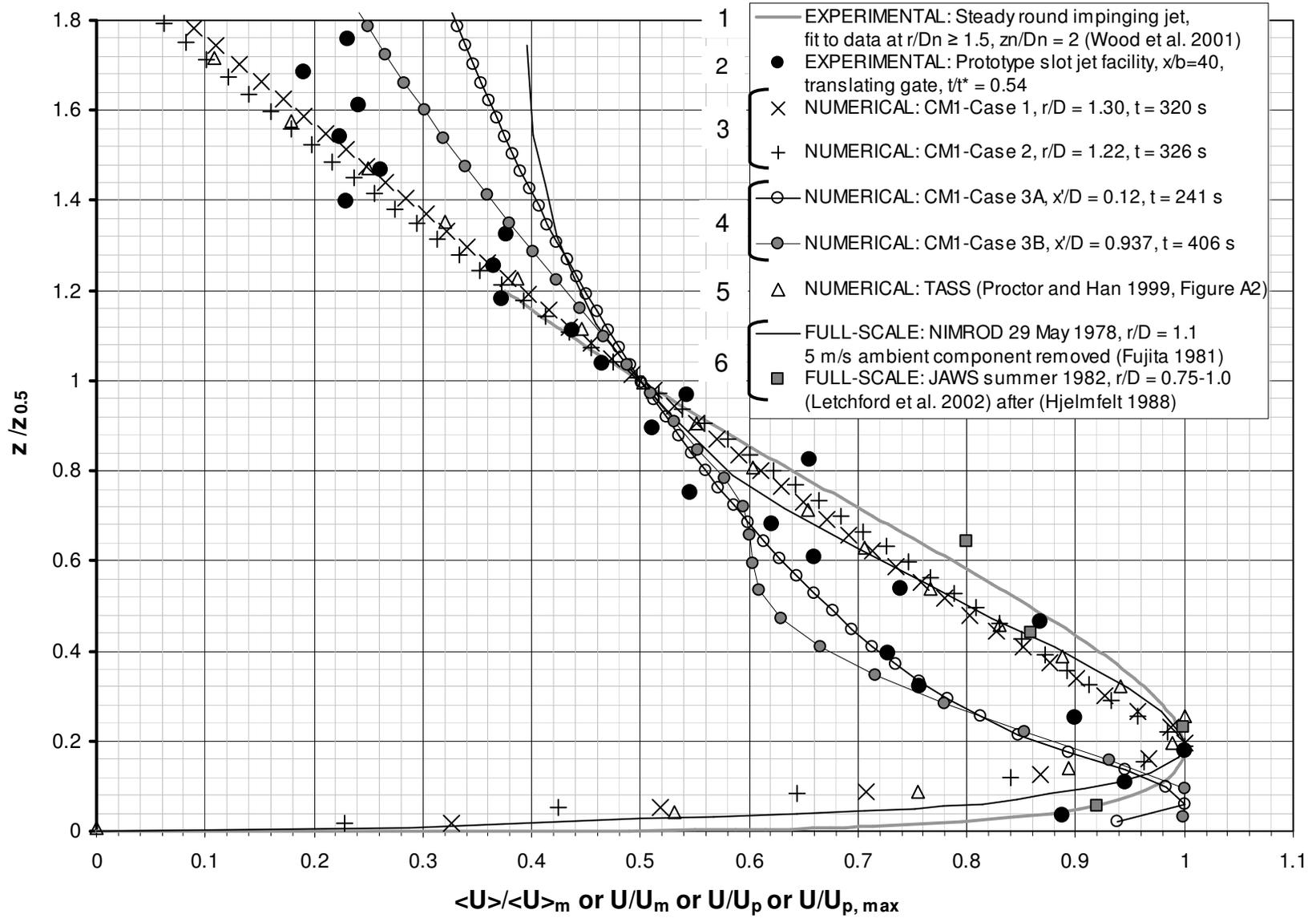
Figure 4.18: Vertical profiles of horizontal wind velocity at various radial locations at the instant of peak maximum U (CM1-Case 1)

4.5.3 Comparison of velocity profiles

Fig. 4.19 compares the following types of vertical profiles:

- (1) U/U_m from Wood *et al.* (2001), which is representative of the steady, round impinging jet (see Fig. 3.9),
- (2) $\langle U \rangle / \langle U \rangle_m$ from the present slot jet experiment,
- (3) U/U_m from the CM1 numerical simulations for a non-translating downburst,
- (4) U/U_p and $U/U_{p, \max}$ from the CM1 numerical simulation for a translating downburst,
- (5) U/U_m from a numerical model that included the full downdraft thermodynamics (Proctor and Han 1999), and
- (6) U/U_m from full-scale studies (Fujita 1981, Hjelmfelt 1988).

Figure 4.19: Comparison of vertical profiles of horizontal wind velocity



The largest value in the second, third, fifth, and sixth profile types listed above occurred within the $z/z_{0.5}$ range of 0.18 to 0.25. Between the ground and profile maximum, the CM1 non-translating downburst profiles (#3) under-predicted the observed velocity profiles, whilst the slot jet velocity profile (#2) tended to exceed the observations. The translating cooling source CM1 profiles (#4) yielded peak velocities at noticeably lower heights than the other profiles.

The experimental profiles (#1, 2) represented numerous realisations, the numerical profiles (#3, 4, 5) were instantaneous and single realisations, and the field profiles (#6) were extracted from radar scans. Although there was the concern that not all of these profiles were instantaneous, Fig. 4.19 gives an indication of the available results.

Recalling that largest horizontal velocity occurred at $z/D = 0.005$ in the present numerical simulations, Fig. 4.20 showed that the corresponding vertical velocity was significantly less ($U_{p, \max} = 47$ m/s in Case 1, $U_{p, \max} = 37$ m/s in Case 2, $U_p = 38$ m/s for Case 3A, and $U_{p, \max} = 69$ m/s for Case 3B). At $z/D < 0.027$ (lowest 40 m AGL), vertical speeds were less than 5 m/s. Vertical velocity was significant only at large z in the downdraft core, as seen with Case 3A. As encountered by Structure A, $W = -10$ m/s at $z = 100$ m AGL, which constituted 48% of U at the corresponding point. At the lesser heights of typical structures (e.g., at $z = 10$ m AGL), W/U was an order of magnitude smaller.

4.5.4 Comparison of velocity histories

Fig. 4.21a compares a translating gate slot jet history at $x/b = 40$ to that of Cases 1 ($U_t = 0$) and 2 ($U_t = 0$, shorter cooling forcing) from the CM1 numerical model. These histories coincided with the height where the largest velocity occurred in the respective vertical profiles. Time was normalised by the peak maximum (or peak) U and downdraft diameter. An effective slot jet downdraft diameter was determined based on a length scale from the numerical simulation. Dividing z (where $U_{p, \max}$ occurred) by D yielded $7.5 \text{ m} / 1500 \text{ m} = 0.5\%$. Thus, the effective slot jet diameter was estimated as $0.0125 \text{ m} / 0.5\% = 2.5 \text{ m}$.

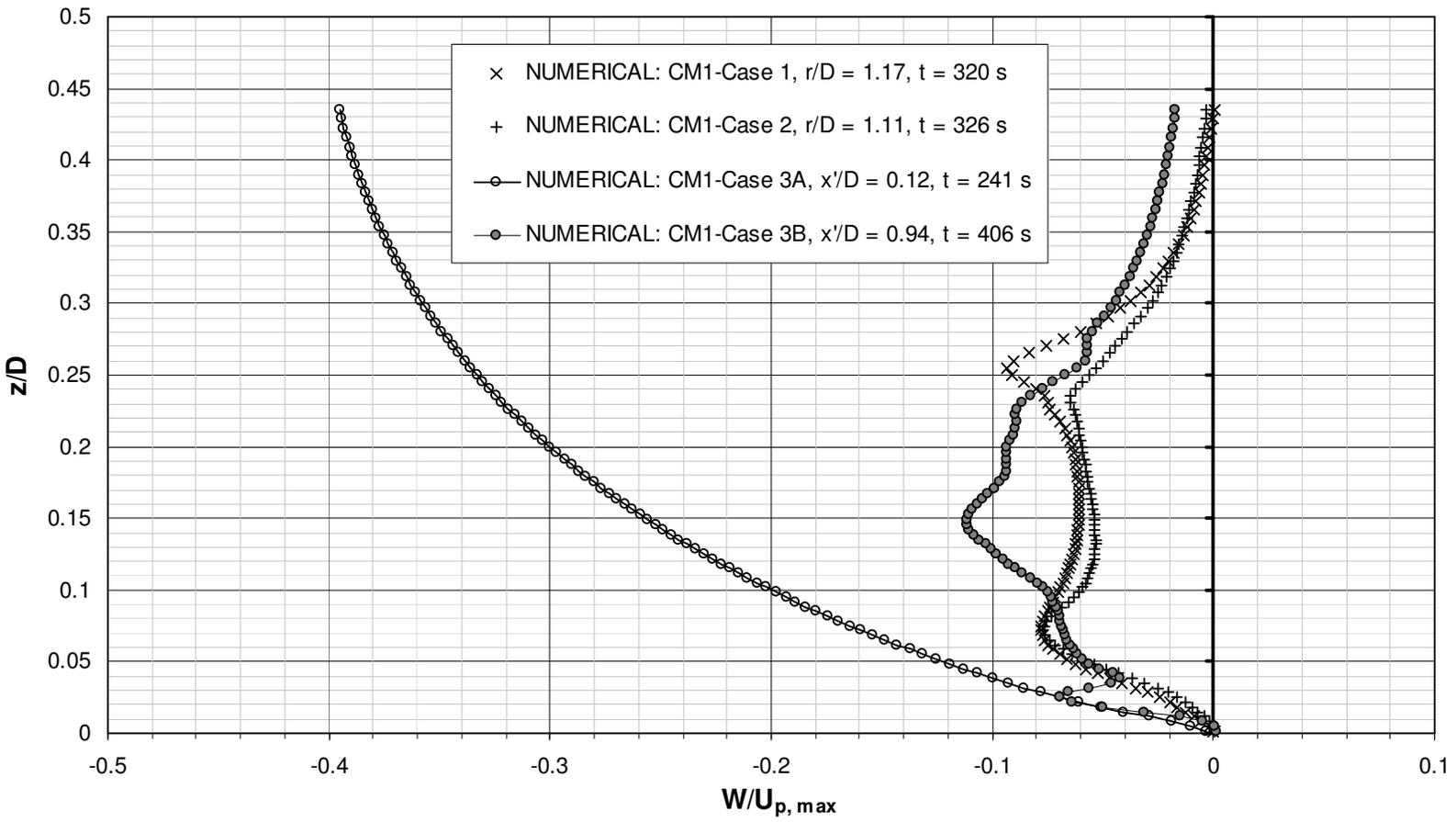
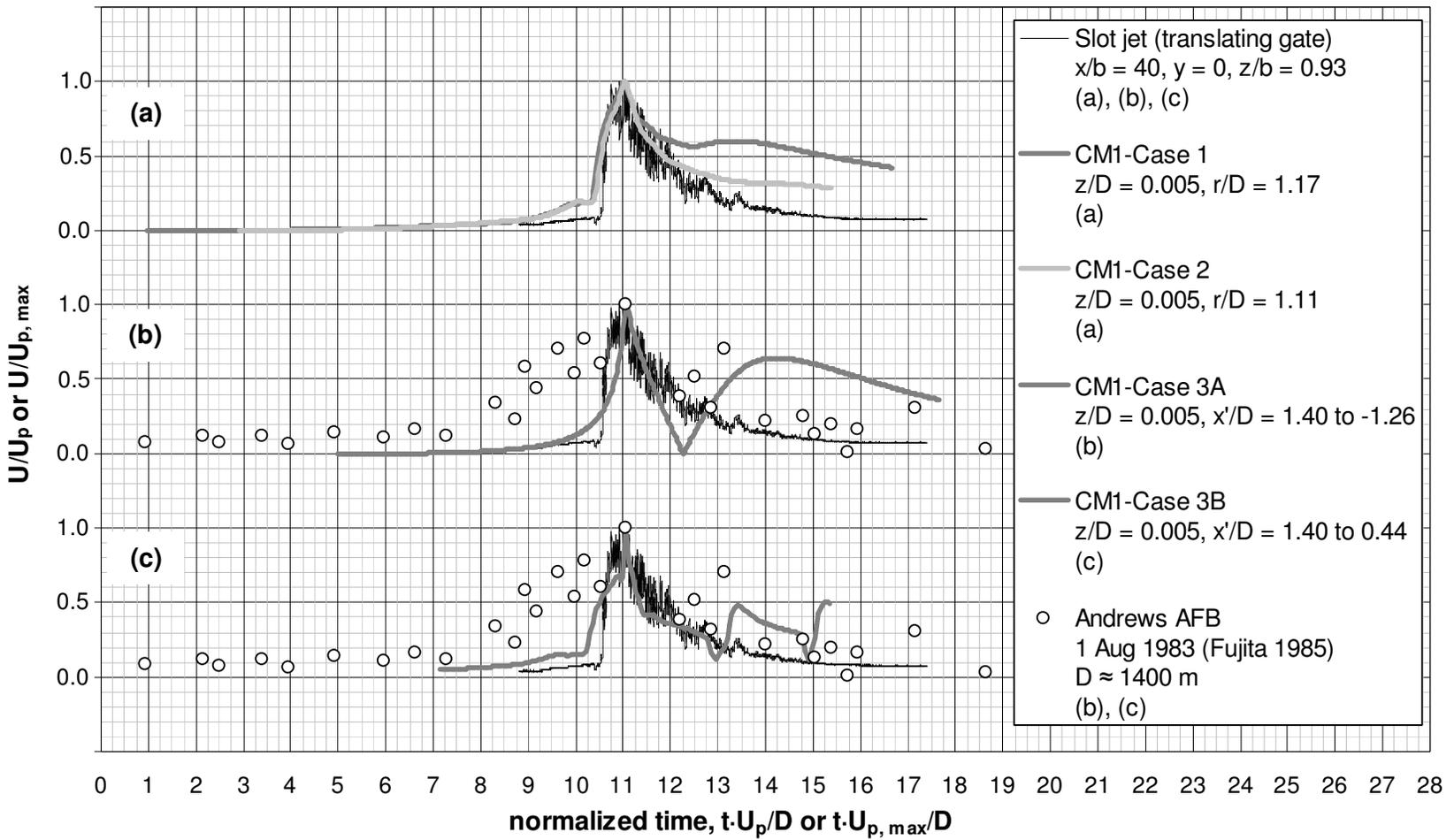


Figure 4.20: Vertical profiles of vertical wind velocity, at the instant of $U_{p, \max}$ (U_p for Case 3A)

Figure 4.21: Comparison of horizontal wind velocity history



After the peak maximum of the CM1-Case 1 history in Fig. 4.21a, the plateau was due to the continued outflow in the wake of the dominant vortex. With a cooling forcing of shorter duration for CM1-Case 2, the computed rise and decay agreed well with the measured slot jet velocity history. Figs. 4.21b and c compared a field observation with the slot jet and translating cooling source numerical simulations (Cases 3A and 3B, $U_t = 8$ m/s). The simulations appeared to develop too quickly relative to the Andrews AFB record of an extreme wet downburst outflow (Wakimoto 1985). In particular, the simulated initial rise was too sharp. However, the decay after the peak maximum in Case 3B (as encountered by the structure that experienced the 69 m/s gust) and the slot jet decay showed fair agreement with the field record.

4.6 Scale of simulations

Table 4.3 summarises the scaling achieved in various time-dependent downburst simulations. The buoyancy-driven flows were the most realistic simulations since they imitate the driving mechanisms of the full-scale event. As well, they inherently simulated the transient nature of the entire downburst flow. However, the resulting outflows were extremely small in length and velocity scale. Impinging jet studies can be an order of magnitude larger, where the model scale was estimated by equating jet nozzle diameter to observed downdraft diameters. However, for impinging jet experiments, laboratory space and cost considerations became prohibitive with increasing D_n . Numerical models (e.g. TASS and CM1) have the capability to reproduce full-scale events. Of course, these results need to be validated against field observations or experiments.

The present velocity measurements were compared to the history from the Andrews AFB downburst outflow to estimate the prototype simulator scale. The characteristic velocity was the peak velocity excess (U_p'). The characteristic time ($T_{0.5 \cdot U_p'}$) was the total duration of the rise to U_p' and the decay to half of U_p' . As indicated in Fig. 4.22, a triangular pulse (Chen and Letchford 2004) was fit to the data points to estimate these values. The length scale of the 2-D transient slot jet simulation was found with Eq. (4.5).

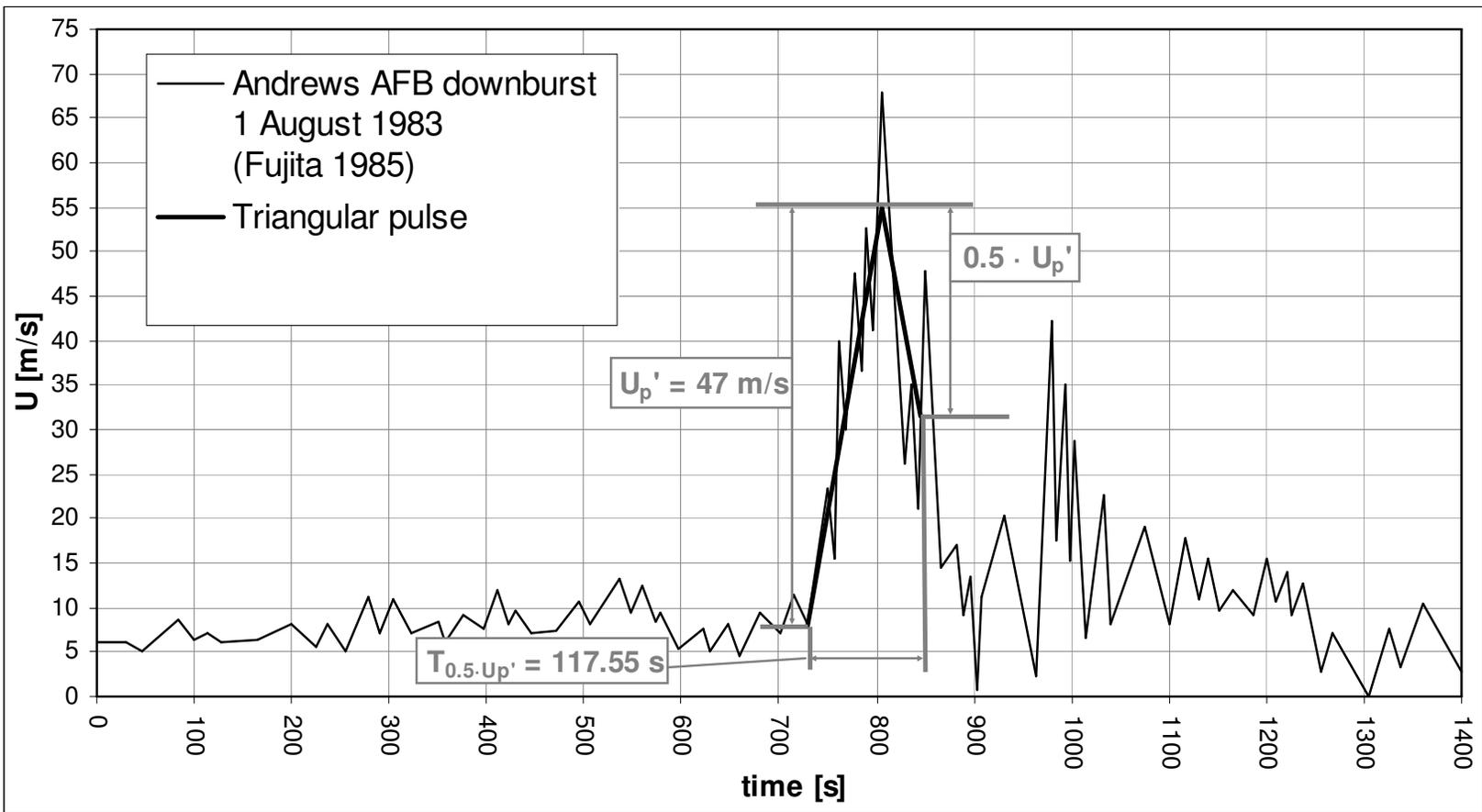
$$\frac{\left(U_p' \cdot T_{0.5 \cdot U_p'} \right)_{\text{full-scale}}}{\left(U_p' \cdot T_{0.5 \cdot U_p'} \right)_{\text{experiment}}} \quad (4.5)$$

It was evident from Fig. 4.21b that by doubling $T_{0.5-U_p}$ from the prototype facility, a better match with the full-scale history would be achieved. As listed in Table 4.3, the achievable length scale with the full-size downburst outflow simulator was estimated to be significantly larger than in previous work. The velocity scale was based on the simulated peak velocity and that observed in the Andrews AFB event.

Table 4.3: Reported and estimated scales for time-dependent experiments

Study	Length scale	Velocity scale	Comments
Buoyancy-driven flow			
TASS, Proctor (1988), numerical	1:1	1:2 - 1:3	Full thermodynamics and microphysics.
Lundgren <i>et al.</i> (1992), experimental	1:9000 - 1:45000	1:85	Release of cylindrical fluid parcel into a tank of ambient fluid of lower density.
Alahyari & Longmire (1995), experimental	1:25000	1:300	
Present cooling source / CM1 implementation, numerical	1:1	1:1	Negative buoyancy generated by increasing and then decreasing potential temperature over time, in an elevated atmospheric region.
Impinging round jet			
Kim <i>et al.</i> (2005), numerical (FLUENT)	1:10500 - 1:52500	1:6.7	Continuous jet with impulsive start.
Mason <i>et al.</i> (2005), experimental	1:2400 - 1:6100	1:3	Continuous jet with impulsive start.
2-D slot jet			
Present prototype facility, experimental	1:2000	1:2	Simulation of outflow region.
Expected full-size facility, experimental	1:700	1:2	Large-scale simulation of outflow region.

Figure 4.22: Characteristic velocity and time for an observed downburst outflow



4.7 Conclusions

The difficulty of downburst field observation has motivated substantial efforts towards physical and numerical simulation. Previous simulations have advanced our understanding of the temporal evolution of the downburst flow field. The logical extension of this knowledge is to engineer structures that can withstand this type of intense wind. Previous approaches to physical modelling did not produce outflows of sufficiently large scale to study the wind loading on common structures. With the addition of an actuated slot in a conventional atmospheric boundary layer wind tunnel, the length scale of the simulated time-dependent outflow was considerably increased.

The Andrews AFB downburst velocity record suggested that the outflow wind direction was fairly constant during the leading side velocity peak. As such, a slot jet approach was applicable for modelling the outflow over the duration that the event attains its highest intensity. A slot jet facility was a practical and realisable approach towards simulating the near-surface peak gust. A translating gate design generated velocity profiles and histories that were comparable to available full-scale data. The present results suggested that the duration of the gate actuation opening phase should be lengthened from the values used in the present study.

Details of the outflow at peak maximum intensity were particularly useful for wind engineering purposes. The Bryan Cloud Model with cooling source forcing permitted the numerical modelling of damaging outflows at high spatial and temporal resolution, whilst retaining a good approximation of the true flow dynamics. The ease of modifying the cooling forcing made it a useful engineering tool for studying the outflow region of isolated downbursts. With respect to the peak maximum horizontal outflow velocity from a non-translating downburst, the present numerical model predicted that the shape of the vertical profile of horizontal outflow velocity resembled a wall jet profile with a pronounced maximum. The instantaneous vertical velocity component corresponding to the peak maximum U was relatively insignificant. In addition to its increased magnitude, the peak maximum U of a translating downburst occurred closer to the surface than that of a non-translating event.

A steady outflow profile generally had a fuller shape than the peak maximum profiles from time-dependent simulations. With respect to profile shape and height where the

largest velocity value occurred, steady flow simulations appeared to adequately represent outflows from non-translating downbursts. However, the computed translating downburst outflow exhibited a strong (albeit, likely short-lived) periodicity, which would be neglected in steady simulations.

The present chapter addressed outflows from isolated downbursts. It is hypothesized that this discussion may be extended to larger convective downdraft phenomena, such as rear-flank downdrafts. The following chapter examines this hypothesis.

4.8 References

- Alahyari, A.A. (1995), "Dynamics of laboratory simulated microbursts", PhD thesis, University of Minnesota, USA.
- Alahyari, A. and Longmire, E.K. (1995), "Dynamics of experimentally simulated microbursts", *AIAA J.*, **33**(11), 2128-2136.
- Bakke, P. (1957), "An experimental investigation of a wall jet", *J. Fluid Mech.*, **2**, 467-472.
- Bryan, G. H. and Fritsch, J.M. (2002), "A benchmark simulation for moist nonhydrostatic numerical models", *Mon. Wea. Rev.*, **130**(12), 2917-2928.
- Caracena, F. (1982), "Is the microburst a large vortex ring imbedded in a thunderstorm downdraft?", *EOS Transactions of the American Geophysical Union*, **63**, 899.
- Charba, J. (1974), "Application of gravity current model to analysis of squall-line gust front", *Mon. Wea. Rev.*, **102**(2), 140-156.
- Chay, M.T. and Letchford, C.W. (2002), "Pressure distributions on a cube in a simulated thunderstorm downburst – Part A: stationary downburst observations", *J. Wind Eng. Ind. Aerodyn.*, **90**, 711-732.
- Chen, L. and Letchford, C.W. (2004), "Parametric study on the along-wind response of the CAARC building to downbursts in the time domain", *J. Wind Eng. Ind. Aerodyn.*, **92**(9), 703-724.
- Chen, L. and Letchford, C.W. (2005), "Proper orthogonal decomposition of two vertical profiles of full-scale nonstationary downburst wind speeds", *J. Wind Eng. Ind. Aerodyn.*, **93**, 187-216.
- Chen, L. and Letchford, C.W. (2006), "Multi-scale correlation analyses of two lateral profiles of full-scale downburst wind speeds", *J. Wind Eng. Ind. Aerodyn.*, **94**, 675-696.
- Choi, E.C.C. and Hidayat F.A. (2002), "Dynamic response of structures to thunderstorm winds", *Prog. Struct. Engng Mater.*, **4**, 408-416.
- Droegemeier, K.K. and Wilhelmson R.B. (1987), "Numerical simulation of thunderstorm outflow dynamics. Part I: Outflow sensitivity experiments and turbulence dynamics", *J. Atmos. Sci.*, **44**(8), 1180-1210.
- Fujita, T.T. (1981), "Tornadoes and downbursts in the context of generalized planetary scales", *J. Atmos. Sci.*, **38**(8), 1511-1534.

- Fujita, T.T. (1983), "Andrews AFB microburst", University of Chicago, Department of Geophysical Sciences, Satellite and Mesometeorology Research Project, Research Paper #205, 38 pp.
- Fujita, T.T. (1985), "The downburst: microburst and macroburst", University of Chicago, Department of Geophysical Sciences, Satellite and Mesometeorology Research Project, Research Paper #210, 128 pp.
- Gast, K.D. and Schroeder, J.L. (2003), "Supercell rear-flank downdraft as sampled in the 2002 Thunderstorm Outflow Experiment", *Proceedings of the 11th International Conference on Wind Engineering*, Lubbock, TX, USA, 2-5 June, 2233-2240.
- Gast, K.D. and Schroeder, J.L. (2004), "Extreme wind events observed in the 2002 Thunderstorm Outflow Experiment", *22nd Conference on Severe Local Storms*, Hyannis, MA, USA, 4-8 October, Paper 7A.6.
- Goff, R.C. (1976), "Vertical structure of thunderstorm outflows", *Mon. Wea. Rev.*, **104**(11), 1429-1440.
- Hjelmfelt, M.R. (1988), "Structure and life cycle of microburst outflows observed in Colorado", *J. Appl. Meteor.*, **27**(8), 900-927.
- Holmes, J.D. and Oliver, S.E. (2000), "An empirical model of a downburst", *Engng. Struct.*, **22**, 1167-1172.
- Holmes, J.D., Hangan, H.M., Schroeder, J.L., Letchford, C.W., and Orwig, K.D. (2008), "A forensic study of the Lubbock-Reese downdraft of 2002", *Wind Struct.*, **11**(2), 137-152.
- Jørgensen, F.E. (2005), *How to measure turbulence with hot-wire anemometers - a practical guide*, Publication No. 9040U6151, Dantec Dynamics A/S, Skovlunde, Denmark.
- Kim, J. and Hangan, H. (2007), "Numerical simulations of impinging jets with application to downbursts", *J. Wind Eng. Ind. Aerodyn.*, **95**, 279-298.
- Letchford, C.W. and Chay, M.T. (2002), "Pressure distributions on a cube in a simulated thunderstorm downburst – Part B: moving downburst observations", *J. Wind Eng. Ind. Aerodyn.*, **90**, 733-753.
- Letchford, C.W., Mans, C., and Chay, M.T. (2002), "Thunderstorms – their importance in wind engineering (a case for the next generation wind tunnel)", *J. Wind Eng. Ind. Aerodyn.*, **90**(12-15), 1415-1433.
- Lin, W.E. and Savory, E. (2006), "Large-scale quasi-steady modelling of a downburst outflow using a slot jet", *Wind Struct.*, **9**(6), 419-440.
- Linden, P.F. and Simpson, J.E. (1985), "Microbursts: a hazard for aircraft", *Nature*, **317**, 601-602.
- Linden, P.F. and Simpson, J.E. (1986), "Gravity-driven flows in a turbulent fluid", *J. Fluid Mech.*, **172**, 481-497.
- Lundgren, T.S., Yao, J., and Mansour, N.N. (1992), "Microburst modelling and scaling", *J. Fluid Mech.*, **239**, 461-488.
- Mason, M., Letchford, C.W., and James, D. (2003), "Pulsed jet simulation of a thunderstorm downburst", *Proceedings of the 11th International Conference on Wind Engineering*, Lubbock, TX, USA, 2-5 June, 2249-2256.
- Mason, M.S., Letchford, C.W., and James, D.L. (2005), "Pulsed wall jet simulation of a stationary thunderstorm downburst, Part A: Physical structure and flow field characterization", *J. Wind Eng. Ind. Aerodyn.*, **93**, 557-580.

- Mason, M.S., Wood, G.S., and Fletcher, D.F. (2009), "Numerical simulation of downburst winds", *J. Wind Eng. Ind. Aerodyn.*, **97**, 523-539.
- Mason, M.S., Wood, G.S., and Fletcher, D.F. (2010), "Numerical investigation of the influence of topography on simulated downburst wind fields", *J. Wind Eng. Ind. Aerodyn.*, **98**, 21-33.
- Orf, L.G. and Anderson, J.R. (1999), "A numerical study of traveling microbursts", *Mon. Wea. Rev.*, **127**(6), 1244-1258.
- Orf, L.G., Anderson, J.R., and Straka, J.M. (1996), "A three-dimensional numerical analysis of colliding microburst outflow dynamics", *J. Atmos. Sci.*, **53**(17), 2490-2511.
- Proctor, F.H. (1988), "Numerical simulations of an isolated microburst. Part I: dynamics and structure", *J. Atmos. Sci.*, **45**(21), 3137-3160.
- Proctor, F.H. (1989), "Numerical simulations of an isolated microburst. Part II: sensitivity experiments", *J. Atmos. Sci.*, **46**(14), 2143-2165.
- Proctor F.H. and Han J. (1999), "Numerical study of wake vortex interaction with the ground using the Terminal Area Simulation System", *37th Aerospace Sciences Meeting & Exhibit*, Reno, NV, USA, 11-14 January, AIAA-99-0754.
- Schlichting, H. (1979), *Boundary-layer theory*, 7th edition, McGraw-Hill, New York, NY, USA, xxii, 817 pp.
- Selvam, R.P. and Holmes J.D. (1992), "Numerical simulation of thunderstorm downdrafts", *J. Wind Eng. Ind. Aerodyn.*, **41-44**, 2817-2825.
- Stull, R.B. (1988), *An introduction to boundary layer meteorology*, Kluwer Academic Publishers, Boston, MA, USA, xii, 666 pp.
- Stull, R.B. (1995), *Meteorology today for scientists and engineer*, West Publishing, Minneapolis/St. Paul, MN, USA, xiii, 385 pp.
- Verhoff, A. (1970), "Steady and pulsating two-dimensional turbulent wall jets in a uniform stream", PhD thesis, Princeton University, 383 pp.
- Vermeire B.C., Orf L.G., and Savory E. (2009), "A comparison of impinging jet and cooling source downburst models", *5th European Conference on Severe Storms*, Landshut, Germany, 12-16 October, 173-174.
- Vermeire, B.C., Orf, L.G., and Savory, E. (2010), "A parametric study of near surface downburst line outflows", *5th International Symposium on Computational Wind Engineering*, Chapel Hill, NC, USA, 23-27 May, 8 pp.
- Wakimoto, R.M. (1985), "Forecasting dry microburst activity over the High Plains", *Mon. Wea. Rev.*, **113**(7), 1131-1143.
- Wakimoto, R.M. (2001), "Convectively driven high wind events", *Meteor. Monogr.*, **28**(50), 255-298.
- Wood, G.S., Kwok, K.C.S., Motteram, N.A., and Fletcher, D.F. (2001), "Physical and numerical modelling of thunderstorm downbursts", *J. Wind Eng. Ind. Aerodyn.*, **89**, 535-552.
- Xu, Z. (2004), "Experimental and analytical modeling of high intensity winds", PhD thesis, The University of Western Ontario, Canada, 169 pp.
- Yao, J. and Lundgren, T.S. (1996), "Experimental investigation of microbursts", *Exp. Fluids*, **21**, 17-25.

CHAPTER 5

UWO WIND TUNNEL 1 DOWNDRAFT OUTFLOW SIMULATOR*

5.1 Introduction

The wind tunnel is a well-established tool for simulating near-surface synoptic winds (i.e. the atmospheric boundary layer), where the wind speed can be approximated as statistically stationary. It is well-known that surface-level outflows from downdrafts have different characteristics than boundary layer winds. For instance, the wind speed in a downdraft outflow is statistically non-stationary.

Observations by the meteorological community (reviewed by Wakimoto 2001) indicate extreme thunderstorm winds are associated with downdraft outflows. Since these extreme wind speeds may represent the design loads in many locales, physical test facilities have been developed to simulate a downdraft outflow. The engineering challenge is to achieve a sufficiently large flow such that the effect of a simulated downdraft outflow on properly-scaled structural models can be studied. The present development (a slot jet installed in a pre-existing, large atmospheric boundary layer wind tunnel) was motivated by this challenge.

Letchford *et al.* (2002) reviewed the early work on physical simulation of downdraft outflows. The conventional approach to downdraft simulation utilised a jet impinging on a flat surface (Walker 1992). The most sophisticated simulations with this approach used a moving jet nozzle (Letchford and Chay 2002, Sengupta and Sarkar 2008) or an actuated aperture at the nozzle (Mason *et al.* 2005, McConville *et al.* 2009). Recent development of impinging jet facilities is towards larger jet nozzles (e.g. 1 m diameter used by McConville *et al.* 2009) to promote fully-turbulent flow.

The objective of the present alternative approach (Lin and Savory 2006, Lin *et al.* 2007) was to simulate only the high-intensity convective downdraft winds near the planetary surface, as this is where most built structures are found. By limiting the simulation domain, a significantly larger scale was achievable, whilst retaining the main features of a convective downdraft outflow. Following the approach of Choi and Hidayat (2002) and Holmes *et al.* (2008), statistically non-stationary wind speed records were

* A condensed version of this chapter is in press for publication in *Wind and Structures*.

separated into mean and residual components by a moving-average procedure. Hereafter, Holmes *et al.* (2008) is abbreviated as H2008.

The facility design and implementation of the downdraft outflow simulator in Wind Tunnel 1 (WT1 DOS) at The University of Western Ontario (UWO) are described in Section 5.2. The hot-wire anemometry set-up and the time-resolved point measurements of wind speed are presented. Analysis of the wind speed in a 2002 rear-flank downdraft outflow (2002 RFD), observed by Orwig and Schroeder (2007), is included to allow a comparison with the simulator results. Section 5.3 compares the time-varying mean components from the WT1 DOS and the 2002 RFD data. Section 5.4 compares the residual component (i.e. the fluctuations about the time-varying mean). Although the former component is of primary concern for designing structures to withstand the extreme loads in this type of wind event, the latter component may have implications for dynamic behaviour or oscillatory response of certain structures. Section 5.5 presents the conclusions of this chapter and indicates the direction of future work.

5.2 Description of the simulator

5.2.1 Facility development

The prototype of Lin *et al.* (2007), which was eleven times smaller in physical size than WT1 DOS, indicated that a slot jet facility can generate the following downdraft outflow features: (1) a dominant horizontal roll vortex, (2) the signature wind speed history, and (3) the expected vertical profile of ensemble-averaged wind speed. The following criteria guided the facility design process:

1. The test section flow must be sufficiently large to model wind effects on built structures. The simulator design was based on modification of an existing atmospheric boundary layer wind tunnel. This approach made optimal use of the existing infrastructure and minimised the overall facility cost.
2. The simulator must generate the signature wind speed history observed from downdraft outflows. A gated nozzle enabled flow pulsation.
3. The ability to augment an outflow wind speed profile with varying levels of ambient winds is desirable. The pre-existing suck-down fan readily generated an ambient

flow. This ambient flow and the slot jet formed a co-flow, which can be likened to a gust front encountering an ambient wind field that contributes to the gust front intensity.

4. The ability to successively test the same structural model under conventional atmospheric boundary layer and downdraft outflow conditions, within the same facility, is desirable.

Storm translation and outflow pulsation with an impinging jet approach have been modelled by other investigators by moving fan equipment on rails (Letchford and Chay 2002, Sengupta and Sarkar 2008) and using intricate nozzle apertures (Mason *et al.* 2005, McConville *et al.* 2009). A slot jet approach is less cumbersome in terms of the requisite equipment and test procedures. The trade-off is that the outflow features are modelled by a plane mixing layer rather than an impinging jet.

5.2.2 Facility characteristics

Wind Tunnel 1 (WT1) at UWO is an open-return wind tunnel that is mainly used to study wind loading on structures. A 30 kW fan draws ambient air through the working section by suction and generates a maximum test section velocity of 15 m/s. In operation, negative gauge pressure is induced in the working section. Along the working section fetch ($X = 30$ m), the tunnel height increases linearly (from $Z = 1.68$ to 2.21 m) to minimise the adverse pressure gradient from test model and roughness element blockage. The tunnel span is $Y = 2.44$ m. Honeycomb and screens at the tunnel inlet reduce turbulence intensity to $\approx 1\%$ in the test section freestream. WT1 is typically used for pressure, force balance, and aeroelastic testing of buildings, towers, masts, and bridges.

At the working section floor of WT1, a secondary flow (i.e. the slot jet) was added for downdraft outflow simulation. The slot jet originated from two centrifugal blowers mounted in the crawl space under the wind tunnel working section as shown by Fig. 5.1. Side inlets on each fan allowed unobstructed inflow from both sides of the facility. The blower discharges were combined into a single flow with custom-made wide-angle diffusers that emptied into ducting leading to the slot assembly. Due to space restrictions, the flow was turned through 180° to the slot nozzle, in the part of the facility labelled ‘section 1’ in Fig. 5.1. The test section modifications were modular and removable.

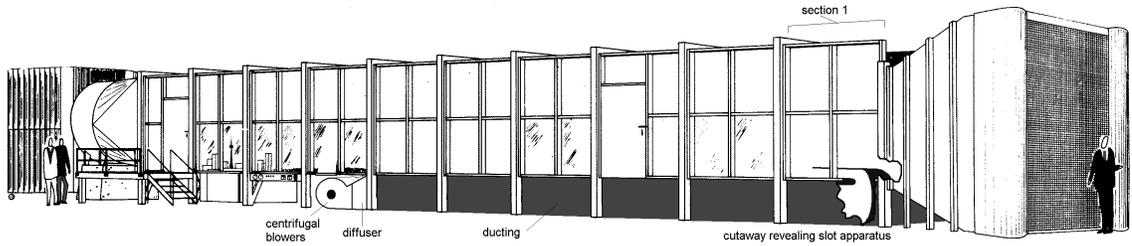


Figure 5.1: Modifications to UWO WT1 for downburst outflow simulation
(adapted from original sketch by UWO BLWTL)

As shown by Fig. 5.2, the simulator assembly was located in the first 7.5 m of fetch. In regular boundary layer testing, the suck-down fan generated a flow from right to left (centreline section view, Fig. 5.2). Twin centrifugal blowers generated the slot jet (Views A and B). The design flow rate was $(2 \times 4.7) \text{ m}^3/\text{s}$ at a pressure rise of 2 kPa. The blowers expelled ambient air into a Y-shaped diffuser that (1) expanded the cross-sectional flow area of the blower outlets to that of the duct, and (2) merged the two streams into a single stream. The duct led to vanes that turned the flow through 180° (View C). This section also contracted the flow cross-section height by a 6:1 ratio, leading to a slot nozzle height of $b = 159 \pm 2 \text{ mm}$ across the 2.44 m span. Slot top thickness was minimised to 4.8 mm with the aid of two support ribs at the side walls and two more ribs at the span-wise 1/3 positions. Each rib had a span-wise thickness of 10.3 mm and tapered to a sharp edge at its downstream end. A Cartesian coordinate system was used (View D). The upstream end of the slot top was faired to the working section floor using an S-shaped profile that covered the first 0.62 m (3.8 b) of fetch. The slot top extended a further 0.79 m (4.9 b) downstream, terminating as the nozzle lip.

A metal plate (6.35 mm thickness) was used to pulse the slot jet (View C). This gate extended across the entire tunnel span. Its motion was limited to vertical translation. The fully-closed and fully-open gate positions were flush with the slot top and working section floor, respectively. The gate was driven by two linear actuators whose motion was synchronised through software. The actuators were rated with $\pm 0.025 \text{ mm}$ repeatability and $\pm 0.400 \text{ mm}$ accuracy. The gate was retractable below the floor, the slot apparatus was removable, and the facility was readily converted back to boundary layer testing within two person-hours of labour.

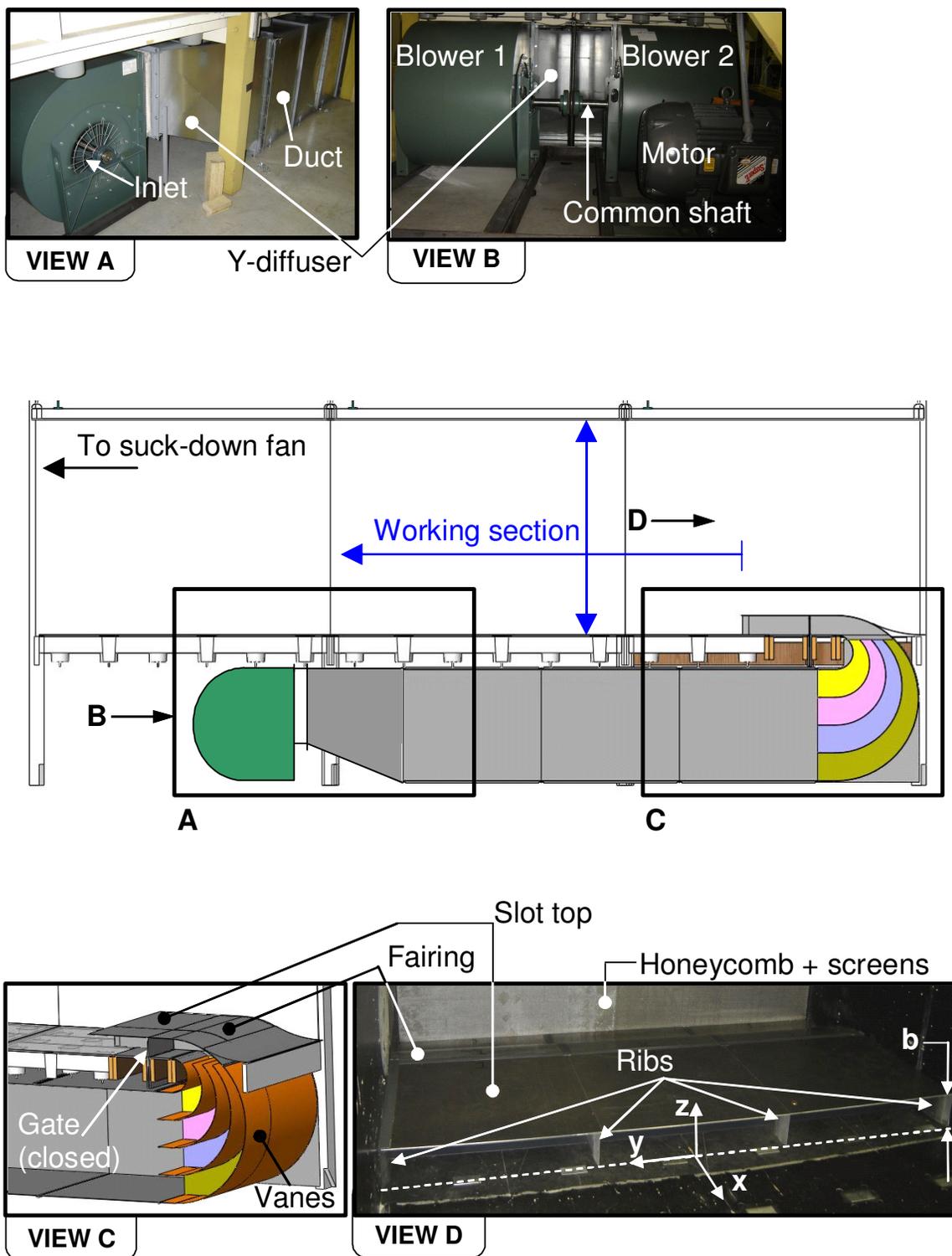


Figure 5.2: WT1 DOS assembly and nomenclature

5.2.3 Anemometry and measurement procedures

Flow visualisations were performed to assess the development of the pulsed slot jet. The tracer particles were an aqueous aerosol of glycol and water droplets. A 4.1 mega-pixel digital camera captured video at a rate of 30 frames per second.

Wind speed histories were acquired using a Dantec Dynamics StreamLine constant temperature anemometry system. Single (55P11) and crossed (55P61) hot-wire probes were used. Hereafter, the single and crossed hot-wire probes are referred to as SHW and CHW, respectively. Signal conditioning was applied to maximise the voltage range. The signals were low-pass filtered at 30 kHz and data were acquired with a computer at a sampling rate of 60 kHz. The hot-wires were calibrated using a Dantec 90H01 unit. The expected accuracy of wind speed measurements was $\pm 5\%$.

Each outflow simulation began with the twin blowers in steady-state operation and the gate fully-closed. A static pressure was built up within the ducting between the blowers and the rear face of the gate. After attaining steady internal pressure in the ducting, the gate was lowered to its fully-open position and then immediately returned to its fully-closed position. This procedure released a single slot jet pulse into the working section.

Opening and closing phases of the gate motion were configured identically with a trapezoidal displacement history. Peak gate speed and acceleration were 1 m/s and 10 m/s^2 , respectively. The gate actuation duration was 0.3 s (from the instant it began opening to its return to top-dead position). The wind tunnel suck-down fan was in steady operation. The ratio of the ambient wind speed to the slot jet wind speed was set as 1:3, because the 2002 RFD gust front speed was 12 m/s (H2008) with peak speed of 40 m/s.

5.2.4 Initial flow conditions

Wind speed measurements of the steady slot jet with no co-flow were performed to characterise the slot jet initial conditions. Vertical profiles were obtained across the 160 mm slot height at three different span-wise positions (Fig. 5.3). The slot span was divided into three compartments by the two ribs shown in Fig. 5.2 (View D), and the Fig. 5.3 profiles were at the three mid-compartment span-wise locations.

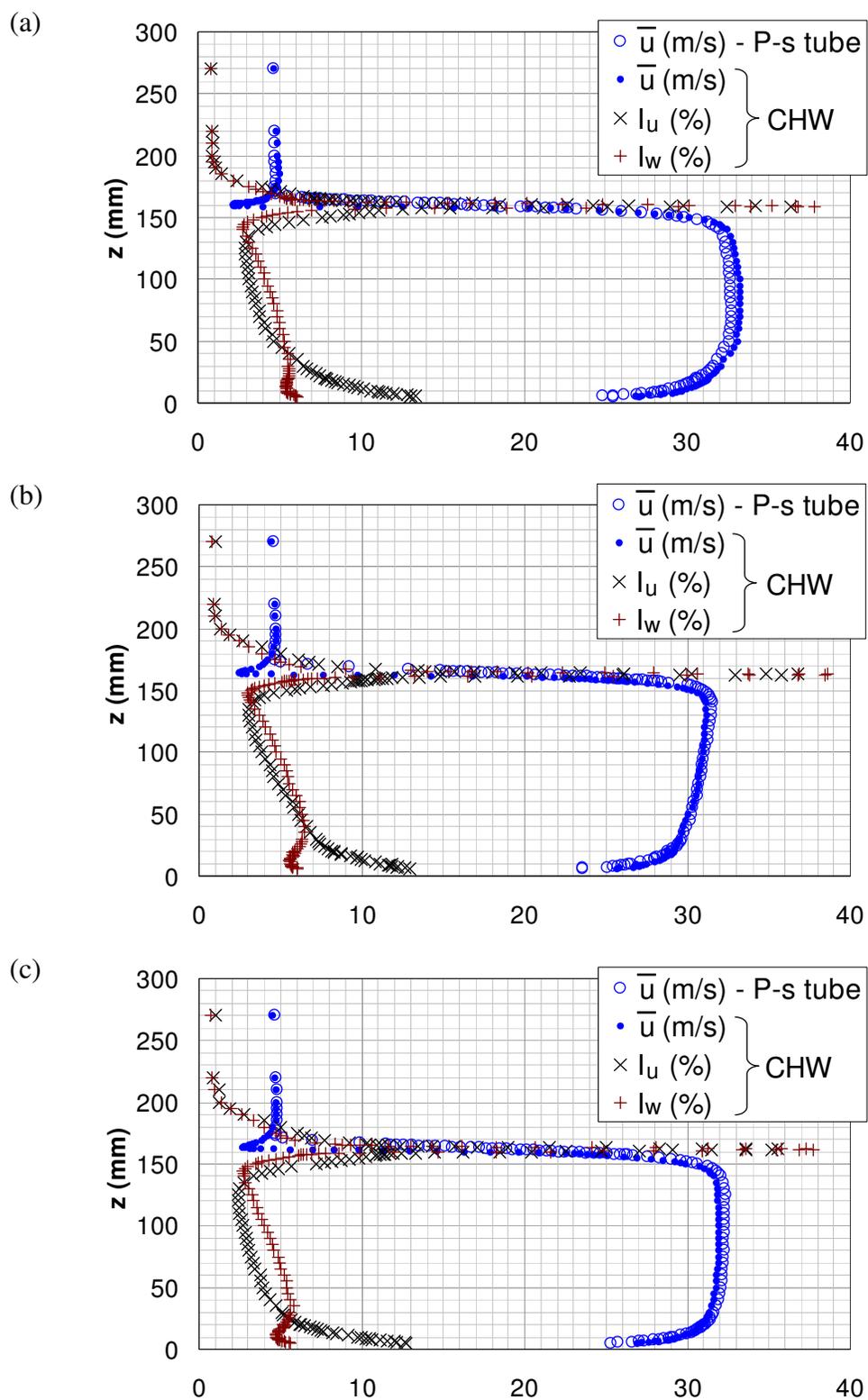


Figure 5.3: Initial conditions of the slot jet at $x/b = 0.04$ and
 (a) $y/Y = +0.33$, (b) $y/Y = 0$, and (c) $y/Y = -0.33$ (WT1 DOS)

At the nozzle exit, the slot jet included boundary layers at the working section floor and the bottom face of the slot top. These two boundary layers flanked the jet core that had relatively uniform mean wind speed. The variation across the central 60 % of the slot height was within ± 4 % of the slot exit bulk wind speed. Across most of the slot height, both turbulence intensity components were in the range of 2 to 6 %.

Displacement and momentum thicknesses were calculated to characterise the initial conditions at the slot nozzle. Simpson's rule was used for piecewise integration between the maximum wind speed point and the nearest data point from a solid boundary. The contribution to the integral from the region between a solid boundary and its nearest measurement point was determined by applying a no-slip condition at the floor, fitting a polynomial function to the measured data, and then evaluating an exact integral.

The plate wake was negligibly thin compared to the slot height, as shown by Fig. 5.3 and the boundary layer thicknesses are summarised in Table 5.1. The boundary layer at the floor was consistently thicker than that at the slot top, for the three span-wise positions. The ratio of displacement thickness to momentum thickness, i.e. the shape factor $H = \delta^*/\Theta$, is an indicator of pressure gradient. The shape factor of turbulent flow over a flat plate is 1.3. With increasing adverse pressure gradient, separation occurs at $H = 2.4$ (White 2003, p. 473). Relative to the aforementioned shape factors, the values in Table 5.1 indicated minimal pressure gradient effects at the slot nozzle.

Table 5.1: Characteristics of the boundary layers at the slot nozzle
(WT1 DOS, $x/b = 0.04$, CHW)

y/Y	Bottom surface of slot top			Floor surface		
	δ^*/b	Θ/b	H	δ^*/b	Θ/b	H
0.33	0.021	0.015	1.4	0.032	0.021	1.5
-0.33	0.012	0.010	1.2	0.024	0.016	1.5
0	0.006	0.006	1.1	0.042	0.030	1.4

5.2.5 Downstream flow conditions

A flow pulse from the WT1 DOS was visualised and a video record showed the passage of the gust front (Fig. 5.4) at ten slot heights downstream of the nozzle

($x/b = 10$). The dominant vortex, associated with peak wind speed, was identifiable. A sense of the outflow size was gained by comparison to the metre rule affixed to the working section window.

As described by Fujita (1981, Figures 27 and 28), the dominant vortex concurrently moved away from the surface boundary and the downdraft column. Mason *et al.* (2005, Figure 8) observed this type of behaviour for a pulsed impinging jet and described the trajectory of the core of the dominant vortex with a cubic polynomial function. For the WT1 DOS, a best-fit with a cubic polynomial function yielded a coefficient of determination of $R^2 = 0.9902$. The trajectory plots had axes for x - and z -position, and the plotted points corresponded to the change in vortex core position with time.

Velocity measurements were conducted with seven different SHW and CHW configurations (Table 5.2). In each configuration, the two probes were located at the same streamwise (x) and vertical (z) position. However, the SHW was always positioned at mid-span ($y = 0$), and the CHW was always offset to one side ($y < 0$ or $y > 0$).

Fig. 5.5 shows a wind speed history as acquired from the SHW. The gate actuation and anemometry systems were synchronised within the limitations of the LabVIEW control software, which had accuracy on the order of milliseconds. The downward motion of the gate and the data acquisition from the anemometer were initiated simultaneously at $t = 0$.

5.2.5.1 Ensemble-averaging

Multiple hot-wire measurements were conducted under identical conditions. The resulting collection of wind speed histories was an ensemble of sample functions or trials, which describes the non-stationary random process, $\{u(c, k, t)\}$. The ensemble average, $\langle u \rangle$, was estimated by performing instantaneous averages over the ensemble of trials forming the process, as described by Eq. (5.1). For instance, $u(1, 1, t)$ in Fig. 5.5 was one of the nine trials that were averaged to determine $\langle u \rangle$, the ensemble average in Fig. 5.6. The parameters, annotated on Fig. 5.6, are described in the Nomenclature.

$$\langle u \rangle = \frac{1}{K} \sum_{k=1}^K u(c, k, t) \quad (5.1)$$

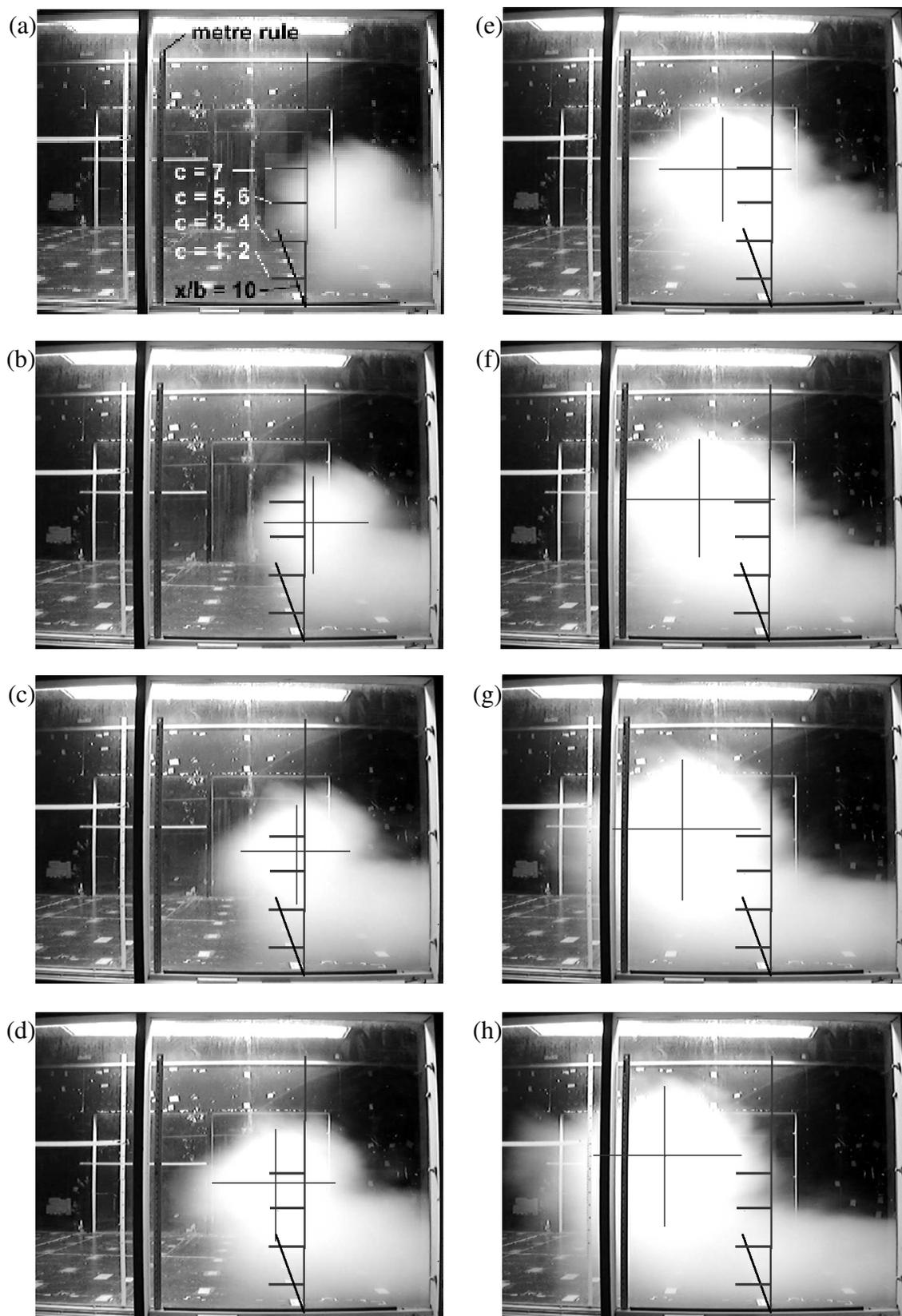


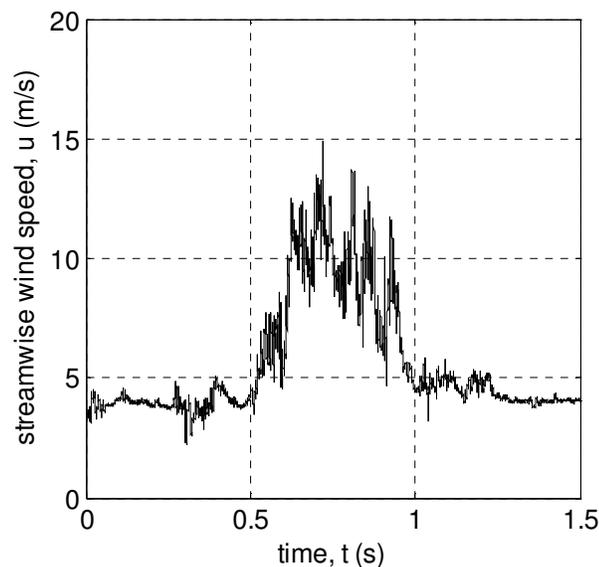
Figure 5.4: Flow visualisation from the WT1 DOS (1/30 s between successive frames)

Table 5.2: Crossed hot-wire probe locations (WT1 DOS)

c	z/b	y/Y
1	0.63	-0.41
2	0.63	+0.40
3	1.56	-0.41
4	1.56	+0.40
5	2.50	-0.41
6	2.50	+0.40
7	3.44	-0.41

5.2.5.2 Sample function averaging

A statistically non-stationary wind speed sample function can be separated into average and residual components. The decomposition involved calculating a central moving-average (i.e. a “running mean”) from the acquired signal, and then calculating the residual as the instantaneous difference between the acquired signal and running mean. Amongst the various digital signal processing procedures available, a moving-average procedure was an appropriate choice for filtering the random fluctuations from a digital signal in the time domain, whilst retaining a sharp step response in the average component. For example, the wind speed history in Fig. 5.5 was decomposed into the running mean in Fig. 5.7(a) and the residual in Fig. 5.7(b).

**Figure 5.5:** Wind speed history from single hot-wire probe (WT1 DOS, $c = 1$, $k = 1$)

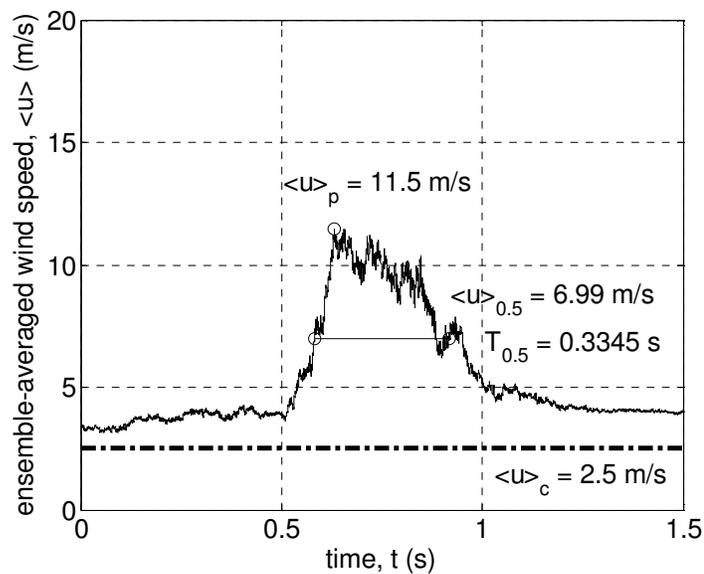


Figure 5.6: Ensemble-averaged wind speed history from single hot-wire probe
(WT1 DOS, $c = 1$, $K = 9$)

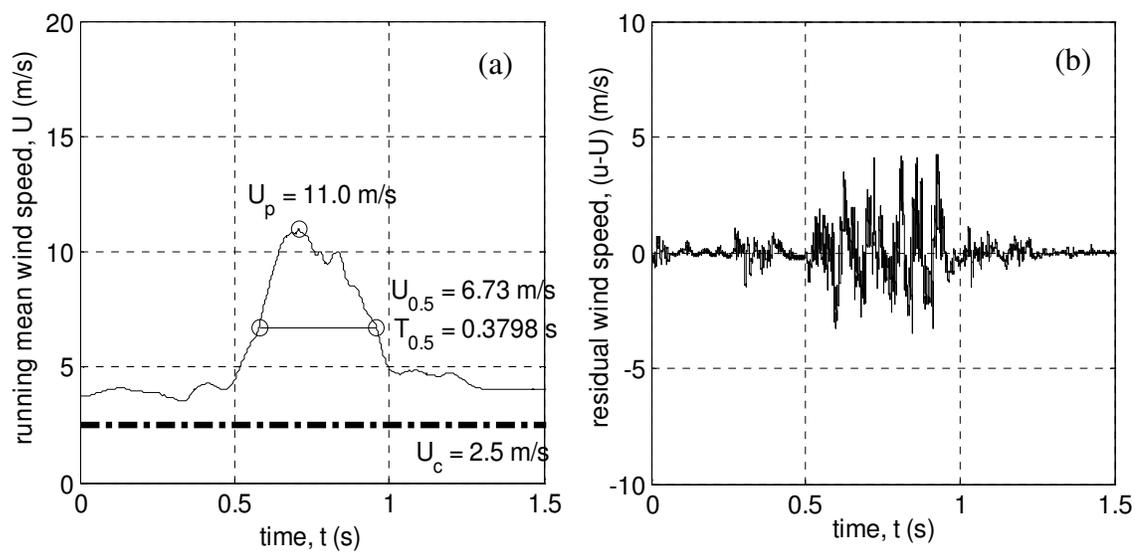


Figure 5.7: (a) Running mean and (b) residual wind speed history
(WT1 DOS, SHW probe, $c = 1$, $k = 1$)

H2008 suggested the following criteria for determining an appropriate averaging time (i.e. the “window” or “filter duration”, T_W): (1) large-scale peaks and troughs in the acquired signal should be retained by the running mean, (2) the time-average of the residual signal should vanish, and (3) the local effect of the filter duration on gust factor (G) should be minimal (i.e. $\partial G/\partial T_W \rightarrow 0$ at the selected T_W). Based on these criteria, a filter size of $M = 5000$ samples was selected. Figs. 5.8 and 5.9 show the findings for the simulated outflow measurements (compare to Figures 6 and 10 of H2008). The selected filter duration for this study was $T_W = M/f_s = (5000 \text{ samples}) / (60000 \text{ Hz}) = 0.083 \text{ s}$, where f_s is the sampling rate. In dimensionless terms, $T_W/T_{0.5} = 25 \%$ for the SHW data, 31 % for the CHW data, and $T_W/T_{0.5} = 40 \text{ s}/160 \text{ s} = 25 \%$ for the 2002 RFD data.

With an appropriate value of M , the running mean wind speed was determined with a central moving-average calculation. For most of the u signal, there existed at least $M/2$ samples before and after the j -th point being calculated, permitting a full window to be used. Approaching the leading and trailing edges of the signal, the window incrementally reduces to one-sided about j , with a width of $M/2$ samples.

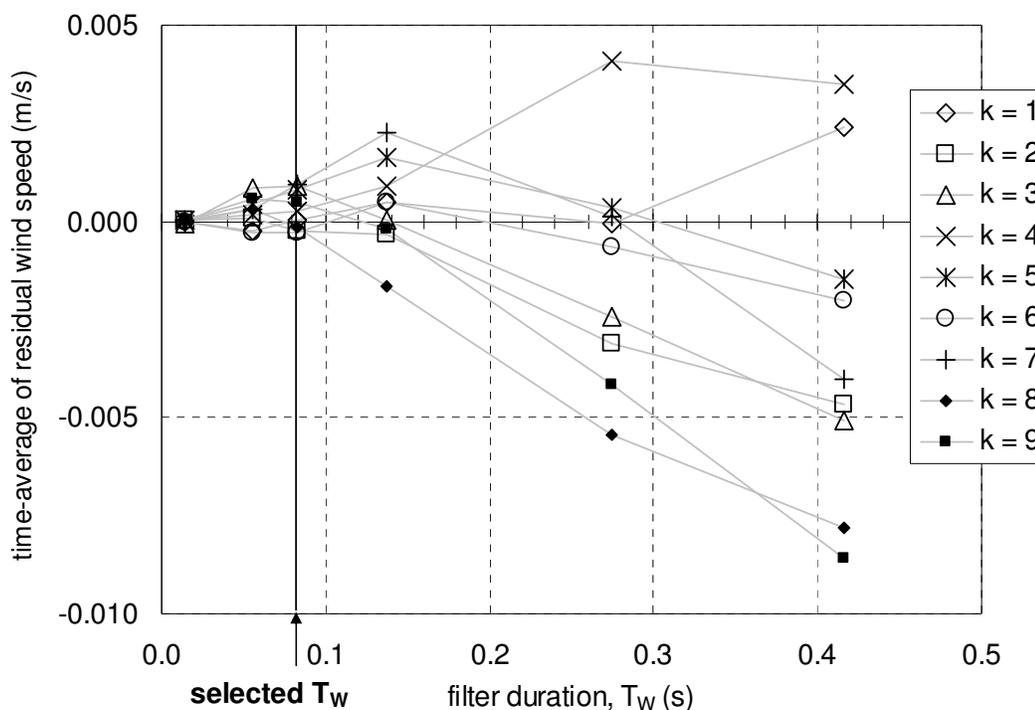


Figure 5.8: Effect of moving-average filter duration on time-averaged residual (WT1 DOS, SHW probe, $c = 1$)

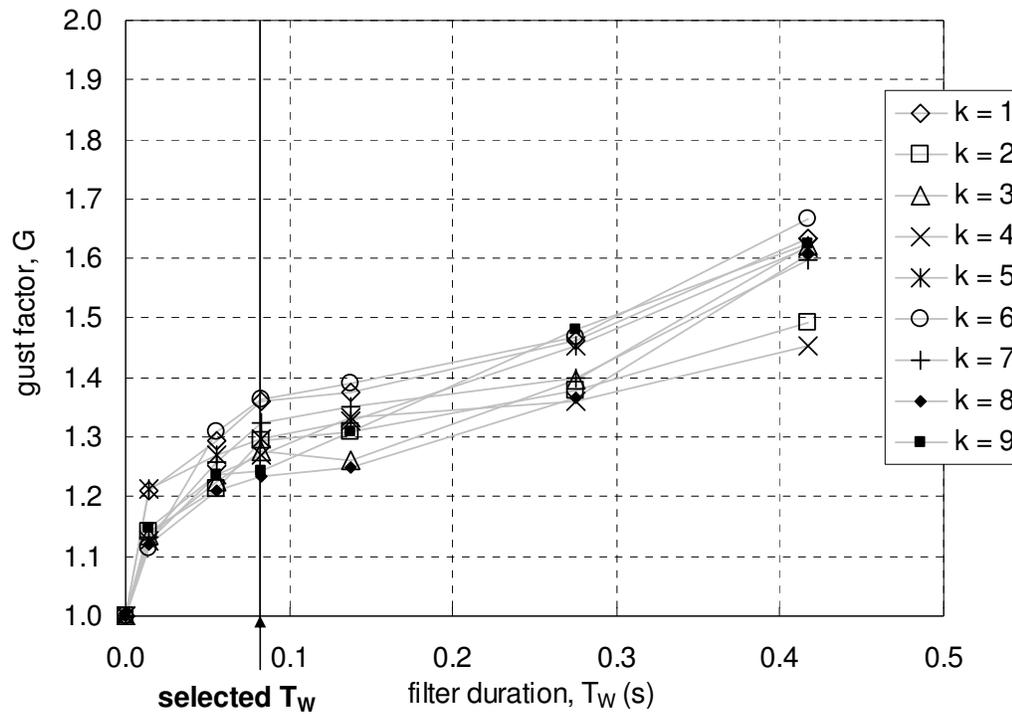


Figure 5.9: Effect of moving-average filter duration on gust factor
(WT1 DOS, SHW probe, $c = 1$)

A random process is ergodic if its ensemble-average is equal to the corresponding sample function average from any single record (Bendat and Piersol 1986). Comparison of Figs. 5.6 and 5.7(a) gave an indication of the ergodicity of the non-stationary outflow wind speed process. Further detailed comparisons indicated that, near the instant of peak gust occurrence, the ensemble-average was representative of the running mean. The high-frequency fluctuations of the ensemble-average would be smoothed out by increasing the ensemble size - in which case, Eq. (5.2) would be a reasonable statement.

$$\lim_{K \rightarrow \infty} \langle u \rangle = U(c, t) \quad (5.2)$$

The ergodicity property is useful because it allays the necessity of performing numerous trials since the statistics from a single trial are representative of those of the process.

5.3 Time-varying mean wind speed from simulator and field observations

Field measurements from a 2002 RFD near Lubbock, Texas, USA were conducted by Orwig and Schroeder (2007). Wind velocity was sampled at 1 Hz from a north-south line of seven towers. The spacing between adjacent towers was 263 m.

The largest observed wind speeds were $u_p \approx 40$ m/s at anemometers on Towers 1 to 4. For the outflow simulator, the peak wind speed and the two prominent changes of wind direction were of primary interest. The time segment ($t_1 \leq t \leq t_2$), during which the peak wind speed occurred and wind direction was approximately constant, was identified (Fig. 5.10). This portion of the wind speed record was relevant for comparison to the slot jet simulator data. The central tower in the line encountered the outflow ~ 50 seconds before the flanking towers did, which was consistent with a curved radar echo in plan.

The 2002 RFD wind speed records were decomposed into running mean and residual components. A central moving-average scheme was used ($T_W = 40$ s as recommended by H2008). This allowed an assessment of the WT1 DOS data against the field observations.

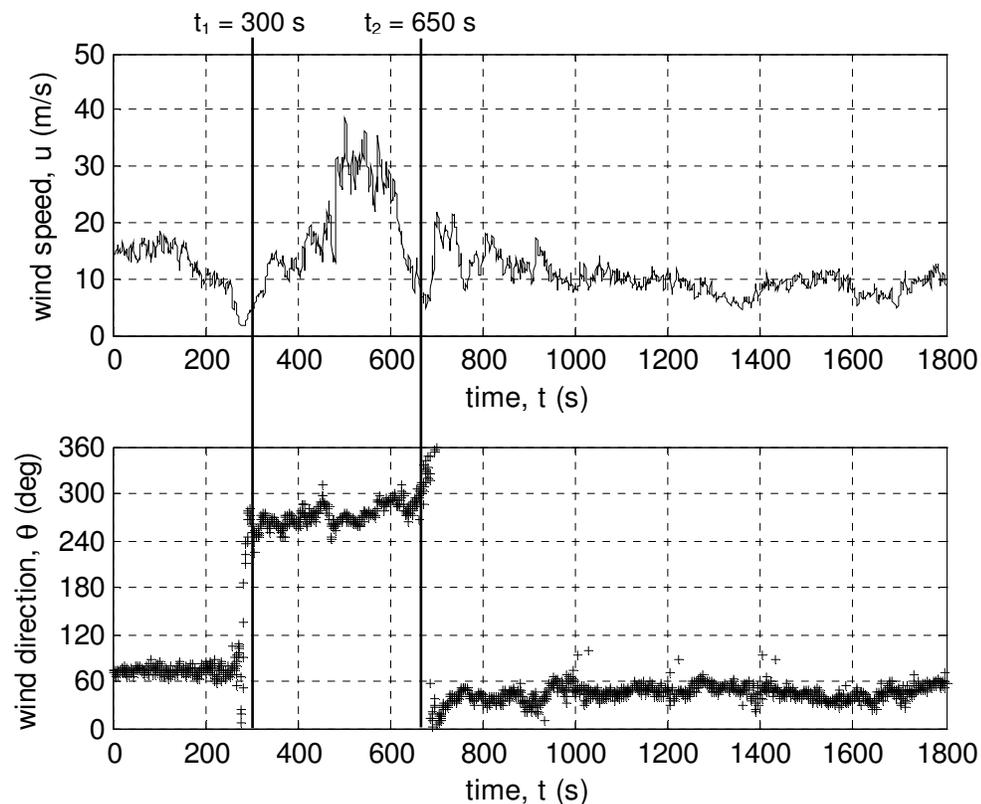


Figure 5.10: Velocity history from 2002 RFD (Tower 4, 10 m AGL)

5.3.1 Comparison metrics

From a downdraft outflow wind speed record, a half-speed ($U_{0.5}$) can be determined from the peak (U_p) and advective (U_c) speeds, as shown by Eq. (5.3).

$$U_{0.5} = \frac{(U_p - U_c)}{2} + U_c \quad (5.3)$$

The notation in Eq. (5.3) is for a running mean, but the same approach applies to an ensemble-average, $\langle u \rangle$. With an idealised wind speed signal, $U_{0.5}$ occurs exactly twice. The half-duration ($T_{0.5}$) is the duration between these two occurrences.

The dominant vortex in the outflow simulator was conveyed by the slot jet stream. At $x/b = 10$, a constant advective wind speed was estimated as $U_c = 2.5$ m/s. The centre of the dominant vortex was identified as shown in Fig. 5.4. U_c was estimated from the displacement (in pixels) of the vortex centre from one frame to the next. The results from two outflow trials indicated that the centre had approximately constant streamwise speed, at the location of interest (Fig. 5.11). The origin of Fig. 5.11 corresponds to the first video frame in which the extent of the vortex can be estimated. For instance, $t = x = 0$ for the Trial A data series corresponds to Fig. 5.4(a). For the 2002 RFD, H2008 determined $U_c = 12$ m/s based on radar echo motion, and wind speed observations at Reese and Lubbock Airports.

U_p and $T_{0.5}$ characterised a downdraft outflow wind speed record from a fixed near-surface point. The parameters in Table 5.3 were determined from the WT1 DOS ensemble-averages (Section 5.2.5.1), as annotated on Fig. 5.6. The parameters in Table 5.4 were determined from the WT1 DOS running means (Section 5.2.5.2), as annotated on Fig. 5.7(a). The parameters in Table 5.5 were determined from the Lubbock downdraft outflow running means.

Simulator and full-scale wind speed histories were compared in non-dimensional form by normalising by these characteristic parameters. Peak wind speed in the simulator and full-scale records were aligned at $t/T_{0.5} = 0$. The evolution and duration of the extreme wind speeds, in full-scale and in the simulator, were then assessed.

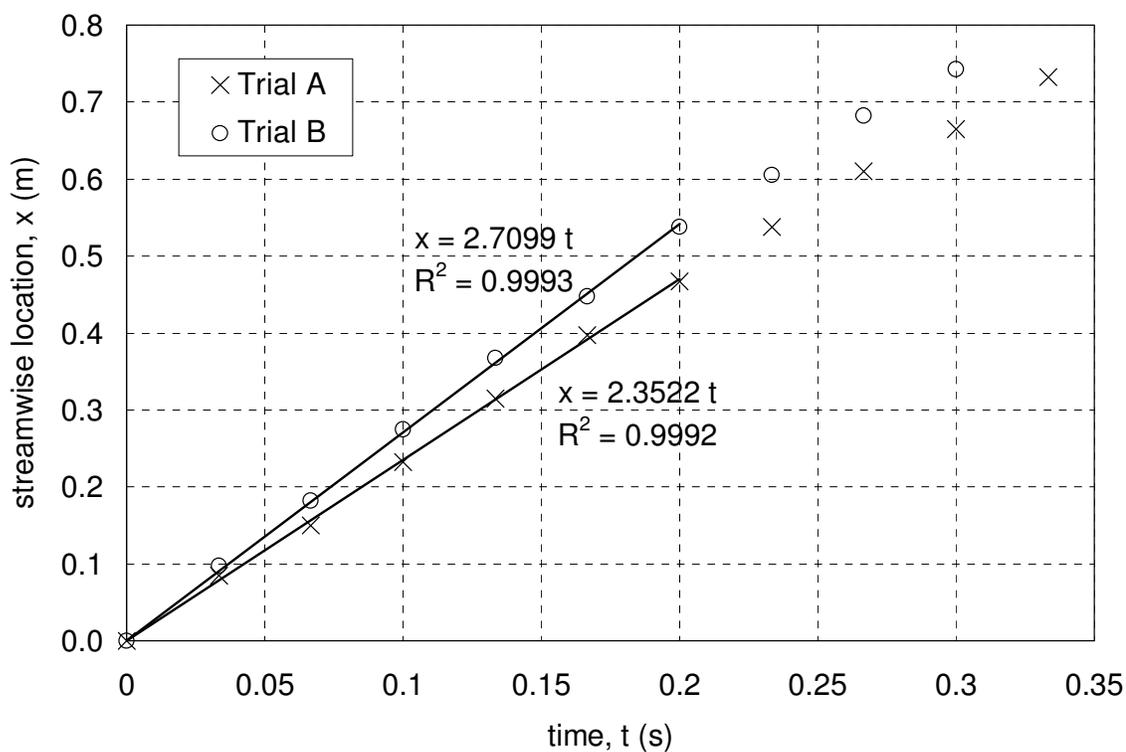


Figure 5.11: Streamwise advection of the dominant vortex centre (WT1 DOS)

Table 5.3: Characteristics of ensemble-averaged wind speed histories (WT1 DOS)

c	K	probe	$\langle u \rangle_p$ (m/s)	$\langle u \rangle_{0.5}$ (m/s)	$T_{0.5}$ (s)
1	9	SHW	11.5	7.0	0.33
		CHW	10.0	6.3	0.27
2	7	SHW	12.2	7.4	0.30
		CHW	10.8	6.7	0.24
3	9	SHW	9.9	6.2	0.17
		CHW	7.5	5.0	0.20
4	10	SHW	9.8	6.1	0.14
		CHW	7.4	4.9	0.12
5	10	SHW	9.4	6.0	0.15
		CHW	7.1	4.8	0.21
6	10	SHW	9.0	5.8	0.17
		CHW	8.0	5.3	0.14
7	10	SHW	6.0	4.3	0.34
		CHW	4.9	3.7	0.22

Table 5.4: Characteristics of running mean wind speed histories (WT1 DOS)

c	probe	k	U_p (m/s)	$U_{0.5}$ (m/s)	$T_{0.5}$ (s)
1	SHW	1	11.0	6.7	0.38
		2	10.3	6.4	0.39
		3	10.9	6.7	0.30
		4	10.3	6.4	0.42
		5	10.8	6.7	0.38
		6	10.9	6.7	0.34
		7	10.5	6.5	0.36
		8	11.7	7.1	0.30
		9	10.9	6.7	0.32
		mean	10.8	6.7	0.35
		range/mean	13%	10%	36%
	CHW	1	9.6	6.1	0.30
		2	9.7	6.1	0.31
		3	9.7	6.1	0.29
		4	9.6	6.1	0.31
		5	9.7	6.1	0.29
		6	10.0	6.2	0.26
		7	9.8	6.2	0.35
8		9.6	6.1	0.35	
9		9.4	6.0	0.33	
	mean	9.7	6.1	0.31	
	range/mean	5%	4%	29%	
2	SHW	1	11.7	7.1	0.34
		2	11.2	6.9	0.32
		3	11.0	6.8	0.33
		4	11.1	6.8	0.37
		5	11.1	6.8	0.31
		6	11.2	6.9	0.36
		7	11.2	6.9	0.31
		mean	11.2	6.9	0.33
		range/mean	6%	5%	17%
	CHW	1	9.2	5.8	0.31
		2	10.2	6.3	0.35
		3	9.9	6.2	0.30
		4	9.9	6.2	0.36
		5	9.9	6.2	0.26
6		10.3	6.4	0.26	
7		10.7	6.6	0.27	
	mean	10.0	6.3	0.30	
	range/mean	15%	12%	34%	

Table 5.5: Characteristics of running mean wind speed histories (2002 RFD)

Tower	Anemometer height (m AGL)	U_p (m/s)	$U_{0.5}$ (m/s)	$T_{0.5}$ (s)
1	3	28.5	20.3	83
3	10	31.5	21.8	154
4	2	29.5	20.8	144
4	4	31.1	21.6	143
4	6	29.8	20.9	140
4	10	31.1	21.5	139
4	15	31.8	21.9	140
5	3	29.1	20.5	139
5	6	29.2	20.6	136
5	10	30.1	21.1	137
6	10	27.7	19.9	158
7	3	25.4	18.7	149
mean		29.6	20.8	138.5

A simple approach for comparing the evolution was to examine the slope of piecewise linear segments of the normalised wind speed histories. The rate of change (m) of normalised wind speed with normalised time was calculated with Eq. (5.4).

$$m = \frac{\Delta U}{U_p} \cdot \frac{T_{0.5}}{\Delta t} \quad (5.4)$$

Positive slope prior to the peak wind speed and negative slope after the peak wind speed were denoted as m_1 and m_2 , respectively. Additional nomenclature was required to allow for wind speed records with more than one distinct positive and one distinct negative slope. The first positive-slope segment was denoted as m_{1a} , the following one was m_{1b} , etc. The first negative-slope segment after the peak wind speed was denoted as m_{2a} , the following one was m_{2b} , etc.

The duration of the extreme wind speeds was quantified by determining the difference in time between the instant of the first up-crossing and the instant of the last down-crossing of a threshold value. Thresholds of $U/U_p = 0.6$ and 0.8 were suitable for the records examined in this study. $T_{n,0.6}$ and $T_{n,0.8}$ corresponded to the former and latter

threshold values, respectively. These two durations and the slopes of the piecewise linear segments of the wind speed histories were the characteristic parameters of interest for comparing full- and model-scale normalised wind speed histories (Table 5.6).

A comparison of the simulator flow to the Lubbock outflow characterised the facility performance and identified possible refinements of the simulator test conditions. With Fig. 5.12, the ensemble-averaged wind speed record at the simulator mid-span ($c = 1$) was compared to the 2002 RFD Tower 4 records. A decrease of m_1 magnitude and an increase of m_{2b} magnitude in the simulator would have more closely emulated the Tower 4 observations. The simulator $T_{n,0.6}$ and m_2 values matched the Tower 4 values well.

The normalised wind speed histories at 10 m AGL from Towers 4, 5, and 6 were very similar. The three towers spanned a full-scale horizontal distance of 526 m. Tower 4 and simulator data were compared (Fig. 5.13). The simulator wind speed histories were all for the same height ($z/b = 0.63$). The spacing of the three measurement locations covered 80 % of the tunnel span as shown, with the Lubbock anemometer layout at 1:1200 length scaling, in Fig. 5.14. Bearing in mind that the small-scale fluctuations of the ensemble-averaged wind speed histories would be smoothed with increased ensemble size, the simulator outflow exhibited a similar degree of span-wise uniformity as the full-scale outflow, over a much larger scaled span.

Table 5.6: Comparison of normalised wind speed history characteristics

Case	Slope		Duration	
	m_1	m_2	$T_{n,0.6}$	$T_{n,0.8}$
2002 RFD, Tower 4, 15 m AGL	1.6	-0.3 -1.6	1.10	0.84
2002 RFD, Tower 5, 10 m AGL	3.0 0.8	-0.1 -1.5	1.08	0.89
WT1 DOS, $c = 1$, SHW	2.0	-0.3 -1.5	1.11	0.71

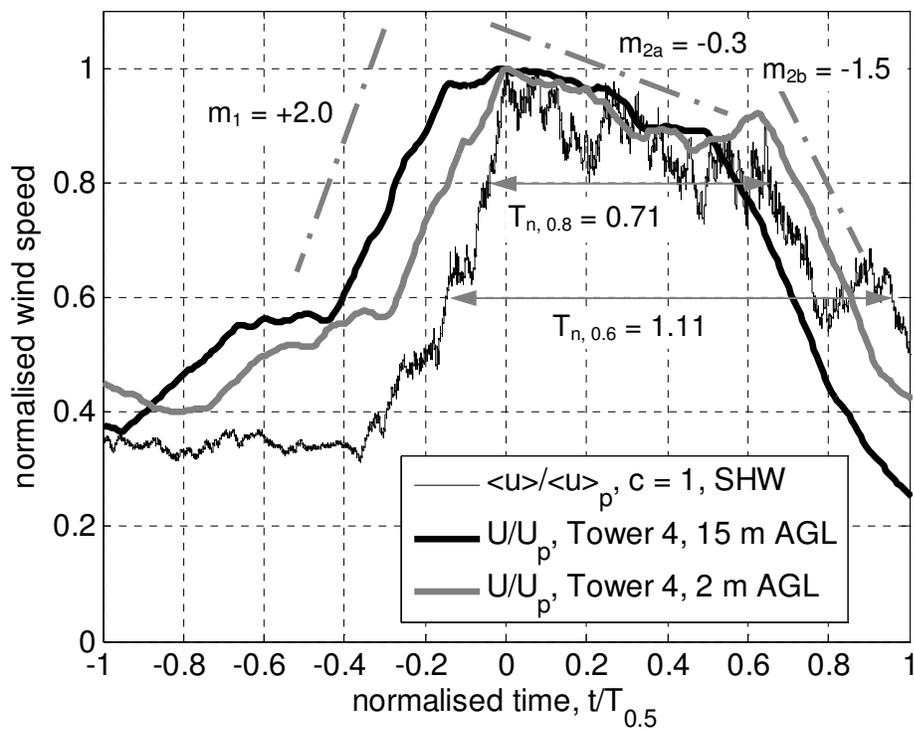


Figure 5.12: Wind speed histories in WT1 DOS ($c = 1, \text{SHW}$) and 2002 RFD (Tower 4)

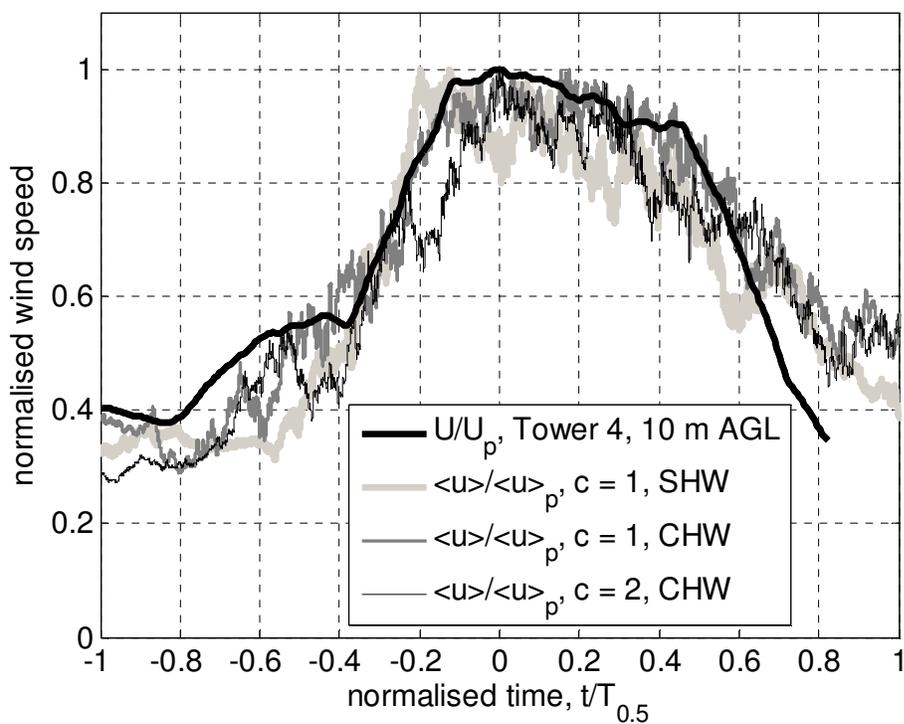


Figure 5.13: Variation of wind speed history with span-wise location (WT1 DOS) compared to 2002 RFD (Tower 4, 10 m AGL)

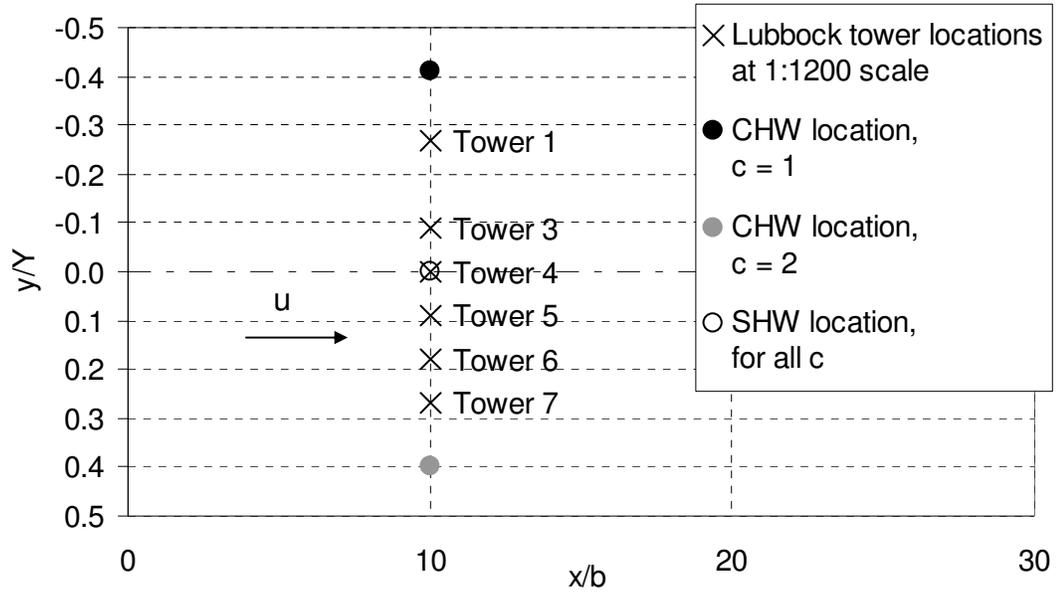


Figure 5.14: Comparison of probe locations for the WT1 DOS and 2002 RFD data sets

5.3.2 Length scaling of the coarse flow features

For modelling purposes, the ratio of the spatial size of the simulator outflow to that of the Lubbock outflow was of interest. A ratio of characteristic times and a ratio of characteristic velocities were determined from Eqs. (5.5) and (5.6), respectively. Length scale, based on the horizontal extent of intense winds, was estimated from Eq. (5.7). The simulator numerical values were shown in Table 5.4 ($c = 1$, SHW, mean, $K = 9$). The full-scale numerical values were shown in Table 5.5 (Tower 4, 15 m AGL).

$$\lambda_T = \frac{(T_{0.5})_{\text{model-scale}}}{(T_{0.5})_{\text{full-scale}}} = \frac{0.35 \text{ s}}{140 \text{ s}} = \frac{1}{400} \quad (5.5)$$

$$\lambda_V = \frac{(U_p)_{\text{model-scale}}}{(U_p)_{\text{full-scale}}} = \frac{10.8 \text{ m/s}}{31.8 \text{ m/s}} = \frac{1}{2.94} \quad (5.6)$$

$$\lambda_L = \frac{\ell_{\text{model-scale}}}{\ell_{\text{full-scale}}} = \frac{(T_{0.5})_{\text{model-scale}} \cdot (U_p)_{\text{model-scale}}}{(T_{0.5})_{\text{full-scale}} \cdot (U_p)_{\text{full-scale}}} = \lambda_T \cdot \lambda_V \approx \frac{1}{1200} \quad (5.7)$$

A 1:1200 length scaling is small for structural modelling, but the following two points are important. First, a rear-flank downdraft is on the larger end of the range of observed downdraft size. Microburst events, with comparable or greater wind speeds, likely occur at a physical size approaching an order of magnitude smaller than the 2002 RFD (i.e. $\lambda_L \sim 1:120$). These smaller outflows may indeed turn out to be the design case for most structures. Second, the simulator conditions can be varied. Increased blower speed will increase $(U_p)_{\text{model-scale}}$ and λ_L . Furthermore, $(U_p)_{\text{model-scale}}$ and λ_L may be increased by modifying the gate actuation.

5.4 Residual wind speed from simulator and field observations

Classical time series analysis rests on the assumption that the signal to be analysed is at least weakly statistically stationary. Residual wind speed records were examined in the following section and the stationarity assumption was evaluated. The distribution, relation to the mean wind speed, auto-correlation, and auto-spectrum of the residual wind speed component were examined.

5.4.1 Stationarity

A time series is weakly stationary if the window of samples, from which the mean and mean square (MS) values were calculated, can be shifted in time without affecting these two values (Bendat and Piersol 1986). Priestley (1988, Section 1.2) noted that this assumption is a mathematical idealisation and in practice, “the most one could hope for is that ... the series would not depart ‘too far’ from stationarity for the results of the analysis to be invalid.” The stationarity of the residual wind speed histories was examined about the time of occurrence of U_p . The moving-average procedure yielded a residual component with a near-zero time-average. The time-averaged residual component (H2008, Figure 6) was not expected to vary significantly with time-shifting, since the averaging window duration was long relative to the short-period fluctuations of the residual wind speed. However, this is not so for the MS residual, which was given further attention in the following analysis.

First, the effect of averaging window duration on MS residual was examined with a window centred at the sample corresponding to U_p occurrence. In Fig. 5.15, for example

if $T_w = 201$, the window of samples (from which MS residual was determined) had 100 samples before and after the sample corresponding to U_p occurrence. By increasing the number of samples on both ends of the window, the variation of MS residual was calculated. The Fig. 5.15 results were due to the residual wind speed characteristics and the imposed window symmetry. The largest fluctuations occurred about the window centre that coincides in time with U_p , so MS residual attained its largest value at small T_w . As T_w increased, more small fluctuation samples were included in the averaging procedure. Eventually, the small fluctuation samples formed most of the window, resulting in a stable MS residual at large T_w . However, the most appropriate averaging time would be an intermediate value that had neither the large variability at small values nor the inclusion of many small fluctuations that were unrepresentative of the extreme winds. The half-duration from Section 5.3.1 was readily identified in typical outflow wind speed histories and served as appropriate averaging window duration. The MS residual, as calculated from the half-duration samples, was identified on Fig. 5.15. In general, $T_{0.5}$ was not exactly symmetric about the occurrence of U_p , so there was a slight deviation from the line calculated from the symmetric window samples. As found from the $T_{0.5}$ samples, the MS residual consistently increased as the probe height decreased.

With averaging window duration equal to the half-duration, the stationarity of the MS residual wind speed was examined. For a stationary signal, the MS residual should be independent of the averaging window location in the time series. As the averaging window was shifted in time over the residual-squared time series, the MS residual varied as shown by Fig. 5.16. The window location (indicated on the abscissa) was in terms of the location of the centre sample of the window. The abscissa datum corresponded to the occurrence of U_p . The range of the plotted points corresponded to shifting the window centre over the half-duration. Locally-stationary residual wind speed segments were identified (Fig. 5.16 arrows). Examining all available records near peak gust, residual wind speed exhibited local stationarity at the central towers in the line (Towers 4, 5, 6), but not at the peripheral towers (1, 3, 7). Near the instant of peak gust occurrence at Tower 4, local stationarity improved with increasing height AGL. The simulated outflow was analysed in the same manner. The findings in Figs. 5.17 and 5.18 were similar to the preceding results for the 2002 RFD.

Figure 5.15: Dependency of MS residual wind speed on averaging window duration
(2002 RFD)

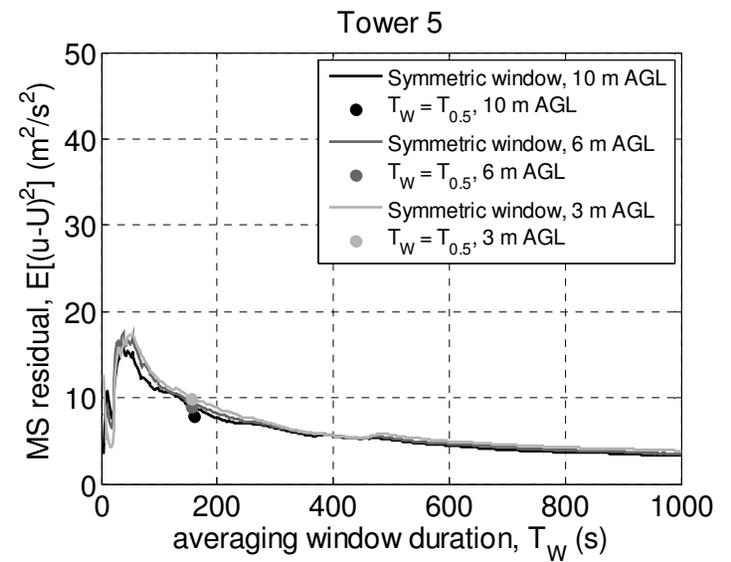
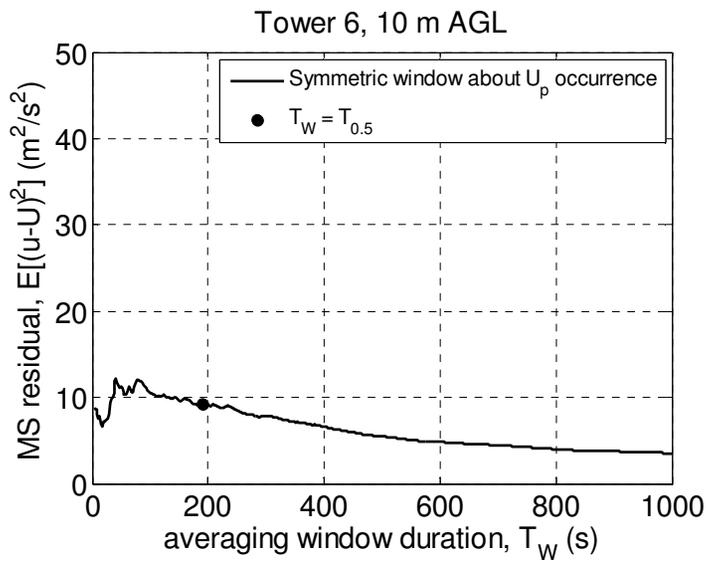
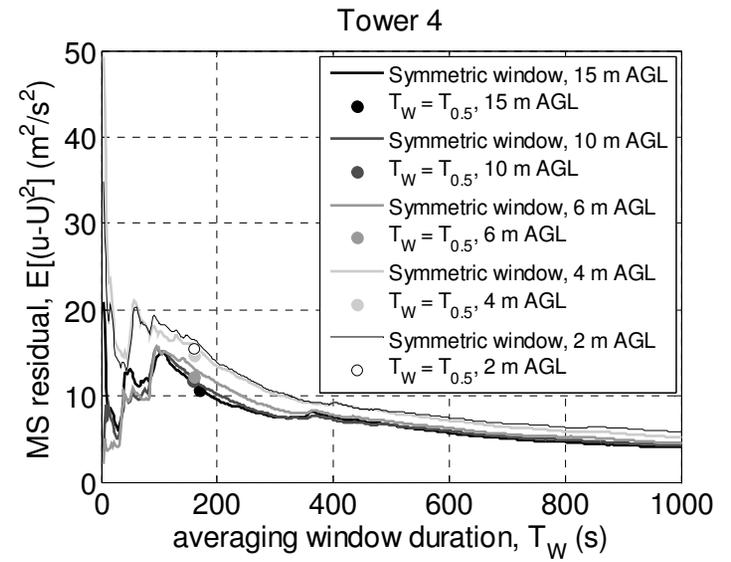
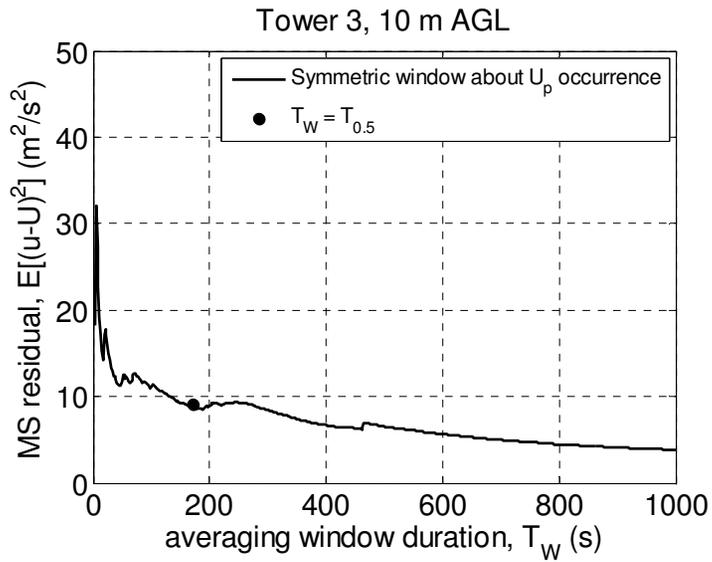


Figure 5.16 continues on following page

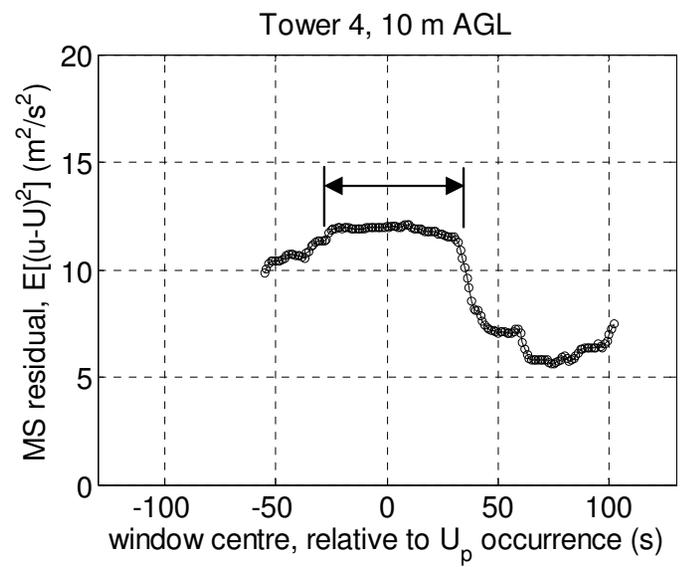
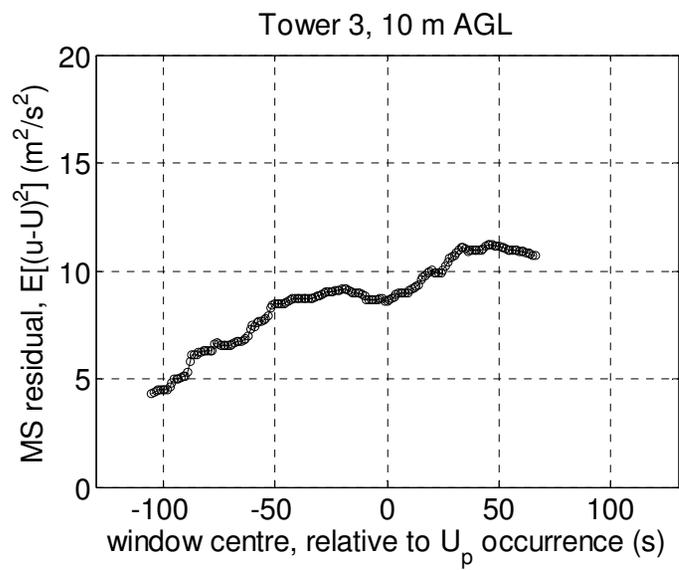
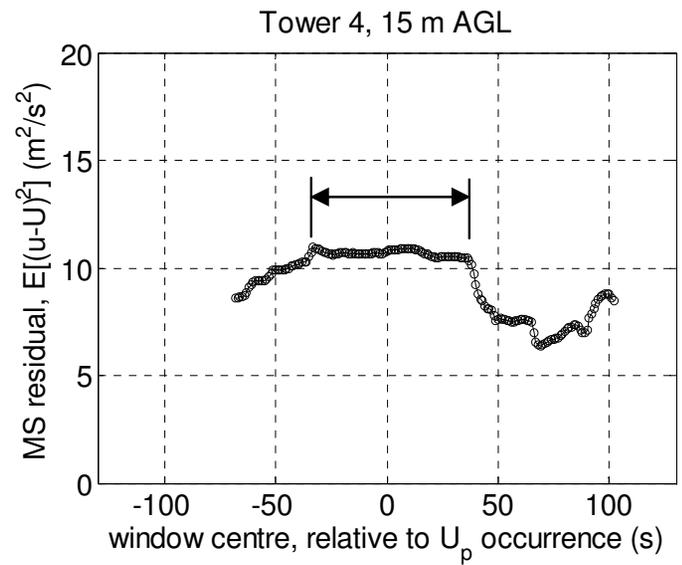
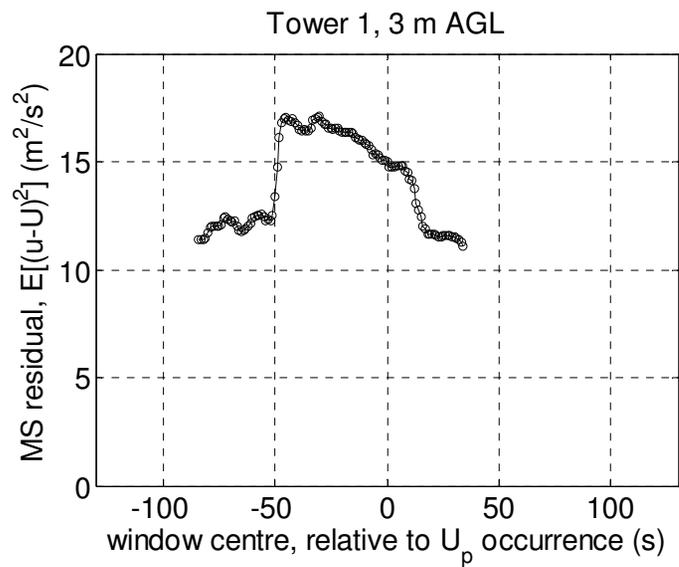
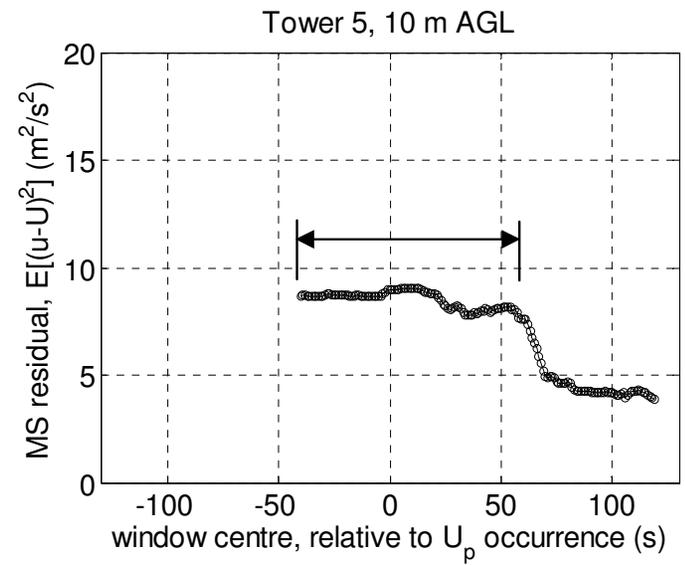
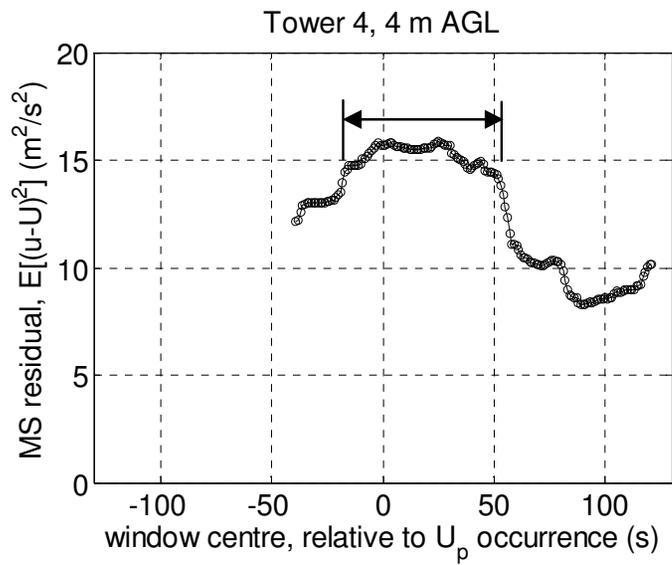
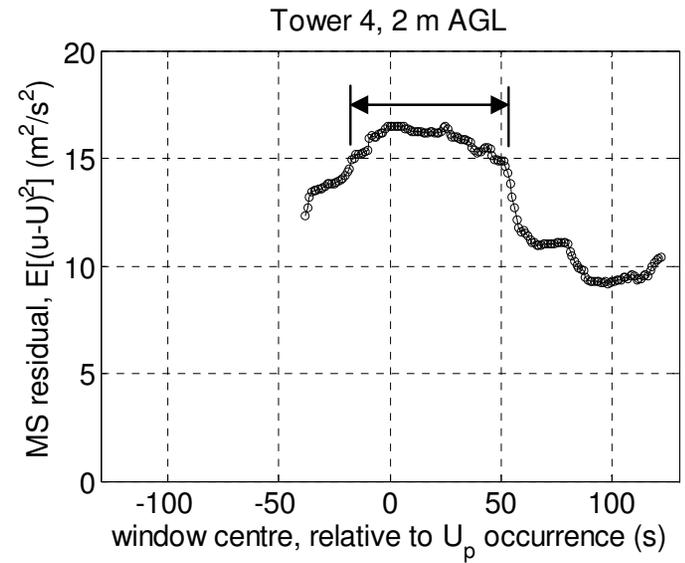
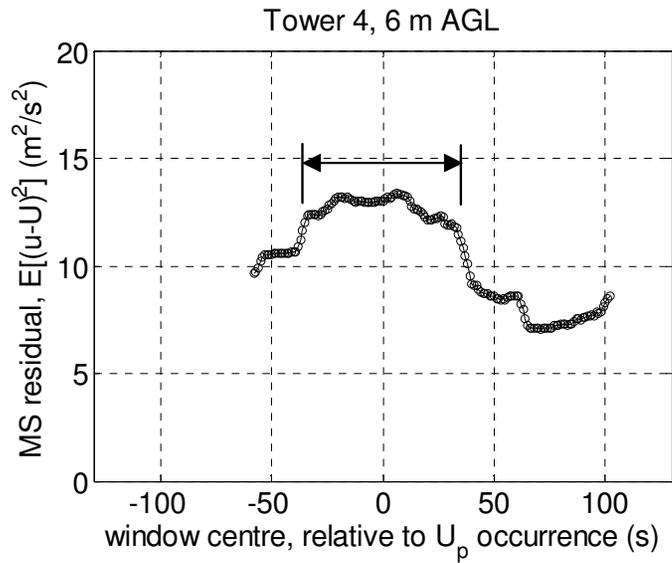


Figure 5.16 continues on following page



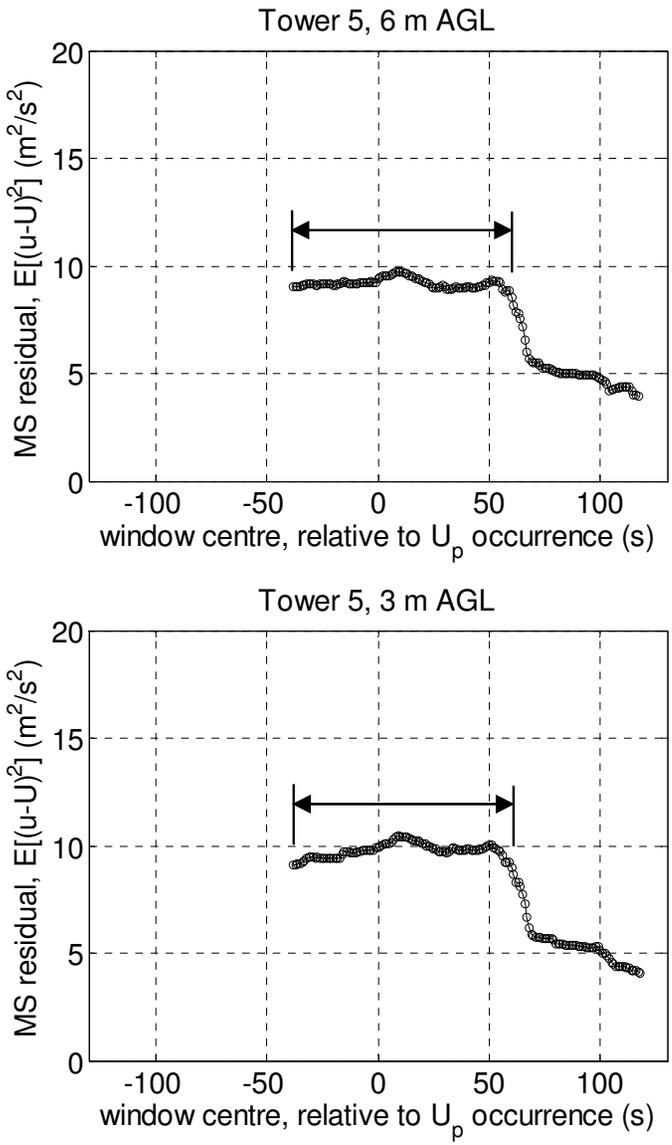
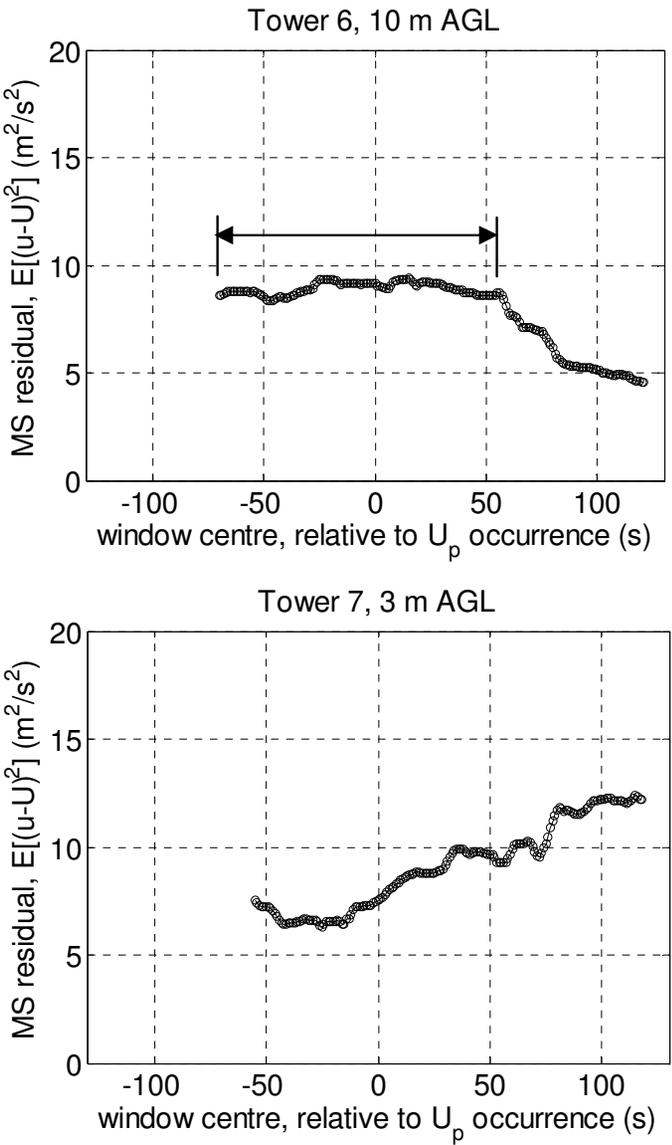


Figure 5.16: Dependency of MS residual wind speed on averaging window location (2002 RFD; results shown for averaging window location moved over the half-duration)

Figure 5.17: Dependency of MS residual wind speed on averaging window duration (WT1 DOS)

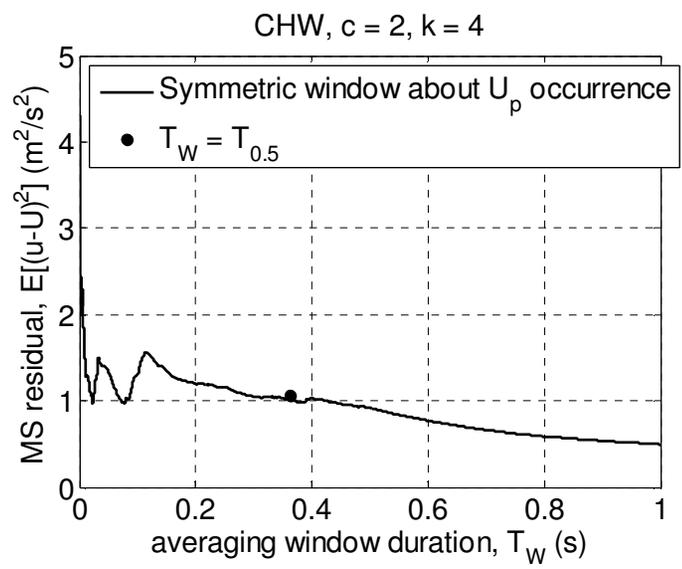
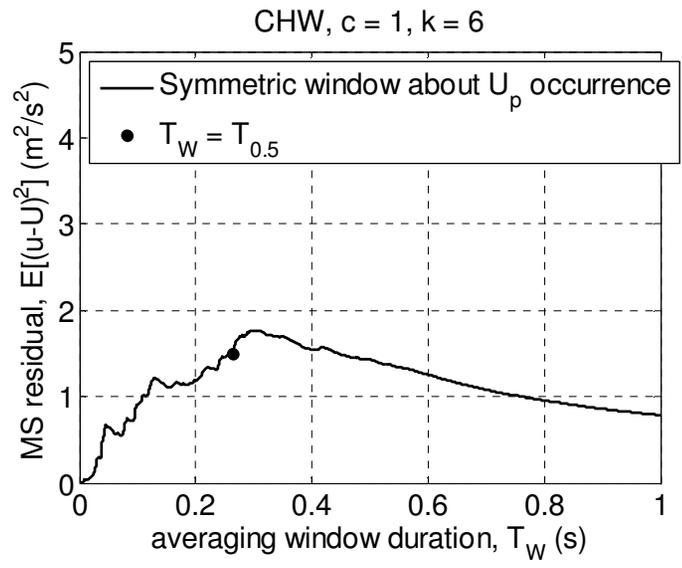
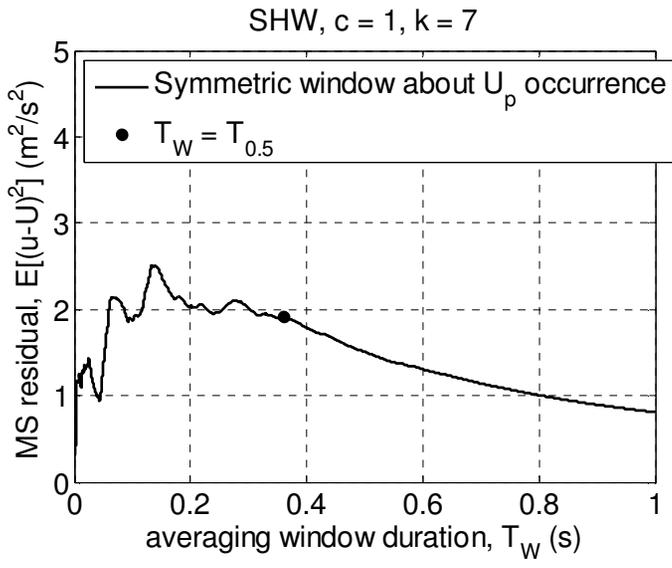
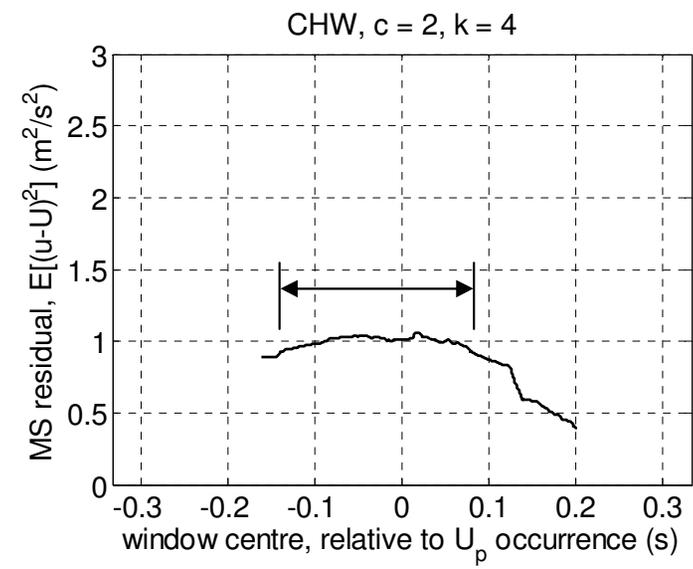
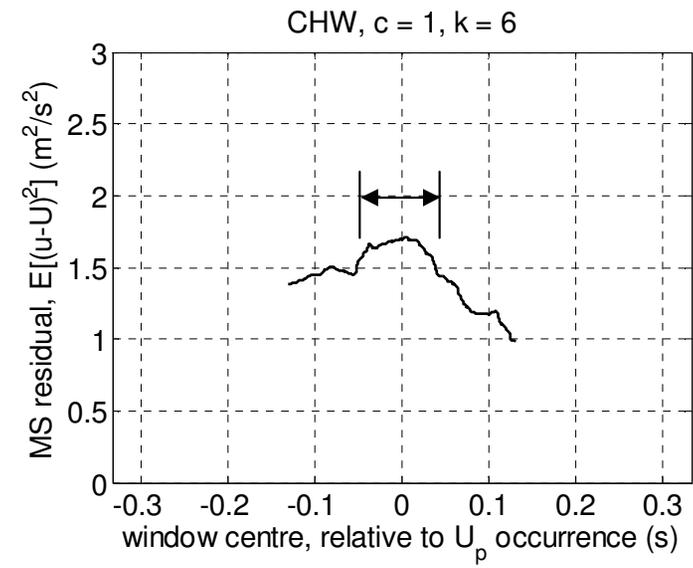
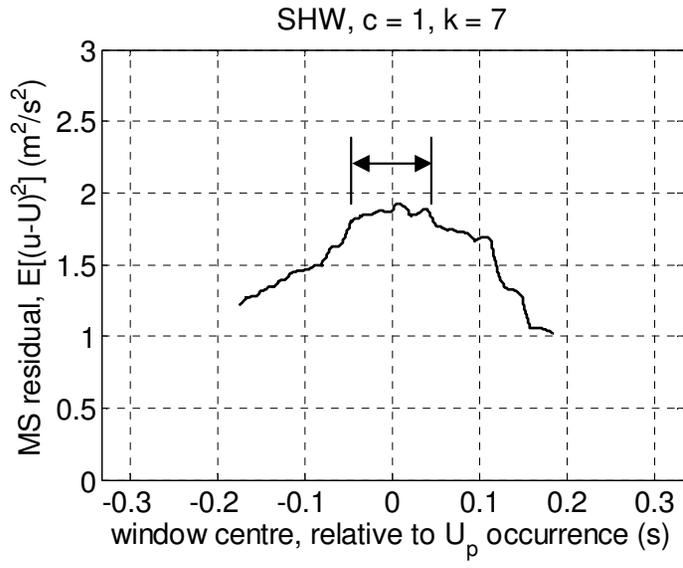


Figure 5.18: Dependency of MS residual wind speed on averaging window location
(WT1 DOS)



5.4.2 Residual wind speed distribution

Section 5.4.1 showed some observed and simulated residual wind speed histories that are weakly stationary, locally about the occurrence of the peak running mean wind speed. As explained by Priestley (1988, Section 1.3), a weakly stationary random process is completely stationary, provided it is also a Gaussian (i.e. normal) process. In this section, residual wind speed histories that conform to an equivalent Gaussian distribution are shown to exist.

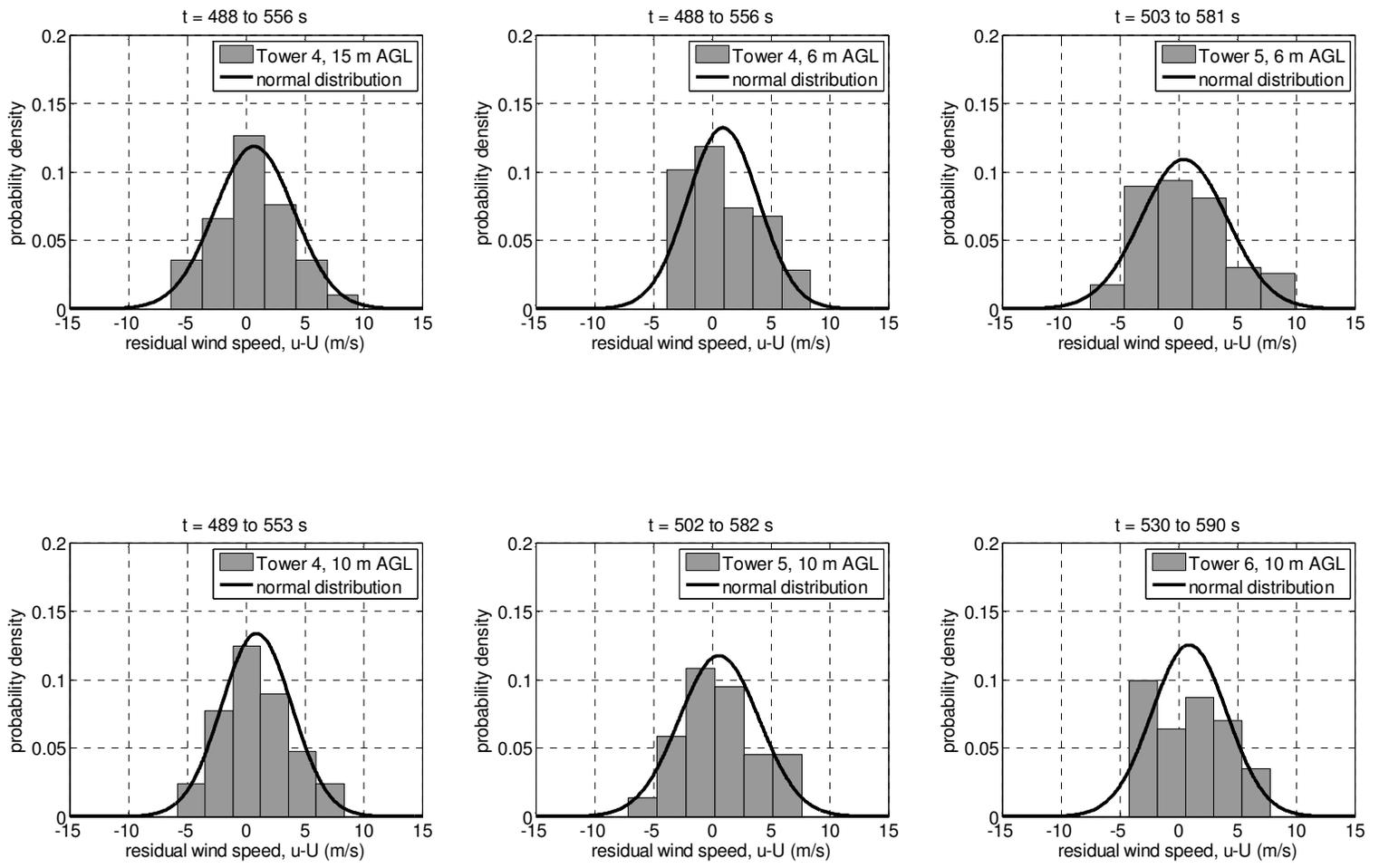
Regarding histograms in general, the choice of bin width can reveal different features of a signal. Theoretical estimates of optimal bin width are available in the literature. Residual wind speed bin widths were determined with Equation (6) from Scott (1979). Probability density is defined as shown by Eq. (5.8). The area covered by all the bins in a given probability density distribution sums to unity.

$$\text{probability density} \equiv \frac{\text{no. of samples in a given bin}}{(\text{total no. of samples}) \cdot (\text{bin width})} \quad (5.8)$$

The distribution of the residual wind speed component, $u(t)-U(t)$, was assessed by plotting the frequency of occurrence of a given wind speed fluctuation. Fig. 5.19 shows histograms for signals that were locally-stationary about the occurrence of U_p . The histograms only included the near- U_p residual fluctuation segments indicated by arrows on Fig. 5.16. The equivalent normal probability density function, with mean and standard deviation calculated from each residual wind speed record, was plotted against each histogram. By definition, a normal distribution is symmetric about the mean and has no skewness.

For the WT1 DOS, Fig. 5.20 shows the histograms for the residual fluctuation segments indicated by arrows on Fig. 5.18. The equivalent normal probability density function, with mean and standard deviation calculated from each residual wind speed record, is plotted against each histogram. All WT1 DOS histograms were uni-modal. The first and third histograms in Fig. 5.20 had mean values that exceeded zero by approximately 0.5 m/s, suggesting a small bias towards positive fluctuations near the occurrence of U_p .

Figure 5.19: Residual wind speed distribution
(2002 RFD, locally-stationary near- U_p durations only)



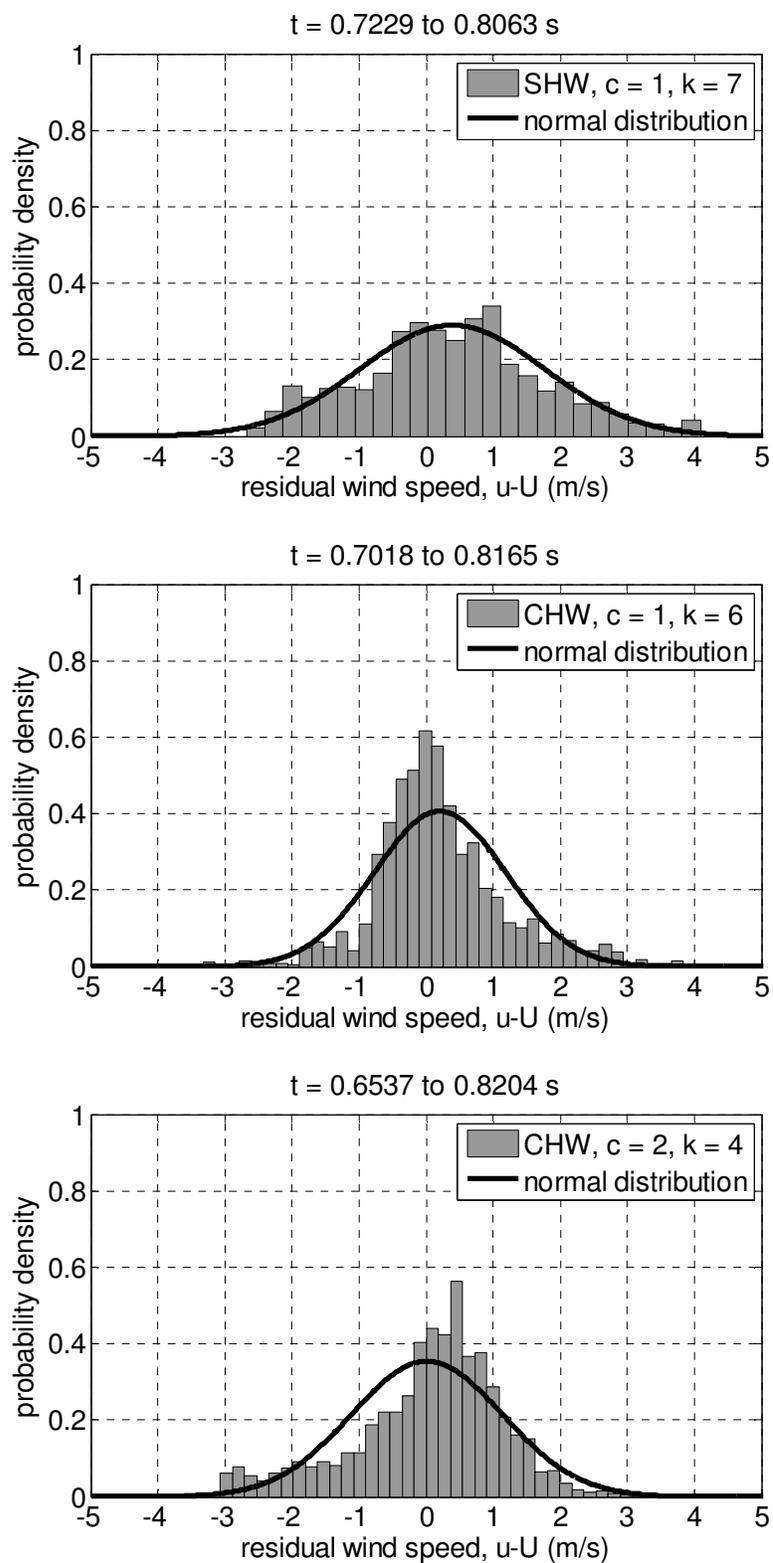


Figure 5.20: Residual wind speed distribution
(WT1 DOS, locally-stationary near- U_p duration only)

The first histogram, from the probe at mid-span, was symmetric and conformed to an equivalent Gaussian distribution. The second histogram exhibited a slight positively-skewed and leptokurtic distribution. Relative to the Gaussian distribution, a greater probability of near-mean values and a lesser probability of intermediate values were evident. However, a relatively greater probability of extreme values (positive excess kurtosis) was not as evident. The third histogram exhibited asymmetry at its extremes, indicating that negative extreme fluctuations were more probable than positive extreme fluctuations. This distribution was as leptokurtic as the previous one for the mirror image position about the wind tunnel centreline.

This analysis confirmed that some downdraft outflow residual wind speed history segments, which were locally-stationary and near the instant of peak gust occurrence, conformed to an equivalent normal distribution. In particular, histograms for central locations in the tower line at, or above, 10 m AGL were reasonably symmetric, conformed to their equivalent normal distribution, and did not show distortions that may arise from lack of stationarity (e.g. large excess kurtosis or multiple modes). Histograms for the simulated flow were adequate.

5.4.3 Residual wind speed relative to mean wind speed

Peak gust and peak running mean wind speeds were determined for all simulation trials and configurations. The portion of the peak wind speed values in the WT1 DOS attributable to the residual component was determined (Fig. 5.21). The largest peak wind speeds occurred at the configurations where the probe was closest to the tunnel floor. For $c = 1$ and 2, $\langle u_p \rangle$ exceeded $\langle U_p \rangle$ by approximately 30 % of the latter. Below the axis of the dominant vortex, peak wind speed diminished with increasing height as expected.

A gust factor indicated the magnitude of the residual component relative to the mean component. Gust factor was found from a ratio of the peak wind speed to the peak running mean wind speed, as shown by Eq. (5.9). By using peak values, this definition related two quantities of primary interest, and was a simple and convenient metric.

$$G = \frac{u_p}{U_p} \quad (5.9)$$

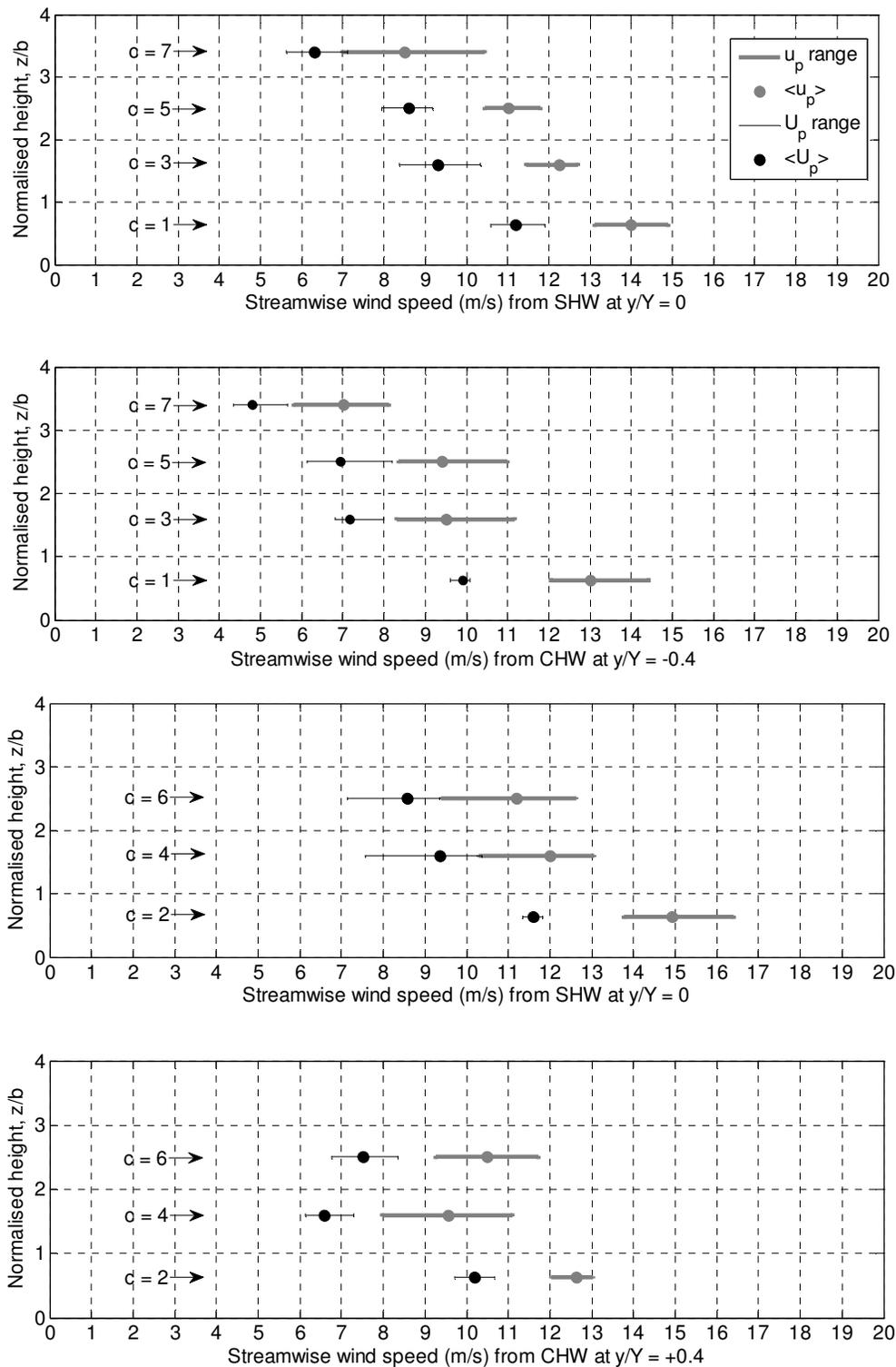


Figure 5.21: Vertical profiles of peak wind speed (WT1 DOS)

N.B. A dot represents the ensemble-average for each configuration. The attached bars indicate the range of peak values in that ensemble.

For $c = 1$ and 2 in Fig. 5.22, $\langle G \rangle$ generally varied between 1.25 and 1.45. For the 2002 RFD, H2008 reported $G \approx 1.25$ for a height range of 2 to 15 m AGL. Ensemble-averaged gust factor and gust factor variability appeared to be directly related to height above ground. $\langle G \rangle$ approached a maximum value of 1.5. The range of G over an ensemble tended to increase fairly consistently with increasing height.

H2008 extended the traditional definition of turbulence intensity (for a statistically stationary record) to examine non-stationary wind speed. Eq. (5.10) defines time-varying turbulence intensity. The overbar here denotes a moving-average with T_w from Section 5.2.5.2.

$$I_u(t) = \frac{\sqrt{\overline{(u(t) - U(t))^2}}}{U(t)} = \frac{(u(t) - U(t))_{\text{RMS}}}{U(t)} \quad (5.10)$$

This definition of turbulence intensity is an instantaneous ratio of time-varying standard deviation and mean. Standard deviation is a simple measure of fluctuation magnitude, but it provides no information about whether deviations are exceedances or deficits from the mean. Where the number of exceedances and deficits from the mean are significantly unequal, standard deviation does not provide a fully adequate description of the process.

Thus, Eq. (5.10) is relevant for residual wind speed histories that are symmetrically-distributed, as discussed in Section 5.4.2. Furthermore, large I_u results from the following two possibilities: (1) large $(u-U)_{\text{RMS}}$ with moderate U , or (2) small U with moderate $(u-U)_{\text{RMS}}$. At the least, some commentary on the relative importance of the numerator and denominator, at instants of interest, helps clarify this ambiguity.

The 2002 RFD had peak I_u in excess of 30 % (Fig. 5.23). By examining the time variations of the signals in Fig. 5.23, it was apparent where peak I_u resulted from either a RMS residual peak or a U trough. Moreover, I_u did not peak — it remained moderate at 10 to 15 % — when U_p occurred. For the WT1 DOS, peak I_u was between 20 and 30 % as indicated by Fig. 5.24. When U_p occurred, I_u was between 8 to 15 %.

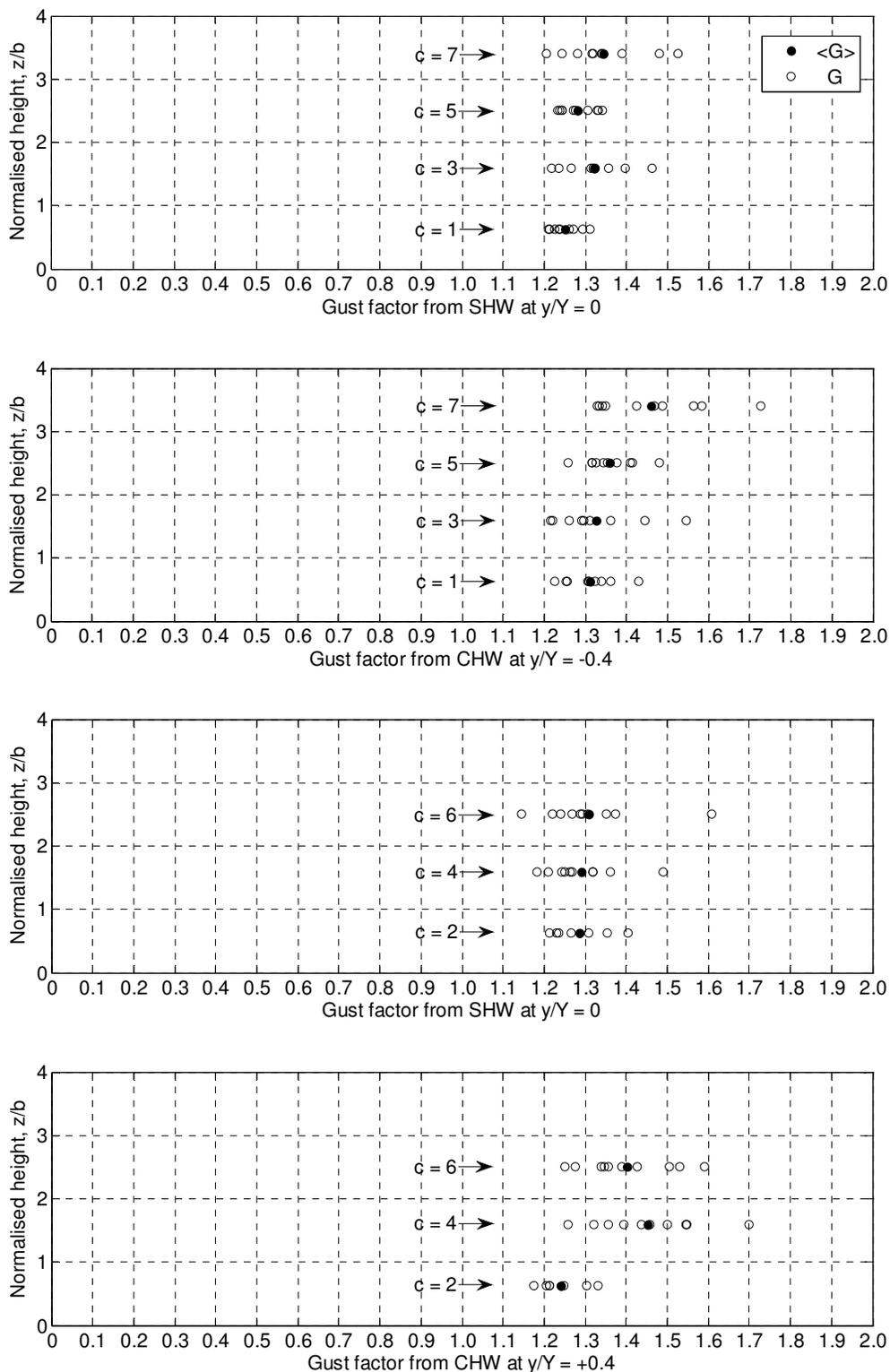


Figure 5.22: Vertical profiles of gust factor (WT1 DOS)

N.B. An unfilled circle represents gust factor for an individual trial. A filled circle represents gust factor found from ensemble-averaged values.

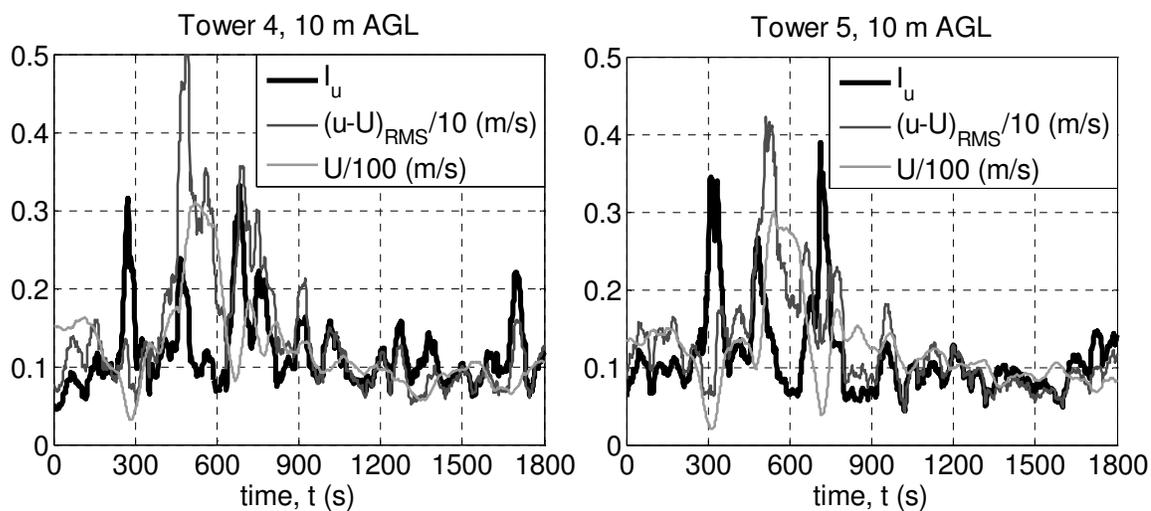


Figure 5.23: Turbulence quantities and moving-averaged wind speed histories
(2002 RFD)

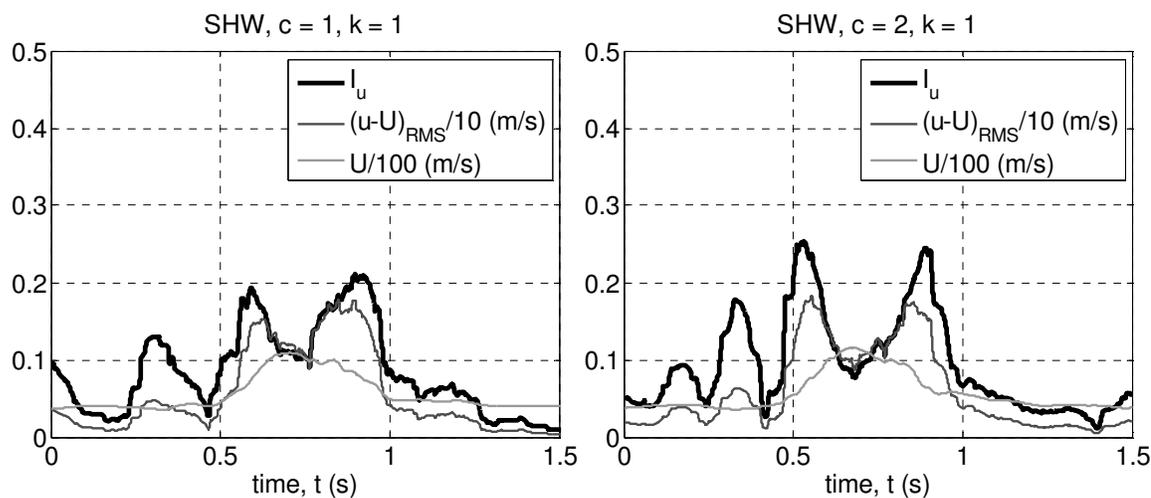


Figure 5.24: Turbulence quantities and moving-averaged wind speed histories
(WT1 DOS)

5.4.4 Correlation and spectral analysis

The residual wind speed segments, which were examined, were the locally-stationary durations near the occurrence of U_p (identified in Section 5.4.1). The auto-correlation coefficient function was computed with Eq. (5.11) and plotted in Fig. 5.25. The integral time scale was computed from Eq. (5.12).

$$\rho_{ss} = \rho_{ss}(\tau) = \frac{E[(s(t) - \bar{s}) \cdot (s(t + \tau) - \bar{s})]}{s^2}, \text{ where } s = u - U \quad (5.11)$$

$$T_I = \int_0^{\text{first abscissa crossing}} \rho_{ss}(\tau) \cdot d\tau \quad (5.12)$$

Between the limits of $\tau = 0$ and the first abscissa crossing, the integral was evaluated by trapezoidal numerical integration. T_I was a consistent value during peak wind intensity at Towers 4 and 5, and $\sim 30\%$ longer at Tower 6, as summarised by Table 5.7. An identical analysis was performed with the WT1 DOS data and integral time scales were determined (Fig. 5.26 and Table 5.8).

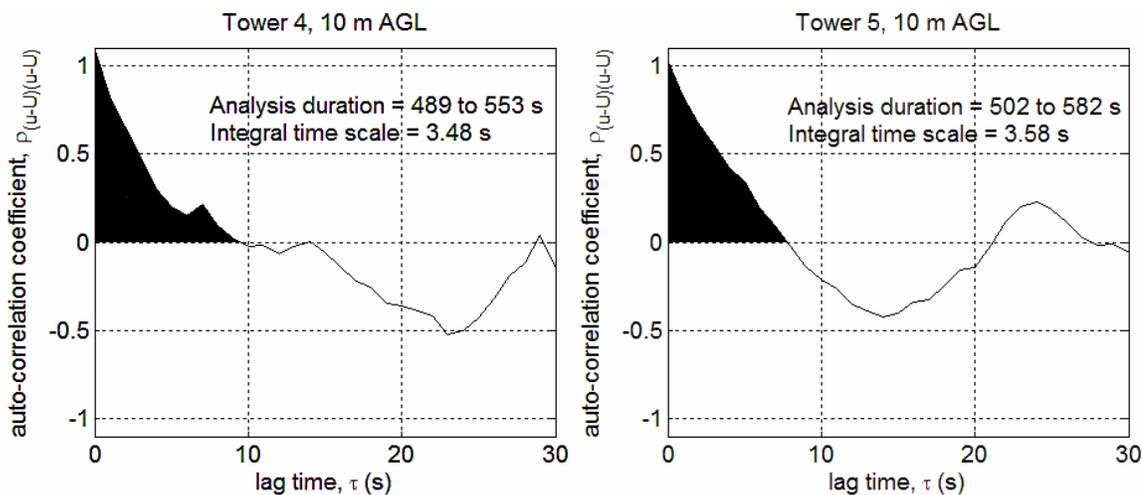
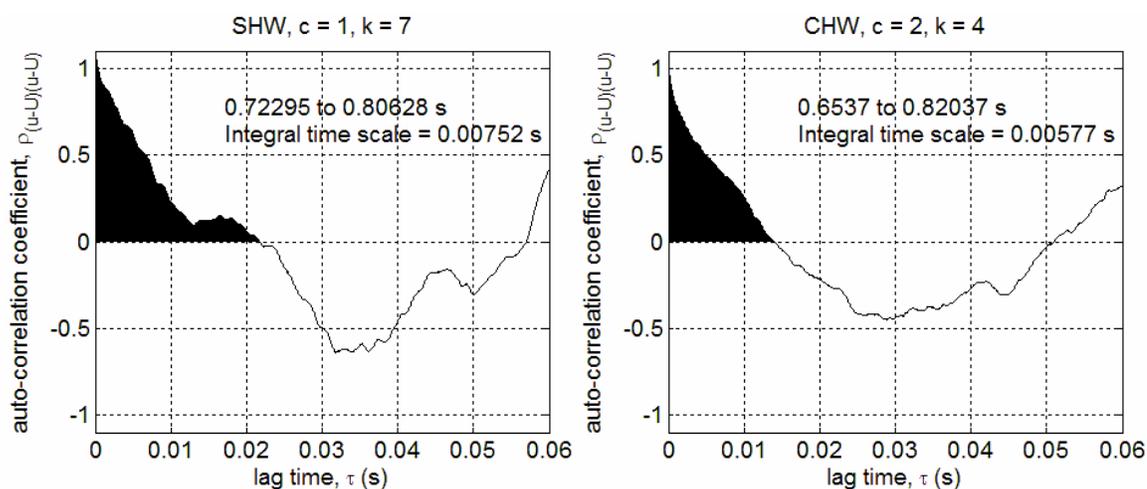


Figure 5.25: Integral time scale of residual wind speed fluctuations
(2002 RFD; locally-stationary and near- U_p duration only)

Table 5.7: Integral time scale of residual wind speed (2002 RFD)

Tower	Anemometer height (m AGL)	T_I (s)
4	6	3.24
4	10	3.48
4	15	3.25
5	6	3.37
5	10	3.58
6	10	4.50
mean		3.6

**Figure 5.26:** Integral time scale of residual wind speed fluctuations (WT1 DOS; locally-stationary and near- U_p duration only)**Table 5.8:** Integral time scale of residual wind speed (WT1 DOS)

c	probe	k	T_I (s)
1	SHW	7	0.00752
1	CHW	6	0.00189
2	CHW	4	0.00577
mean			0.005

The power spectral density of residual wind speed was determined by spectral estimation (Welch 1967). Each 2002 RFD residual wind speed record was divided into segments of thirty-two samples that overlapped by 25% of segment size. WT1 DOS residual wind speed records were broken into overlapping segments of two-hundred fifty-

six samples. A Hamming window (to reduce the spectral bias that may arise from abruptly truncating the complete record into segments) and then a Fast Fourier Transform were applied to each segment. The periodogram of each segment was calculated and averaged to obtain the spectrum estimate.

By scaling the spectrum estimate by the wind speed sampling frequency, $S_{(u-U)(u-U)}$ was computed (i.e. power per unit frequency). The auto-spectrum was normalised according to Eqs. (5.13) and (5.14). Finally, the field and simulator data were plotted together as Fig. 5.27.

$$\text{normalized spectral density} = \frac{f \cdot S_{(u-U)(u-U)}}{(u - U)^2} \quad (5.13)$$

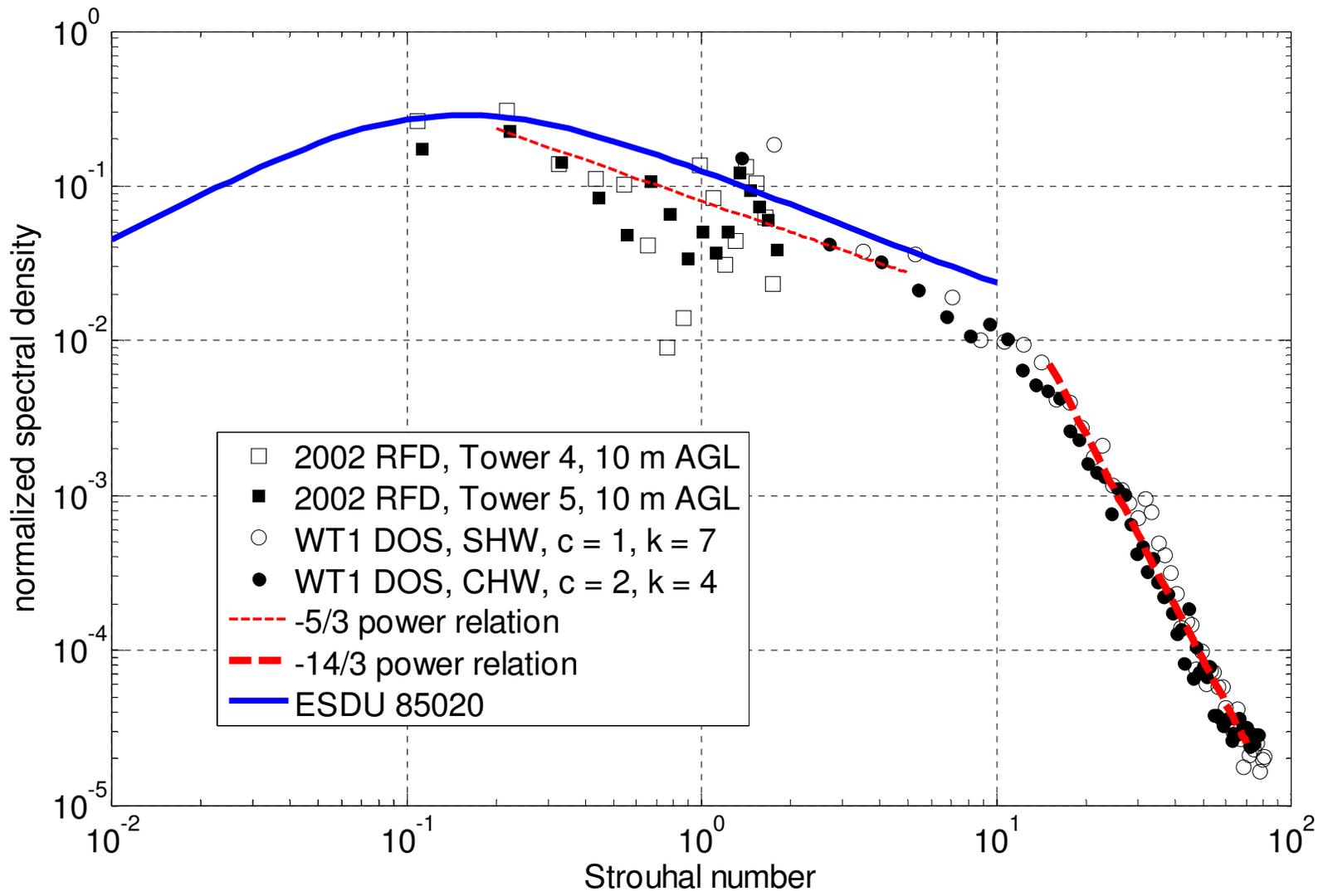
$$\text{Strouhal number} = f \cdot T_l \quad (5.14)$$

The frequency resolution of the WT1 DOS measurements was much higher than that of the 2002 RFD measurements. The normalised spectra of the two data sets matched up in a well-aligned curve. Towards the large energy-containing scales of fluid motion, the slope of the residual wind speed auto-spectra for the rear-flank downdraft outflow was approximately $-5/3$. The dissipative range was characterised by a $-14/3$ power relation.

The modified von Kármán power spectrum, for strong atmospheric boundary layer winds in a neutral atmosphere from Engineering Sciences Data Unit 85020 (ESDU 1993), is included on Fig. 5.27. This spectrum was calculated based on a surface roughness parameter ($z_0 = 0.02$ m) that was representative of Lubbock terrain (rural Texas, USA) and a mean wind speed of 30 m/s (at 10 m height above ground level). The resulting gradient height of the atmospheric boundary layer was 3218 m and the gradient wind speed was 71.3 m/s. At 10 m height AGL, the turbulence intensity was 16.6 % and the integral length scale was 125 m.

The match between the downdraft outflow and atmospheric boundary layer spectra was good. Most of the discrepancy at $0.1 > St > 5$ could be explained by the ± 20 % stated uncertainty for the latter. The ESDU procedure simply extrapolates indefinitely into the higher frequencies based on a constant power relationship, without justification, thus the ESDU spectrum is not extended into the dissipation range on Fig. 5.27.

Figure 5.27: Auto-spectral density of residual wind speed fluctuations



5.4.5 Length scaling of the fine flow features

The full-scale and simulator integral time scales near the peak gust were approximately four seconds and on the order of milliseconds, respectively. A ratio of characteristic times and a ratio of characteristic velocities were determined with Eqs. (5.15) and (5.16), respectively. Length scale was estimated with Eq. (5.17).

$$\lambda_T = \frac{(T_I)_{\text{mod el-scale}}}{(T_I)_{\text{full-scale}}} = \frac{0.00752 \text{ s}}{3.25 \text{ s}} = \frac{1}{432} \quad (5.15)$$

$$\lambda_V = \frac{(U_p)_{\text{mod el-scale}}}{(U_p)_{\text{full-scale}}} = \frac{10.8 \text{ m/s}}{31.8 \text{ m/s}} = \frac{1}{2.94} \quad (5.16)$$

$$\lambda_L = \frac{\ell_{\text{mod el-scale}}}{\ell_{\text{full-scale}}} = \frac{(T_I)_{\text{mod el-scale}} \cdot (U_p)_{\text{mod el-scale}}}{(T_I)_{\text{full-scale}} \cdot (U_p)_{\text{full-scale}}} = \lambda_T \cdot \lambda_V \approx \frac{1}{1300} \quad (5.17)$$

Full-scale and simulator characteristic times were from Table 5.7 (Tower 4, 15 m AGL) and Table 5.8 ($c = 1$, SHW, $k = 7$), respectively. Full-scale and simulator characteristic velocities were from Table 5.5 (Tower 4, 15 m AGL) and Table 5.4 ($c = 1$, SHW, mean, $K = 9$), respectively. The fine flow structure in the simulator was estimated as being 1300 times smaller in spatial size than the 2002 RFD fine flow structure.

5.5 Conclusions and future work

The performance of the WT1 DOS was thoroughly validated against field observations. At the slot nozzle exit, across most of the slot height, the mean wind speed profile exhibited uniformity within $\pm 4\%$ of the bulk wind speed. The corresponding turbulence intensity profiles lay within 2 to 6%. The wake of the slot top plate was negligible. The displacement and momentum thicknesses of the boundary layer at the bottom face of the plate were 2%, or less, of the slot height. Nozzle conditions can be refined by installing honeycomb in the slot. Given the engineering challenges of this large facility, the initial jet conditions were good.

The test section for transient downdraft outflow experiments extended to approximately 20 slot heights downstream of the nozzle. The flow visualisation confirmed that the facility generated a dominant vortex that grew with distance from the slot. The trial-to-trial repeatability of the simulator was as good as expected for a turbulent flow simulation. All wind speed records showed the expected characteristics of a downburst outflow, and running mean wind speed histories were generally within $\pm 10\%$ of their ensemble-average. Increasing the ensemble size by an order of magnitude would remove the high-frequency components of the ensemble average and allow a more accurate assessment of the ergodicity of the simulated outflow.

A moving-average procedure worked well with the simulated outflow wind speed records. The H2008 selection criteria for moving-average filter duration yielded similar dimensionless filter durations for the 2002 RFD and the WT1 DOS data. Appropriate filter duration appeared to be 25% of the half-duration ($T_{0.5}$). Beyond these specific findings, a framework for normalising and comparing full-scale and simulated wind speed histories was presented. Peak wind speed and half-duration indicated the intensity and horizontal extent of the damaging winds, respectively. The success in simulating a target signal was assessed with the slope of piecewise linear segments of the wind speed history and the duration over which wind speed exceeds a threshold.

With analysed records that exhibited statistical stationarity, the methods of classical time series analysis produced a valid quantitative description of downdraft outflow residual wind speed. Near the instant of peak gust occurrence, some 2002 RFD and WT1 DOS residual wind speed histories exhibited weak stationarity and a normal distribution, which was suggestive of complete statistical stationarity at the peak gust. For the 2002 RFD, stationarity was most evident for the wind speed records at central locations in the line of observation towers. Residual wind speed stationarity was evident at all three spanwise locations examined for the WT1 DOS.

H2008 reported a gust factor of 1.25 for the wind speed records at 2 to 15 m AGL. Ensemble-averaged gust factor in the simulator was in the range of 1.25 to 1.3 at near-surface locations. For the full-scale peak gust, time-varying streamwise turbulence intensity (I_u) was in the range of 10 to 15%. For the simulated peak gust, I_u was in the range of 8 to 15%. With respect to parameters that relate the mean and residual

components, the simulated flow matched the full-scale benchmark particularly well. Near the instant of peak gust occurrence, auto-spectra of the full-scale and simulator residual wind speed were described by a power relation (between spectral density and frequency) with an exponent of $-5/3$ for the large scales of motion and $-14/3$ for the dissipative range. The modified von Kármán power spectrum for the atmospheric boundary layer adequately represented the downdraft outflow spectral data.

Based on the half-duration of the time-varying mean wind speed, the coarse horizontal flow structure of the simulated outflow was estimated as 1200 times smaller in spatial size than the 2002 RFD. Based on the integral time scale of the residual wind speed, the simulated fine flow structure was estimated as 1300 times smaller in spatial size than the fine flow structure in the 2002 RFD. This close agreement, across the range of scales of the turbulent motion, was remarkable. Furthermore, the 8 % discrepancy between the coarse and fine length scaling was within the range attributable to uncertainty propagation for wind speed measurements in the simulator and field studies.

Keeping in mind the variability of impinging downdraft size, the 2002 RFD was at the large end of the range. For instance, Wakimoto (2001, Section 7.4) discussed RFDs of ~ 5000 m scale. Fujita and Wakimoto (1981, Figure 1) indicated microburst damage patterns of < 1000 m scale, which would suggest outflow vortex size of ~ 100 m. These microburst outflows would be modelled at 1:100 to 1:500 length scaling in the WT1 DOS, i.e. a range comparable to that of conventional atmospheric boundary layer wind tunnels.

A marriage of photographic evidence and wind speed measurements for a single full-scale event has proven to be elusive. When such simultaneous observations are available, it will be interesting to see how the present approach of estimating length scale (from time and velocity scales) compares to directly taking a ratio of characteristic lengths. To completely describe an outflow event would also require a vertical coarse length scale (e.g. outflow depth). When outflow depth is available with more accuracy, it would make sense to set (1) a vertical length scaling based on the ratio of the simulator slot height to the outflow depth and (2) a gate actuation duration that yields a horizontal coarse length scaling that is consistent with the vertical length scaling.

This chapter presented a viable approach to physical modelling of a high-intensity downdraft outflow. This is a promising method to facilitate structural model testing. Alternatively, an impinging jet approach is clearly favourable when better similarity of the downdraft and outflow are essential to the goals of the experiment. The additional cost exacted for this improvement is estimated as one order of magnitude in facility footprint area and two orders of magnitude in price to achieve an equivalent scaling.

5.6 References

- Bendat, J.S. and Piersol, A.G. (1986), *Random data: analysis and measurement procedures*, 2nd edition, John Wiley & Sons, New York, NY, USA, xvii, 566 pp.
- Choi, E.C.C. and Hidayat F.A. (2002), “Dynamic response of structures to thunderstorm winds”, *Prog. Struct. Engng Mater.*, **4**, 408-416.
- Engineering Sciences Data Unit (1993), “Characteristics of atmospheric turbulence near the ground”, ESDU 85020 with Amendments A to F, London, UK.
- Fujita, T.T. (1981), “Tornadoes and downbursts in the context of generalized planetary scales”, *J. Atmos. Sci.*, **38**(8), 1511-1534.
- Fujita, T.T. and Wakimoto, R.M. (1981), “Five scales of airflow associated with a series of downbursts on 16 July 1980”, *Mon. Wea. Rev.*, **109**, 1438-1456.
- Holmes, J.D., Hangan, H.M., Schroeder, J.L., Letchford, C.W., and Orwig, K.D. (2008), “A forensic study of the Lubbock-Reese downdraft of 2002”, *Wind Struct.*, **11**(2), 137-152.
- Letchford, C.W. and Chay, M.T. (2002), “Pressure distributions on a cube in a simulated thunderstorm downburst. Part B: moving downburst observations”, *J. Wind Eng. Ind. Aerodyn.*, **90**, 733-753.
- Letchford, C.W., Mans, C., and Chay, M.T. (2002), “Thunderstorms – their importance in wind engineering”, *J. Wind Eng. Ind. Aerodyn.*, **90**, 1415-1433.
- Lin, W.E. and Savory, E. (2006), “Large-scale quasi-steady modelling of a downburst outflow using a slot jet”, *Wind Struct.*, **9**(6), 419-440.
- Lin, W.E., Orf, L.G., Savory, E. and Novacco, C. (2007), “Proposed large-scale modelling of the transient features of a downburst outflow”, *Wind Struct.*, **10**(4), 315-346.
- Mason, M.S., Letchford, C.W., and James, D.L. (2005), “Pulsed wall jet simulation of a stationary thunderstorm downburst, Part A: Physical structure and flow field characterization”, *J. Wind Eng. Ind. Aerodyn.*, **93**, 557-580.
- McConville, A.C., Sterling, M. and Baker, C.J. (2009), “The physical simulation of thunderstorm downbursts using an impinging jet”, *Wind Struct.*, **12**(2), 133-149.
- Orwig, K.D. and Schroeder, J.L. (2007), “Near-surface wind characteristics of extreme thunderstorm outflows”, *J. Wind Eng. Ind. Aerodyn.*, **95**, 565-584.
- Priestley, M.B. (1988), *Non-linear and non-stationary time series analysis*, Academic Press, London, UK, viii, 237 pp.

- Scott, D.W. (1979), "On optimal and data-based histograms", *Biometrika* **66** (3), 605–610.
- Sengupta, A. and Sarkar, P.P. (2008), "Experimental measurement and numerical simulation of an impinging jet with application to thunderstorm microburst winds", *J. Wind Eng. Ind. Aerodyn.*, **96**, 345-365.
- Wakimoto, R.M. (2001), "Convectively driven high wind events", *Meteor. Monogr.*, **28**(50), 255-298.
- Walker, G.R. (1992), "Wind engineering beyond the boundary layer wind tunnel", *J. Wind Eng. Ind. Aerodyn.*, **41-44**, 93-104.
- Welch, P.D. (1967), "The use of Fast Fourier Transform for the estimation of power spectra: A method based on time averaging over short, modified periodograms," *IEEE Trans. Audio Electroacoustics*, **AU-15** (June), 70-73
- White, F.M. (2003), *Fluid mechanics*, 5th edition, McGraw Hill, USA, xiii, 866 pp.

CHAPTER 6

CLOSURE

6.1 Summary

This thesis documented the implementation and validation of a novel physical test facility. A slot jet wind tunnel was developed for downdraft outflow simulation. The main problem addressed was that of generating a flow that is (1) a realistic representation of the high-intensity, near-surface winds in a convective downdraft outflow and (2) sufficiently large in physical size, such that it is feasible to construct appropriately-scaled structural models for subsequent testing in the downdraft outflow simulator.

6.2 Conclusions

Minimal discrepancies were found between the streamwise mean velocity profiles for the developed plane wall jet ($x/b \geq 50$) and the developing radial wall jet ($r/D = 2.0$). Near the wall, the difference between mean velocity profiles from plane and radial wall jets was essentially less than the experimental uncertainty. The uncertainty of the hot-wire anemometry measurements presented in this thesis was typically less than $\pm 8\%$ of the measured value.

Self-similarity of plane wall jet turbulence quantity profiles depended upon the slot top boundary condition. Turbulent quantity profiles tended towards a self-similar state for an infinitely-thick slot lip, whereas turbulent quantities continued to increase in magnitude with streamwise distance for a thin slot lip. The slot top boundary condition did not appear to significantly affect the inner layer of the wall jet, though. The inner layer is the region that is critical for wind engineering applications.

Turbulence quantity profiles for the developing radial wall jet ($r/D \approx 2.0$) provided the best match with the well-developed plane wall jet profiles. This was where the maximum turbulence intensities and turbulent kinetic energy production occurred for the radial wall jet. The shape of plane and radial wall jet turbulence profiles showed general likeness.

The findings regarding the fundamental aspects of steady wall jets were applied to the quasi-steady modelling of downdraft outflows. A slot jet approach addressed the problem

of generating a flow, which closely represents a downburst outflow and is of sufficient size for wind engineering applications. Time-averaged downdraft outflow wind speed profiles, from field observations, were reproduced with a slot jet apparatus. Direct comparison of the developed plane wall jet profiles with profiles in the intense flow region of radial wall jets indicated good agreement. The turbulence quantity profiles of the developed plane wall jet matched the corresponding profiles from the developing radial wall jet slightly downstream of where the maximum radial mean velocity was located in field observations.

Implementation of a translating gate at the slot nozzle allowed simulation of a transient outflow gust. Velocity profiles and histories were comparable to available full-scale data. The present results suggested that the duration of the gate actuation opening phase should be slightly lengthened from the values used in the present study.

A steady outflow profile generally had a fuller shape than the peak maximum profiles from the transient gust simulations. With respect to profile shape and height where the largest velocity value occurred, steady flow simulations adequately represented outflows from non-translating downdrafts. A more accurate simulation requires consideration of the transient nature of downdraft outflows.

The performance of the Wind Tunnel 1 downdraft outflow simulator (WT1 DOS) met expectations. The flow quality at the slot nozzle exit was thoroughly examined. Across the central 60 % of the slot height, the variability of the mean wind speed profile was within ± 4 % of the bulk mean wind speed. Turbulence intensity was in the range of 2 to 6 %. The wake of the slot top was negligible at downstream locations of interest. The trial-to-trial repeatability of the simulator was as good as expected for a turbulent flow simulation. All wind speed records showed the expected characteristics of a downburst outflow, and running mean wind speed histories were generally within ± 10 % of their ensemble-average.

A moving-average procedure was appropriate for decomposing the measured wind speed histories into mean and fluctuating components. In dimensionless terms, the optimal moving-average filter durations for the 2002 rear-flank downdraft near Lubbock (2002 RFD) and the WT1 DOS data sets were almost identical. Generally, an appropriate filter duration appeared to be 25 % of the half-duration ($T_{0.5}$).

Classical time series analysis methods were appropriate for describing the fluctuating wind speed component. Near the instant of peak gust occurrence, some 2002 RFD and WT1 DOS residual wind speed histories exhibited weak stationarity and a normal distribution, which was suggestive of complete statistical stationarity at the peak gust. For the 2002 RFD, stationarity was most evident for the wind speed records at central locations in the line of observation towers. Residual wind speed stationarity was evident at all three spanwise locations examined for the WT1 DOS.

With respect to parameters that relate the mean and residual components, the simulated flow matched the full-scale benchmark particularly well. Gust factor was approximately 1.25 for both the WT1 DOS and the 2002 RFD. Time-varying I_u was between 8 to 15 % for the WT1 DOS and between 10 to 15 % for the 2002 RFD.

Near the instant of peak gust occurrence, auto-spectra of the full-scale and simulator residual wind speed were described by a power relation (between spectral density and frequency) with an exponent of $-5/3$ for the large scales of motion and $-14/3$ for the dissipative range. The modified von Kármán power spectrum for the atmospheric boundary layer adequately represented the downdraft outflow spectral data.

Agreement in length scaling across a wide range of scales of the turbulent flow was found. The length scale of the coarse horizontal flow structure of the simulated outflow was estimated as 1200 times smaller in spatial size than that of the 2002 RFD. Based on the integral time scale of the residual wind speed, the length scale of the fine flow structure of the simulated outflow was estimated as 1300 times smaller in spatial size than the fine flow structure in the 2002 RFD. The 8 % discrepancy, between the length scalings of the coarse and fine flow structure, was within the range attributable to measurement uncertainty.

With respect to the observed variation of impinging downdraft size, the 2002 RFD near Lubbock was at the large end of the range. It is important to take this into account, because a larger length scaling can result from either generating a physically larger model flow or making a comparison to a physically smaller full-scale flow. Based on available observations, it is plausible to model microburst outflows at 1:100 to 1:500 length scaling in the WT1 DOS, i.e. a range comparable to that of conventional boundary layer wind tunnels.

6.3 Recommendations

It is recommended that further fundamental investigations of the plane wall jet focus on the sensitivity of the jet evolution to the facility characteristics. A parametric study of the effect of t/b on the jet spread and decay would address a gap in the literature. In addition, the effect of incrementally varying the slot top condition on self-similarity of downstream turbulence intensity profiles could be investigated.

Increasing the ensemble size by an order of magnitude in WT1 DOS would remove the high-frequency components of the ensemble average. This would allow a more accurate assessment of the ergodicity of the simulated outflow. In practice, it is desirable to perform the minimum number of simulator trials to obtain test results at a desired confidence level.

When simultaneous photographic evidence and wind speed measurements for a single downdraft outflow is obtained, it will be interesting to see how the present approach of estimating length scale (from time and velocity scales) compares to directly taking a ratio of characteristic lengths. To completely describe an outflow event would also require a vertical coarse length scale (e.g. outflow depth). When outflow depth is available with more accuracy, it would make sense to set (1) a vertical length scaling based on the ratio of the simulator slot height to the outflow depth and (2) a gate actuation duration that yields a horizontal coarse length scaling that is consistent with the aforementioned vertical length scaling.

Furthermore, when sufficient field observations are available to classify the wind velocity field of downdraft and downdraft line outflows into critical wind loading cases for specific types of built structures, it would be sensible to investigate modifications to the slot jet apparatus to produce these critical cases. Presently, the Wind Tunnel 1 downdraft outflow simulator at UWO can be used to expose a structural model to a basic downdraft outflow wind load. Whether the transient features of a downdraft outflow need to be considered in structural design depends on the characteristics of the structure (e.g. modes of structural vibration and how the corresponding natural frequencies relate to the forcing from a downdraft outflow). This type of investigation and comparison to wind loading from a conventional atmospheric boundary layer, using the same structural model and test facility, is the most immediate challenge.

CURRICULUM VITÆ

Name: William E. Lin

Place of Birth: Vancouver, British Columbia, Canada

Year of Birth: 1980

Post-secondary Education and Degrees: University of Waterloo
Waterloo, Ontario, Canada
1998-2003 B.A.Sc.

The University of Western Ontario
London, Ontario, Canada
2003-2005 M.E.Sc.

The University of Western Ontario
London, Ontario, Canada
2006-2010 Ph.D.

Selected Honours and Awards: Natural Sciences and Engineering Research Council of Canada
Postgraduate Scholarship
2008-2010

Association of Universities and Colleges of Canada
Public Safety Canada Research Fellowship
2007-2008

Related Work Experience Teaching Assistant
The University of Western Ontario
2003-2009

Selected Publications:

Lin, W.E. and Savory, E. (2010), Physical modelling of a downdraft outflow with a slot jet, *Wind Struct.* in press.

Lin, W.E., Orf, L.G., Savory, E. and Novacco, C. (2007), Proposed large-scale modelling of the transient features of a downburst outflow, *Wind Struct.* 10:315-346.

Lin, W.E. and Savory, E. (2006), Large-scale quasi-steady modelling of a downburst outflow using a slot jet, *Wind Struct.* 9:419-440.

Lin, W.E. and Savory, E. (2007), A slot jet facility for downburst outflow simulation, *12th International Conference on Wind Engineering*, 1-6 July, Cairns, Australia, Proceedings Vol. 2: 1439-1446.